National Library
of Canada

Canadian Theses Service

Ottawa, Canada
K1A 0N4

Bibliothèque nationale
du Canada

Service des thèses canadiennes

NOTICE

The quality of this microform is heavily dependent upon the quality of the original thesis submitted for microfilming. Every effort has been made to ensure the highest quality of reproduction possible.

If pages are missing, contact the university which granted the degree.

Some pages may have indistinct print especially if the original pages were typed with a poor typewriter ribbon or if the university sent us an inferior photocopy.

Previously copyrighted materials (journal articles, published tests, etc.) are not filmed.

Reproduction in full or in part of this microform is governed by the Canadian Copyright Act, R.S.C. 1970, c. C-30.

AVIS

La qualité de cette microforme dépend grandement de la qualité de la thèse soumise au microfilmage. Nous avons tout fait pour assurer une qualité supérieure de reproduction.

S'il manque des pages, veuillez communiquer avec l'université qui a conféré le grade.

La qualité d'impression de certaines pages peut laisser à désirer, surtout si les pages originales ont été dactylographiées à l'aide d'un ruban usé ou si l'université nous a fait parvenir une photocopie de qualité inférieure.

Les documents qui font déjà l'objet d'un droit d'auteur (articles de revue, tests publiés, etc.) ne sont pas microfilmés.

La reproduction, même partielle, de cette microforme est soumise à la Loi canadienne sur le droit d'auteur, SRC 1970, c. C-30.

NL-339 (r. 88/04)

Canada

THE UNIVERSITY OF ALBERTA

A CONTRIBUTION TO THE INTERPRETATION OF MAGNETOVARIATION FIELDS

by

Ⓒ XI-SHUO WANG

A THESIS
SUBMITTED TO THE FACULTY OF GRADUATE STUDIES AND RESEARCH
IN PARTIAL FULFILMENT OF THE REQUIREMENTS FOR THE DEGREE
OF DOCTOR OF PHILOSOPHY
IN
GEOPHYSICS

PHYSICS

EDMONTON, ALBERTA
FALL 1987

Permission has been granted to the National Library of Canada to microfilm this thesis and to lend or sell copies of the film.

The author (copyright owner) has reserved other publication rights, and neither the thesis nor extensive extracts from it may be printed or otherwise reproduced without his/her written permission.

L'autorisation a été accordée à la Bibliothèque nationale du Canada de microfilmer cette thèse et de prêter ou de vendre des exemplaires du film.

L'auteur (titulaire du droit d'auteur) se réserve les autres droits de publication; ni la thèse ni de longs extraits de celle-ci ne doivent être imprimés ou autrement reproduits sans son autorisation écrite.

ISBN 0-315-40997-5

June 15, 1987

Dr. Kanasewich :

The Graduate Studies indicated that for the microfilming purpose of my Ph.D thesis, I need a written permission for reproducing the Fig. 10 in your following paper :

Kanasewich, E.R., Hajnal, Z., Green, A.G., Cummings, G.L., Mereu, R.F., Clowes, R.M., Morel-a-l'Huissier, Chiu, S., Congram, A.M., Macrides, C.G. and M. Shahriar, Seismic studies of the crust under the Williston Basin, Can. J. Earth Sci., submitted 1987.

I would appreciate it very much if you kindly write me such a permission.

Best regards.

Yours truly

XI-SHUO WANG
(XI-SHUO WANG)

Permission Granted
E. R. Kan

THE UNIVERSITY OF ALBERTA

RELEASE FORM

NAME OF AUTHOR XI-SHUO WANG

TITLE OF THESIS A CONTRIBUTION TO THE INTERPRETATION OF MAGNETOVARIATION FIELDS

DEGREE FOR WHICH THESIS WAS PRESENTED DOCTOR OF PHILOSOPHY

YEAR THIS DEGREE GRANTED FALL 1987

Permission is hereby granted to THE UNIVERSITY OF ALBERTA LIBRARY to reproduce single copies of this thesis and to lend or sell such copies for private, scholarly or scientific research purposes only.

The author reserves other publication rights, and neither the thesis nor extensive extracts from it may be printed or otherwise reproduced without the author's written permission.

(SIGNED) XI-SHUO WANG

PERMANENT ADDRESS:

Geophysical Institute, State
Seismological Bureau, Beijing.
P. R. CHINA

DATED JUNE 10, 1987

THE UNIVERSITY OF ALBERTA

FACULTY OF GRADUATE STUDIES AND RESEARCH

The undersigned certify that they have read, and recommend to the Faculty of Graduate Studies and Research, for acceptance, a thesis entitled A CONTRIBUTION TO THE INTERPRETATION OF MAGNETOVARIATION FIELDS submitted by XI-SHUO WANG in partial fulfilment of the requirements for the degree of DOCTOR OF PHILOSOPHY in GEOPHYSICS.

D.I. Gough

Supervisor

F.E. Vermeulen

R C Bailey

External Examiner

Date JUNE 10, 1987

DEDICATION

To

My parents

ABSTRACT

The magnetovariation fields observed by a two-dimensional array are separated and the internal fields are inverted to the causative current systems. The normal parts of the fields are estimated by plane-wave expansion. The analysis of normal fields also provides criteria for choosing suitable frequency components for further analysis. The wave-number domain analysis of the fields adjusts and separates the fields into internal and external parts. These two parts are proved to be mutually orthogonal.

The fields are inverted to horizontal current sheets in a stratified conducting Earth's model through a matrix formulation. Analytic boundary conditions for an arbitrary conductivity-depth dependence are also derived.

The fields are also inverted to 3-D linear currents and to constant-width current sheets in free space. This inversion is regulated by modified *LSI* (Least Squares with Inequality constraints) and modified *LDP* (Least Distance Programming) techniques. The systematic errors in the data are compensated by a W-stabilization procedure. The newly developed methods in chapters 3-5 are tested with models and applied to the field data. A conductive structure that crosses the Rocky Mountains in the depth range 30-120 km is located. The structure is either in the upper mantle or in the lower crust, and may be related to a seismic low velocity zone.

ACKNOWLEDGEMENT

I am greatly in debt to my supervisor Professor D.I. Gough, for his guidance and great enthusiasm for and ingenuity in science, for the financial support both at the University and during my study visits to the University of British Columbia. I thank Professor J.C. Samson, my co-supervisor, for his guidance in general and particularly in the mathematical physics aspects of the research and the writing of the thesis. I thank Professor D.W. Oldenburg for his kind help and guidance in the inversion parts of the thesis during my two visits to University of British Columbia. I warmly thank Dr. D.McA. McKirdy for his guidance (when Professor Gough was on study leave) and for continuous helpful discussion. Mrs. K. Wilson and Mr. Chen shared the data acquisition procedure and are thanked.

I thank the Killams and the Killam Scholarship Committee for the Izaak Walton Killam Memorial Scholarship which in large measure supported my graduate studies for three years at the University of Alberta. I thank the department of physics for partial financial support through a Teaching Assistantship.

Table of Contents

Chapter Page

1. INTRODUCTION 1
   - 1.1 REVIEW OF PREVIOUS WORK 2
     - 1.1.1 DATA REPRESENTATION 2
     - 1.1.2 MODELS AND INVERSION 4
   - 1.2 CONTRIBUTIONS OF THIS THESIS 9
2. NORMAL FIELD ESTIMATION IN MAGNETOVARIATION STUDIES .12
   - 2.1 PLANE WAVE EXPANSION OF THE NORMAL FIELD 13
   - 2.2 AN ALGORITHM FOR WAVE PARAMETER ESTIMATION 16
   - 2.3 STATISTICAL ANALYSIS OF NORMAL FIELDS 18
   - 2.4 COMPARISON WITH OTHER NORMAL FIELD REPRESENTATIONS 29
3. SEPARATION OF FIELDS INTO INTERNAL AND EXTERNAL PARTS 32
   - 3.1 REPRESENTATION OF A POTENTIAL FIELD IN CARTESIAN SPACE AND WAVENUMBER DOMAINS 33
   - 3.2 SEPARATION OF THE FIELD INTO EXTERNAL AND INTERNAL PARTS 35
   - 3.3 CURL-FREE ADJUSTMENT OF THE FIELD 37
   - 3.4 UNIFIED POTENTIAL AS WEIGHTED AVERAGE OF POTENTIALS OF EACH COMPONENT 40
   - 3.5 APPLICATIONS TO SYNTHETIC DATA 42
   - 3.6 EDGE EFFECTS 51
   - 3.7 APPLICATION TO FIELD DATA 52
4. INVERSION TO A SHEET CURRENT AT A SPECIFIC DEPTH 60
   - 4.1 BASIC EQUATIONS 63
   - 4.2 BOUNDARY CONDITION AT A SOURCE-FREE LAYER INTERFACE 66
   - 4.3 BOUNDARY CONDITION AT A CURRENT SHEET 68
   - 4.4 SOLUTION FOR Z IN AN UNIFORM CONDUCTIVE LAYER ..70

4.5 SOLUTION FOR Z IN FREE SPACE 72

4.6 PLANE LAYERED EARTH MODEL 73

4.7 MATRIX REPRESENTATION OF BOUNDARY CONDITIONS ...75

4.8 SOLUTION IN V SPACE 77

4.9 THE SHIELDING PROPERTY OF A LAYERED EARTH 79

4.10 CURRENT SHEET INVERSION RESULTS 86

5. INVERSION OF CHANNELLED CURRENT 96

5.1 THE LINEAR CURRENT MODEL AND OBSERVATION COORDINATE SYSTEM 97

5.2 CURRENT COORDINATE SYSTEM AND O-C TRANSFORMATION 99

5.3 FORWARD PROBLEM FOR A LINEAR CURRENT 101

5.4 FORWARD PROBLEM FOR A SHEET CURRENT OF CONSTANT WIDTH 103

5.5 THE DERIVATIVES 106

5.6 THE INVERSION 107

5.7 UNIQUENESS AND ERROR CONTROL 110

5.8 W-STABILIZATION OF THE INVERSION PROCESS 112

5.9 CONSTRAINED LEAST SQUARES PROGRAMMING 116

5.10 LEAST DISTANCE PROGRAMMING AND ERROR COMPRESSION 119

5.11 TEST INVERSION OF SYNTHESIZED DATA 122

  5.11.1 TEST 1: SINGLE LINE CURRENT MODEL 125

  5.11.2 TEST 2: SHEET CURRENT MODEL 131

  5.11.3 TEST 3: PRISM CURRENT MODEL 143

5.12 A TEST FOR CURRENT CHANNELLING BY MEANS OF THE KARHUNEN-LOEVE TRANSFORM 150

5.13 INVERSION OF SEPARATED INTERNAL FIELDS OF THE SABC ANOMALY 158

  5.13.1 DATA DESCRIPTION 159

5.13.2 INVERSION WITH LOOSE CONSTRAINTS ON DEPTH 162

5.13.3 INVERSION WITH CONSTRAINTS IN FAVOUR OF SHALLOWER MODELS 170

5.13.4 INVERSION TO CURRENT SHEET OF CONSTANT WIDTH 178

5.13.5 INVERSION WITH OTHER MODELS AND DATA SETS 182

5.14 SUMMARY OF THE GEOMETRY OF THE CURRENT CHANNEL 185

5.15 STRUCTURAL IMPLICATIONS OF THE CURRENT INVERSION 189

6. CONCLUSIONS 198

BIBLIOGRAPHY 202

APPENDIX 1: NATURE OF THE INDUCTION MATRIX D 209

APPENDIX 2: ANALYTIC SOLUTION FOR ARBITRARY DEPTH-DEPENDENCE OF THE CONDUCTIVITY 212

APPENDIX 3: W_1 VECTOR 216

List of Tables

Table — Page

2.1 Division of magnetovariation spectra into 5 period bands. 19

2.2 Energy in plane waves for the 5 period bands. 28

3.1 Correlation coefficients between original field components and those separated with and without data expansion. 52

5.1 Goodness of Fit for Test Model 1 using the *LDPNL* method. 125

5.2 Goodness of Fit for Test Model 1 using the *LSINL* method. 126

5.3 Goodness of Fit for Test Model 2, sheet width 70 km. Sheet current inverted to a line current using the *LDPNL* method 132

5.4 Goodness of Fit for Test Model 2. Sheet current inverted to a line current using the *LSINL* method 133

5.5 Goodness of Fit for Test Model 2. Sheet current inverted to a sheet current using the *LSINL* method 133

5.6 Goodness of Fit for wider (100 km) test Model 2. Sheet current inverted to a line current using the *LSINL* method 139

5.7 Goodness of Fit for wider (100 km) test Model 2. Sheet current inverted to a sheet current using the *LSINL* method 143

5.8 Goodness of Fit for Test Model 3. Prism current inverted to a line current using the *LDPNL* method 144

5.9 Goodness of Fit for Test Model 3. Prism current inverted to a line current using the *LSINL* method 144

5.10 K-L transform results 154

5.11 Goodness of Fit for the *LDPNL* inversion 164

5.12 Goodness of Fit for the *LSINL* inversion 169

5.13 Goodness of Fit for the *LSINL* inversion, PNZ biased data, weak current constraint. 176

Table Page

5.14 Goodness of Fit for the *LSINL* inversion, ZZZ biased data, weak current constraint. 177

5.15 Goodness of Fit for the *LSINL* inversion to a sheet current of 80 km width. 178

5.16 Goodness of Fit for the *LSINL* inversion to a sheet current of 80 km width. 182

List of Figures

Figure | Page

2.1 Azimuths of major axes of polarization ellipses, and horizontal projections of wave vectors for normal fields in five period bands: (a)T ≥ 65.79, (b)37.00 - 54.79, (c)16.45 - 37.00, (d)10.53 - 16.45, (e)T ≤ 10.53 minutes. The lengths of lines are proportional to (i)averaged semi-major axis of polarization ellipse for azimuths of the axis; and (ii)magnitude of horizontal normal field for horizontal projection of wave vectors. Both are normalized within each period band. 21

2.2 $\mathrm{Im}(K_z)$ (km^{-1}) versus period, 102 periods in total. (a)Results for first term plane-waves, 66 are internal dominant ($\mathrm{Im}(K_z) \geq 0$) and 36 are external dominant ($\mathrm{Im}(K_z) \leq 0$); (b)Results for second term plane-wave, 25 are internal dominant and 27 are external dominant. 22

2.3 Horizontal wavelength (km) vs. period for (a)the first and (b)the second plane-wave terms. Internal- and external-dominant terms are plotted separately (see Fig.2.2). 25

3.1 (a)Calculated field components for a horizontal internal line current of 40 kA flowing 80 km below the (X-Y) plane. (b)Separated field components for the same current. Unit: nT. 44

3.2 (a)Calculated field components for a horizontal external line current of 90 kA flowing 90 km above the (X-Y) plane. (b)Separated field components for the same current. Unit: nT. 45

Figure Page

3.3 (a)Components of the combined original field of external and internal line currents (see Figs.3.1 and 3.2). (b)Curl-free horizontal components of the combined fields. Unit: nT. 46

3.4 (a)Calculated field components for a three-segment 40 kA internal line current, and horizontal projection of the current. (b)Separated field components for the same current. Unit: nT. 48

3.5 (a)Calculated field components for a three-segment 90 kA external line current, and horizontal projection of the current. (b)Sepated field components for the same current. Unit: nT. 49

3.6 (a)Components of the combined original field of three-segment external and internal line currents (see Figs.3.4 and 3.5). (b)Curl-free horizontal components of the combined fields. Unit: nT. 50

3.7 Components of the field of the internal three-segment line current (see Fig.3.4) separated (a)with mirror-image expansion of the area of known field, (b)without expansion. Figs. 4b and 7a are the same. Unit: nT. 53

3.8 Maps of Fourier transforms of real and imaginary parts of a variation event at period 23 minutes, recorded by an array in southwestern Canada. The start of the time sequence was chosen to give maximum power in the real part of the field. 55

3.9 Curl-free horizontal components of the real part of the magnetovariation event of Fig.3.8. 57

Figure Page

3.10 Components of the real separated internal and external fields observed by the magnetometer array. Compare Fig.3.8. 58

4.1 A cartoon of magnetometer arrays on land, modified from Fig.1 of Banks (1979). Far away from the external source region, induction between the external source and the local structure is less important than in the region directly below the external source. 61

4.2 Relation between contours of current function and direction and density of surface current. 71

4.3 Layered Earth's model. 74

4.4 Shielding property of a plane layered Earth, for a two layer model with various layer 1 conductivities. The conductivities are 3.0x10^{-1}, 3.0x10^{-2} and 3.0x10^{-3} S/m. 82

4.5 Similar to Fig.4.4 but a thin surface layer of good conductor is added to simulate sea water or wet sediments. 83

4.6 Shielding property of a plane layered Earth, for a two layer model with various layer 1 thicknesses. The thicknesses are 200, 100 and 50 km. 84

4.7 Similar to Fig.4.6 but a thin surface layer of good conductor. See also Fig.4.5. 85

Figure Page

4.8 The layered Earth models for current sheet (Figs.4.10-4.12) inversion. One model has all conductivties 10 times those in the other. The depths, 45, 55 and 65 km, at which current sheets are inverted, are marked by horizontal lines. 88

4.9 The separated internal field for period 69 minutes for a variational event on July 19th, 1983. 90

4.10 Current sheets inverted from the field of Fig.4.9, at 45, 55 and 65 km, for the less conductive model (Fig.4.8). 91

4.11 Current sheets inverted from the field of Fig.4.9, at 45, 55 and 65 km, for the more conductive model (Fig.4.8). 92

4.12 Current sheet inverted from the field of period 23 min. separated in chapter 3, Fig.4.10, at 55 km depth, for the less conductive model (Fig.4.8). 93

5.1 (a)Line current in observation coordinates system (OCS), with numbering convention of the nodes and segments. (b)The j th current coordinate system (CCS) and its relation to OCS. The y axis of CCS is always parallel to the XOY plane of OCS. 98

5.2 Geometry of sheet current model. (a)3-D view of a sheet segment. The two ends of the segment are parallel to the y axis of the CCS and therefore parallel to XOY plane of the OCS. (b)a plane view of the connection of two segments. Because of the change in the horizontal direction of the sheet segments, the "inner corner" draws more current than the "outer corner". 104

Figure Page

5.3 Iteration process for the *LDPNL* inversion of test model 1 (Fig.5.4). Top to bottom: Horizontal projection of line current, only nodes under the array are shown, and constraints on the horizontal positions of nodes are superimposed.
XOZ projection of the current, X north and Z down, two horizontal lines showing constraints on depth of nodes.
Misfit of total field H. Both maximum and root-mean-square values are plotted. The "error added" is the r.m.s error in total field resulting from Gaussian error of 10 nT standard deviations added to each of the three components of field at all the 25 data points. See also Fig.5.4. 127

5.4 Test model 1 is a single line current. The *LSINL* method used for inversion, with an initial model which is the best model achieved by the *LDPNL* inversion (Fig.5.3). The misfit of the inverted model is with respect to calculated accurate data. 128

5.5 Iteration process for the *LSINL* inversion in Fig.5.4. See also Fig.5.3. 129

5.6 Iteration process for the inversion of test model 2, a sheet current 70 km wide. Using the *LDPNL* method the fields are inverted to a line current. 134

5.7 Test model 2 (70 km wide sheet) is inverted to a line current using the *LSINL* method. The initial model is the final model inverted by the *LDPNL* method (Fig.5.6). 135

5.8 Iteration process for the *LSINL* inversion in Fig.5.7. 136

Figure Page

5.9 Similar to Fig.5.7 but inverted to a sheet current with the *LSINL* method. The width of the sheet is: true model, 70 km; initial model 40 km; final model 77 km. 137

5.10 Iteration process for the *LSINL* iversion in Fig.5.9. 138

5.11 Iteration process for test model 2, a wider (100 km) sheet current. Using the *LSINL* method the fields are inverted to a line current. The initial nodes are 20 km off the horizontal positions of the true nodal positions and at 40 km depth for the intermediate nodes. 140

5.12 Test-model 2 (100 km wide sheet) is inverted to a sheet current using the *LSINL* method. The initial model is the best model achieved by line current inversion, Fig.5.11. The initial width is 60 km, finally inverted is 103.7km. 141

5.13 Iteration process for the *LSINL* inversion in Fig.5.12. 142

5.14 Test model 3 is a prism current, inverted to a line current using the *LDPNL* method. 4 data points, 12 data were used for the inversion. 145

5.15 Iteration process for the *LDPNL* inversion in Fig.5.14. 146

5.16 Similar to Fig.5.14 but with the *LSINL* method. 5 by 5 data points, 75 data were used for the inversion. 147

5.17 Iteration process for the *LSINL* inversion in Fig.5.16. 148

Figure Page

5.18 First two principal components of the internal real Z field of five frequency components analyzed. Notice that the second principal component is much smoother and weaker. 155

5.19 The real Z fields from the 5 periods, which have been taken for the K-L transformation (Fig.5.18), and the first principal component of these. 156

5.20 (a)*PNZ* averaged internal field from 10 periods (66.7≤T≤225.5 min.); (b)standard deviation of the averaged data. 161

5.21 Constraints on horizontal positions of nodes. For the 6 nodes inside the survey area, the horizontal positions are restricted to fall within the 6 strips, approximately 30 by 100 km. 163

5.22 The fields of Fig.5.20 have been inverted to a 10 node model by the *LDPNL* method. The 9 grid points are marked, and the resolved current is projected on the map. A tilting plane normal field is added to the data to stabilize the inversion. (a)inverted fields; (b)misfit. 165

5.23 Iteration process for the *LDPNL* inversion in Fig.5.22. 166

5.24 Same as Fig.5.22, but with the *LSINL* method, the initial model is the best model achieved by the *LDPNL* method, Figs.5.22 and 5.23. 167

5.25 Iteration process for the *LSINL* inversion in Fig.5.24. See also Fig.5.22. 168

Figure Page

5.26 Iteration process for the *LDPNL* inversion with shallow depth constraints. 171

5.27 Inversion with weak (66 percent) current constraint using the *LSINL* method. 172

5.28 Iteration process for the *LSINL* inversion in Fig.5.27. 173

5.29 Inversion with weak (55 per cent) current constraint, the *LSINL* method was used with data from the *ZZZ* biased set. 174

5.30 Iteration process for the *LSINL* inversion in Fig.5.29. 175

5.31 With weak (55 percent) current constraint the *PNZ* biased data have been inverted to a 10 node sheet current of width 80 km (constrained between 20 and 80) using the *LSINL* method. 179

5.32 Iteration process for the sheet current inversion in Fig.5.31. 180

5.33 With weak (55 percent) current constraint the *PNZ* biased data have been inverted to a 5 node sheet current of 80 km width (constrained between 20 and 80) using the *LSINL* method. 183

5.34 Iteration process for the sheet current inversion in Fig.5.33. 184

5.35 Best fitting models from various inversions. Models are from the inversions in Figs.5.23, 5.25, 5.28, 5.30, 5.32, and 5.34. Both XOZ and YOZ projections of the models are given. 187

Figure Page

5.36 Fig.2 of Kanasewich (1968). The area of the magnetometer array and the current channel inverted are superimposed. 191

5.37 Fig.2 of Gough (1986). The area of the magnetometer array and the current channel inverted are superimposed. 192

5.38 Depth of the Moho in km, Fig.10 of Kanasewich et al (1987). 195

1. INTRODUCTION

In this thesis I will develop an efficient strategy for the interpretation of magnetovariation fields. The specific goal of this interpretation is the parameterization of regional geoelectrical structures in the Earth.

The physical basis for such interpretation is Faraday's Law of electromagnetic induction (e.g., Jackson, 1975). The Earth's magnetic field interacts with the solar wind and becomes unstable in time. The changing field flux in turn induces currents in the conductive Earth. The fields of these induced currents may have large spatial gradients near a local good conductor which is close to the surface. By observing and analyzing the non-uniform space-time behavior of such fields, information about the geoelectric structure can be extracted. This approach to the investigation of electric structure is termed GDS, Geomagnetic Depth Sounding. At present, simultaneous recordings of the magnetovariational fields with an array of magnetometers over a two-dimensional area provide the best data sets (Gough and Ingham, 1983).

The natural sources of magnetovariation fields have wide frequency spectra and large enough power to penetrate the Earth to depths of tens to hundreds of kilometers, inducing detectable currents in conductive structures. The drawback of these natural sources is that we have no control over them and the data inevitably contain unwanted components and various types of noise. Consequently the first step in any strategy for the interpretation of the data includes analyses which use different representations of the data. These representations of the data allow the researcher to determine some of the general characteristics of the sources, and whether local induced or channelled currents dominate the magnetovariation fields. Then appropriate models are chosen in order to approximate or represent the conducting structures at depth. These models are described by specific parameters which are functionals of the magnetovariation data. Finally, the model parameters are in turn estimated through an inversion scheme. The overall quality of the whole strategy for interpretation can be evaluated by comparison of the results with other geophysical and geological data.

1.1 REVIEW OF PREVIOUS WORK

1.1.1 DATA REPRESENTATION

The analogue magnetometer records contain three traces for the three field components, on 35 mm film (Gough and Reitzel, 1967). These traces are digitized by hand. Selected disturbance events are represented as magnetograms showing time series of either H, D and Z or X, Y and Z components, in geomagnetic or geographic coordinates respectively. The time series can also be represented at each station by a magnetic hodograph, which is the temporal trace of the tip of the horizontal disturbance vector (Woods and Lilley, 1980). This representation reveals the overall polarization of the horizontal field and should be combined with coherence analysis to reveal the polarized parts of the signal (Jones, 1979). The polarization character is related to the structure and/or external current configuration (Gough and Ingham, 1983).

The magnetograms are Fourier transformed and the Fourier transform amplitude and phase, or real and imaginary parts, are then contoured to reveal the spatial changes of a particular frequency component of the disturbance. Jones (1980) maps "smoothed" Fourier transform estimates whereas Gough and Ingham (1983) use "stationary" Fourier contour maps of components at periods at which the spectra of the horizontal components have stationary values across the array.

Polarization analysis (Lilley and Bennett, 1972) is usually carried out for the horizontal components of the field observed at each station for a given spectral component. Jones (1979) discussed the difference between polarization and coherence. Fowler et al (1967) gave, for the two dimensional case, formulae for extracting the totally polarized signal from a time sequence. Their results can be generalized to the three dimensional case with a proper covariance matrix presentation (Means, 1972; Samson and Olson, 1980).

Transfer function analysis is more or less a standard method employed in GDS data representation (Schmucker, 1964, 1970; Berdichevsky and Zhdanov, 1982, chap. 6). Most researchers work in the frequency domain (Schmucker, 1970), but time domain analysis has also been suggested (McMechan and Barrodale, 1985). Frequency domain analysis results in a pair of complex transfer functions. Therefore a pair of induction arrows, in-phase and quadrature-phase, can be defined (Gough and Ingham, 1983). The reversed in-phase arrow is believed to be parallel to the Parkinson arrow, which generally points towards induced currents in good conductors (Parkinson and Jones, 1979; Gregori and Lanzerotti, 1980; Jones, 1981). The quadrature arrow has aroused considerable discussion of its meaning and sign convention (Lilley and Arora, 1982; Chen and Fung, 1985; Berdichevsky and Zhdanov, 1984, Part C). Generally, there is a substantial phase difference between normal and anomalous fields. One example of the importance of the quadrature arrow in the interpretation of data is given by Alabi et al (1975). The general implication of different roles of in-phase and quadrature-phase arrows is summarized in Rokityansky (1982, p.286-288). Other methods of representing the transfer function analysis have been suggested (Gough and Ingham, 1983). Among these, the hypothetical event analysis method (Bailey et al, 1974) is widely employed.

1.1.2 MODELS AND INVERSION

Magnetometer array data are usually used to interpret local conductive anomalies, but can also be used in one-dimensional (1-D) inversion. The two magnetic response functions (Schmucker, 1970; Kuckes, 1973; Parkinson, 1983, chap.5), defined by the three components of the field, X, Y and Z, and its horizontal gradient by,

(1.1) $c=Z/(\partial X/\partial x+\partial Y/\partial y)$

(1.2) $c_m=Z/H$,

are related to the magnetotelluric impedance Z_{mt} (e.g. Rokityansky, 1982, chap.5) by

(1.3) $Z_{mt}=i\omega\mu_0 c$

(1.4) $Z_{mt}=(-\omega\mu_0/\nu)c_m$

where ν is the horizontal wave-number and μ the magnetic permeability. Therefore, similar techniques for 1-D inversion in magnetotelluric sounding (Kaufman and Keller, 1981) can be modified to invert 1-D geoelectrical profiles from these electromagnetic response functions. In estimating the horizontal gradients (see (1.1)), the fields are often fitted to polynomial surfaces (Woods and Lilley 1979), usually to the second order, and the vanishing vertical curl of the polynomial presentation of normal fields can be used to constrain the parameters (Jones, 1980). The resolved profiles are in general agreement with the results of global geomagnetic depth sounding.

Woods and Lilley (1979) suggested that, in principle, combining normal structure profiling and the transfer function technique by representing the vertical field as

$$(1.5) \qquad Z_{total} = Z_{anomalous} + Z_{normal} = T_{zx}X + T_{zy}Y + c(\partial X/\partial x + \partial Y/\partial y),$$

where T_{zx} and T_{zy} are transfer functions, can separate the two effects. Obviously, where transfer function analysis is appropriate, the "normal" term above would help to depress the contamination of normal Z, and at the same time the resolved c might not, as noted by the authors, be properly determined.

As the skin depth of a time-harmonic field is proportional to the square root of the period T (e.g. Jackson, 1975), the response function c_m for different period components along a profile when contoured against $\sqrt{T}$ as vertical scale and station positions as horizontal scale, indicates conductivity contrast beneath the profile. Such contouring is the Z/H pseudosection (Ingham et al, 1983). As equation (1.4) indicates, to make such pseudosections more meaningful, the wavelength of the fields comes into play. Consequently 2-D array data are needed.

Local studies have found that near surface structures are seldom truly 1-D, so that interpretation must be based on 2- or 3-D models. There is no analytic solution for general 2- or 3-D structures and numerical solutions are sought with various schemes.

In 2-D cases the Maxwell equations are decoupled for E- and/or H-polarization for which only E or H have components parallel to the strike of the 2-D structure. For the E-polarization, the governing equations are (e.g. Gough and Ingham, 1983),

$$(1.6) \qquad \nabla^2 E = i\omega\mu_0\sigma E$$

and for H-polarization,

$$(1.7) \qquad \nabla^2 H = \nabla\sigma \cdot \nabla H/\sigma + i\omega\mu_0\sigma H.$$

Forward numerical modelling techniques involve large amounts of computing. Therefore, the inversion schemes based on such modeling often involve trial-and-error processes (Rokityansky, 1982, chap.3). For an experienced researcher, however, such trial-and-error schemes may be quite efficient.

The finite difference method (Jones and Pascoe, 1971; Brewitt-Taylor and Weaver, 1975) and the integral equation method (Tripp and Hohmann, 1984; Wannamaker et al, 1984) are widely used to solve equations for local induction models. These methods result in a number of linear equations for the electromagnetic fields. Since the number of equations to be solved increases rapidly with the model complexity, models so far treated have been simple. Another approach to modelling ~~is~~ based on the thin sheet approximation (Dawson and Weaver, 1979; McKirdy et al, 1985). This is suitable for a layered lateral inhomogeneity, and is especially good for coast effect studies. McKirdy (1986) developed it into a thick sheet approximation which more closely resembles 3-D models.

The inversion of conductive structure for local magnetovariation studies is at an early stage of development, and the validity of such inversions, in some cases, is open to discussion (chapters 4 and 5 of this thesis). 2-D inversions have been attempted but the amount of numerical calculation is enormous (Neumann, 1986). 3-D inversion is even worse, as can be expected from the difficulties encountered in 3-D forward modelling.

Conversely, current inversion is less computationally prohibitive and has been developed for different models. Banks (1979) inverted the anomalous field to a horizontal current sheet in free space to reveal the configuration of conductive bodies at depth. Stinson and Oldenburg (1982) inverted linear array data to its 2-D current source using linear programming techniques which proved to be important in regulating the inversion process and in reducing the non-uniqueness of the solutions.

1.2 CONTRIBUTIONS OF THIS THESIS

A two-dimensional magnetometer array, in the region 112°37′-118°8′W, 49°3′-52°2′N, using 29 Gough-Reitzel magnetometers (Gough and Reitzel, 1967), was set up in southern Alberta and British Columbia in the summer of 1983 (hereafter referred to as the 1983 array), and continuously recorded the three magnetovariation field components for two months. The data collected are used to test the interpretation strategy developed in this thesis.

The magnetovariation fields employed in local studies at middle latitudes are mainly geomagnetic substorms (Kamide, 1982). At the 1983 array location, we observe the substorm fields far from the ionospheric sources (Rostoker, 1972). The uniform external fields are difficult to separate from the internal fields (Oldenburg, 1969; Porath et al, 1970; chapter 3 of this thesis), and consequently the normal fields cannot be effectively isolated. Local induction studies are therefore less justified because of the lack of proper boundary conditions (the normal fields). Models based on current inversion is not so restricted by such difficulties.

To prepare the data for current inversion, the frequency components of the observed data are processed by new techniques developed in chapters 2 and 3. In chapter 2, I estimate the normal fields by plane-wave expansions of the observed fields. Such expansions also provide bases for choosing proper frequency components of the fields for further analysis. In chapter 3 I separate the fields into internal and external parts in the wave-number domain. Such separation provides the data base for the current inversion in chapters 4 and 5. After separation, the current channelling features in the internal fields becomes more obvious than in the total fields.

Current inversion is carried out by two different approaches. In chapter 4, I invert the fields to a horizontal current sheet based on the work by Banks (1979), but within a conducting layered Earth model. In chapter 5, I invert the fields to 3-D linear or constant-width sheet currents in free space. Such inversions are suitable for channelled currents. To justify such inversion, I use the Karhunen-Loeve transform to confirm the presence of current channelling in the observed fields.

The channelled current inversion is formulated in the general form of parametric inversion. For such inversions, I develop programming techniques, *LSINL* (Least Squares with Inequality constraints for linearized Non-Linear problem) and *LDPNL* (Least Distance Programming for linearized Non-Linear problem) to regulate the unstable inversion process based on existing *LSI* and *LDP* programming (corresponding method for linear problems). In recognition of some systematic errors in the data generated by imperfect separation I introduce the W-stabilization technique to compensate for them.

The methods developed in chapters 3 and 5 are tested with synthesized data. The geometry of the inverted conductive structure is summarized and the structural implications of the conductor are discussed in chapter 5.

2. NORMAL FIELD ESTIMATION IN MAGNETOVARIATION STUDIES

A time varying magnetic field observed by a magnetometer array generally contains a regional trend which varies smoothly over the array. Such a regional field cannot be separated into external and internal parts by usual techniques, and causes problems in interpretation. As in other cases of geophysical data processing, the regional or normal field has to be removed to expose the anomalous field of interest. Further, in forward modelling of induced currents it may be desired to normalize the anomalous field in terms of the normal field.

One definition of the normal field is the field which would be observed if the anomalous conductive structure were absent. It is the sum of the fields of external currents and those of induced currents in the normal conductive structure, usually taken to be horizontally layered. Because of mutual coupling between the anomalous body and the normal structure, the internal part of the normal field is not the same as the fields produced by actual induced currents in the normal conductive structure. It follows that even after the removal of the normal fields, defined as above, one still has to consider the contribution to the anomalous fields of currents in the normal structure. The definition given thus has limited validity, but is a convenient approximation for many modelling purposes.

Many researchers regard the normal field as represented by the smoothly changing, regional part of the observed field. This is justified as long as the distance between the external currents and the array is much larger than the span of the magnetometer array, so that the external field and the induced normal field are smooth over the array. Over an array which is too close to external currents, the normal field is no longer smooth.

The normal field can be estimated by fitting first and second order polynomials to "normal" stations of the array (Porath et al, 1970; Ingham et al, 1983; Jones, 1980). Such polynomial representations cause divergence at infinity. Further, they tell us nothing about additions by the methods themselves to the "normal" fields removed.

In this chapter I represent the normal field as a set of plane waves with parameters fitted to the field values at reference stations where the field is regarded as "normal". The wave parameters indicate whether external or internal fields are dominant in the normal field. The validity of such representation is discussed by Berdichevsky and Zhdanov (Chap.9, 1984) and in references there quoted.

2.1 PLANE WAVE EXPANSION OF THE NORMAL FIELD

Expand the normal field in terms of plane waves:

$$(2.1) \qquad \mathbf{H}_n(\mathbf{r}) = {}^1\mathbf{h}\exp[-i\,{}^1\mathbf{K}\cdot\mathbf{r}] + {}^2\mathbf{h}\exp[-i\,{}^2\mathbf{K}\cdot\mathbf{r}] + \cdots$$

$$i = \sqrt{-1}$$

in which r is a position vector, K and h are a wave vector and the complex vector amplitude of that plane wave respectively. The superscripts indicate different wave terms. In practice the first term in the plane wave expansion is much larger than the others. This statement will be substantiated in section 2.3. For the present, assuming its correctness, only one term is taken, and the superscripts are dropped. The field represented by (2.1) is then fitted in the least square sense to m reference stations at $\mathbf{r}=\mathbf{r}_1, \mathbf{r}_2, \cdots \mathbf{r}_m$ by minimizing

$$\Theta = \sum_j |\mathbf{H}(\mathbf{r}_j)-\mathbf{H}_n(\mathbf{r}_j)|^2 \tag{2.2}$$

where, $\mathbf{H}(\mathbf{r}_j)$ is the observed field at $\mathbf{r}_j$.

The normal field represented by (2.1) is in free space and should satisfy curl-free and divergence-free conditions:

$$\mathbf{K}\times\mathbf{h} = 0 \tag{2.3}$$

$$\mathbf{K}\cdot\mathbf{h} = 0 \tag{2.4}$$

Equation (2.3) can be violated slightly, because even in the air very weak currents flow and contribute to the curl of the magnetic field (Chapman and Bartels, 1940). A small, but nonzero curl of the normal field is therefore tolerated corresponding to negligible current density. Fields with zero curl *and* divergence give only the trivial plane-wave solutions of uniform fields when displacement current is neglected.

On the other hand (2.4) should be strictly satisfied in the absence of magnetic monopoles. The condition of zero divergence will be used to retrieve certain parameters of the wave.

The real part of the wave-number vector **K** represents an oscillatory character of the normal field. The horizontal components, K_1 and K_2, of **K** are assumed to be real. This stabilizes the iteration for estimating the parameters (next section), and its effect is to adopt the phase of the horizontal fields as reference for the vertical field in each wave term. The corresponding horizontal wavelength is

$$\lambda_{xy} = 2\pi/\sqrt{(K_x^2+K_y^2)}$$

The condition (2.4) will, in general, require a non-zero imaginary part of the vertical component wave-number K_3. This $\mathrm{Im}(K_3)$ is informative of the nature of the normal field plane wave. With downward z positive (the convention of (2.1)) a positive $\mathrm{Im}(K_3)$ represents a downward increasing field and implies a normal field dominated by internal currents, while negative $\mathrm{Im}(K_3)$ implies that external currents are dominant in the normal field. Actual normal fields will include both internal and external parts, since both the external currents and the currents induced in large-scale regional structures contribute to them.

2.2 AN ALGORITHM FOR WAVE PARAMETER ESTIMATION

On a plane Earth, magnetometer arrays are always close to the horizontal plane z=0, and condition (2.4) that the field has zero divergence leads to an explicit expression for K_3:

$$K_3 = -(K_1h_1+K_2h_2)/h_3 \tag{2.3a}$$

As noted above, K_1 and K_2 are assumed to be real. Setting $\partial\Theta/\partial h_n$ and $\partial\Theta/\partial \mathbf{K}$ to zero, from (2.1) and (2.2):

$$h_i = \{\sum_j H_i(\mathbf{x}_j)\exp[i\mathbf{K}\cdot\mathbf{x}_j]\}/m \tag{2.5}$$

$$A_{s1}K_1+A_{s2}K_2 = B_s, \quad s=1,2 \tag{2.6}$$

where

$$\mathbf{A} = \sum_j \mathrm{Re}\{\mathbf{H}^\dagger(\mathbf{r}_j)\mathbf{h}\}\begin{bmatrix} x_j^2 & x_jy_j \\ y_jx_j & y_j^2 \end{bmatrix}$$

$$\mathbf{B} = \sum_j \mathrm{Im}\{\mathbf{H}^\dagger(\mathbf{r}_j)\mathbf{h}\exp[-i\mathbf{K}\cdot\mathbf{r}_j]\}\begin{bmatrix} x_j \\ y_j \end{bmatrix}$$

in which, † denotes Hermitian adjoint of a vector, and x_j and y_j are components of the position vector $\mathbf{r}_j$ in a Cartisian coordinate system with x axis pointing north and y east. Equations (2.5) and (2.6) are non-linear in **K** and **h** and are solved iteratively. Initial values of K_1 and K_2 can be taken as zero because of the smooth nature of the normal fields. With the initial values of K_1 and K_2 known, (2.5) can be solved for **h**. These are substituted in (2.6) to give estimates of **A** and ~~B, and better~~ values of K_1 and K_2 are found. Iteration continues until stationary values are obtained.

The convergence criterion is that the next iteration changes all parameters less than a small fraction, say one percent. In practice, tens of iterations are needed for the parameters of the first plane wave term in (2.1) to converge. The resolved K_1 and K_2 are of the order of 10^{-4}~ 10^{-3} km^{-1} and so represent long wavelengths. These require equivalent current densities of the order of 10^{-4} A/km^2 at most, which correspond to the maximum **h** resolved. Thus the curl-free condition is, in practice, well approximated by this long-wavelength first plane-wave term.

After removal of the first plane wave, the residual field can be fitted to a second wave term. In an application of the method to array data (section 2.4), convergence of the second wave term required considerably more iterations than the first. The second-term waves had wavelengths shorter than those of the first-term waves by a factor of order 100, and less than one percent of the energy. The normal fields recorded by our array are therefore well approximated by a single plane wave term.

The anomalous field is contained within a well designed magnetometer array, and superimposes short wavelength components on the long wavelength normal field. This normal field is dominant at all recording stations if the anomalous structure is not too shallow, in which case the reference stations can be the entire array. In the example given this is the case. An anomalous fields such as that of the North American Central Plains conductor (Alabi et al, 1975) may be comparable to the normal field at some stations. In such cases the reference stations would be a subset of the array, excluding those very near the anomaly.

The resolved plane wave amplitudes represent the (complex) spectra of the fields at the resolved (real) horizontal wavenumbers. The way these spectra are obtained is different from traditional FFT analysis: my method determines *both* the wavenumber *and* the spectral amplitudes simultaneously by least squares, whereas the FFT approach fixes the wavenumbers (by fixed data sampling) and determines *only* the spectrum by least squares.

2.3 STATISTICAL ANALYSIS OF NORMAL FIELDS

The 1983 magnetovariation array had 29 magnetometers, but for most of the events 27 stations or less provided data. The time sequences of three components were Fourier transformed for 15 selected magnetovariational events and amplitudes and phases were noted at stable peaks and/or troughs in the spectra at 114 periods in the range 4.8 to 225.5 minutes. These frequency domain data were divided into five period bands specified in Table 2.1, with the corresponding skin depths in a half-space of conductivity

0.1 S/m.

Table 2.1

T min	Skin depth (σ=0.1 S/m)
≤ 10.53	≤ 40 km
10.53 - 16.45	40 - 50
16.45 - 37.00	50 - 75
37.00 - 65.79	75 -100
> 65.79	>100

The conductivities in the crust of southern Alberta will be generally lower than 0.1 S/m (Gough, 1986), and the fields will penetrate deeper than the skin depths listed in Table 2.1.

The polarizations of the fields (before removal of normal fields) are summarized in Fig.2.1. The major and minor half-axes, A and B, of the polarization ellipse, and the azimuth ϕ of the major axis, positive anti-clockwise from the east, are averaged with the following weighting factors:

$$
\begin{array}{lll}
 & A_j^2 & \text{for } A \\
(2.7) & B_j^2 & \text{for } B \\
 & (A_j^2+B_j^2)(1-B_j/A_j) & \text{for } \phi
\end{array}
$$

in which A_j and B_j are the major and minor half axes of the polarization ellipse at station j. The weighting factors for A and B are proportional to the energy of the field at each station, and that for ϕ gives greater weight to the azimuths of more elongated polarization ellipses.

Fig.2.1 shows the azimuthal distribution of the major axes of polarization ellipses of events, weighted as in (2.7), in the five period bands. Events in which internal currents are dominant are shown separately from those with external currents dominant. As the period increases the largest polarizations rotate from the NW-SE quadrant towards N-S. Fig.2.1 also gives the azimuths of wave vectors in the same five period bands. It is interesting to note the differences in the azimuths of both polarization ellipses and wave vectors between internal-dominant and external-dominant normal fields. The former are presumably more affected by large scale anisotropy in the geology, the latter by the geometries of current systems in the magnetosphere and ionosphere. It should be remembered, however, that all these normal fields contain both external and internal parts, so that too much should not be read into the differences between the internal-dominant and external-dominant groups.

Fig.2.2 shows $\mathrm{Im}(K_z)$ versus period for the first plane-wave terms at 102 periods, and for the second plane-wave terms at 52, of the 114 periods analyzed. Those plotted were selected on three criteria:

(2.8) $${}^1\lambda_{xy} > {}^2\lambda_{xy}$$

(2.9) $${}^1\lambda_{xy} > 350\ \mathrm{km}$$

(2.10) $$1000\ \mathrm{km} > {}^2\lambda_{xy} > 80\ \mathrm{km}$$

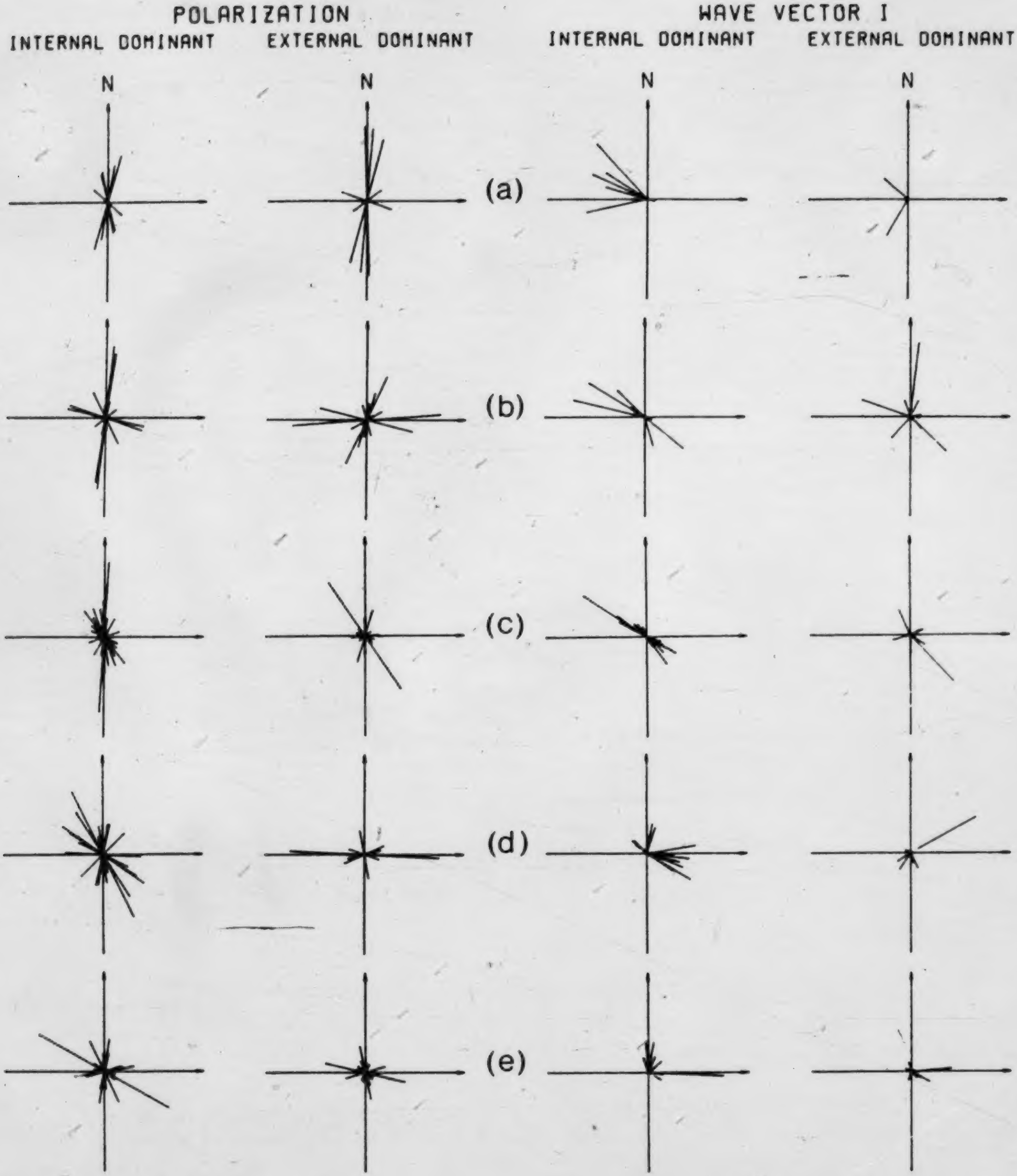

Figure 2.1 Azimuths of major axes of polarization ellipses, and horizontal projections of wave vectors for normal fields in five period bands: (a)$T \geq 65.79$, (b)37.00 - 54.79, (c)16.45 - 37.00, (d)10.53 - 16.45, (e)$T \leq 10.53$ minutes. The lengths of lines are proportional to (i)averaged semimajor axis of polarization ellipse for azimuths of the axis; and (ii)magnitude of horizontal normal field for horizontal projection of wave vectors. Both are normalized within each period band.

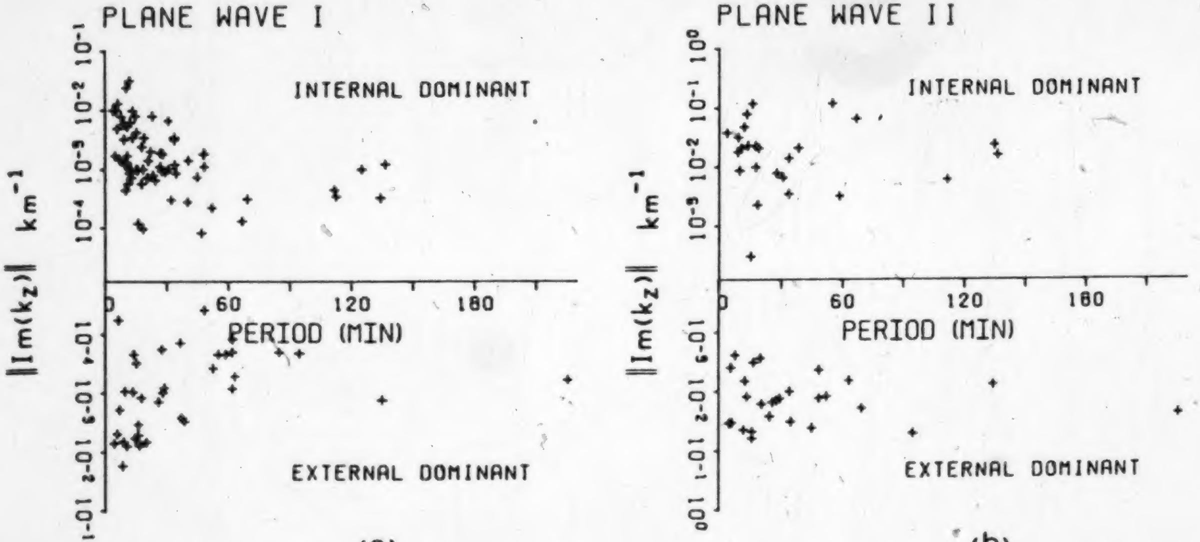

(a) (b)

Figure 2.2 $\mathrm{Im}(K_z)$ (km^{-1}) versus period, 102 periods in total. (a)Results for first term plane-waves, 66 are internal dominant ($\mathrm{Im}(K_z)\geq 0$) and 36 are external dominant ($\mathrm{Im}(K_z)\leq 0$); (b)Results for second term plane-wave, 25 are internal dominant and 27 are external dominant.

where $^1\lambda_{xy}$ and $^2\lambda_{xy}$ are the horizontal wavelengths of the first and second plane-wave terms. The criteria are designed to discriminate against noise, using three expected properties of the magnetovariation signals and considering the resolving power of the available data set. Condition (2.8) requires the second term to represent a shorter wavelength than the first term; (2.9) requires that the first term has wavelength larger than the array width; and (2.10) that the second term has wavelength less than 1000 km and larger than twice the average station spacing (40 km) in the array. The upper limit is chosen to exclude a second wave term of wavelength more than twice the array diagonal, on the grounds that two very long waves cannot be discriminated by the array. The lower limit is based on the consideration that signals of wavelengths shorter than the "Nyquist wavelength" (e.g. Kanasewich, 1981) cannot be resolved and will be heavily contaminated with noise. Throughout this thesis, only frequency components of fields satisfying these criteria are possible candidates for any further analysis.

Fig.2.2 shows the vertical quadrature-phase wavenumbers $\mathrm{Im}(K_z)$ for the first and second plane wave periods which satisfy the criteria (2.8-2.10). Of the 102 first plane wave periods, Fig.2.2(a), 66 are found to be internal-dominant ($\mathrm{Im}(K_z) > 0$) and 36 are external-dominant ($\mathrm{Im}(K_z) < 0$). The fact that our array recorded almost two internal-dominant normal fields for each external-dominant one may correct any notion that the normal fields are simply those of external currents. The induced currents within the Earth are presumably weaker than those in the magnetosphere and ionosphere, but flow closer to the Earth's surface and to the array. The magnitude $|\mathrm{Im}(K_z)|$ shows values widely dispersed at the shorter periods, but concentrated between 10^{-3} and 10^{-4} km^{-1} at periods greater than one hour. Such small values of the vertical wavenumber indicate nearly equal external and internal fields, corresponding to current concentrations in the ionosphere and upper mantle.

The second plane wave values of $\mathrm{Im}(K_z)$, shown in Fig.2.2(b), exhibit distributions generally similar to those of the first plane waves, but with concentrations of the magnitudes between 10^{-1} and 10^{-2} km^{-1}, corresponding to nearer currents and shorter wavelengths of fields. Of the 52 spectral periods which satisfy the criteria (8-10), 25 are internal-dominant and 27 external-dominant. The contributions of external and internal currents are more nearly equal than in the first plane-wave terms.

The horizontal wavelengths of the first and the second plane-wave terms are plotted against period in Fig.2.3(a,b), for the set of frequency-domain events selected on criteria (2.8-2.10) whose $\mathrm{Im}(K_z)$ values are shown in Fig.2.2. The internal-dominant and external-dominant wavelengths are separated by means of the sign of $\mathrm{Im}(K_z)$ for each. The internal-dominant first-term plane waves have wavelengths in the range 2000 - 10^5 km, with a concentration in the range

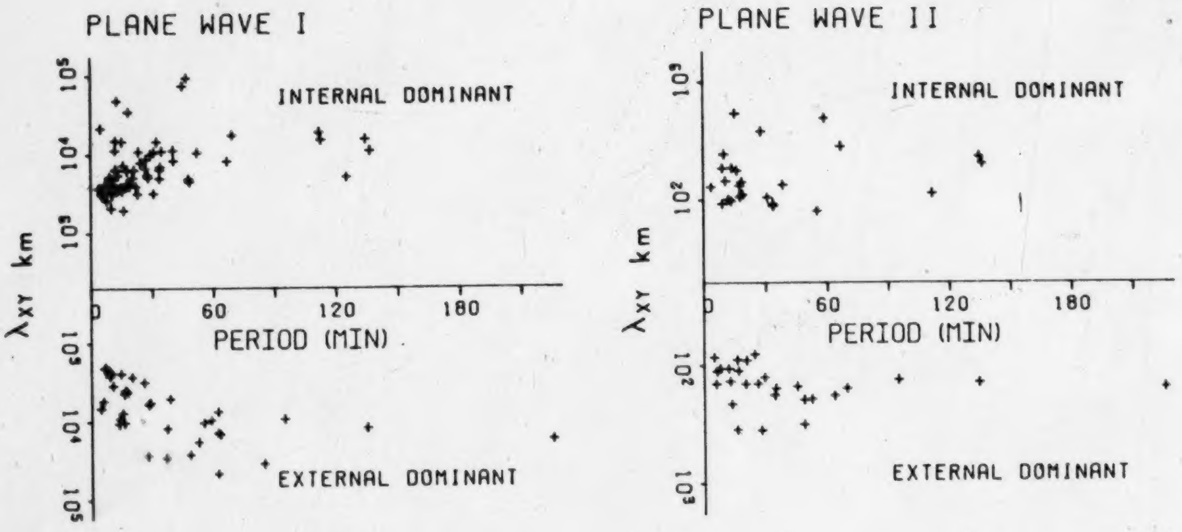

(a)

(b)

Figure 2.3 Horizontal wavelength (km) vs. period for (a)the first and (b)the second plane-wave terms. Internal- and external-dominant terms are plotted separately (see Fig.2.2).

2000 - 10^4 km at periods below 60 minutes. This represents the scale of the internal induced currents, which range from continental scale to the planetary diameter. Once again it must be remembered, however, that external currents contribute to internal-dominant fields, so that the fields of some of the longer wavelengths may be increased by magnetospheric currents. The external-dominant fields at periods less than 30 minutes have wavelengths in the range 2000 - 10^4 km, like the internal-dominant fields. At periods over 30 minutes, however, the wavelengths are concentrated between 10,000 and 80,000km, suggesting current lengths and/or distances characteristic of the magnetosphere.

The second term plane waves have wavelengths in the range 80 - 800 km in both internal- and external-dominant sets (Fig.2.3(b)). Denoting the numbers in these two sets N_i and N_e respectively, the ratio N_i/N_e is 25/27 or 0.93. A question of some interest is which part of these second wave terms belongs to the normal field and which to the anomalous field. Clearly the second wave terms are not entirely anomalous, because N_i/N_e is close to unity with N_e slightly larger than N_i, and external fields are part of the normal field, by definition. To examine the question further it is interesting to consider the energies of the plane waves, not simply N_i and N_e.

The energy E in a plane wave term increases as the square of its complex amplitude:

(2.11) $E \propto |h_n|^2$,

or in terms of the horizontal wave number and potential of the fields, Φ:

(2.12) $E \propto (K_x^2+K_y^2)|\Phi|^2$

Following the treatment in chapter 3, the plane-wave terms have been separated into internal and external parts of the potential, Φ_{in} and Φ_{ex}. The energies in the internal and external fields were then estimated from (2.12) for each wave term. The estimates invariably confirm the internal or external dominance inferred from the sign of $\mathrm{Im}(K_z)$, providing a check of the calculations. Table 2.2 shows the energies, in arbitrary units, for the external parts of the magnetovariation fields, E_{ex}, and the ratio E_{in}/E_{ex}, in five period bands.

Table 2.2

Period min	No. of periods Wave 1	 Wave 2	E_{in}/E_{ex} Wave 1	 Wave 2	E_{ex} Wave 1	 Wave 2
≤ 10.5	21	8	1.11	1.65	676	1
10.5 - 16.4	21	11	1.21	0.69	942	2
16.4 - 37.0	32	17	1.32	0.73	14700	41
37.0 - 65.8	17	8	0.89	1.30	28000	186
> 65.8	11	8	0.48	0.96	63100	83
4.8 -225.5	102	52	0.71	1.13	107400	313

(The unit of energy is arbitrary)

The estimates of E_{ex} show two things. First, the natural magnetovariation spectrum provides much more energy at periods greater than 16 minutes than in the shorter period bands. Second, the second plane-wave in each band has less than one percent of the energy in the first. The first plane-wave term thus closely represents the total observed normal field.

The values of the ratio E_{in}/E_{ex} for the first plane wave (Table 2.2) show that in the two longest period bands, which contain most of the energy, the external fields are dominant. This is true in the total energy for the complete range of periods, which is controlled by the long-period wave energies. At periods less than 37 minutes the internal currents provide more than half of the energy in the normal fields, probably because these induced currents flow higher in the Earth and closer to the array as the period decreases.

The ratios E_{in}/E_{ex} for the second plane-wave terms show essentially only that the contributions of internal and external currents are comparable. The energies are too small for their ratio to have much significance. It is probable that this term includes contributions from the normal and anomalous fields. The wavelengths resolved for these second-term plane waves (of order 100 km) are within the resolving power of traditional spectral analysis, which is controlled by the array dimensions and station spacing. Therefore, the general wavenumber domain analysis (next chapter) can be expected to give reliable results for these frequency events.

2.4 COMPARISON WITH OTHER NORMAL FIELD REPRESENTATIONS

A widely used assumption regarding the normal field is that it is uniform. This model has the merit of simplicity and is a useful first approximation in some respects. The currents induced in an anomalous conductor 10 or 100 km wide will be nearly the same for a normal field of wavelength 10^4 km as for infinite wavelength. The contributions of internal and external currents to a uniform field cannot be distinguished, and it is difficult to express the anomalous field as a fraction of the normal field. These limitations severely restrict quantitative modelling of structures, as Porath et al. (1970) have shown.

Some authors have represented the normal field by a first order polynomial, or plane, fitted by least squares to the fields at stations considered normal (Ingham et al., 1983). Such representations are divergent at large distances, and the physical meaning of the constant gradients of the normal field is not clear. The divergence-free condition for the normal field can be used, in principle, to estimate $\partial H_z/\partial z$, and to recognize whether the tilted plane represents an internal- or external-dominant field, but to my knowledge this has not been tried. Higher order polynomials have been used to represent the normal field (Jones, 1980), but the physical meanings of the coefficients remain unclear and divergence at great distances remains a problem.

Berdichevsky and Zhdanov (1984, chap.11) have developed an elaborate procedure for estimation of the normal field which goes beyond simple polynomial representations. This procedure depends on the accurate separation of external and internal parts of the field, and on the choice of a normal geoelectric section for the region. The second requirement is rather severe, as these authors note, particularly for local studies. The first is even worse, if the array is far from the external current source. In this case the external field is nearly uniform over the array, and is therefore poorly separated (next chapter). Even if the geoelectric section is accurately known the method then fails. If channelled currents (Gough and Ingham, 1983) are present they greatly increase the difficulties of this approach.

The plane-wave representation of the normal field improves on the other methods in four respects. First, it discriminates between normal fields dominated by internal and external currents. Second, it offers a guide in the choice of frequency components for further analysis. Third, it allows estimation of the normal field magnitude and the expression of the anomalous field as a fraction of the normal field. This is a prerequisite for forward modelling of conductive structures to fit three components of the magnetovariation fields. Fourth, it should work for both locally induced and channelled anomalous currents.

3. SEPARATION OF FIELDS INTO INTERNAL AND EXTERNAL PARTS

The interpretation of time-varying magnetic fields recorded at the Earth's surface involves the problem of separation of the observed field components into parts due to external and internal currents. Global data are usually expressed in spherical harmonics for this purpose (Chapman and Bartels, 1940) but for fields recorded over a limited area numerical integration is very often employed (Vestine, 1941; Price and Wilkins, 1963; Weaver, 1964; Porath et al., 1970). Such numerical calculations are usually carried out in the space domain. The use of the wave number domain has two notable advantages: computing time is saved through the fast Fourier transform (FFT), and the results are ready for application of the induction equations in more easily soluble form. Wiese (1965) was the first to separate internal and external fields in the wave number domain, using a formulation which differed from this study in two respects. Working before the development of the FFT, Wiese considered only the real part of the Fourier transform, whereas the the FFT provides the full complex values; and where the two horizontal components gave different estimates of parameters he used mean values. This is an *ad hoc* procedure without formal theoretical basis.

In this chapter I present a unified technique of potential field analysis in the wavenumber domain. The observed field is adjusted to be curl-free by calculating an optimum potential and separated into external and internal parts, if both exist. Magnetovariation data are here considered, but the technique is readily applicable to other potential fields.

3.1 REPRESENTATION OF A POTENTIAL FIELD IN CARTESIAN SPACE AND WAVENUMBER DOMAINS

Consider a vector field **H** in a source-free region, here the observed magnetovariation field, derivable from a scalar potential Φ:

$$\mathbf{H}(\mathbf{X})=-\nabla\Phi(\mathbf{X}) \tag{3.1}$$

where $\Phi(\mathbf{X})$ satisfies Laplace's equation:

$$\nabla^2\Phi(\mathbf{X})=0 \tag{3.2}$$

The position vector **X** of a magnetometer has components x (true north), y (east) and z(down). With z=0 in the plane of observation, $\mathbf{X}=(x,y,0)$. The 2-dimensional Fourier transform of the potential is

$$\Phi(\mathbf{K},z)=\int\int\Phi(x,y,z)\exp[iK_x x+iK_y y]\, dxdy \tag{3.3}$$

Equation (3.2) then has the solution

$$\Phi(\mathbf{K},z)=B(\mathbf{K})\exp[-\nu z]+A(\mathbf{K})\exp[\nu z] \tag{3.4}$$

where

$$\nu=\sqrt{(K_x^2+K_y^2)}$$

in the wavenumber domain, and A and B are terms representing internal and external sources respectively. Introducing vectors K_a and K_b:

$$(3.5)\qquad K_a=\exp(\nu z)\begin{bmatrix} iK_x \\ iK_y \\ -\nu \end{bmatrix} \quad K_b=\exp(-\nu z)\begin{bmatrix} iK_x \\ iK_y \\ \nu \end{bmatrix}$$

the magnetic field vector in K space takes the compact form:

$$(3.6)\qquad H(K)=A(K)K_a+B(K)K_b$$

K_a and K_b are linearly independent vectors in a unitary space (e.g. Samson, 1983) representing internal and external fields respectively. They are mutually orthogonal:

$$(3.7)\qquad K_a{}^{\dagger}K_b=0$$

Field components satisfying (3.6) are necessarily curl-free, as they are derivatives of a scalar potential: equation (3.6) is the wave number domain equivalent of (3.1). Because of (3.7) a more general conclusion about the orthogonality of internal and external fields can be reached:

(3.7a) $$\iint H_{in}^{\dagger}(X)H_{ex}(X)dxdy = 0$$

since, in (3.7a) $H_{in}(X)$ and $H_{ex}(X)$ can be replaced by their Fourier expansion, the cross terms of K in the inner product vanish because of the orthogonality of different harmonics, and the remaining terms vanish because of (3.7). A more precise statement of (3.7a) is: the magnetic fields observed by a finite array can best (in a least-squares sense) be separated into internal and external parts such that the inner product of these vanishes when integrated over the array.

3.2 SEPARATION OF THE FIELD INTO EXTERNAL AND INTERNAL PARTS

To separate the field into external and internal parts in the wavenumber domain, the sum-square error Q is minimized at z=0:

(3.8) $$Q=\sum_{k}[H(K)-A(K)K_a-B(K)K_b]^{\dagger}[H(K)-A(K)K_a-B(K)K_b]$$

Setting $\partial Q/\partial A^*(K)=\partial Q/\partial B^*(K)=0$, where $*$ denotes complex conjugate,

(3.9) $$K_a^{\dagger}[H(K)-A(K)K_a-B(K)K_b]=0$$

(3.10) $$K_b^{\dagger}[H(K)-A(K)K_a-B(K)K_b]=0,$$

and as $K_a^{\dagger}K_b=0$, we have:

$$(3.11) \qquad A(K) = \frac{K_a^{\dagger} H(K)}{K_a^{\dagger} K_a}$$

$$(3.12) \qquad B(K) = \frac{K_b^{\dagger} H(K)}{K_b^{\dagger} K_b}$$

Explicitly in terms of magnetic field components:

$$(3.11a) \qquad A(K) = -\frac{1}{2\nu}\left[\frac{iK_x H_x(K)}{\nu} + \frac{iK_y H_y(K)}{\nu} + H_z(K)\right]$$

$$(3.12a) \qquad B(K) = -\frac{1}{2\nu}\left[\frac{iK_x H_x(K)}{\nu} + \frac{iK_y H_y(K)}{\nu} - H_z(K)\right]$$

The inverse Fourier transforms of A(K) and B(K) give the potentials in the space domain for internal and external fields respectively. From Parseval's theorem, the potential spectra defined above will give, within their resolution, the curl-free magnetic field closest to the original data.

We can rewrite the internal and external parts of the fields, H_{in} and H_{ex}, in a very elegant way. Normalize K_a and K_b at z=0:

$$(3.5a) \qquad k_a = \frac{1}{2\nu^2}\begin{bmatrix} iK_x \\ iK_y \\ -\nu \end{bmatrix} \quad k_b = \frac{1}{2\nu^2}\begin{bmatrix} iK_x \\ iK_y \\ \nu \end{bmatrix},$$

then by (3.6), (3.11) and (3.12) we simply have H_{in} and H_{ex} expressed as *similarity transformations* of the observation H(K) by their normalized basic vectors:

(3.11b) $H_{in}(K) = A(K)k_a = k_a^{\dagger}H(K)k_a$

(3.12b) $H_{ex}(K) = B(K)k_b = k_b^{\dagger}H(K)k_b$

3.3 CURL-FREE ADJUSTMENT OF THE FIELD

If the field is entirely external or internal then all the components can be adjusted to make the field curl-free. Thus, for an entirely external field, only B(K) is finite in (3.6) and substitution of (3.12a) and (3.5) into (3.6) will adjust observed field components $H_x(K)$ etc into H_x etc as:

$$\mathit{H}_x=\frac{1}{2\nu}\left[\frac{K_x^2H_x(K)}{\nu}+\frac{K_xK_yH_y(K)}{\nu}+iK_xH_z(K)\right]$$

(3.6a) $$\mathit{H}_y=\frac{1}{2\nu}\left[\frac{K_y^2H_y(K)}{\nu}+\frac{K_yK_xH_x(K)}{\nu}+iK_yH_z(K)\right]$$

$$\mathit{H}_z=\frac{1}{2\nu}\left[-iK_xH_x(K)-iK_yH_y(K)+\nu H_z(K)\right]$$

In (3.6a) all three components are adjusted. This is possible because of the known source. With only external or only internal currents, so that either A(K) or B(K) is neglected, (3.4) gives the field variation with elevation. This makes possible the prediction of vertical derivatives of the field components required for complete curl-free adjustment.

In the presence of both external and internal sources, substitutions from (3.11) and (3.12) in (3.6) give the curl-free adjustment equations:

$$\begin{aligned} &\mathit{H}_x=[K_x^2H_x(K)+K_xK_yH_y(K)]/\nu^2 \\ (3.6b)\quad &\mathit{H}_y=[K_y^2H_y(K)+K_yK_xH_x(K)]/\nu^2 \\ &\mathit{H}_z=H_z \qquad \text{(not adjustable)} \end{aligned}$$

Here only the horizontal components are adjusted because with both external and internal sources, the vertical gradient of the field cannot be predicted before separation.

Curl-free adjustment of the field before separation ensures that the gradients of the two horizontal components are consistent with one another. If the adjusted field is highly correlated with the original data, separation can proceed.

Singularities arise in (3.6a) and (3.6b) for uniform fields (ν=0). In practice such fields are inseparable, as are certain partially uniform components. In the H_x (H_y) field a component uniform in the x (y) direction having zero K_x (K_y) is dropped from the observation and is neither adjustable nor separable. In (3.6a), for instance, spectrum components of all three field components having zero K_x do not contribute to the adjusted field H_x. In practice the limitation is to fields of spatial wavelengths comparable to the array dimensions, or less. Similar limitations arise in separation in the space domain (Oldenburg, 1969; Porath et al., 1970).

A quantitative measure of the spatial similarity of two-dimensional complex fields x and y, specified in discrete values x(i,j), y(i,j) at grid points, is the correlation coefficient

$$(3.13) \qquad C=\lambda_{xy}/\sqrt{(\lambda_{xx}\lambda_{yy})}$$

where

$$\lambda_{xy}=\sum_{i}\sum_{j}[x(i,j)-X][y(i,j)-Y]^{*}$$

$$\lambda_{xx}=\sum_{i}\sum_{j}[x(i,j)-X][x(i,j)-X]^{*}$$

$$\lambda_{yy}=\sum_{i}\sum_{j}[y(i,j)-Y][y(i,j)-Y]^{*}$$

in which X, Y are the averages of the two fields over the area. Correlation coefficients C will be used to compare analytically calculated maps of test field components with corresponding curl-free adjusted maps; and with separated components of internal or external currents. It is important to note the meaning of a high value of C, approaching unity. C is large for two mapped variables x and y if these have high spatial correlation of maxima and minima. However, x and y need not be equal. Thus C=1.0 if $y=ax+b$ with a real and positive. C is a suitable measure of the spatial similarity between an original, known field and a separated one. In the analyses of the data (to follow later) I shall use the Fourier coefficients of the time series in place of x and y in (3.13) and consequently C will be complex. Imaginary parts of C represent any resemblance of the real part of one field to the imaginary part of the other.

3.4 UNIFIED POTENTIAL AS WEIGHTED AVERAGE OF POTENTIALS OF EACH COMPONENT

Here we examine more closely how the three components of observed fields contribute to the potential.

Suppose only external sources contribute to the observation from (3.6), one would expect the following three potentials

$$\Phi_x(K)=H_x(K)/(iK_x)$$

(3.14) $$\Phi_y(K)=H_y(K)/(iK_y)$$

$$\Phi_z(K)=H_z(K)/\nu$$

to be identical to each other, but in practice this is not true due to both the existence of the non-potential field and aliasing problem in data processing. The B(K) given in (3.12a) can be visualized as a unified potential averaging the three potentials in (3.14):

(3.12c) $$\Phi(K)=B(K)=R_x\Phi_x+R_y\Phi_y+R_z\Phi_z$$

with the weighting factors:

$$R_x=K_x^2/2\nu^2$$

(3.15) $$R_y=K_y^2/2\nu^2$$

$$R_z=1/2$$

From (3.12c) and (3.15) we see that in retrieving the potential spectrum the two horizontal components together take the same weight as the vertical component itself. For the purpose of analytic continuation of the field (e.g. in Berdichevsky and Zhdanov, 1984, chap.8) the unified potential given by (3.12c) is the optimum potential at the surface, not Φ_z. Alternatively, one can use Φ_z and Φ_{xy},

$$\Phi_{xy}=2(R_x\Phi_x+R_y\Phi_y), \tag{3.14a}$$

for comparison. Such comparison was once believed impossible (Banks, 1979). The fact that the two horizontal components are equivalent to the vertical component in retrieving the potential is a useful tool for source current inversion (Banks, 1979).

When both external and internal source terms are present, from (3.6) we see that the horizontal and the vertical components are determined by different combinations of the two source terms:

$$\begin{aligned} H_x(K)&=iK_x\Phi_+(K) \\ H_y(K)&=iK_y\Phi_+(K) \\ H_z(K)&=\nu\Phi_-(K) \end{aligned} \tag{3.6c}$$

where,

$$\Phi_{\pm}(K)=B(K)\pm A(K) \tag{3.16}$$

$\Phi_{+}(K)$ can be derived as a weighted average:

$$(3.17)\qquad \Phi_{+}(K)=R_x\Phi_x+R_y\Phi_y$$

$$R_x=K_x^2/\nu^2$$

$$R_y=K_y^2/\nu^2$$

$\Phi_{-}(K)$ is derived only from the vertical component of the field:

$$(3.18)\qquad \Phi_{-}(K)=H_z(K)/\nu$$

Then, from (3.16) we get the potential spectrum of the internal field, $A(K)$, and that of the external field, $B(K)$, separated as follows:

$$(3.19)\qquad A(K)=[\Phi_{+}(K)-\Phi_{-}(K)]/2$$

$$(3.20)\qquad B(K)=[\Phi_{+}(K)+\Phi_{-}(K)]/2$$

(3.19) and (3.20) are equivalent to (3.11) and (3.12) but one sees more clearly how the horizontal fields are combined to give a unified potential $\Phi_{+}(K)$.

3.5 APPLICATIONS TO SYNTHETIC DATA

Tests have been made with synthetic and field data. Two synthetic models that consist of line currents above and below the (x,y) plane of observation are employed. The vector magnetic field is calculated analytically at 15x15 grid points at 20 km spacing in x and y. The curl-free adjustment is applied only to the horizontal field as both external and internal fields are present, and the fields are separated. To reduce distortion near the edges, the data array is expanded symmetrically north-south and east-west before Fourier transformation of the magnetic field components (Kanasewich, 1981, p.58). As uniform fields can not be separated, the average value for the expanded array is subtracted.

The first model consists of horizontal line currents in orthogonal azimuths, one of 90 kA situated 90 ~~km~~ above the (x,y) plane and the other of 40 kA situated 80 km below it. The calculated fields, with straight contours, are shown in Figs.3.1a and 3.2a, and the combined original fields are shown in Fig.3.3a. The curl-free horizontal fields are shown in Fig.3.3b. Comparison of Fig.3.3a and 3.3b indicates that the curl-free adjustment has not greatly altered the X and Y contour patterns, and this is confirmed by correlation coefficients between curl-free and original fields of 0.857 for X and 0.957 for Y over the 225 grid points. As the calculated fields are curl-free, the minor changes introduced in the curl-free adjustment must arise from the finite area of separation and the finite grid spacing.

The separated fields are shown in Figs.3.1b and 3.2b. The central parts of the maps preserve the parallel straight contours of the original fields. As expected, edge effects distort the margins. The correlation coefficients between

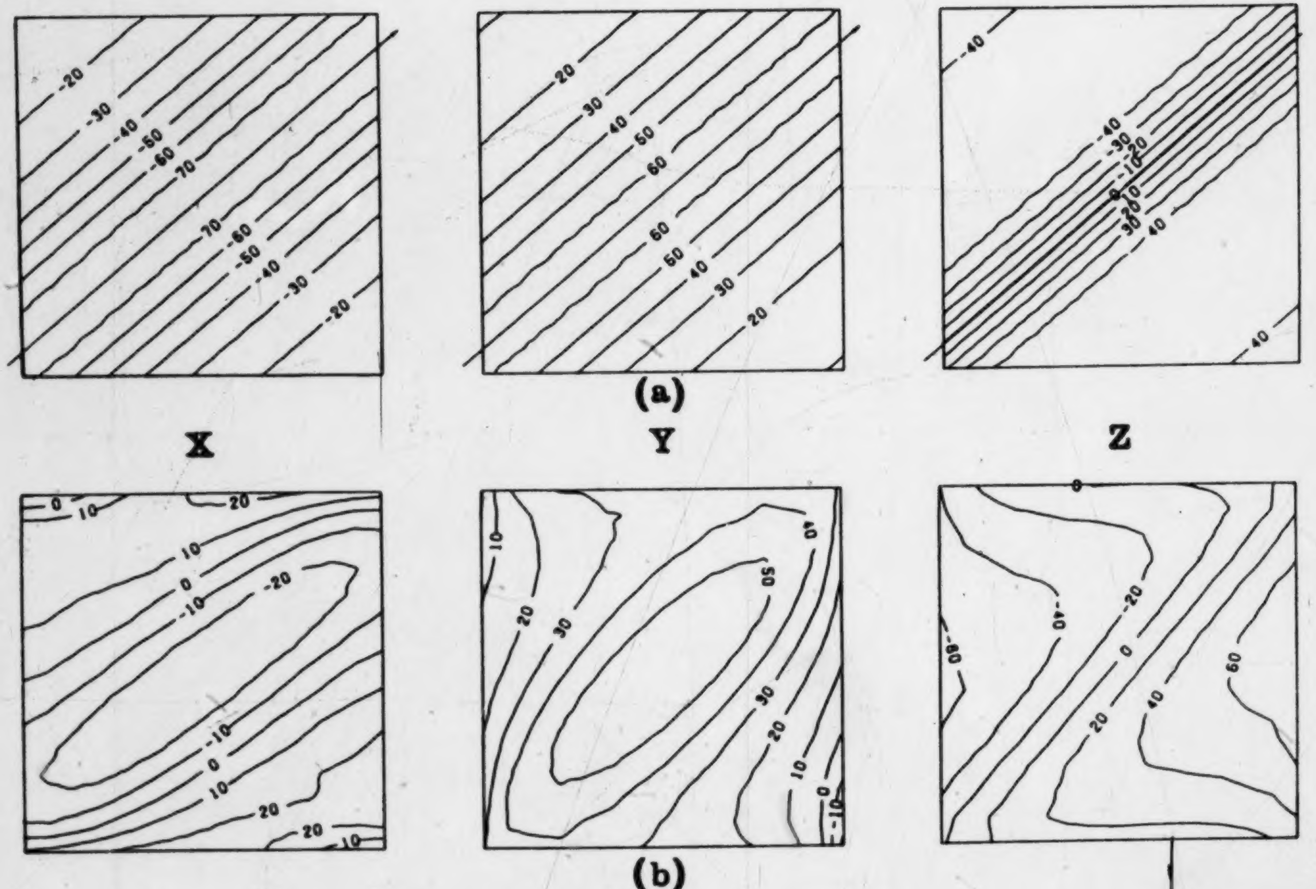

Figure 3.1 (a)Calculated field components for a horizontal internal line current of 40 kA flowing 80 km below the (X-Y) plane. (b)Separated field components for the same current. Unit: nT.

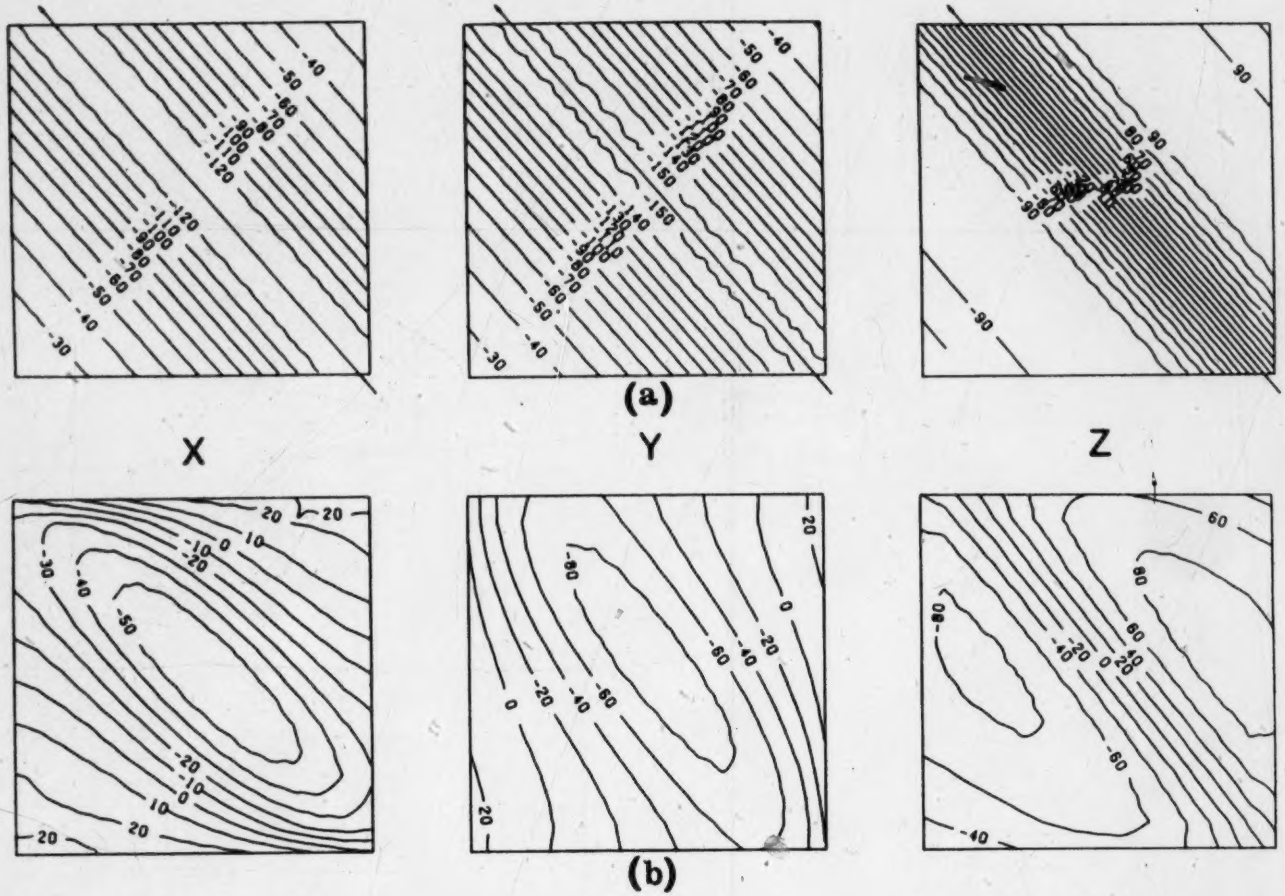

Figure 3.2 (a)Calculated field components for a horizontal external line current of 90 kA flowing 90 km above the (X-Y) plane. (b)Separated field components for the same current. Unit: nT.

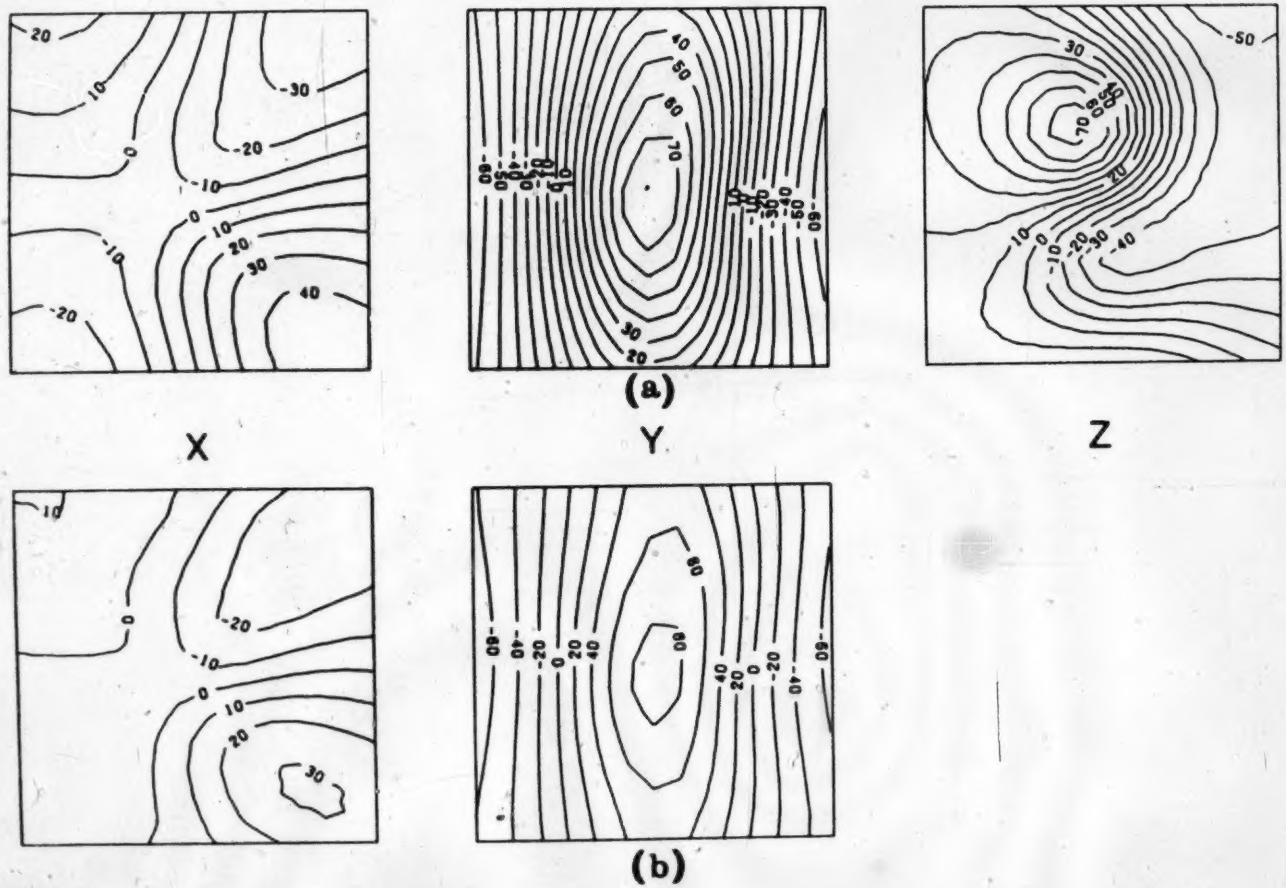

Figure 3.3 (a)Components of the combined original field of external and internal line currents (see Figs.3.1 and 3.2). (b)Curl-free horizontal components of the combined fields. Unit: nT.

the calculated and separated internal fields are 0.826 for X, 0.819 for Y and 0.849 for Z. For the external components these are 0.854, 0.888 and 0.984. This model, with its two-dimensional currents and fields, necessarily contains large totally and partially uniform, and so inseparable, parts. It provides a severe test of the method, with satisfactory results.

For the second synthetic model the external and internal fields are produced by two line currents, each in three segments, none horizontal. The external current is 90 kA and the internal 40 kA. The end segments of each flow from and to infinity: those of the internal current make angles of 75 and 70° with the downward z axis and connects with the middle segment at depths z=80 and 75 km. The from (to) infinity segment of the external current makes angle 110 (120°) with the z axis and connect with the middle segment at z=-80 (-90) km. These three-dimensional currents have no large, inseparable parts and in consequence the separation is much more successful than for the previous model. Figs.3.4a and 3.5a show the internal and external calculated fields, with horizontal projections of the currents, and Fig.3.6a the total field. The curl-free horizontal fields of Fig.3.6b closely resemble the calculated total fields, with correlation coefficients 0.886 for X and 0.981 for Y. The separated fields, shown in Figs.3.4b and 3.5b, match the model fields well: correlation coefficients for the calculated and separated internal and

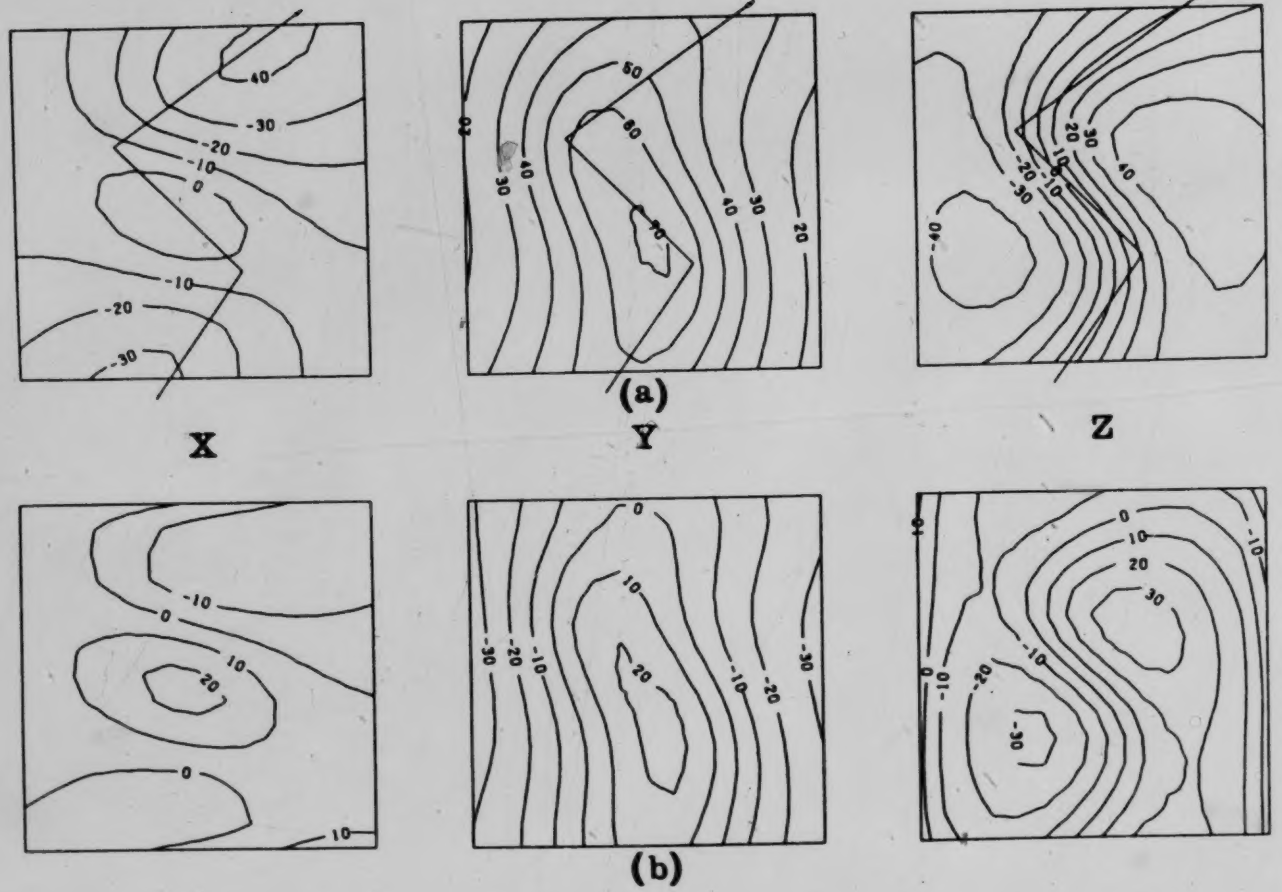

Figure 3.4 (a)Calculated field components for a three-segment 40 kA internal line current, and horizontal projection of the current. (b)Separated field components for the same current. Unit: nT.

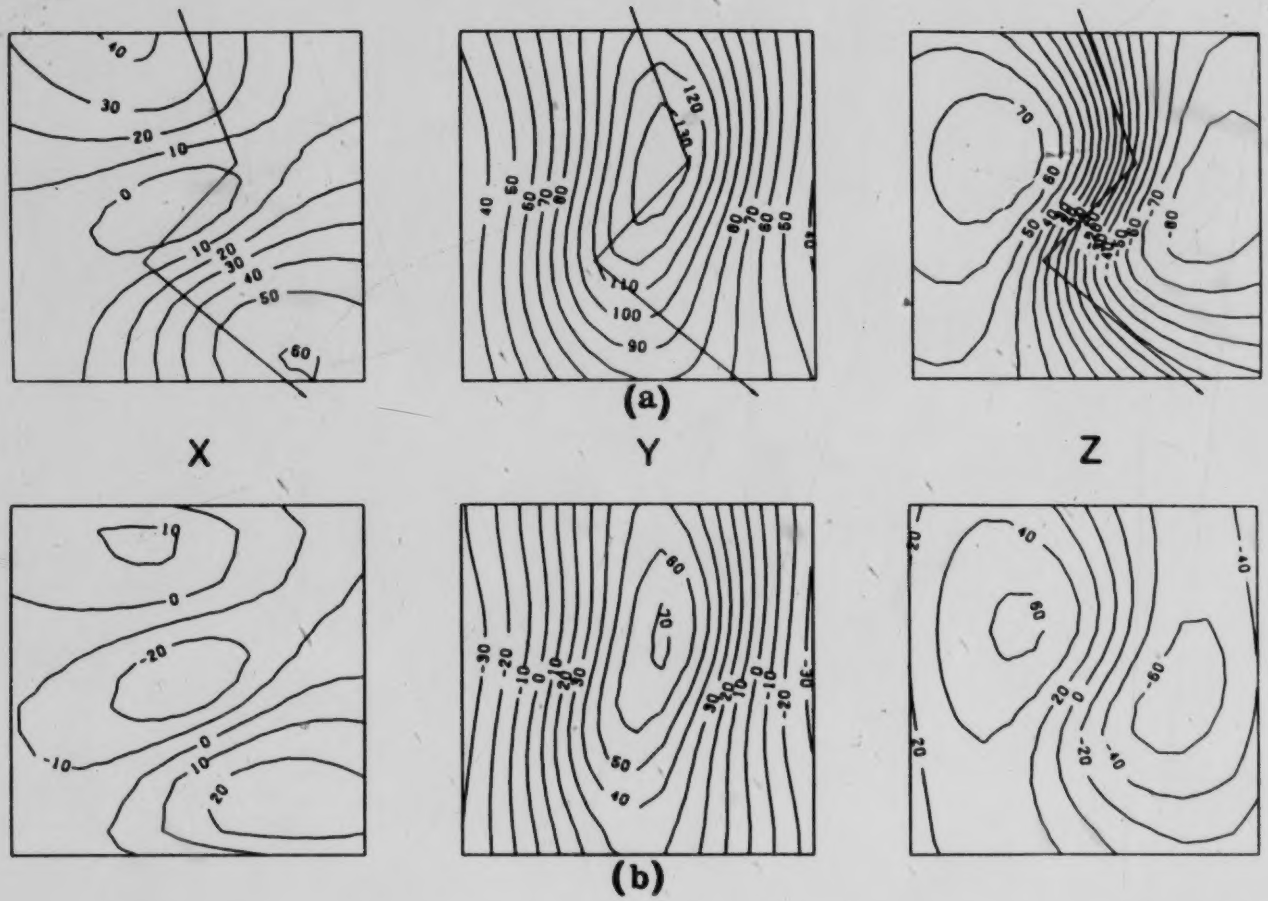

Figure 3.5 (a)Calculated field components for a three-segment 90 kA external line current, and horizontal projection of the current. (b)Sepated field components for the same current. Unit: nT.

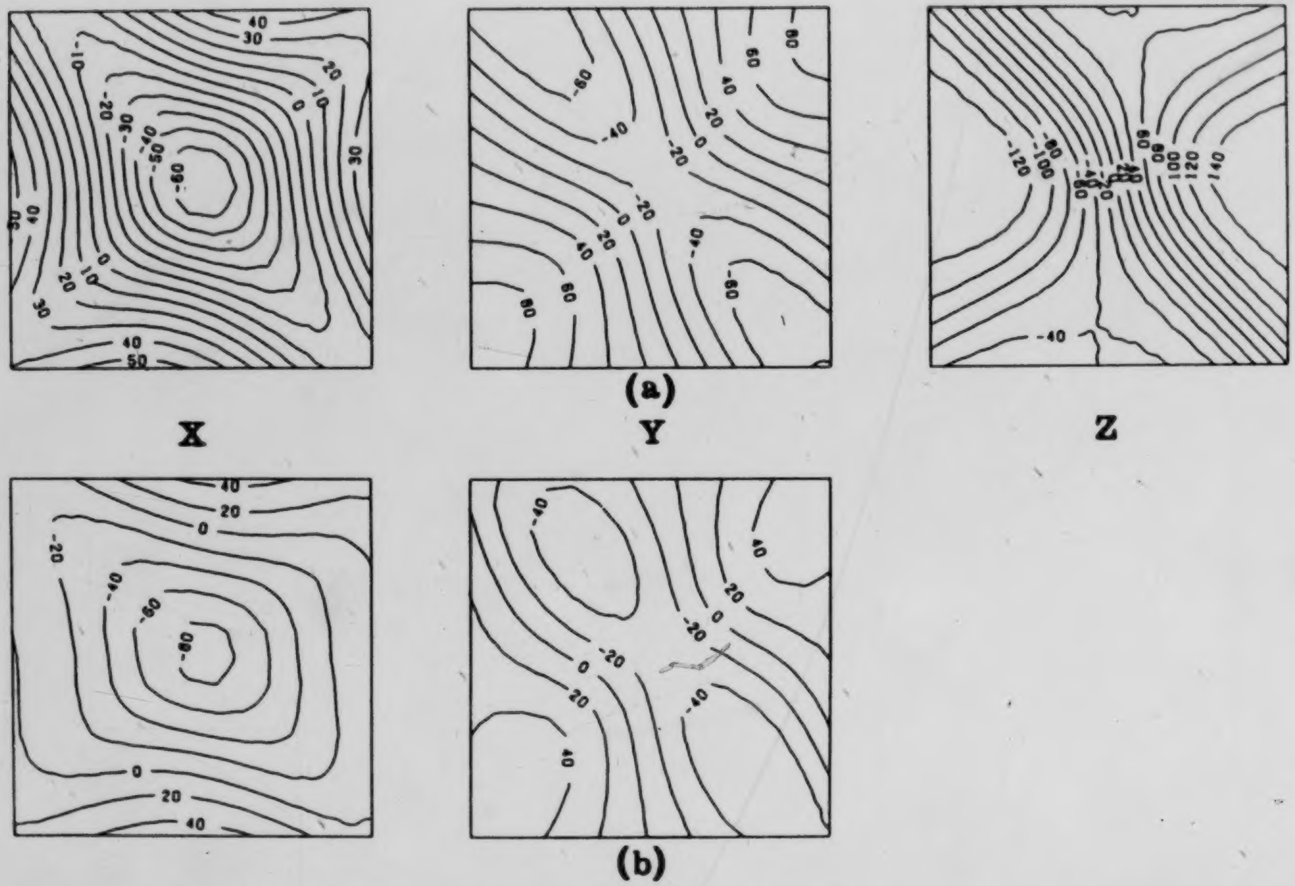

Figure 3.6 (a)Components of the combined original field of three-segment external and internal line currents (see Figs.3.4 and 3.5). (b)Curl-free horizontal components of the combined fields. Unit: nT.

external fields are given in Table 3.1.

3.6 EDGE EFFECTS

Separation of fields known over a limited area results in repetition of those fields to infinity along both x and y axes. If *AB* represents the known fields in the space domain, the field separated is

......ABABAB*AB*ABABAB......

Distortions are produced, specially near the edges of the area of known field, arising mainly from the large discontinuities there. These edge effects can be reduced by expanding the known area to repeat the known fields in mirror image, as

......BAABBA*AB*BAABBA......

to remove the edge discontinuities (Kanasewich, 1981). The fields separated in Sections 3.5 and 3.7 have been expanded in this way.

An example of the improvement produced by the mirror-image expansion is provided in Fig.3.7, which shows the internal parts of the magnetic field for the second synthetic data set, separated with and without expansion. The fields separated using expansion are also shown in Fig.3.4, together with the analytically calculated fields of the internal current. Considerable distortions can be seen in the internal fields from the unexpanded separation of Fig.3.7b, notably near the north and south edges of the X component map and the east and west edges of the Y map. Table 3.1 shows the correlation coefficients between the original and the separated components, from expanded and unexpanded data. It is reassuring to note that the central part of each map is similar for separation of expanded and unexpanded fields.

Table 3.1

Correlation coefficients between original field components and those separated with and without data expansion

	C	
Field Component	Expanded	Unexpanded
Internal X	0.929	0.833
Y	0.983	0.837
Z	0.749	0.620
External X	0.947	0.848
Y	0.988	0.960
Z	0.965	0.948

3.7 APPLICATION TO FIELD DATA

The separation technique developed here has been applied to a set of maps of Fourier transform coefficients at a period of 23 minutes, from a single magnetovariation event recorded at 27 stations (Fig.3.8). This frequency component of the fields has a plane-wave normal field (chapter 2) of very long wavelength, 20,800 km, and has been

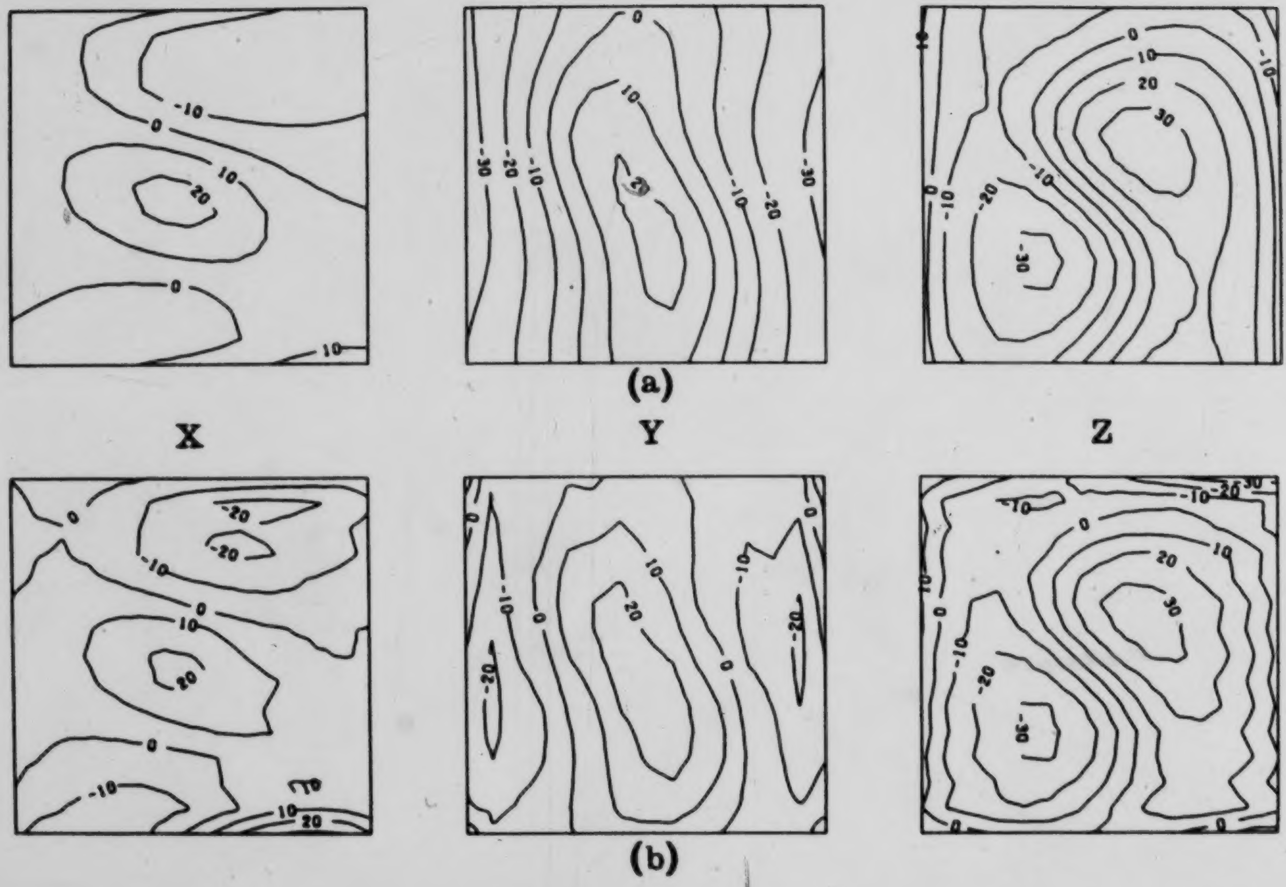

Figure 3.7 Components of the field of the internal three-segment line current (see Fig.3.4) separated (a)with mirror-image expansion of the area of known field, (b)without expansion. Figs. 4b and 7a are the same. Unit: nT.

removed from the data. Its second plane-wave term has a wavelength of 126 km and so satisfies the three criteria (2.8-2.10) for promising further analysis, and has therefore been chosen for separation. The preparation and use of such maps has been described by Gough and Ingham (1983). For the present separation, common phase maps must be used, showing "real" and "imaginary" fields relative to an arbitrary zero phase (Porath et al., 1970). In Fig.3.8 the zero phase has been chosen to maximize the changes in the real fields, so as to maximize power in one set of maps (see section 5.13.1 for details). In the three upper maps of Fig.3.8 the fields of currents flowing NE-SW are immediately apparent.

The Nyquist wavelength (e.g. Kanasewich, 1981), the shortest wavelength resolvable, for this array is around 80 km, twice the minimum station spacing. The data can be interpolated on, at the finest, a 9 by 9 grid, so that the equivalent sampling intervals are 43 (N-S) and 48 (E-W) km. In all wavenumber domain calculations the spectrum should be truncated when

$$2\pi/\nu < 80 \text{ km.} \tag{3.21}$$

This truncation rule has the desired circular symmetry (Lavin and Devane, 1970), that is that the rotation of the XOY plane will not affect the truncated spectrum. The spectrum is dominated by long wavelengths. The aliasing is not serious and retention of wavelengths shorter than the

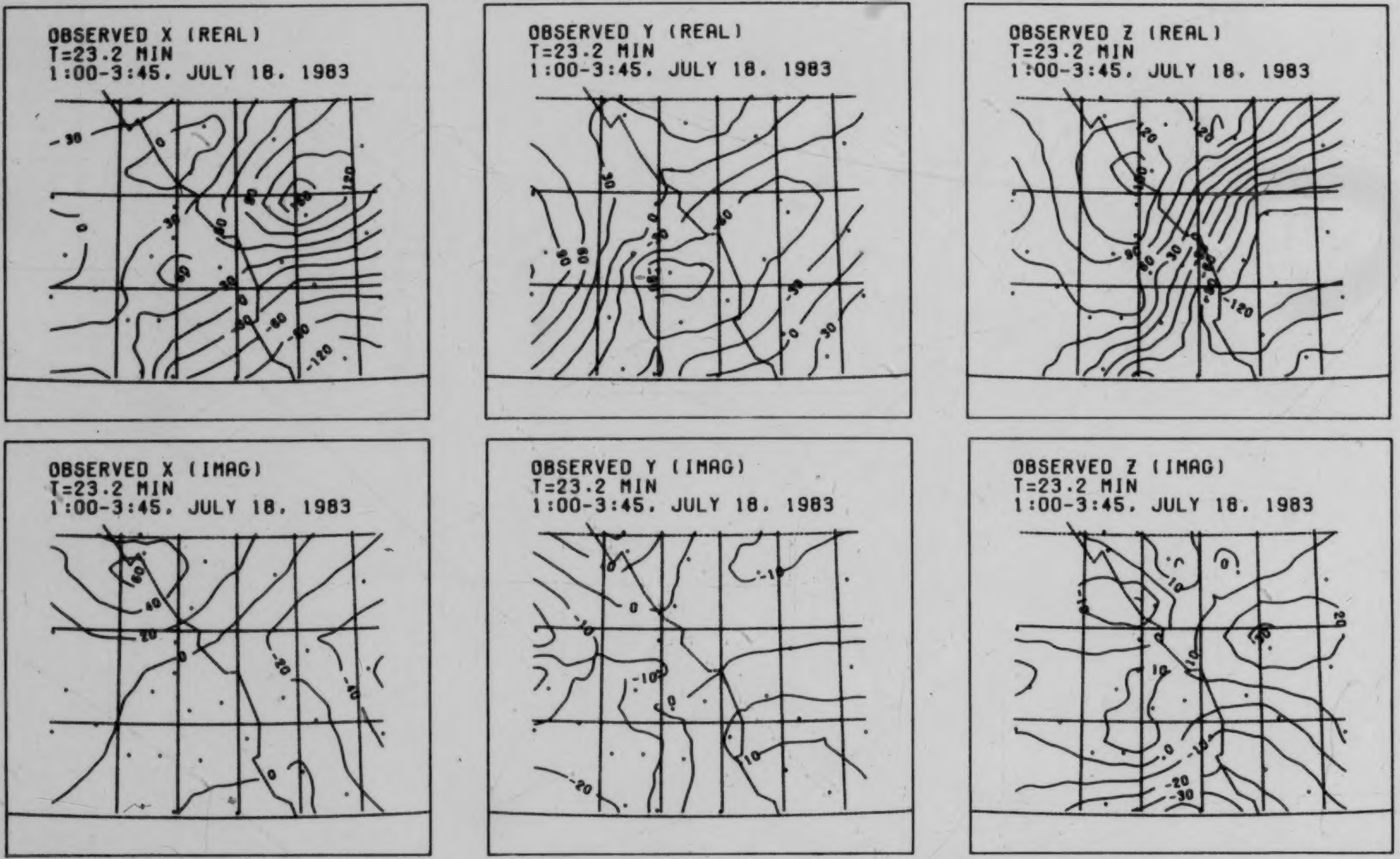
OBSERVED X (REAL)
T=23.2 MIN
1:00-3:45. JULY 18. 1983
OBSERVED Y (REAL)
T=23.2 MIN
1:00-3:45. JULY 18. 1983
OBSERVED Z (REAL)
T=23.2 MIN
1:00-3:45. JULY 18. 1983
OBSERVED X (IMAG)
T=23.2 MIN
1:00-3:45. JULY 18. 1983
OBSERVED Y (IMAG)
T=23.2 MIN
1:00-3:45. JULY 18. 1983
OBSERVED Z (IMAG)
T=23.2 MIN
1:00-3:45. JULY 18. 1983

Figure 3.8 Maps of Fourier transforms of real and imaginary parts of a variation event at period 23 minutes, recorded by an array in southwestern Canada. The start of the time sequence was chosen to give maximum power in the real part of the field.

Nyquist wavelength essentially gives the same separation results. Nevertheless, the station data are interpolated on a 9 by 9 grid for separation, and spectra satisfying (3.21) are truncated.

Horizontal real components adjusted to be curl-free are shown in Fig.3.9. The correlation coefficients over 225 grid points with the values of Fig.3.8 are $0.957+0.044i$ for the X and $0.886-0.033i$ for the Y component. For the real maps the correlation is good. The smaller imaginary parts (not shown) show less significant correlation and are clearly more noise-contaminated.

In Fig.3.10 the internal fields are larger and show more structure than external parts. Some contamination of the latter with internal fields is suggested by features in the external maps similar to the much larger anomalies in the internal maps. The limited size of the array and the edge effects probably produce some leakage of the internal fields into the external maps.

The maps of internal fields indicate a current curving from a north-northeast azimuth at the southern edge of the array to ENE at the eastern limit. The separation exercise supports the view that these currents are internal. The maps of external parts are contaminated with imperfectly separated internal fields and do not properly represent the fields of external currents.

For modelling of conductive structures one needs to estimate both external and internal fields, and to normalize

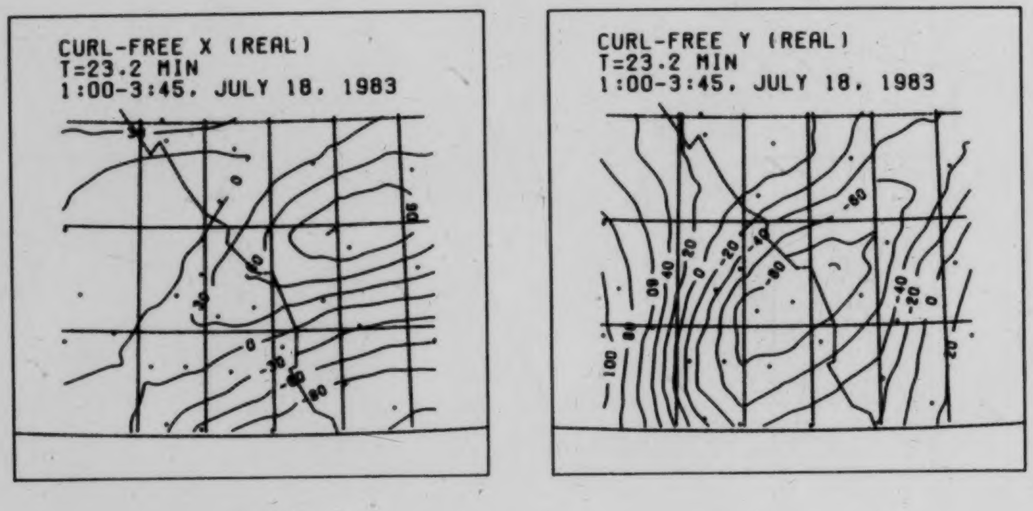
CURL-FREE X (REAL)
T=23.2 MIN
1:00-3:45. JULY 18. 1983
30
0
60
90
30
0
-30
-60
-90
CURL-FREE Y (REAL)
T=23.2 MIN
1:00-3:45. JULY 18. 1983
-60
-40
-20
20
0
-80
40
60
80
100
-40
-20
0
20

Figure 3.9 Curl-free horizontal components of the real part of the magnetovariation event of Fig.3.8.

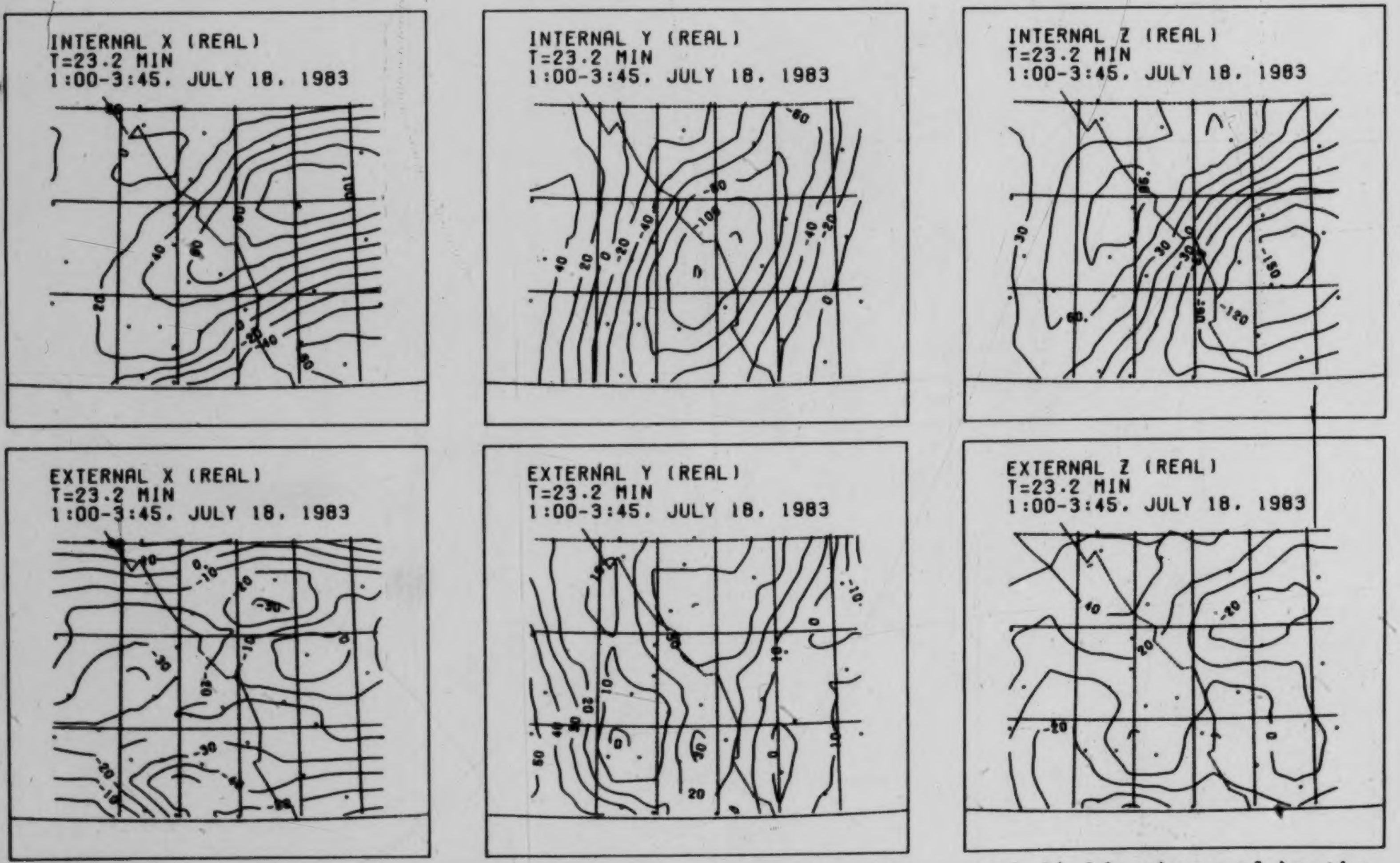
INTERNAL X (REAL)
T=23.2 MIN
1:00-3:45. JULY 18. 1983
INTERNAL Y (REAL)
T=23.2 MIN
1:00-3:45. JULY 18. 1983
INTERNAL Z (REAL)
T=23.2 MIN
1:00-3:45. JULY 18. 1983
EXTERNAL X (REAL)
T=23.2 MIN
1:00-3:45. JULY 18. 1983
EXTERNAL Y (REAL)
T=23.2 MIN
1:00-3:45. JULY 18. 1983
EXTERNAL Z (REAL)
T=23.2 MIN
1:00-3:45. JULY 18. 1983

Figure 3.10 Components of the real separated internal and external fields observed by the magnetometer array. Compare Fig.3.8.

the latter in terms of the former. Here the finite array, and the inseparability of fields of wavelengths larger than the array, presents a formidable problem. Any uniform, or very long wavelength, field cannot be separated. If the external field is mainly of this kind, it cannot be determined and normalization is impossible. The problem has been discussed by Oldenburg (1969), Porath at al. (1970) and by Gough and Ingham (1983).

4. INVERSION TO A SHEET CURRENT AT A SPECIFIC DEPTH

Banks (1979) suggested that determination of the distribution of anomalous currents should be the first stage in any modelling of magnetovariation anomalies. He designed a method using wave-number domain filtering to invert surface observations to a current sheet. We can push his argument to an extreme and emphasize the importance of current inversion. Far away from the source region a "small" magnetometer array observes only a diminishing tail of the external field and a mixture of channelled and locally induced currents (Fig.4.1). Since the extent of a magnetometer array is usually small compared with both the external and internal current sources, any modelling of these magnetometer array data in terms of induction is dangerous in the absence of proper boundary conditions. Furthermore, the inducing external fields cannot be properly defined (chapter 3 of this thesis). Current inversion is less restricted by these limitations. As long as the scale of the internal structure under consideration is comparable with the span of the array the internal fields can be reasonably isolated (chapter 3 of this thesis). Inversion to current models does not then critically depend on the boundary conditions at the array edges. Current inversion is thus more reliable and therefore preferred.

Electromagnetic induction in a layered Earth has been closely studied by a number of researchers. Schmuker (1970) considered the downward continuation of EM fields and gave

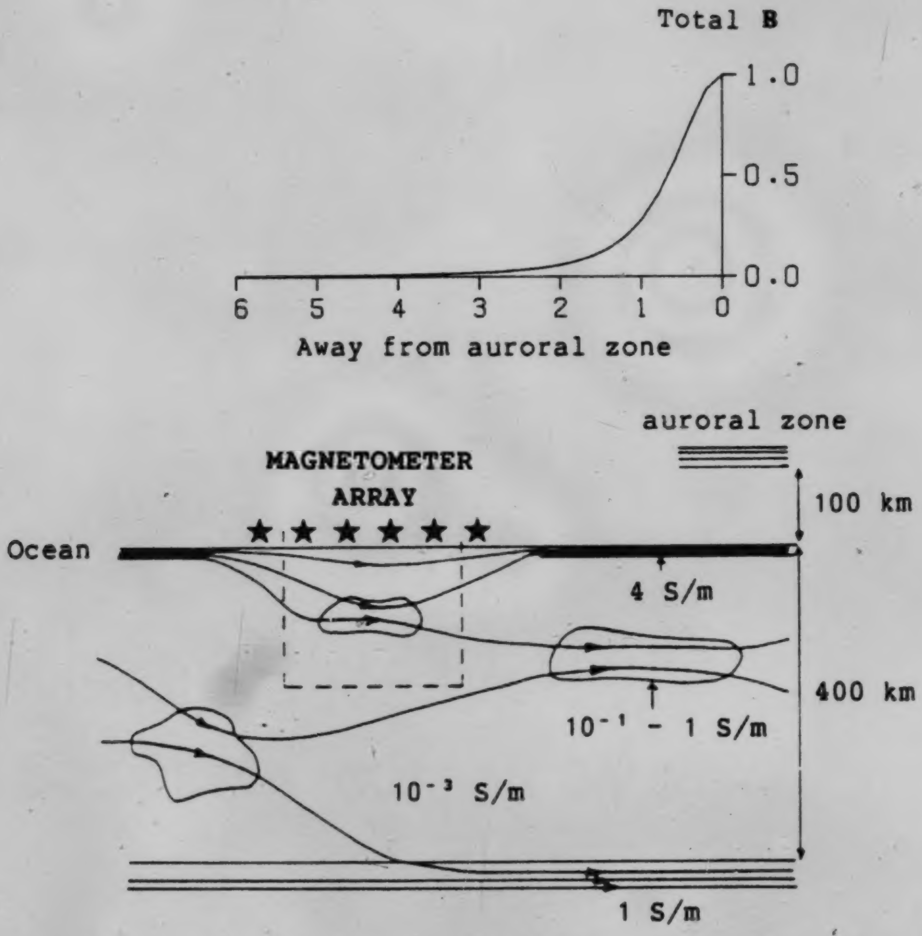
Total B
1.0
0.5
0.0
6
5
4
3
2
1
0
Away from auroral zone
auroral zone
MAGNETOMETER
ARRAY
Ocean
100 km
4 S/m
400 km
10^{-1} - 1 S/m
10^{-3} S/m
1 S/m

Figure 4.1 A cartoon of magnetometer arrays on land, modified from Fig.1 of Banks (1979). Far away from the external source region, induction between the external source and the local structure is less important than in the region directly below the external source.

an elegant recursive formula. Banks (1969) dealt with a spherically layered Earth and presented a matrix formulation for the solution of EM fields in successive layers. The work in this chapter is closely parallel to their work with new developments.

An ideal model of the Earth should clearly be three-dimensional, but for the "anomalous box" monitored by a small array (Fig.4.1), outside the anomalous body, the Earth can be taken as a layered conductor. The surface fields can be downward continued analytically (Berdichevsky and Zhdanov, 1984, chap.13) in such a layered Earth. The separation technique developed in chapter 3 provides a basis for such continuation that is more suitable than other schemes. On reaching the anomalous body, the layered Earth model is no longer valid and further downward continuation will become unstable. The effects of the anomalous body on the fields at depth can be replaced by a current sheet at or near the upper surface of the body to reveal the anomalous current concentration in it. If segmented anomalous bodies lie approximately along some depth in the normal geological setting (a layered structure), the inverted current sheet is expected to represent the actual current concentration in these bodies reasonably well and consequently to predict the locations and shapes of such bodies.

In the inversion of surface fields to a current sheet the writer considers the shielding effect of the conductive Earth, whereas Banks considered a current sheet in free space. The derivation closely follows C.-Y. Fu et al (1978). In Appendix 2 boundary conditions are derived for an arbitrary conductivity-depth function, which may be useful for a wide range of problems in mathematical physics.

4.1 BASIC EQUATIONS

In SI units the Maxwell equations are

$$\nabla \times \mathbf{H}(\mathbf{r},t) = \mathbf{j}(\mathbf{r},t)+\partial \mathbf{D}(\mathbf{r},t)/\partial t \tag{4.1}$$

$$\nabla \times \mathbf{E}(\mathbf{r},t) = -\mu \partial \mathbf{H}(\mathbf{r},t)/\partial t \tag{4.2}$$

$$\nabla \cdot \mathbf{D}(\mathbf{r},t) = \rho(\mathbf{r},t) \tag{4.3}$$

$$\nabla \cdot \mathbf{B}(\mathbf{r},t) = 0 \tag{4.4}$$

where **H** and **B** are magnetic field and induction, **E** and **D** are electric field and induction, j the volume current density, ρ the volume electric charge density, μ is the magnetic permeability (taken at vacuum value, $\mu_0=4\pi\times10^{-7}$ H/m). It is assumed that every function of space and time has $\exp[i\omega t]$ time dependence,

$$f(\mathbf{r},t) \rightarrow f(\mathbf{r})\exp[i\omega t]$$

With the $\exp[i\omega t]$ factor dropped and $\partial/\partial t$ replaced by $i\omega$ (4.1) - (4.4) become:

$$\nabla \times \mathbf{H}(\mathbf{r}) = \mathbf{j}(\mathbf{r})+i\omega \mathbf{D}(\mathbf{r}) \tag{4.1a}$$

$$\nabla \times \mathbf{E}(\mathbf{r}) = -i\omega\mu \mathbf{H}(\mathbf{r}) \tag{4.2a}$$

(4.3a) $\nabla \cdot \mathbf{D}(\mathbf{r}) = \rho(\mathbf{r})$

(4.4a) $\nabla \cdot \mathbf{B}(\mathbf{r}) = 0$

In a layered Earth with all physical properties only z dependent, we can choose the electric field as toroidal (Price, 1950):

(4.5) $\mathbf{E}(\mathbf{r}) = -\mathbf{e}_z \mathrm{x} \nabla\psi(\mathbf{r})$

where $\mathbf{e}_z$ is a unit vector along the z axis and ψ is the toroidal amplitude function. We then have

(4.6) $\mathbf{E} \cdot \nabla\sigma(z) \equiv 0.$

Equation (4.3a) becomes

(4.3b) $\nabla \cdot \mathbf{E}(\mathbf{r}) = 0,$

since under condition (4.6) any previously existing free charge ρ would decay exponentially with time (C-Y. Fu et al, 1978). For the toroidal electric field **E**, (4.3b) is automatically satisfied. Expressing ψ with separated variables:

(4.7) $\psi(\mathbf{r}) = Z(z)p(x,y)$

the electric field **E** is written as:

(4.5a) $\mathbf{E}(r) = [\partial p(x,y)/\partial y, -\partial p(x,y)/\partial x, 0]Z(z)$

Under condition (4.6) and at low frequencies (Price, 1950), the Maxwell equations lead to the diffusion equation of the electric field:

(4.8) $\nabla^2\mathbf{E}(r,t) = \mu\sigma(z)\partial\mathbf{E}(r,t)/\partial t$

or, with $\exp[i\omega t]$ time dependence,

(4.8a) $\nabla^2\mathbf{E}(r) = i\omega\mu\sigma(z)\mathbf{E}(r)$

Substituting (4.5a) into (4.8a) and separating variables:

(4.8b) $\partial^2 p(x,y)/\partial x^2+\partial^2 p(x,y)/\partial y^2+\nu^2 p(x,y) = 0$

(4.8c) $d^2Z(z)/dz^2 = [\nu^2+i\omega\mu\sigma(z)]Z(z)$

in which ν^2 is a constant of separation of the variables. Substituting (4.5a) into (4.2a),

(4.9) $\mathbf{H}(r) = i[Z_{,z}p_{,x}, Z_{,z}p_{,y}, \nu^2 Zp]/(\omega\mu)$

In (4.9) the time variable dependence of all the functions is dropped and the subscripts ",*x*", ",*y*", ",*z*" are used to represent the derivatives with respect to x, y and z. With this notation (4.5a) is rewritten as

$$(4.5b)\qquad \mathbf{E}(\mathbf{r}) = [p_{,y},\ -p_{,x},\ 0]Z$$

Once functions Z and p are determined (4.5b) and (4.9) give the electromagnetic fields.

The solution for p is familiar:

$$(4.10)\qquad p(x,y) = \exp[imx]\exp[iny] \equiv p(m,n)$$
$$m^2+n^2 = \nu^2$$

The solution for the function Z depends on the conductivity distribution in the region under consideration and will be considered in sections 4.4 and 4.5.

4.2 BOUNDARY CONDITION AT A SOURCE-FREE LAYER INTERFACE

In the plane layered model of the Earth the boundary conditions for the magnetic field, at an interface free of surface currents, are

$$(4.11)\qquad \mu^+H_z^+ = \mu^-H_z^-$$
$$(4.12)\qquad (\mathbf{H}^+-\mathbf{H}^-)\times\mathbf{e}_z = 0$$

in which the superscripts "-" and "+" denote the quantities above and below the interface respectively. A corresponding boundary condition at an interface bearing surface current will be considered in section 4.4.

Since the free charge density is everywhere zero we will not consider the case of a charged interface. For the chosen toroidal electric field the continuity of the normal component of electric displacement D_z is always satisfied even for a discontinuity in the dielectric constant ϵ, since D_z is always zero. We have to consider only the continuity of the tangential electric field:

$$(4.13) \qquad (\mathbf{E}^{+}-\mathbf{E}^{-})\times \mathbf{e}_z = 0$$

For the toroidal electric field (4.5) and time dependence $\exp[j\omega t]$ (4.9) gives:

$$(4.14) \qquad H_z = \frac{j\nu^2}{\omega\mu} p(m,n)Z(\nu)$$

Since the discussion hereafter is in terms of the solutions for $p(x,y)$ and $Z(z)$ to satisfy equations (4.8b) and (4.8c), which depend on the parameters m, n and ν, the notation of (4.14) explicitly depends on these parameters.

It is known that the family of functions $p(m,n)$ with different m and/or n are linearly independent. This fact greatly facilitates the fitting of boundary conditions since one has to compare only the electromagnetic field component characterized by the same element from the family of functions $p(m,n)$, not the summation of these solutions over m and n.

On a current-free interface, by (4.9), (4.12) leads to:

$$(4.12a) \qquad Z^{+}_{;z}/\mu^{+} = Z^{-}_{;z}/\mu^{-}$$

The relations (4.11) and (4.13) are equivalent, that is, the continuity of tangential **E** requires the continuity of normal **B**. By (4.14), (4.11) requires

$$\frac{j\nu^2}{\omega}p(m,n)Z^+(\nu) = \frac{j\nu^2}{\omega}p(m,n)Z^-(\nu)$$

or,

$$(4.11a) \quad Z^+(\nu) = Z^-(\nu)$$

Again, by (4.5b), (4.13) requires

$$[p_{,y}(m,n),-p_{,x}(m,n)]\cdot Z^+(\nu) = [p_{,y}(m,n),-p_{,x}(m,n)]\cdot Z^-(\nu)$$

which leads to (4.11a). Thus continuity of normal **B** and that of tangential **E** are equivalent. Hence only the boundary conditions (4.11) and (4.12), or (4.11a) and (4.12a), are considered in what follows.

4.3 BOUNDARY CONDITION AT A CURRENT SHEET

For a current sheet (4.12) is modified to:

$$(4.12b) \quad (\mathbf{H}^+-\mathbf{H}^-)\mathrm{x}\mathbf{e}_z = -\mathbf{J}$$

The surface current density J can be expressed in terms of a current function $\phi(x,y)$:

$$J(x,y) = e_z \times \nabla\phi(x,y). \tag{4.15}$$

With $\phi(x,y)$ expanded in harmonics $p(m,n)$ (4.10) gives:

$$\phi(x,y) = \Sigma\, \phi(m,n) \equiv \Sigma\, c_{mn} p(m,n). \tag{4.16}$$

$J(x,y)$ has harmonic components like

$$J(m,n) = [-p_{,y}(m,n),\ p_{,x}(m,n),\ 0] \cdot c_{mn} \tag{4.17}$$

Then by (4.9) and (4.17), (4.12b) leads to:

$$-i\omega c_{mn} = Z^{+}_{;z}/\mu^{+} - Z^{-}_{;z}/\mu^{-} \tag{4.18}$$

The current function defined here has the following properties:

1. The contour lines of the current function are current lines.

   Since ϕ is a function of x and y only, we have:

   $$e_z \cdot \nabla\phi(m,n) = 0$$

   Therefore $\nabla\phi(m,n)$ is in the xy plane. From (4.15) we have:

   $$J(m,n) \cdot e_z = J(m,n) \cdot \nabla\phi(m,n) = 0$$

Hence **J** is in the xy plane and perpendicular to $\nabla\phi$, that is, parallel to contours of ϕ. The relation of the actual direction of **J** with the configuration of contour lines of the current function ϕ is shown in Fig.4.2.

2. The amount of current flowing between two contour lines, ϕ_1 and ϕ_2, is $\phi_2-\phi_1$.

In Fig.4.2, 1 and 2 are arbitrary points on contours ϕ_1 and ϕ_2, l is an arbitrary curve in the horizontal plane connecting 1 and 2, and $\mathbf{e}_n$ and $\mathbf{e}_t$ are unit vectors normal and tangential to the line element dl. The amount of current flowing from one side of l to the other is:

$$\begin{aligned} I &= \int_1^2 \mathbf{J}\cdot\mathbf{e}_n dl \\ &= \int_1^2 (\mathbf{e}_z x \nabla\phi)\cdot\mathbf{e}_n dl \\ &= \int_1^2 (\mathbf{e}_n x \mathbf{e}_z)\cdot\nabla\phi dl \\ &= -\int_1^2 \mathbf{e}_t\cdot\nabla\phi dl \\ &= \int_1^2 \partial\phi/\partial l \; dl \\ &= \phi_2-\phi_1 \end{aligned}$$

4.4 SOLUTION FOR Z IN AN UNIFORM CONDUCTIVE LAYER

For a layer of constant conductivity σ_0, the solution to (4.8c) is

$$Z(z) = A\cdot\exp[\theta z]+B\cdot\exp[-\theta z] \qquad (4.19)$$

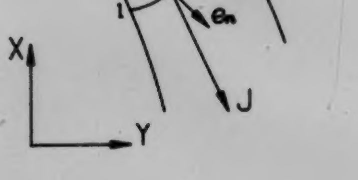
$\Phi_2 > \Phi_1$
Φ_2
2
Φ_1
l
e_t
$\nabla\Phi$
dl
1
e_n
X
J
Y

Figure 4.2 Relation between contours of current function and direction and density of surface current.

$$(4.20)\qquad \theta = \sqrt{(i\omega\mu\sigma_0+\nu^2)}$$

Without losing generality we can take Re[θ] positive. A and B in (4.19) then represent the contributions of current below and above the layer.

The magnetic field in the layer is:

$$(4.21)\qquad \mathrm{H} = \frac{i}{\omega\mu}\begin{bmatrix} (A\cdot\exp[\theta z]-B\cdot\exp[-\theta z])\theta p_{,x} \\ (A\cdot\exp[\theta z]-B\cdot\exp[-\theta z])\theta p_{,y} \\ (A\cdot\exp[\theta z]+B\cdot\exp[-\theta z])\nu^2 p \end{bmatrix}$$

4.5 SOLUTION FOR Z IN FREE SPACE

With $\sigma_0=0$ in section 4.4 the solution for free space is:

$$(4.22)\qquad Z(z) = A_0\exp[\nu z]+B_0\exp[-\nu z]$$

Here again with $\nu\geq0$, A and B represent the contributions of internal and external currents. Substituting (4.22) into (4.9) and putting $\mu=\mu_0$ for free space,

$$(4.23)\qquad \mathrm{H} = \frac{i\nu}{\omega\mu_0}\begin{bmatrix} (A_0\exp[\nu z]-B_0\exp[-\nu z])p_{,x} \\ (A_0\exp[\nu z]-B_0\exp[-\nu z])p_{,y} \\ (A_0\exp[\nu z]+B_0\exp[-\nu z])\nu p \end{bmatrix}$$

In free space the magnetic induction can be derived from a potential $\Phi(r)$ by

(4.24) $$\mathbf{B}(\mathbf{r}) = -\nabla\Phi(\mathbf{r})$$

with the potential given below:

(4.25) $$\Phi(r) = -i\nu\{A_0\exp[\nu z]-B_0\exp[-\nu z]\}p(x,y)/\omega$$

Comparing the form of potential adopted in chapter 3 the source terms are:

(4.26) $$A = -i\nu A_0/\omega \qquad B = i\nu B_0/\omega$$

Or in matrix form:

(4.26a) $$\begin{bmatrix} A_0 \\ B_0 \end{bmatrix} = \frac{i\omega}{\nu}\begin{bmatrix} 1 & 0 \\ 0 & -1 \end{bmatrix}\cdot\begin{bmatrix} A \\ B \end{bmatrix}$$

4.6 PLANE LAYERED EARTH MODEL

Consider the model shown in Fig.4.3, with the surface of the Earth at $z=0$, z positive down. Free space lies between $z=0$ and $z=-h$, where h is the height of the ionosphere, a conductive region not considered in this thesis.

The free space is denoted layer 0, and the layer denoted j has upper surface at z_{j-1}, lower surface at z_j and thickness z_j-z_{j-1}. All physical parameters of layer j are subscripted j, and relative magnetic permeability is identically 1.

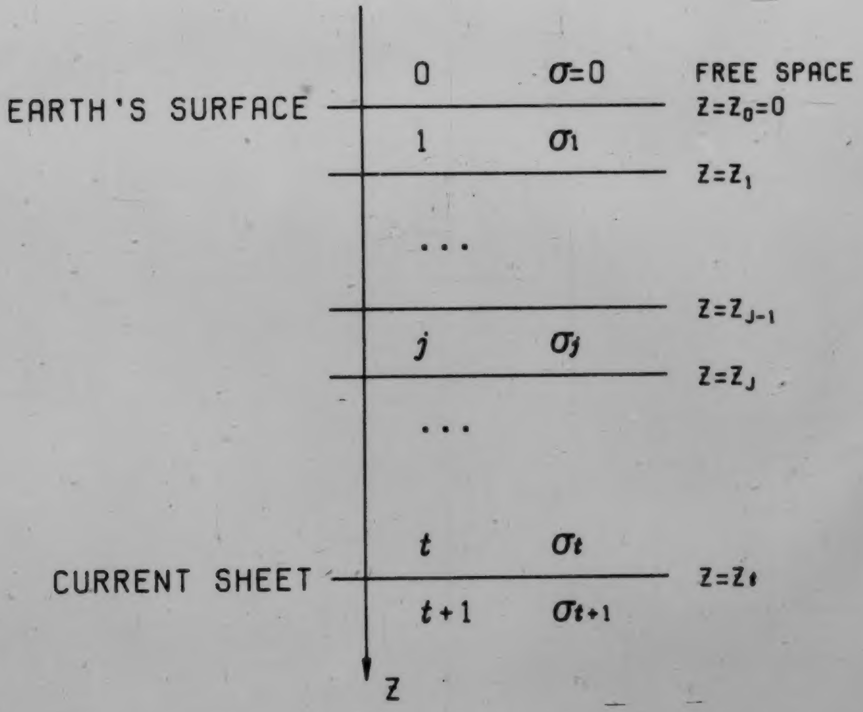
0
σ=0
FREE SPACE
EARTH'S SURFACE
Z=Z0=0
1
σ1
Z=Z1
...
Z=ZJ-1
j
σj
Z=ZJ
...
t
σt
CURRENT SHEET
Z=Zt
t+1
σt+1
Z

Figure 4.3 Layered earth's model.

The model comprises t+1 layers with a current sheet at $z=z_t$ underlaid by a uniform conductive half space. This sheet current can be located at a depth where an anomalous conductive structure is expected.

4.7 MATRIX REPRESENTATION OF BOUNDARY CONDITIONS

Two types of boundary conditions are best represented in matrix form both for computing convenience and for further mathematical development. These are boundary conditions (1)at layer interfaces bearing no current and (2)at the current sheet.

(1).At interface $z=z_j$, $j = 0, 1, \cdots t-1$, tangential **H** and **E** are continuous, substitute (4.22) into (4.12a) and (4.11a)

$$\begin{aligned}
&\theta_j(A_j\exp[\theta_j z_j]-B_j\exp[-\theta_j z_j]) = \\
&\qquad \theta_{j+1}(A_{j+1}\exp[\theta_{j+1}z_j]-B_{j+1}\exp[-\theta_{j+1}z_j]) \\
&A_j\exp[\theta_j z_j]+B_j\exp[-\theta_j z_j] = \\
&\qquad A_{j+1}\exp[\theta_{j+1}z_j]+B_{j+1}\exp[-\theta_{j+1}z_j] \\
&\qquad j = 1, 2, \cdots t-1
\end{aligned}$$

In matrix form:

$$(4.27)\qquad D_j^+ v_j = D_{j+1}^- v_{j+1},$$

In (4.27), subscript j indicates quantities related to layer j, and superscript +/- indicates that the z coordinate in the matrix is the lower/upper surface of the layer. In (4.27),

$$(4.28)\qquad \mathbf{v}_j = \begin{bmatrix} A_j \\ B_j \end{bmatrix}$$

$$(4.29)\qquad \mathbf{D}_j^{+} = \begin{bmatrix} \theta_j \exp[\theta_j z_j] & -\theta_j \exp[-\theta_j z_j] \\ \exp[\theta_j z_j] & \exp[-\theta_j z_j] \end{bmatrix}$$

$$(4.30)\qquad \mathbf{D}_{j+1}^{-} = \begin{bmatrix} \theta_{j+1} \exp[\theta_{j+1} z_j] & -\theta_{j+1} \exp[-\theta_{j+1} z_j] \\ \exp[\theta_{j+1} z_j] & \exp[-\theta_{j+1} z_j] \end{bmatrix}$$

$$\text{with} \quad j = 0,\ 1,\ \cdots\ t-1$$

At the Earth's surface, $z=z_0=0$, the boundary conditions correspond to $j=0$ and $\theta=\nu$ in the above expressions. Here the matrices simplify:

$$\mathbf{D}_0^{+} = \begin{bmatrix} \nu & -\nu \\ 1 & 1 \end{bmatrix}$$

$$\mathbf{D}_1^{-} = \begin{bmatrix} \theta_1 & -\theta_1 \\ 1 & 1 \end{bmatrix}$$

(2).At the current sheet, $z=z_t$, tangential **H** is discontinuous, substitute (4.22) into (4.18) and (4.11a), and neglect terms with $A_{t+1}\exp[\theta_{t+1}z]$ because of its singularity as $z \rightarrow \infty$:

$$\theta_t(A_t \exp[\theta_t z_t] - B_t \exp[-\theta_t z_t]) =$$
$$-\theta_{t+1} B_{t+1} \exp[-\theta_{t+1} z_t] + i\omega\mu_0 c$$

$$A_i\exp[\theta_i z_i]+B_i\exp[-\theta_i z_i] = B_{i+1}\exp[-\theta_{i+1} z_i]$$

In matrix form:

$$(4.31)\qquad D_i^+ v_i = D_{i+1}^- v_{i+1}$$

where

$$(4.32)\qquad v_{i+1} = \begin{bmatrix} C \\ B_{i+1} \end{bmatrix}$$

$$(4.33)\qquad D_{i+1}^- = \begin{bmatrix} i\omega\mu_0 & -\theta_{i+1}\exp[-\theta_{i+1} z_i] \\ 0 & \exp[-\theta_{i+1} z_i] \end{bmatrix}$$

4.8 SOLUTION IN V SPACE

For any layer, once v_j is known, the magnetic field can be calculated from (4.21) for a conducting layer or from (4.23) for free space. The electric field is then obtained from (4.5a). The current function, which defines the current sheet, can be inverted from v_{i+1} (see 4.32). The v_j vector can thus be considered the *solution in* v *space* for the electromagnetic field. Such a solution can be constructed as follows.

For a particular Fourier component, (ω, m, n), of the magnetic field the internal and external fields can be separated to yield the vector v_0 by the method developed in chapter 3 with the supplementary transform (4.26a). For a layered Earth model described in section 4.6 the matrices D_j

defined in section 4.7 can be calculated. Then from a known solution in an upper layer the solution in the adjacent lower layer can be calculated from (4.27):

$$(4.27a)\qquad \mathbf{v}_{j+1} = (\mathbf{D}_{j+1}^{-})^{-1}\mathbf{D}_j^{+}\mathbf{v}_j$$

Starting with layer zero, the free space (Fig.4.3), (4.27a) is applied recursively to obtain

$$(4.27b)\qquad \mathbf{v}_{j+1} = (\mathbf{D}_{j+1}^{-})^{-1}\{\mathbf{D}_j^{+}(\mathbf{D}_j^{-})^{-1}\}\cdots\{\mathbf{D}_1^{+}(\mathbf{D}_1^{-})^{-1}\}\mathbf{D}_0^{+}\mathbf{v}_0$$

$$j = 0,\ 1,\ \cdots\ t$$

In (4.27b) $(\mathbf{D}_j^{-})^{-1}$ is the inverse matrix of $\mathbf{D}_j^{-}$, from (4.30) and (4.33),

$$(4.30a)\qquad (\mathbf{D}_j^{-})^{-1} = \frac{1}{2}\begin{bmatrix} \exp[-\theta_j \mathbf{z}_{j-1}]/\theta_j & \exp[-\theta_j \mathbf{z}_{j-1}] \\ -\exp[\ \theta_j \mathbf{z}_{j-1}]/\theta_j & \exp[\ \theta_j \mathbf{z}_{j-1}] \end{bmatrix}$$

$$j = 1,\ 2,\ \cdots\ t$$

$$(4.33a)\qquad (\mathbf{D}_{t+1}^{-})^{-1} = \begin{bmatrix} -i/(\omega\mu_0) & -i\theta_{t+1}/(\omega\mu_0) \\ 0 & \exp[\theta_{t+1}\mathbf{z}_t] \end{bmatrix}$$

Finally, as the quantity in each pair of brackets "{}" in (4.27b) is related only to one conducting layer, (4.27b) can be written in a compact form:

$$(4.27c)\qquad \mathbf{v}_{j+1} = (\mathbf{D}_{j+1}^{-})^{-1}\mathbf{D}_j\cdots\mathbf{D}_1\mathbf{D}_0^{+}\mathbf{v}_0$$

Here D_j is the *induction matrix* of the jth layer:

$$D_j = D_j^{+}(D_j^{-})^{-1} \qquad (4.34)$$

From (4.29), the induction matrix is

$$D_j = \begin{bmatrix} ch(\theta_j h_j) & sh(\theta_j h_j)\cdot\theta_j \\ sh(\theta_j h_j)/\theta_j & ch(\theta_j h_j) \end{bmatrix} \qquad (4.35)$$

in which $h_j = z_j - z_{j-1}$, is the thickness of the layer.

The nature of the induction matrices is examined in Appendix 1. When the number of layers approaches infinity, the boundary conditions applied to an infinite number of layers can be used to solve the problem for any conductivity-depth relation. The product of an infinite number of induction matrices for layer elements is derived in Appendix 2. This treatment may be applicable in other problems of mathematical physics.

4.9 THE SHIELDING PROPERTY OF A LAYERED EARTH

The shielding property of the layered Earth upon the anomalous currents is examined.

Consider a simple Earth model with only two layers and a field at the Earth's surface consisting of internal source terms only. From section 4.8 the linear relation existing between current function amplitude, c_{mn}, and internal source term, $A_0(m,n)$ is:

(4.36) $c_{mn} = d_{11} A_0(m,n)$

where

(4.37) $d_{11}=-i[(\theta_1+\theta_2\nu/\theta_1)*sh(\theta_1h_1)+(\theta_2+\nu)*ch(\theta_1h_1)]/(\omega\mu_0)$

The complex quantity d_{11} represents the shielding property of the layered Earth. To make it dimensionless we consider the following quantity:

(4.38) $b\cdot\exp[i\phi] = i\omega/(\nu\mu_0)\cdot d_{11}$

when $\sigma_1=\sigma_2=0$ we have:

(4.39) $b_0 = b(\sigma=0) \equiv sh(\nu h_1)+ch(\nu h_1)$

$\phi \equiv 0$

The quantity b_0 represents the geometrical spreading effect of the field of the sheet current source. The following ratio:

(4.40) $B = b(\sigma\neq0)/b(\sigma=0)$

represents induction effects in the conducting Earth, and it is called the *physical attenuation factor* (Rikitake, 1951), given by:

$$(4.41) \qquad B = \frac{|(\theta_1+\theta_2\nu/\theta_1)*sh(\theta_1h_1)+(\theta_2+\nu)*ch(\theta_1h_1)|}{2\nu[\ sh(\nu h_1)+ch(\nu h_1)\ ]}$$

The definition of the quantity θ, equation 4.20, shows that for field components with very long wave length (small ν) the induction effect is stronger, while for short wave length components the conductive medium is more "transparent" and the geometrical attenuation is dominant.

The physical attenuation factors B and phase delays ϕ have been calculated for a set of models. A reasonable first approximation model of the Earth is taken as: h_1=50 km, $\sigma_1=3.0\text{x}10^{-2}$ S/m., σ_2=1 S/m. With two of the above three parameters fixed the third is varied: h_1=50, 100, 200 km or $\sigma_1=3.0\text{x}10^{-1}$, $3.0\text{x}10^{-2}$, $3.0\text{x}10^{-3}$ S/m. The shielding effects of the models are shown in Figs.4.4-4.7. The period range covered is 5-320 minutes and the wavelength range 50 to 400 km.

It is noted that with the models considered the physical attenuation is insensitive to the variation of h_1 and σ' but quite sensitive to the addition of a highly conducting thin surface layer. The other combinations of the model parameters do not realistically represent the Earth's crust and upper mantle we know today (Parkinson, 1983, p.324-328). Figs.4.4-4.7 show that physical attenuation is only noticeable for field components with wavelength longer than 100 km, but phase delay occurs for wavelengths above 50 km or so. This suggests that with

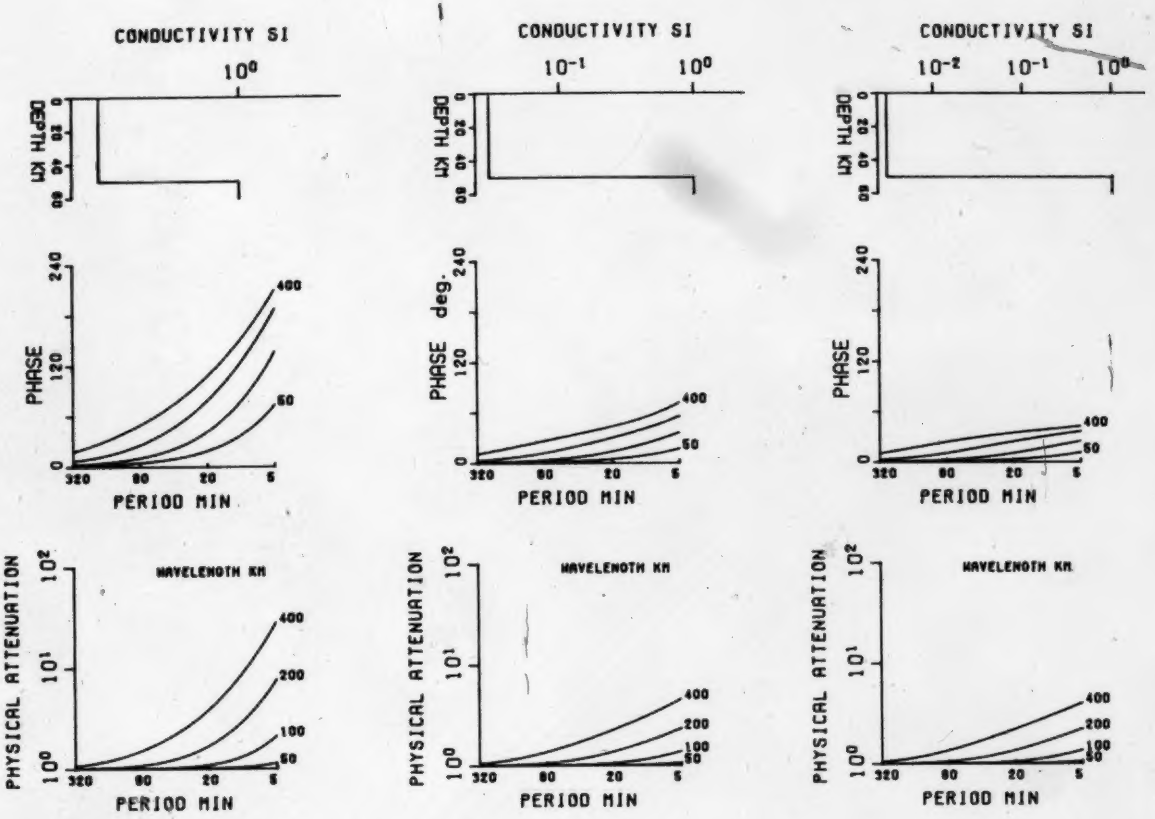

Figure 4.4 Shielding property of a plane layered Earth, for a two layer model with various layer 1 conductivities. The conductivities are 3.0×10^{-1}, 3.0×10^{-2} and 3.0×10^{-3} S/m.

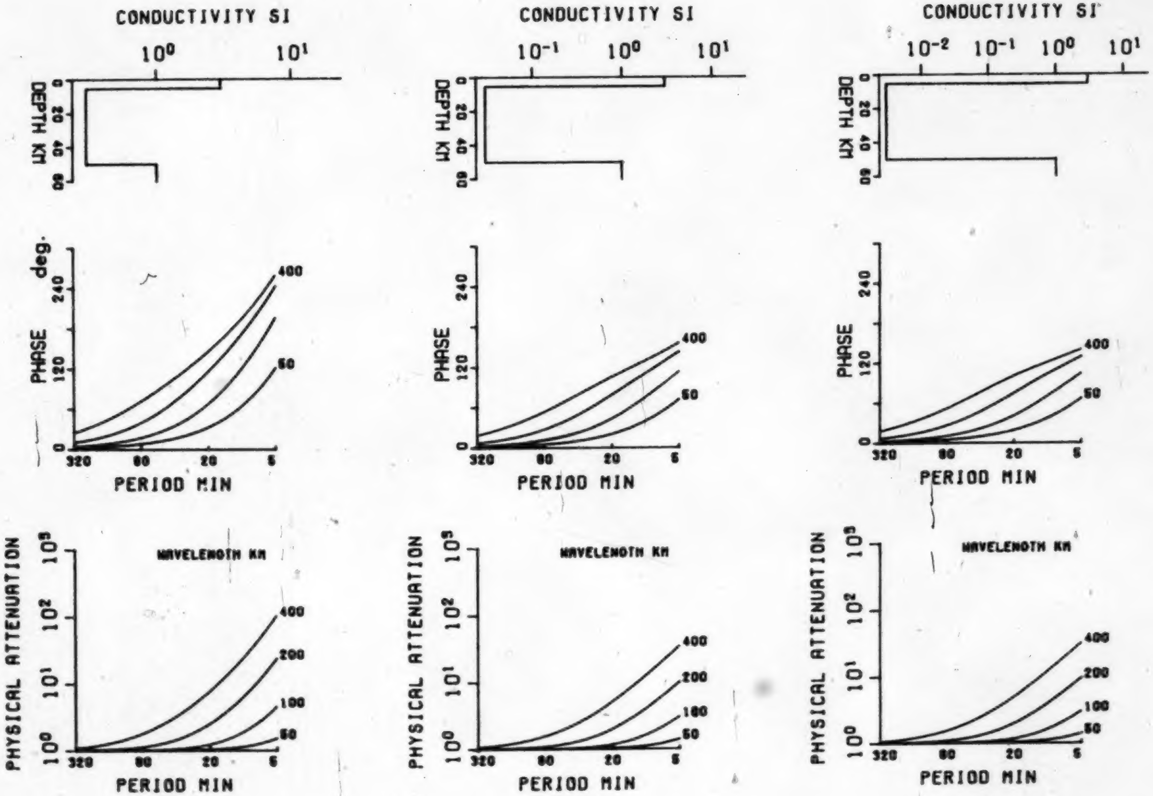

Figure 4.5 Similar to Fig.4.4 but a thin surface layer of good conductor is added to simulate sea water or wet sediments.

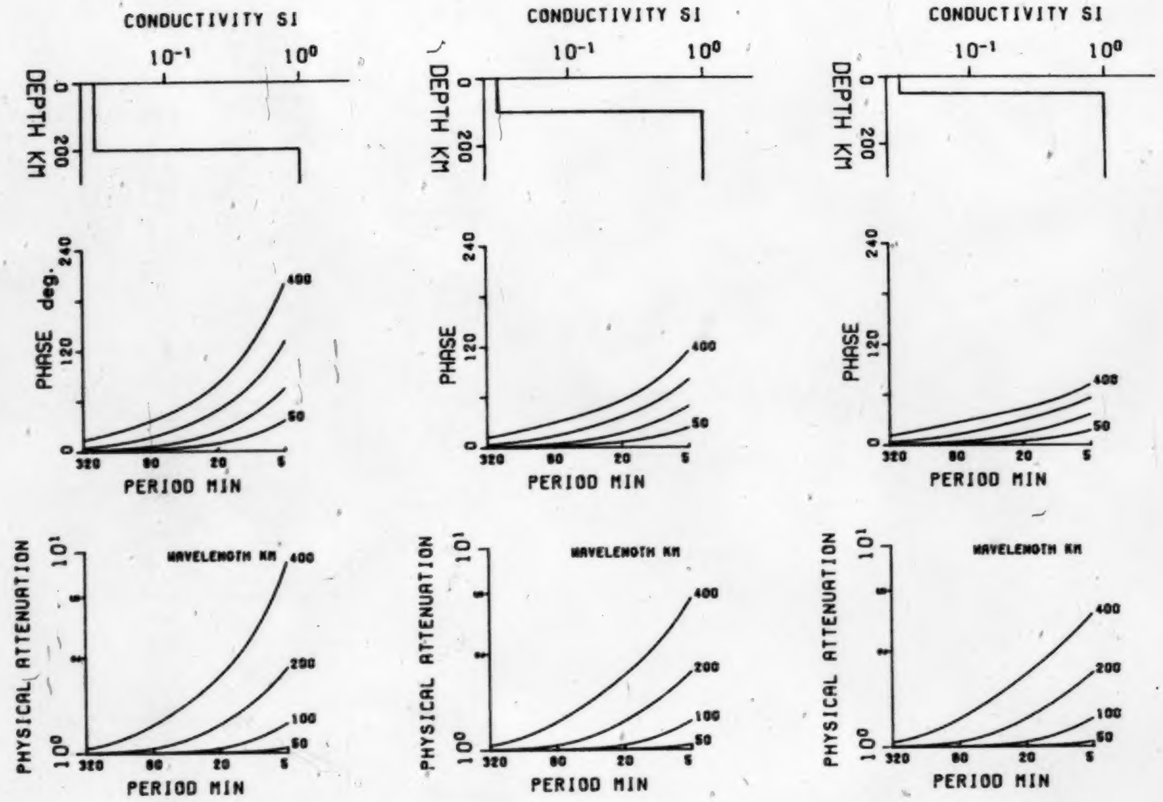

Figure 4.6 Shielding property of a plane layered Earth, for a two layer model with various layer 1 thicknesses. The thicknesses are 200, 100 and 50 km.

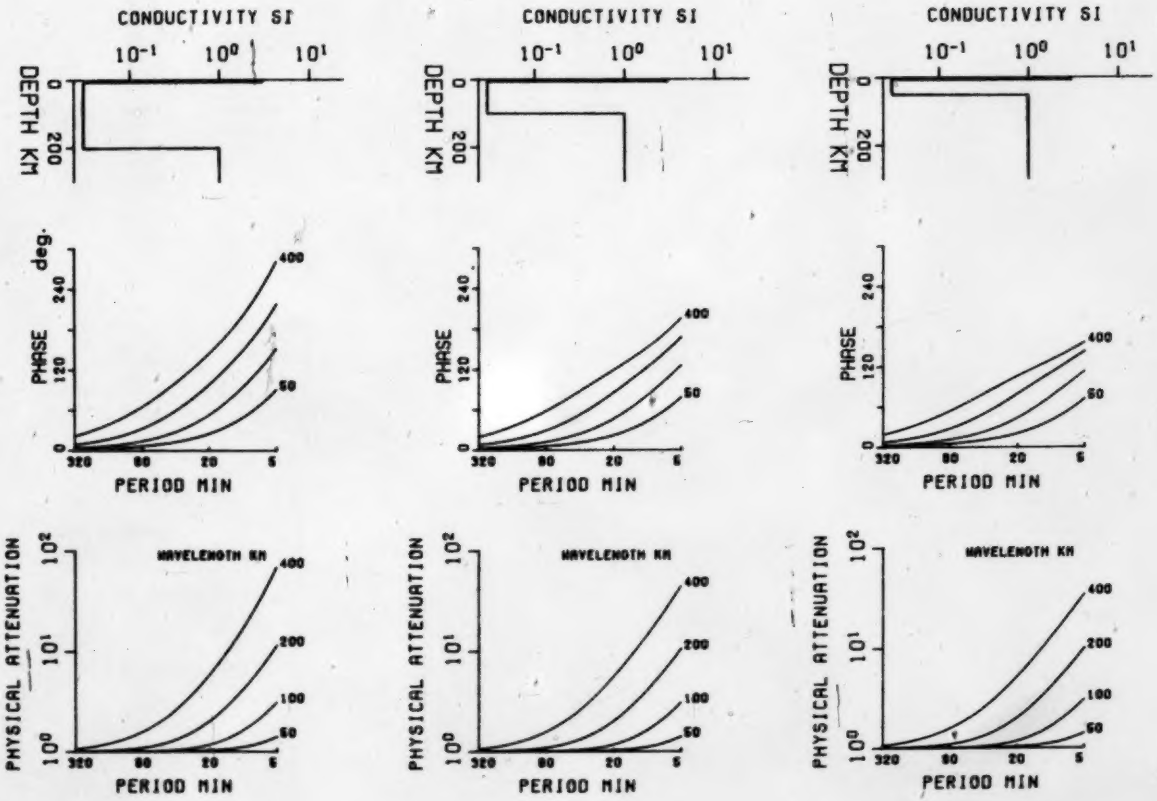

Figure 4.7 Similar to Fig.4.6 but a thin surface layer of good conductor. See also Fig.4.5.

the wavelengths resolvable from an ordinary magnetometer array, which spans at most a few hundred kilometers, the induction effects may be more apparent in the phase data of a magnetovariational event. Of course if the area under consideration is derectly above a current channel so that local induction is hardly detectable, the amplitude spectrum rather than phase might provide more information concerning the structure.

Within the resolvable wavelength and period range the depth of the conductive structure (h_1) and the conductivity of the layers (σ_1) are difficult to invert. It is even more so when a thin surface layer of a good conductor is present.

The above conclusions are drawn from the layered Earth model, and have to be modified in actual 3-D cases. However it does give a qualitative guideline about what we can and what we cannot investigate with the available magnetometer array data in local induction studies.

4.10 CURRENT SHEET INVERSION RESULTS

Field data at two periods, from the 1983 magnetovariation array in southern Alberta and southern British Columbia, have been inverted to current sheet sources. The two layer 1-D geoelectric section chosen for the inversion has taken into account the local geological information and Banks' argument (1979) supporting the current sheet model.

It is shown in Fig.4.8 that one model contains a conducting surface layer simulating the sediments covering the area, mostly of Mesozoic and Paleozoic ages (Wright, 1984). The thickness of this layer is taken as h_1=5 km and σ_1=0.05 S/m. Below it is a uniform half space with σ=0.005 S/m, a very poor conductor which allows the current to be channelled through the underlying good conductor, possibly in segmented pieces, to form the current sheet (Banks, 1979). In Fig.4.8, another 1-D geoelectrical section, with all conductivities 10 times larger, is also shown. The current sheet is also inverted with this more conductive model to assess the effects of the layered Earth on the inversion. The depth of the current sheet can be taken around the skin depth, h_1, of the field in the first layer:

$$h_1=1/\sqrt{(0.5\omega\mu_0\sigma_1)}$$

A stable inversion can be made to a current sheet at any depth shallower than the depth at which the inverted current function actually diverges. The criterion of divergence is flexible within certain limits. Near the divergence depth the current function amplitude increases dramatically and the shortest wavelength components effectively dominate the fields. This change in general indicates that the assumed depth is approaching the true depth of the current sheet. In this illustration it is placed at a depth which is reasonable in the light of

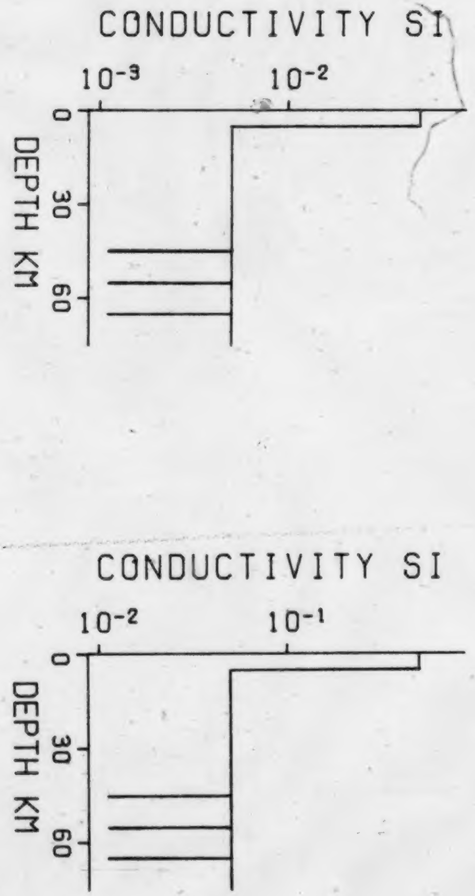

Figure 4.8 The layered Earth models for current sheet (Figs.4.10-4.12) inversion. One model has all conductivties 10 times those in the other. The depths, 45, 55 and 65 km, at which current sheets are inverted, are marked by —— horizontal lines.

existing knowledge of the structure and not too far from the skin depth given above.

The Nyquist wavelength (Kanasewich, 1981; Chapter 3 of this thesis) controls the resolution of the depth estimates. Because of the sparse station spacing the short wavelength components of the fields are not resolvable so that the inverted current function will diverge at a depth somewhat greater than the true depth of the anomalous structure.

The inverted inverted has a period of 69 minutes, corresponding to a skin depth in the first layer of 145 km. This spectral component comes from a magnetovariational event of duration 2.5 hours on July 19th, 1983 from 0:30 to 3:00 universal time. Its plane-wave normal field (chapter 2) has a long wavelength, 17,300 km, and has not been removed from the data. The second plane-wave term has a wavelength of 157 km which can be reasonably well analyzed by the array. For this period the current sheets are placed at three different depths, 45, 55 and 65 km. Fig.4.9 shows the separated internal field and Fig.4.10 the current sheets inverted with the less conductive Earth's model of Fig.4.8.

The in-phase component of the current sheet is about four times stronger than the out-of-phase component. Since the phase spectrum has a larger error, as will be discussed in Chapter 5, the out-of-phase component is less accurate. The in-phase component shows a current concentration across the Alberta-B.C. border and the Rocky Mountains. This current concentration is the clearest in the sheet placed at

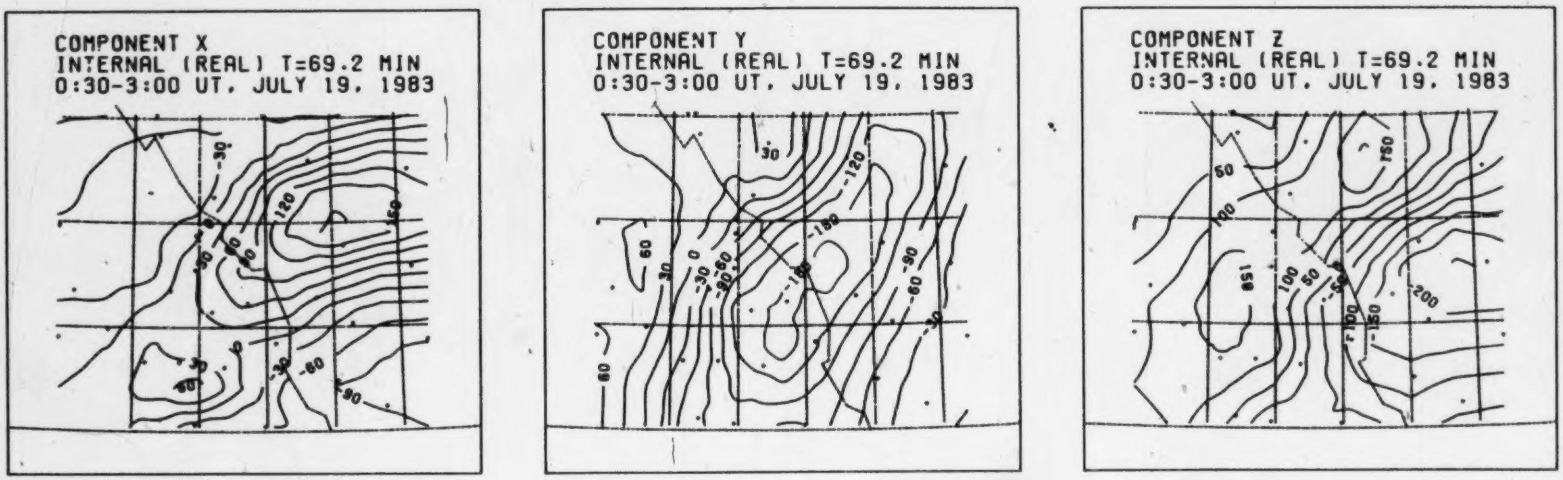
COMPONENT X
INTERNAL (REAL) T=69.2 MIN
0:30-3:00 UT. JULY 19. 1983
-30
120
150
60
90
-30
0
-30
-60
-90
30
60
COMPONENT Y
INTERNAL (REAL) T=69.2 MIN
0:30-3:00 UT. JULY 19. 1983
30
-120
-150
-180
60
30
0
-30
-60
-90
-60
-30
60
COMPONENT Z
INTERNAL (REAL) T=69.2 MIN
0:30-3:00 UT. JULY 19. 1983
150
50
100
150
100
50
-50
-100
-150
-200

Figure 4.9 The separated internal field for period 69 minutes for a variational event on July 19th, 1983.

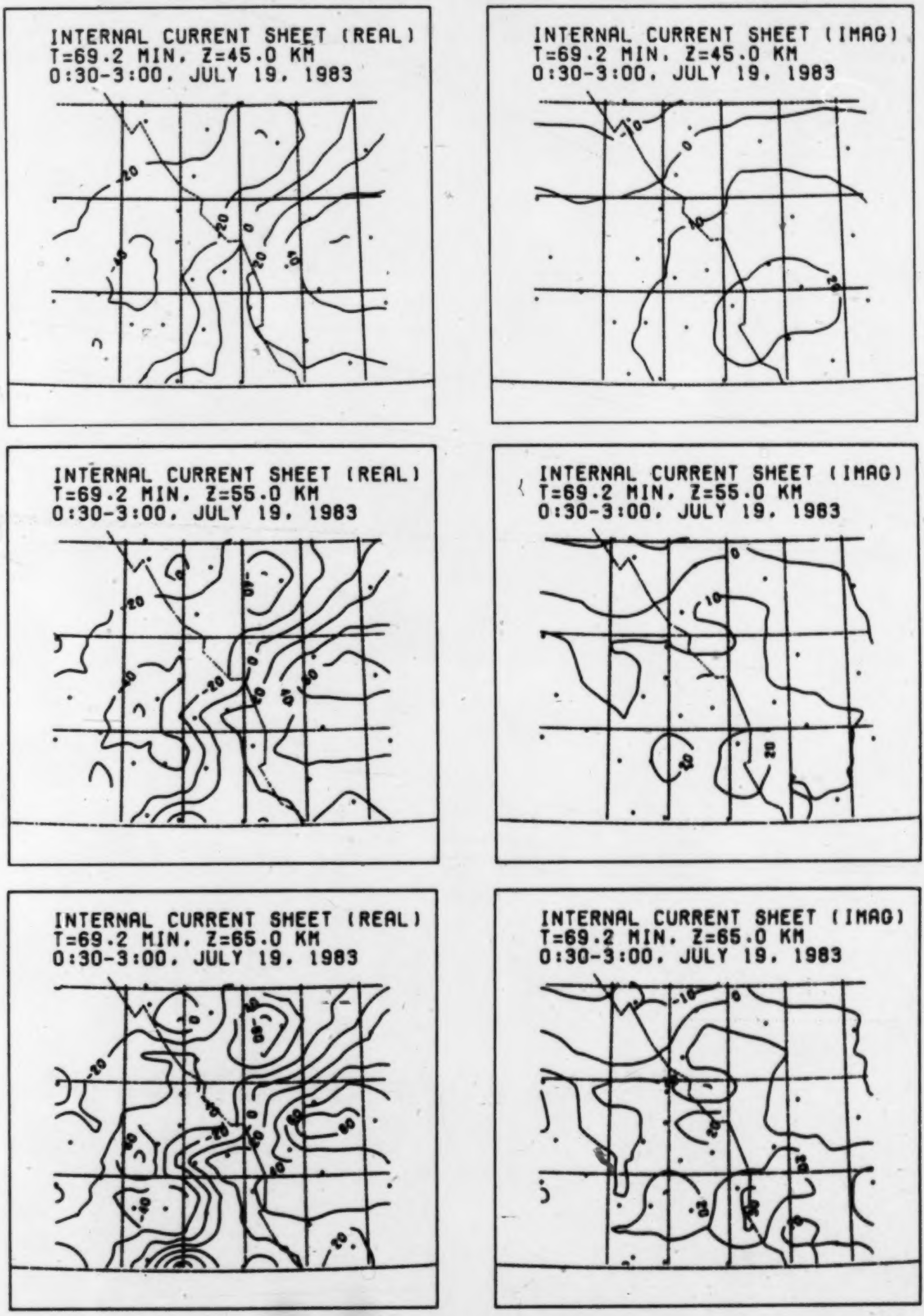
INTERNAL CURRENT SHEET (REAL)
T=69.2 MIN. Z=45.0 KM
0:30-3:00. JULY 19. 1983
INTERNAL CURRENT SHEET (IMAG)
T=69.2 MIN. Z=45.0 KM
0:30-3:00. JULY 19. 1983
INTERNAL CURRENT SHEET (REAL)
T=69.2 MIN. Z=55.0 KM
0:30-3:00. JULY 19. 1983
INTERNAL CURRENT SHEET (IMAG)
T=69.2 MIN. Z=55.0 KM
0:30-3:00. JULY 19. 1983
INTERNAL CURRENT SHEET (REAL)
T=69.2 MIN. Z=65.0 KM
0:30-3:00. JULY 19. 1983
INTERNAL CURRENT SHEET (IMAG)
T=69.2 MIN. Z=65.0 KM
0:30-3:00. JULY 19. 1983

Figure 4.10 Current sheets inverted from the field of Fig.4.9, at 45, 55 and 65 km, for the less conductive model (Fig.4.8).

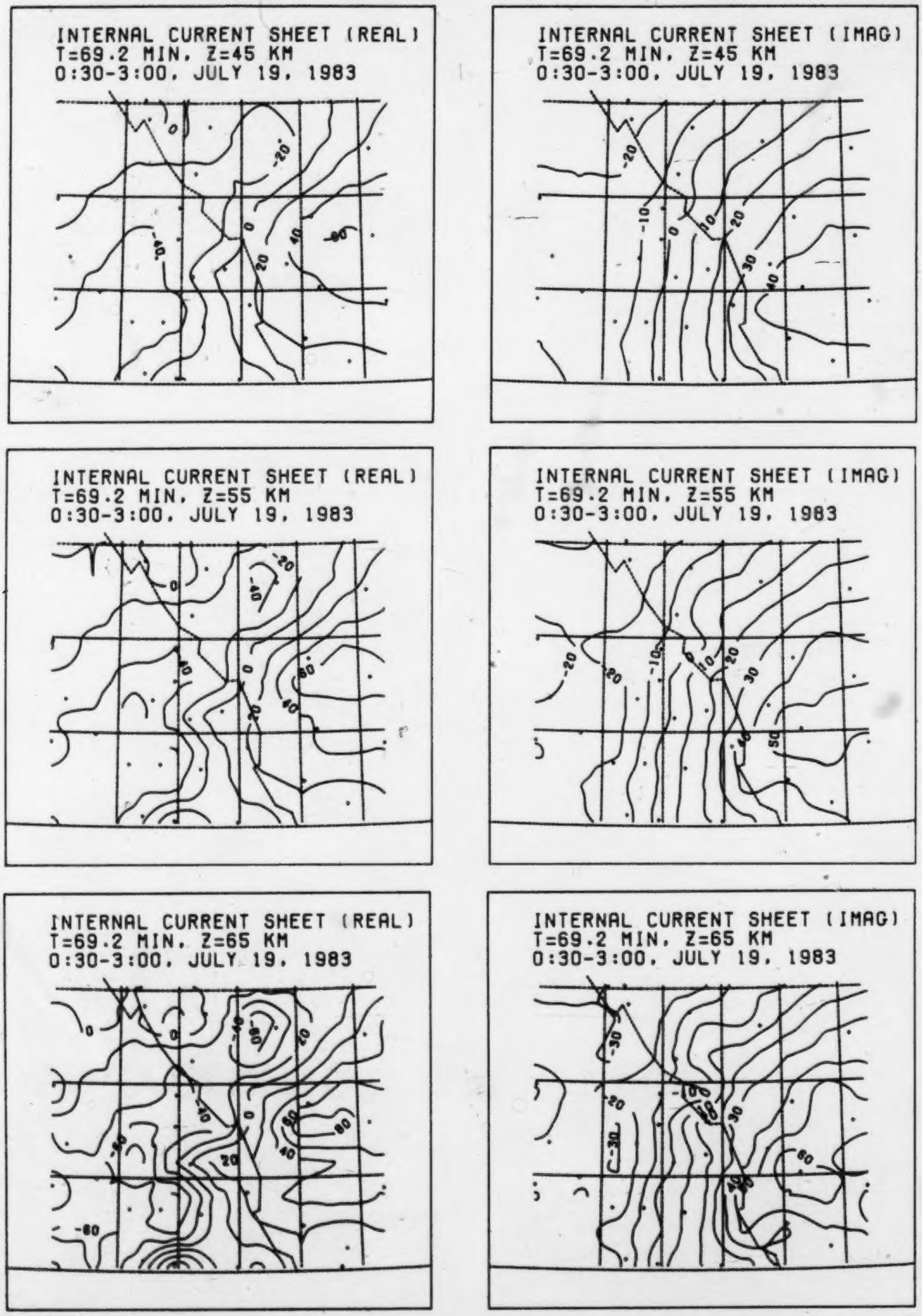

INTERNAL CURRENT SHEET (REAL)
T=69.2 MIN. Z=45 KM
0:30-3:00. JULY 19. 1983

INTERNAL CURRENT SHEET (IMAG)
T=69.2 MIN. Z=45 KM
0:30-3:00. JULY 19. 1983

INTERNAL CURRENT SHEET (REAL)
T=69.2 MIN. Z=55 KM
0:30-3:00. JULY 19. 1983

INTERNAL CURRENT SHEET (IMAG)
T=69.2 MIN. Z=55 KM
0:30-3:00. JULY 19. 1983

INTERNAL CURRENT SHEET (REAL)
T=69.2 MIN. Z=65 KM
0:30-3:00. JULY 19. 1983

INTERNAL CURRENT SHEET (IMAG)
T=69.2 MIN. Z=65 KM
0:30-3:00. JULY 19. 1983

0
-20
0
40
-60
20
-20
-10
0
10
20
30
40
0
-20
-40
10
0
60
40
20
-20
-10
0
10
20
30
40
50
0
-40
-60
20
0
-40
60
40
-60
-80
-30
-20
-10
0
30
-30
60
40

Figure 4.11 Current sheets inverted from the field of Fig.4.9, at 45, 55 and 65 km, for the more conductive model (Fig.4.8).

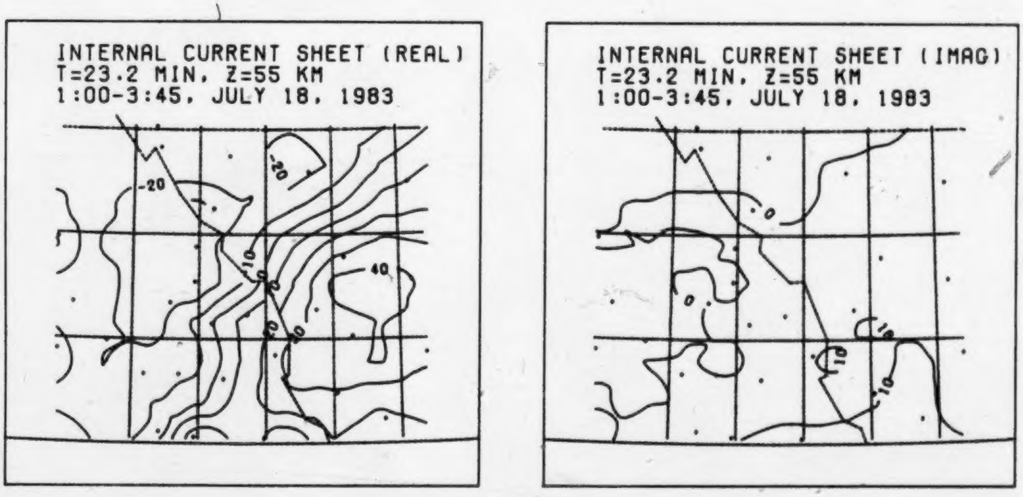
INTERNAL CURRENT SHEET (REAL)
T=23.2 MIN, Z=55 KM
1:00-3:45, JULY 18, 1983
-20
-20
40
INTERNAL CURRENT SHEET (IMAG)
T=23.2 MIN, Z=55 KM
1:00-3:45, JULY 18, 1983
0
0
10
-10

Figure 4.12 Current sheet inverted from the field of period 23 min. separated in chapter 3, Fig.4.10, at 55 km depth, for the less conductive model (Fig.4.8).

45 km depth. The sheet at 55 km depth has some rough features showing that the short wavelength components are stronger and the actual current depth is being approached. In the last current sheet at 65 km, though the current across the Rockies is still seen, the map is dominated by local current eddies. The actual currents are probably around 55 km, near the base of the thick crust of southern Alberta (Chandra and Cumming, 1972; Spence et al, 1977), or shallower.

The the current function contours are concentrated near the centre of the array, indicating the dense current concentration there. Between the ±20 contours 40 kA of current flow from NNE to SSW. This unit of current is corresponding to the unit of magnetic field in Fig.4.10 as being nT. This belt is estimated to define the approximate width of the current channel. The current outside this strip contributes less to the surface fields. Some current will, of course, leak into the surrounding rocks because the electric fields are continuous.

With the 10 times more conductive Earth's model (Fig.4.8), the same fields (Fig.4.9) are inverted to current sheets at the same depths, in Fig.4.11. The features of the in-phase current sheets in Fig.4.11 are essentially the same as those noticed (Fig.4.10) from the inversion based on the less conductive model (Fig.4.8), with the current intensity slightly increased. The quadrature-phase current sheets resemble the in-phase sheets because the phase shift generated by this more conductive model is now important (section 4.9).

With the less conductive Earth's model, fields of period 23 min. separated in chapter 3, Fig.3.10, are inverted to a current sheet at 55 km depth, in Fig.4.12. This frequency component has a skin depth shallower than the previous one, T=69 min., by a factor of 1.7 (=$\sqrt{[69/23]}$). The major features of the current sheet in Fig.4.12 are still quite similar to those of the sheet at the same depth (Fig.4.10).

The upper surface of the anomalous conductive structure appears to be around 55 km with a width of about 60 to 80 km. The depth is probably overestimated because the loss of short wavelength components of the fields, due to large station spacing, tends to delay the onset of instability of the current function when the sheet is placed at progressively greater depths. The minimum depth of the conductor will be estimated by means of a different approach in the next chapter.

5. INVERSION OF CHANNELLED CURRENT

Elongated magnetovariation anomalies, like that presented in Chapter 3, are often observed, and may be produced by current in a long conductor of small cross section. An effort is made in this chapter to invert such anomalies to a linear current or to a narrow sheet current of constant width. It is desirable to place such a current in a conducting half space, but except for very simple geometries no analytic solutions exist. Though numerical solution is always possible the solution of the forward problem may be difficult. As a result, the corresponding inverse problem would require prohibitive computing. The fact that the normal geoelectrical structure is not well known makes the possibility of success in such effort still more remote. In this chapter the model line or sheet current is placed in free space.

A smoothly curved line or sheet current could be described by a continuous model with an infinite number of unknowns, but this would be difficult to solve. Therefore, the model is parameterized to reduce the number of unknowns and to simplify the calculation. To solve the forward problem I introduce two coordinate systems (sections 5.1 and 5.2) to simplify the formulation. A transformation (section 5.2) connects the two systems and serves as the final link to solve the forward problem, summarized in section 5.3. The Karhunen-Loeve transformation is employed to test for the current channelling phenomenon. Inversion regulated by constrained least squares and least distance programming is developed and used in inversion of an anomalous field to give estimates of the depths and shapes of the corresponding currents.

5.1 THE LINEAR CURRENT MODEL AND OBSERVATION COORDINATE SYSTEM

The observation coordinate system, OCS, is taken as a Cartesian coordinate system with Z axis vertically downwards, X pointing north and Y east.

The linear current consists of N-1 straight segments connected one to one in sequence at N nodes, with a bend allowed at each node. The segments at both ends should extend to infinity but it suffices to make them much longer than the diameter of the survey area. The cross-section of all segments is taken as zero, and constant current I flows through the whole conductor. The segment between node j and j+1 is denoted segment j. The geometry of the linear conductor and the numbering convention is shown in Fig.5.1a.

For each segment j I define a positive direction, $\mathbf{p}^j$, which is the same as the direction of conventional current. This direction can be defined by two angles, α^j, the angle between $\mathbf{p}^j$ and the Z axis, and β^j, the angle between the horizontal projection of $\mathbf{p}^j$ and the X axis (positive when measured in the direction from the X axis toward the Y axis). For segment j these angles can be determined as follows (Fig.5.1):

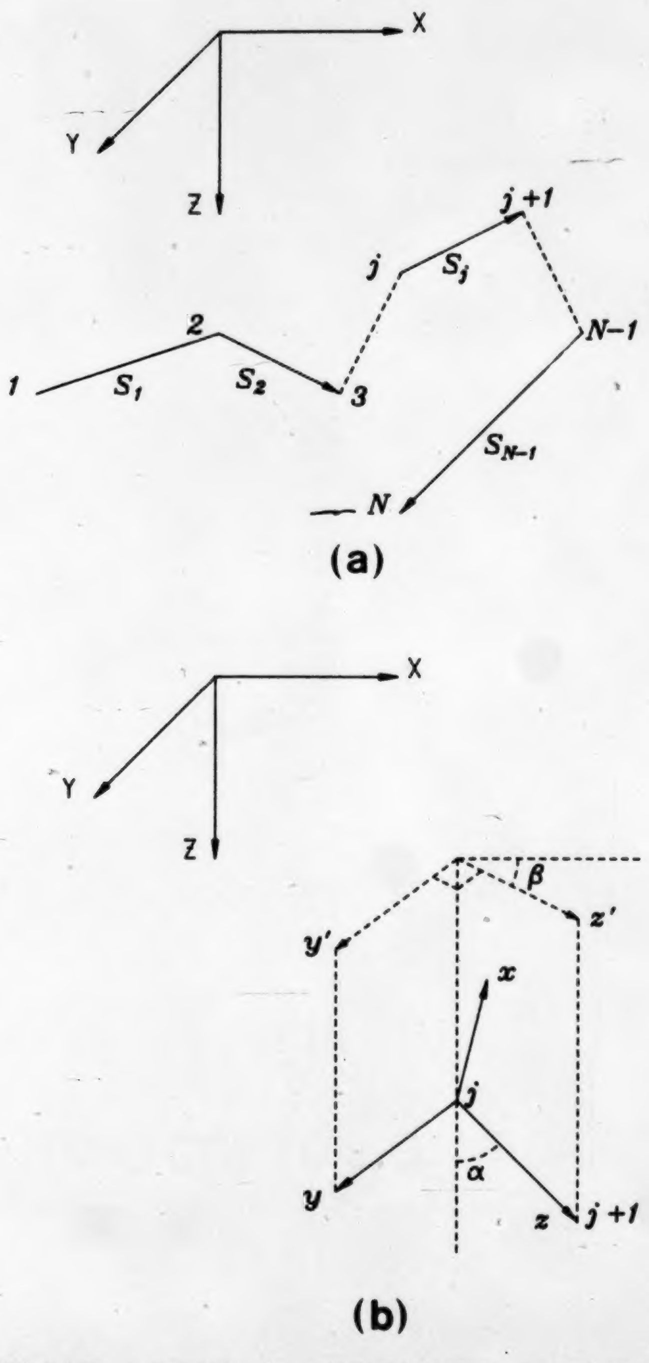
X
Y
Z
j +1
j
S_j
2
N−1
1
S_1
S_2
3
S_{N-1}
N
(a)
X
Y
Z
β
y'
z'
x
j
α
y
z
j +1
(b)

Figure 5.1 (a)Line current in observation coordinates system (OCS), with numbering convention of the nodes and segments. (b)The j th current coordinate system (CCS) and its relation to OCS. The y axis of CCS is always parallel to the XOY plane of OCS.

$$\begin{aligned} \cos(\alpha^j)&=(Z^{j+1}-Z^j)/L^j \\ \sin(\alpha^j)&=\ell^j/L^j \\ \cos(\beta^j)&=(X^{j+1}-X^j)/\ell^j \\ \sin(\beta^j)&=(Y^{j+1}-Y^j)/\ell^j \end{aligned} \tag{5.1}$$

$$\begin{aligned} \ell^j&\equiv\sqrt{[(X^{j+1}-X^j)^2+(Y^{j+1}-Y^j)^2))]} \\ L^j&\equiv\sqrt{[(Z^{j+1}-Z^j)^2+(\ell^j)^2]} \end{aligned}$$

in which $X^j \ldots Z^{j+1}$ etc are coordinates of the two ends of segment j in OCS. L^j is the length of the segment and ℓ^j its horizontal projection. We take the coordinates of the N nodes in OCS and the current I in the linear conductor as model parameters that are to be inverted from observed fields at the surface.

5.2 CURRENT COORDINATE SYSTEM AND O-C TRANSFORMATION

The magnetic field in OCS is difficult to formulate directly. Therefore, a current coordinate system, CCS, is introduced for each current segment. For the j th segment the origin of CCS is taken at the j th node, Fig.5.1b. The z^j axis is along $\mathbf{p}^j$, the y^j axis is parallel to the XOY plane and forms an angle $\beta^j+\pi/2$ with the X axes. The x^j axis is then determined by $\mathbf{e}_x^j=\mathbf{e}_y^j \times \mathbf{e}_z^j$. The direction cosines between the two sets of axes are,

$$(5.2)\qquad \begin{array}{cccc} & x & y & z \\ X & l_1 = \cos(\alpha)\cos(\beta) & m_1 = -\sin(\beta) & n_1 = \sin(\alpha)\cos(\beta) \\ Y & l_2 = \cos(\alpha)\sin(\beta) & m_2 = \cos(\beta) & n_2 = \sin(\alpha)\sin(\beta) \\ Z & l_3 = -\sin(\alpha) & m_3 = 0 & n_3 = \cos(\alpha) \end{array}$$

These can be calculated from (5.1).

The rotation matrix $\underset{\sim}{\mathbf{R}^j}$ is given by

$$(5.3)\qquad \mathbf{R}^j = \begin{bmatrix} l_1 & l_2 & l_3 \\ m_1 & m_2 & m_3 \\ n_1 & n_2 & n_3 \end{bmatrix}$$

The relation to determine the coordinates in OCS, X_l, to those of the same point in the j th CCS, x^j_k, is

$$(5.4)\qquad x^j_k = \sum_l R_{kl}(X_l - X^j_l)$$

And the relation to connect the component of a vector in OCS, F_l, to those in the j th CCS, f^j_k, is

$$(5.5)\qquad F_l = \sum_k R^j_{kl} f^j_k$$

Formulae (5.4) and (5.5) give the transformation between OCS and CCS, the O-C transformation.

To distinguish the two coordinate systems uppercase characters are used to represent quantities in OCS and lowercase in CCS. Superscript j refers to quantities related to the j th CCS or j th node. Components of position and field vectors are denoted by subscripts 1, 2 and 3 or x, y and z.

5.3 FORWARD PROBLEM FOR A LINEAR CURRENT

In order to formulate the inverse problem the corresponding forward problem must be solved: one can then calculate, either analytically or by finite differences, the derivatives of model fields with respect to unknown model parameters. These derivatives are needed to form the coefficient matrix of the normal equation to which solutions are sought to improve the model (e.g. Kanasewich, 1981).

The forward problem is to calculate the components B_x, B_y, B_z of the magnetic field at a point with coordinates X, Y and Z in OCS. This includes the contribution of all the N-1 current segments:

$$(5.6) \qquad B_k(\mathbf{X};G,I)=\sum_{j=1}^{N-1} B_k(\mathbf{X};G^j,I)$$

in which G denotes the model geometry and is the manifold of G^j, the geometrical parameters of the j th segment,

$$(5.7) \qquad G^j=\mathbf{X}^j,\mathbf{X}^{j+1};\ j=1,2,\ldots N-1$$

The forward problem (5.6) is solved by the following steps:

1. For each current segment j, calculate the three components of magnetic field in the j th CCS in terms of the coordinates in the same CCS:

$$(5.6a) \qquad \mathbf{b}(\mathbf{x}^j;G^j,I);$$

2. Express (5.6a) in terms of the coordinates $\mathbf{X}$ in OCS. In other words, replace $\mathbf{x}^j$ in (5.6a) by $\mathbf{X}$:

$$(5.6b) \qquad \mathbf{b}(\mathbf{x}^j;G^j,I) \rightarrow \mathbf{b}(\mathbf{X};G^j,I);$$

3. Rotate the magnetic field in j th CCS, $\mathbf{b}(\mathbf{X};G^j,I)$ into the field in OCS, $\mathbf{B}$:

$$(5.6c) \qquad \mathbf{b}(\mathbf{X};G^j,I) \rightarrow \mathbf{B}(\mathbf{X};G^j,I);$$

4. Take summation of the results in step (3) over current segments like (5.6).

Steps (2) and (3) were solved in section 5.2, formulae (5.4) and (5.5). Step (4) is trivial and step (1) is given below. By simple integration, it can be shown that:

$$(5.8) \qquad \begin{aligned} b_1(\mathbf{x}^j;G^j,I) &= -y^j F(\mathbf{x}^j) \\ b_2(\mathbf{x}^j;G^j,I) &= x^j F(\mathbf{x}^j) \\ b_3(\mathbf{x}^j;G^j,I) &= 0 \end{aligned}$$

where

$$(5.8a) \quad F(\mathbf{x}^j) \equiv \left\{ \frac{z^j}{\sqrt{[{x^j}^2+{y^j}^2+{z^j}^2]}} - \frac{z^j-L^j}{\sqrt{[{x^j}^2+{y^j}^2+(z^j-L^j)^2]}} \right\} \frac{\mu_0 I}{4\pi({x^j}^2+{y^j}^2)}$$

(5.8) is the actual format of (5.6a) required in step 1 of the forward problem for a linear current. Carrying through the steps (1) to (3) to give an explicit formula for

$B(X;G^j,I)$ is tedious and pointless for numerical calculation, and is omitted.

5.4 FORWARD PROBLEM FOR A SHEET CURRENT OF CONSTANT WIDTH

Real current distributions in space are always three dimensional. A linear current model is an extreme case of such real current distributions. A sheet current is closer to reality. The current sheet model considered in chapter 4 is simply horizontal. The linear current model can be extended to a sheet of constant width by parallel straight linear current segments in a plane.

Fig.5.2 shows the geometry of a plane current sheet segment of width 2w. Such a sheet segment is no longer "horizontal" except when the two nodes of its axis are at the same depth. Such a sheet is horizontally wide in the sense that its width, when projected onto a horizontal plane, is unchanged. When the sheet segments change horizontal direction, the connections between segments are not "perfect". Each sheet segment ends at a node on a horizontal line perpendicular to the axis of the segment (Fig.5.2). On changing direction, the inside corner therefore draws more current than the outside corner. This is perhaps desirable since when a conductor bends the current is likely to make a "short cut" so as to concentrate more around the "inside corner".

This current sheet segment, of length L and constant width 2w in the yoz plane of CCS, with uniform current

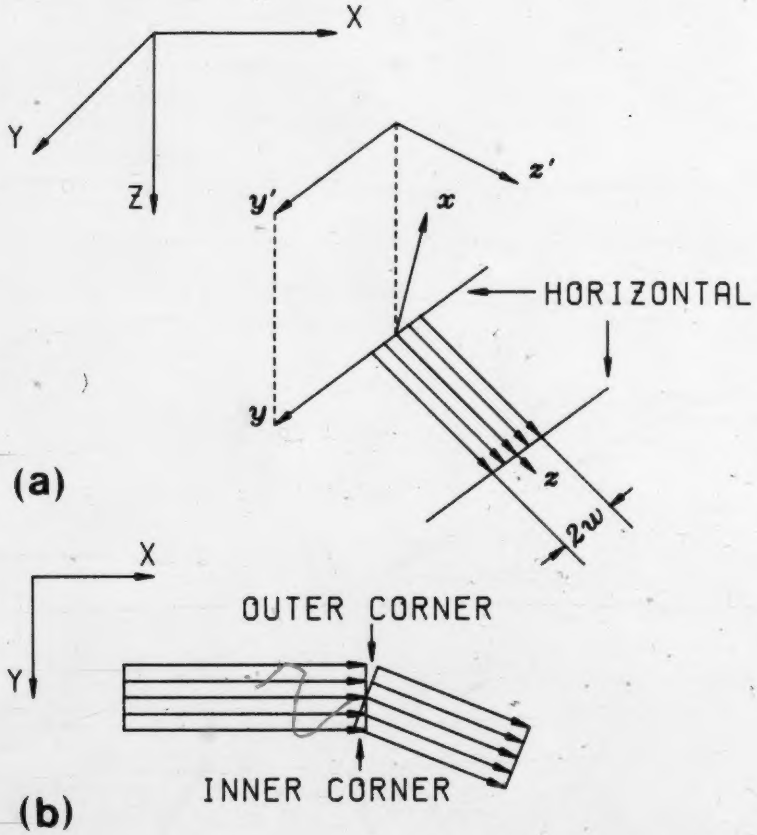
X
Y
Z
z'
y'
x
HORIZONTAL
y
z
2w
(a)
X
Y
OUTER CORNER
INNER CORNER
(b)

Figure 5.2 Geometry of sheet current model. (a)3-D view of a sheet segment. The two ends of the segment are parallel to the y axis of the CCS and therefore parallel to XOY plane of the OCS; (b)a plane view of the connection of two segments. Because of the change in the horizontal direction of the sheet segments, the "inner corner" draws more current than the "outer corner".

density flowing along the positive z direction, can be formed by moving a linear current parallel to the z axis from y=-w to y=+w in the yoz plane. The fields of such a sheet in CCS are obtained by integrating (5.8):

$$b_1(x^j;G^j,I)=\int_{-w}^{w}-(y^j-u)F(x^j,y^j-u,z^j)du$$

$$b_1(x^j;G^j,I)=\int_{-w}^{w}x^jF(x^j,y^j-u,z^j)du \tag{5.8b}$$

$$b_3(x^j;G^j,I)=0$$

Neglecting superscript j, the above integrations result in:

$$b_1(x,G,I)=-\frac{\mu_0 I}{16\pi w}\{\ln\frac{r_0-z}{r_0+z}-\ln\frac{r_1-(z-L)}{r_1+(z-L)}\}\Bigg|_{u=y-w}^{u=y+w}$$

$$b_2(x,G,I)=\frac{\mu_0 I}{8\pi w}\{\tan^{-1}\frac{zu}{xr_0}-\tan^{-1}\frac{(z-L)u}{xr_1}\}\Bigg|_{u=y-w}^{u=y+w} \tag{5.8c}$$

$$r_0\equiv\sqrt{[x^2+z^2+u^2]}$$

$$r_1\equiv\sqrt{[x^2+(z-L)^2+u^2]}$$

(5.8c) is equivalent to (5.8), and takes the place of (5.6a) in the steps of the forward problem of the fields produced by a sheet current consisting of sheet segments (Fig.5.2). The other steps for the forward problem of the sheet current model remain unchanged as listed in section 5.3.

5.5 THE DERIVATIVES

From (5.6) and (5.7) one can see that at most two terms on the right hand side of (5.6) contribute to a particular derivative w.r.t. nodal positions:

$$(5.9)\qquad \partial B(X;G,I)/\partial X^j = \partial B(X;G^j,I)/\partial X^j + \partial B(X;G^{j-1},I)/\partial X^j$$

The formulae for such derivatives, even with the O-C transformation, are still lengthy:

$$(5.10)\qquad \frac{\partial B_i(X;G,I)}{\partial X^j_m} =$$

$$\sum_{n=j}^{j-1} \sum_k R^n_{ki} \{ \frac{\partial b^n_k}{\partial L^n} \frac{\partial L^n}{\partial X^j_m} + \sum_s \frac{\partial b^n_k}{\partial x^n_s} [\sum_t \frac{\partial R^n_{st}}{\partial X^j_m} (X_t - X^n_t) - \delta^j_n R^j_{sm}] \} + \frac{\partial R^n_{ki}}{\partial X^j_m} h^n_k$$

$$i,m=1,2,3 \qquad j=1,2,\cdots N$$

in which δ is the Kronecker delta. For j=1 (N) the summation in (5.10) reduces to only n=1 (N-1) terms. In (5.10) derivatives like $\partial b^j_k/\partial x^j_s$ can be readily calculated from (5.8) (or 5.8c for sheet current). The $\partial R^j/\partial X^j_k$ etc are rather tedious (subscript j is neglected on the r.h.s.):

$$(5.11)\qquad l^j \cdot \partial R^j/\partial X^j_k = \begin{bmatrix} n_1 l_3 l_k - l_2 m_k & n_2 l_3 l_k + l_1 m_k & l_3 n_3 l_k \\ -m_2 m_k & m_1 m_k & 0 \\ n_1 l_3 n_k - l_3 \delta_{1k} & n_2 l_3 n_k - l_3 \delta_{2k} & -l_3 l_3 l_k \end{bmatrix}$$

It is easy to prove that $\partial R^j/\partial X^j_k$ differs from $\partial R^j/\partial X^{j+1}_k$ only in sign. The derivative w.r.t. the current is the magnetic field produced by unit current.

The analytic formulae for derivatives w.r.t. coordinates of nodes involve many layers of summation and are computationally inefficient. Therefore in practice the central finite difference approximation of each derivative is employed:

$$\partial B_i(X;G,I)/\partial X_m^j \cong$$
$$[B_i(X;G\{X_m^j+\Delta\},I) - B_i(X;G\{X_m^j-\Delta\},I)]/(2\Delta)$$

The step size 2Δ is taken as 3 km for nodes under the array area and 6 km for nodes outside. The derivatives w.r.t. the width of the current sheet are calculated with step size the same as that for the intermediate nodes, but not larger than one tenth of the sheet width when the width of the sheet is narrower than 30 km.

5.6 THE INVERSION

Suppose we have 3 components of the magnetic field simultaneously recorded at M sites. They form a 1-D observation vector $\{D_k\}$ with 3M components,

$$\{D_k\}=\{B_x^1,B_y^1,\cdots,B_z^M\}^t \tag{5.12}$$

where ^{t} stands for matrix transform. The model parameters form a model vector $\{P_l\}$ with 3N+2 components, where N is the number of nodes,

$$\{P_i\}=\{X_1, Y_1 \cdots, Z_n, I, w\}^t \tag{5.13}$$

If the model is simply a linear current, the dimension of the model vector reduces to 3N+1 components, omitting the half width of a sheet, w. With the first guess of $\{P_i\}$, $\{P_i^o\}$, a derivative matrix A of the order of 3M by 3N+2 (3N+1 for a linear current) is formed,

$$A_{ik}=\begin{bmatrix} \partial B_x^1/\partial X^1 & \ldots & \partial B_x^1/\partial Z^n & \partial B_x^1/\partial I & \partial B_x^1/\partial w \\ \partial B_y^1/\partial X^1 & \ldots & \partial B_y^1/\partial Z^n & \partial B_y^1/\partial I & \partial B_y^1/\partial w \\ \partial B_z^1/\partial X^1 & \ldots & \partial B_z^1/\partial Z^n & \partial B_z^1/\partial I & \partial B_z^1/\partial w \\ \partial B_x^2/\partial X^1 & \ldots & \partial B_x^2/\partial Z^n & \partial B_x^2/\partial I & \partial B_x^2/\partial w \\ \multicolumn{5}{c}{\cdots\cdots\cdots\cdots\cdots\cdots\cdots\cdots\cdots\cdots} \\ \partial B_z^m/\partial X^1 & \ldots & \partial B_z^m/\partial Z^n & \partial B_z^m/\partial I & \partial B_z^m/\partial w \end{bmatrix} \tag{5.14}$$

The fields at observation points are calculated with the initial model $\{P_i^o\}$:

$$\begin{aligned} \{D_k^o\}^t &= \{B_x^{o\,1}, B_y^{o\,1}, \cdots, B_z^{o\,M}\} \\ &\equiv \{B_x^1,\ B_y^1,\ \cdots,\ B_z^M\}\Big|_{\{P_i\}=\{P_i^o\}} \end{aligned} \tag{5.15}$$

Then the correction to $\{P_i^o\}$, $\{\delta P_i^o\}$:

$$\{\delta P_i^o\}=\{P_i\}-\{P_i^o\} \tag{5.16}$$

can be estimated from

$$(5.17)\qquad \delta D_k^o=\sum_l A_{kl}\,\delta P_l^o$$

in which δD_k^o is the model misfit,

$$(5.18)\qquad \delta D_k^o = D_k-D_k^o \equiv \delta B_j^i \equiv B_j^i-B_j^{o\,i}$$

$$k=3*(i-1)+j \quad i=1,2,\cdots M \quad j=1,2,3$$

where B_j^i is j th component of field at i th data point. On solving the correction to the model parameter one gets a better model and iteration continues until a satisfactory model is achieved.

Equation (5.17) is often solved by singular value decomposition of matrix **A**,

$$(5.19)\qquad \mathbf{A}=\mathbf{ULV}^t$$

where columns of **U** and **V** are eigenvectors of $\mathbf{AA}^t$ and $\mathbf{A}^t\mathbf{A}$:

$$(5.20)\qquad \mathbf{AA}^t\mathbf{U}=\mathbf{UL}^2$$

$$(5.21)\qquad \mathbf{A}^t\mathbf{AV}=\mathbf{VL}^2$$

and $\mathbf{L}^2$ is the diagonal matrix of non-negative eigenvalues λ_l^2. The Lanczos (1961) inverse, $\mathbf{A}^\dagger$, of **A** is then given by:

$$(5.19a)\qquad \mathbf{A}^\dagger=\mathbf{VL}^{-1}\mathbf{U}^t$$

In practice the elements of $\mathbf{L}^{-1}$, $1/\lambda_i$, are often replaced by

$$(5.22) \qquad \lambda_i/(\lambda_i^2+\theta^2).$$

θ^2 is known as the *regression factor* or *damping factor* (Marquardt, 1963) and has the effect of truncating unimportant parameters and thus stabilizing the inversion iteration. "Hard" truncation, throwing away some small eigenvalues and the corresponding eigenvectors, has also been suggested (Wiggins, 1972).

5.7 UNIQUENESS AND ERROR CONTROL

For inversion to conductivity from a continuum of an infinite number of data, unique solutions have been shown to exist in a few special cases. For the 1-D electromagnetic sounding problem we have the Tikhonov (1965) uniqueness theorem for a plane layered Earth and the Bailey (1970) uniqueness theorem for a spherically layered Earth, both based on the diffusion equation of the fields. The practical usefulness of these theorems is limited for two reasons. First, the data required are difficult or impossible to obtain. Second, at high frequency the diffusion equation is inapplicable. The Tikhonov theorem is limited in an additional way. This theorem assumes vertically incident plane wave fields. Such fields can be approximated by fields of long wavelength, which can only be isolated by observations over an increasingly large area. This will eventually make the plane Earth assumption invalid.

The inversion of magnetic fields to recover the causative currents is non-unique. The non-uniqueness of inversion of a finite data set to a continuous model is intrinsic to the problem; a finite data set can be exactly fitted by an infinite number of solutions involving a much larger number of parameters. In mathematical terms, the situation is an underdetermined case.

The non-uniqueness of line current inversion can be proved by giving an example with more than one solution. Suppose that near the surface the Earth is plane layered and that we have an infinite number of data points at the surface. From the discussion in chapter 4 the surface fields can be inverted to current sheets at different depths. Each of these current sheets can be replaced by a large number of line currents of appropriate intensities. The non-uniqueness of current sheet inversion immediately leads to the same conclusion for the line current inversion even if the data set is infinite.

The errors in the parameters of the inversion are related to the errors in the data and to the adequacy of the model (Rokityansky, 1982, chap.3). For an underdetermined case, the better the model resolution, the greater the errors are mapped into its resolved parameters, or the increments of these (Wiggins, 1972; p.76, Menke, 1984). This "universal" trade-off argument is not very essential for an inadequate model inverted from an overdetermined problem since in this case one usually cannot fit the data very well. The line current model is a simple one and thus inadequate. In such overdetermined cases we do not have to pay much attention to how to truncate "unimportant" parameters by throwing away some eigenvectors corresponding to small eigenvalues (section 5.6). For the constrained least square programming approach, truncation of eigenvalues is not allowed (section 5.9). For underdetermined cases I modify the *Least Distance Programming* method (section 5.10) to control the error contamination.

5.8 W-STABILIZATION OF THE INVERSION PROCESS

Even for the case in which the linear current model gives a good approximation of the observed field and the starting model is not too far away from the true model, the inversion process tends to be unstable if the observations contain systematic error.

In induction studies the data are very often of a relative nature, as where a simplified normal field has been subtracted from the observed field (chapter 3; Ingham et al., 1983), or where a field has been separated into parts of external and internal origin. In the latter case a trend in the field, inseparable because of the finite observation area, is deducted from the data set (chapter 3). Such missing normal fields contribute to systematic error.

To compensate for this error, I replace the model misfit vector $\delta\mathbf{D}^{0}$ with $\delta\mathbf{D}^{+}$ by introducing a **W** vector into the misfit vector:

$$(5.23) \qquad \delta\mathbf{D}^\circ \rightarrow \delta\mathbf{D}^+ \equiv \delta\mathbf{D}^\circ + \mathbf{W}$$

so that either the misfit vector or the correction to the model is minimized:

$$(5.24a) \qquad \phi_r \equiv |\delta D^+|^2 = \text{minimum}$$

$$(5.24b) \qquad \phi_l \equiv |\delta P^\circ)|^2 = \sum_i \sum_k (A^\dagger_{ik}\, \delta D^+_k)^2 = \text{minimum}$$

in which, $A^\dagger$ is the generalized inverse of matrix A, subscript *r* or *l* of the objective function ϕ refers to stabilization from *right* or *left* hand side of the misfit equation, and the corresponding **W** vector will be referred to as $\mathbf{W}_r$ or $\mathbf{W}_l$. The **W** vector is taken to simulate the neglected internal part of the normal fields, the systematic error contained in the data. The recovery of this normal field has the effect of improving the model fitting, and stabilizing the inversion process. I name this scheme as *W-stabilization*.

Properly choosing the type of **W** is important. The numbers of degrees of freedom in **W**, i.e. the number of independent parameters forming it, must be less than the dimension of the data vector. Otherwise, taking **W** as $-\delta\mathbf{D}^\circ$ would force both (5.24a) and (5.24b) to zero. The normal field at (X,Y) is taken as:

$$B_{nx}=B_{0x}+a_xX$$

$$\text{(5.25)}\qquad B_{ny}=B_{0y}+a_yY$$

$$B_{nz}=B_{0z}.$$

The reason for this particular form of normal field follows the property of the separation of the field in the wave number domain (Chapter 3). In all three components the totally uniform field lost after separation is represented by constant triplets, $\{B_{0x},\ B_{0y},\ B_{0z}\}$. In addition, in the X (Y) component of the field the partially uniform field B_x (B_y) with zero K_x (K_y) is lost. To a first order approximation this can be considered as a linear term in X (Y). Now the **W** vector, with five degrees of freedom, has the form:

$$\text{(5.26)}\qquad \mathbf{W}=\{\cdots,\ B_{0x}+a_xX_i,\ B_{0y}+a_yY_i,\ B_{0z},\ \cdots\}^t$$

where X_i and Y_i are coordinates of the i th data point. The objective function for the least squares problem (5.24a) is

$$\text{(5.27)}\qquad \phi_r=\sum_{i=1}^{M}(\delta B_x^i+B_{0x}+a_xX_i\ +\ \delta B_y^i+B_{0y}+a_yY_i\ +\ \delta B_z^i+B_{0z})^2$$

where the summation is carried over M data points. Setting $\partial\phi_r/\partial\alpha$ to zero, $\alpha = B_{0x},a_x;\ B_{0y},a_y;\ B_{0z}$, we get three sets of decoupled equations for the five parameters:

$$\begin{bmatrix} C_{xx} & C_x \\ C_x & M \end{bmatrix}\begin{bmatrix} a_x \\ B_{0x} \end{bmatrix} = \begin{bmatrix} b_{1x} \\ b_1 \end{bmatrix}$$

$$\begin{bmatrix} C_{yy} & C_y \\ C_y & M \end{bmatrix}\begin{bmatrix} a_y \\ B_{0y} \end{bmatrix} = \begin{bmatrix} b_{2y} \\ b_2 \end{bmatrix} \tag{5.28}$$

$$M \cdot B_{0z} = b_3$$

where,

$C_{xx}=\Sigma X_i^2 \quad C_x=\Sigma X_i$

$C_{yy}=\Sigma Y_i^2 \quad C_y=\Sigma Y_i$

$b_{1x}=-\Sigma \delta B_x^i X_i$

$b_{2y}=-\Sigma \delta B_y^i Y_i$

$b_j=-\Sigma \delta B_j^i \quad j=1,2,3$

Once the 5 parameters have been found as solutions of (5.28), the $\mathbf{W}_r$ vector can be calculated from (5.26). The above results are readily applicable to the case of totally uniform normal fields, as will be tested in section 5.11. In this simplified case $\mathbf{W}$ has three degrees of freedom. The three components of the normal field form the $\mathbf{W}$ vector as:

$$\mathbf{W}=\{\cdots, B_{0x}, B_{0y}, B_{0z}, \cdots\}^t$$

The three components of the normal field are determined similarly using the third equation in (5.28):

$$M \cdot B_{0i} = b_i \quad i=x,y,z$$

Solving the least squares problem (5.24b) we get an alternative **W** vector, denoted as $\mathbf{W}_1$, referring to stabilization from the left hand side of the misfit equation. The formulae for this are lengthy and are given in Appendix 3. When physical constraints are employed to regulate the inversion process (discussed in the next two sections) the correction to the model is not readily expressed in the form of a general inverse with a misfit vector as suggested in (5.24b). It is thus difficult to use $\mathbf{W}_1$. Further discussion of $\mathbf{W}_1$ is omitted.

5.9 CONSTRAINED LEAST SQUARES PROGRAMMING

Constrained least squares and least distance programming are very powerful tools in parametric inversion (Lawson and Hanson, 1974; Oldenburg, 1984). They are discussed in this section and the next.

One general problem of constrained least squares for a linear problem is to find the solution to

$$(5.29) \qquad |\mathbf{AP-D}|^2=\text{minimum}$$

subject to the linear inequality constraints:

$$(5.30) \qquad \mathbf{FP} \geq \mathbf{h}$$

in which **A**, **P** and **D** are the coefficient matrix, unknown vector, and free vector of a linear system of equations, **F** is the constraint matrix, and **h** the r.h.s. of inequality constraints. This can be solved by a standard method known as *LSI*, the Least Squares problem with Inequality constraints (Lawson and Hanson, 1974). It should be noted that equality constraints can be accommodated in the form of inequality constraints. For instance, $x=5$, can be presented as $x\geq5$ and $-x\geq-5$, etc.

Our linearized nonlinear problem is to solve:

$$|\mathbf{A}\delta\mathbf{P}-\delta\mathbf{D}|^2=\text{minimum} \quad (5.29a)$$

subject to the linear inequality constraints (5.30). The solution to (5.29a) is the correction to unknowns while the constraints are on the unknowns themselves. To use *LSI* our problem must be transformed to fit the forms of *LSI*. The writer found that the inequality constraints are readily transformed into constraints on the correction of the unknowns, and the **h** vector has to be transformed thus:

$$\mathbf{h} \Rightarrow \mathbf{h}'\equiv\mathbf{h}-\mathbf{F}\mathbf{P}_0$$

This follows if we write **P** as:

$$\mathbf{P}=\mathbf{P}_0+\delta\mathbf{P}$$

then (5.30) can be written as,

(5.30a) $\mathbf{F\delta P \geq h - FP_0}$.

Now (5.29a) and (5.30a) have the same forms as (5.29) and (5.30) respectively, and the algorithm *LSI* is readily applicable. This modified version of *LSI* will be called *LSINL*, Least Squares with Inequality constraints for linearized Non-Linear problems.

A detailed discussion of *LSI* is given by Lawson and Hanson (1974) and is outlined here only for discussion of some precautions for use of the method.

After some transformations (Lawson and Hanson, 1974):

$$\mathbf{F,P,h,A,D \rightarrow F',P',h'}$$

the *LSI* problem is transformed into *LDP*, Least Distance Programming (Lawson and Hanson, 1974) in which:

$$|\mathbf{P'}|^2\text{=minimum}$$

subject to constraints:

$$\mathbf{F'P' \geq h'}$$

The writer noticed that after such transformation the original inequality constraints (5.30) are actually replaced by:

(5..30b) $\mathbf{FVV^tP \geq h}$

where the V matrix is obscure V in the singular value decomposition of matrix **A** (see (5.19) in section 5.6). One recognizes that $\mathbf{VV^t}$ is the model resolution matrix (e.g., Kanasewich, 1981), and is a unit matrix when $\mathbf{A^tA}$ has no eigenvalue equal to zero and no eigenvectors are thrown away in forming the matrix **V**. Otherwise, $\mathbf{VV^t}$ is not a unit matrix, and consequently constraints (5.30b) are not equivalent to (5.30). The constraints (5.30) will then be violated. Therefore, while using *LSI* and/or *LSINL* methods, attention should be paid to the condition of the matrix **A**. If some of the eigenvalues are very small, $\mathbf{VV^t}$ is likely to deviate appreciably from a unit matrix due to computational error alone and constraints will be violated. In the work done for this thesis such situation has never happened after data and parameters have been properly weighted (next section).

5.10 LEAST DISTANCE PROGRAMMING AND ERROR COMPRESSION

The method *LDP*, Least Distance Programming (Lawson and Hanson, 1974), can also be used to regulate the inversion after some modifications. This has the advantages of accommodating error in the observations, and reducing the amount of computation compared to the *LSI* or *LSINL* methods because no singular value decomposition is needed. If errors are known to exist in the observations one usually does not want to fit the data very well. The model we seek fits the data within error bars, e, and is as close as possible to an initial reasonable and smooth model. In mathematical language we want to solve,

$$(5.31) \qquad |\delta P|^2 = \text{minimum}$$

subject to inequality constraints (5.30a) and

$$(5.32) \qquad \begin{matrix} A\delta P \geq \delta D - e \\ -A\delta P \geq -\delta D - e \end{matrix}$$

The inequality constraints on δP can be written together:

$$(5.33) \qquad F_e \delta P \geq h_e$$

where subscript "e" stands for "expanded"; (5.33) represents

$$(5.33a) \qquad \begin{bmatrix} F \\ A \\ -A \end{bmatrix} \delta P \geq \begin{bmatrix} h - FP^{\circ} \\ \delta D - e \\ -\delta D - e \end{bmatrix}.$$

(5.31) and (5.33a) can be solved by standard *LDP* programming (a FORTRAN code given in Lawson and Hanson, 1974). The process will be called *LDPNL*, Least Distance Programming for linearized Non-Linear problems. The *LDPNL* approach is preferred in underdetermined cases with more model parameters than data. In such cases it is possible, but usually not justified, to fit the data accurately. If the error allowed is not large enough, or the model is too far from the best fitting one, the constraints (5.33a) may be internally incompatible. In such a situation the constraints may be relaxed to get a sensible answer.

One flexible way to deal with this is the method of *error compression* designed by the writer. Parts of the constraints in (5.33) corresponding to (5.32) are relaxed to tolerate the inaccuracy of models during iterations. The error bar to be tolerated is reset at each iteration. At each iteration the misfit is calculated using the old model, and the largest misfit is singled out as the reference level of error tolerance. Error bars are then reset as a fraction, the *compression factor*, of this reference level but not less than a lower limit for each datum. The standard deviation of each datum is taken as this lower limit of error. Iteration continues by shrinking the error bars at each step until either the lower limit of error for every datum, or the incompatibility, is encountered. The compression factor is chosen such that incompatibility is not reached too soon, without making convergence too slow. This factor should always be smaller than unity or the correction to the model becomes zero. To accelerate convergence a smaller compression factor, say 0.7, can be used initially. If incompatibility comes too soon the factor can be floated to a larger value. The square root of the factor is used here.

On the other hand, if convergence is too slow the factor can be floated to a smaller value, such as the factor squared. In this way one can control the speed of convergence. In practice the initial compression factor is set between 0.7 and 0.8 and left floating. If the compression factor floats up to a very large value, say 0.99, and incompatibility is still encountered, the model fit cannot be further improved. Otherwise the data can be fitted to a better degree whether or not this is judged as desirable.

Model parameters and data can be weighted to improve the resolution of the model or to take account of data quality. In the present case one has no preference for any particular model parameter and different columns in the derivative matrix are roughly equally important. This latter condition is met by expressing the derivatives in nT/km (for $\partial B/\partial X^j$ and $\partial B/\partial w$) and nT/(kilo-Ampere) (for $\partial B/\partial I$), and the parameters are not further weighted. Data weighting is not quite sensible in an overdetermined case but is often set by the reciprocals of standard deviations (Oldenburg, 1984). When using the *LDPNL* approach, data weighting is generally trivial (e.g., $x \geq 0.5$ is the same as $2x \geq 1$) and is neglected.

5.11 TEST INVERSION OF SYNTHESIZED DATA

Three internal current models are used to test the algorithm. Fields are calculated on a 15 by 15 grid over a 280 by 280 km plane at Z=0. Data are taken among these grid points as uniformly as possible. Errors with a uniform distribution in the interval ±20 nT, or Gaussian error of 10 nT standard deviation, are added to the data. These errors are about 10 per cent of the calculated fields. A uniform field is subtracted from the calculated values in order to simulate real data with a nearly uniform normal field missing after separation.

Inequality constraints are applied to the positions of current nodes to regulate the inversion. Each node is constrained to be inside a rectangular box with its faces parallel to coordinate planes. Such boxes are larger for end nodes (outside the array) because the positions of these are less accurately determined by "observations" far from them. These constraints will be depicted in the figures to follow.

The starting model can be chosen to be a horizontal line current approximately beneath the zero contour of the Z component. The depth and the initial current magnitude can be taken by analogy to a horizontal straight line current. If one happens to choose the wrong sequence of nodes, the resolved current intensity will be negative.

The solution is considered to have converged either if the model fitting is not improving significantly, or if the model is not changing significantly. Certain thresholds are set in advance for stopping the iteration.

The goodness of model fit and the quality of data are examined by using several parameters. These include the root mean square of the relative error of the data, for each component:

$$R(\Delta B_i) \equiv \sqrt{\{\Sigma \Delta B_i^2 / \Sigma B_i^2\}}, \tag{5.34a}$$

where, M is the number of data points (stations), summation is over M data points and ΔB_i is the standard deviation of B_i, and for the total field:

$$R(\Delta B) \equiv \sqrt{\{\Sigma (\Delta B/B)^2 / M\}} \tag{5.34b}$$

$$\Delta B \equiv \sqrt{(\Delta B_1^2 + \Delta B_2^2 + \Delta B_3^2)}.$$

The root mean square of relative misfit of the inverted field, for each component:

$$R(\delta B_i) \equiv \sqrt{\{\Sigma \delta B_i^2 / \Sigma B_i^2\}}, \tag{5.34c}$$

where, δB_i is the misfit in B_i, and for the total field:

$$R(\delta B) \equiv \sqrt{\{\Sigma (\delta B/B)^2 / M\}} \tag{5.34d}$$

$$\delta B \equiv \sqrt{(\delta B_1^2 + \delta B_2^2 + \delta B_3^2)}.$$

In the above definition the factors for the total field and those for each component are different: for the total field the summation is taken over the ratio, while for the components the ratio is taken after the summation. This form accommodates points at which a particular component is very small.

Other parameters that are examined are the ratio of misfit to error, for the total field:

(5.34e) $R(\delta/\Delta B) \equiv \sqrt{\{\Sigma\delta B^2/\Sigma\Delta B^2\}}$,

and for each component:

(5.34f) $R(\delta/\Delta B_i) \equiv \sqrt{\{\Sigma\delta B_i^2/\Sigma\Delta B_i^2\}}$.

The correlation coefficients (chapter 3) between the inverted fields and the calculated (or observed) fields are also calculated as a measure of fit. All these factors are useful in the inversion of real data as well.

5.11.1 TEST 1: SINGLE LINE CURRENT MODEL

The first model, Figs.5.3-5.5 and Tables 5.1 and 5.2, is a 3-D line current with 5 nodes. Data are taken as 3 field components at 25 equally spaced points of a square grid. We have altogether 75 data and 16 unknown parameters, giving an overdetermined case.

Table 5.1

	total field	X	Y	Z
$R(\delta B)$	0.114	0.208	0.074	0.108
$R(\Delta B)$	0.147	0.266	0.087	0.120
$R(\delta/\Delta B)$	0.846	0.884	0.923	0.948
correlation		0.960	0.994	0.998
field subtracted		16.5	22.7	16.5
recovered in W_r		12.7	17.0	9.8

Table 5.2

	total field	X	Y	Z
R(δB)	0.047	0.096	0.032	0.050
R(ΔB)	0.147	0.266	0.087	0.120
R(δ/ΔB)	0.382	0.600	0.604	0.646
correlation		0.996	0.998	0.999
field subtracted		16.5	22.7	16.5
recovered in W_r		13.2	21.0	20.5

Before error contamination (see caption of Fig 5.3) a uniform field is subtracted from the calculated field to make the X component negative, the Y component positive, and the Z component with a zero average. Such treatment is to simulate the feature of a horizontal straight line current, internal to the Earth and approximately following the model current from south-west to north-east. Constraints on nodal position are imposed and the depth range and horizontal projection of the constraint "boxes" for nodes under the "survey area" are plotted in the figures (Figs.5.3 and 5.5 and similar figures to follow for other tests and field data inversion).

Using the *LDPNL* method, after 14 iterations the solution converged (Fig.5.3). The error compression factor was initially set to 0.7, and was floated up to 0.837 (=$\sqrt{0.7}$) after 7 iterations because incompatibility was encountered. After another 7 iterations the model stabilized, with changes in nodal positions less than 1 km for all nodal coordinates. The initial model (Fig.5.3) was

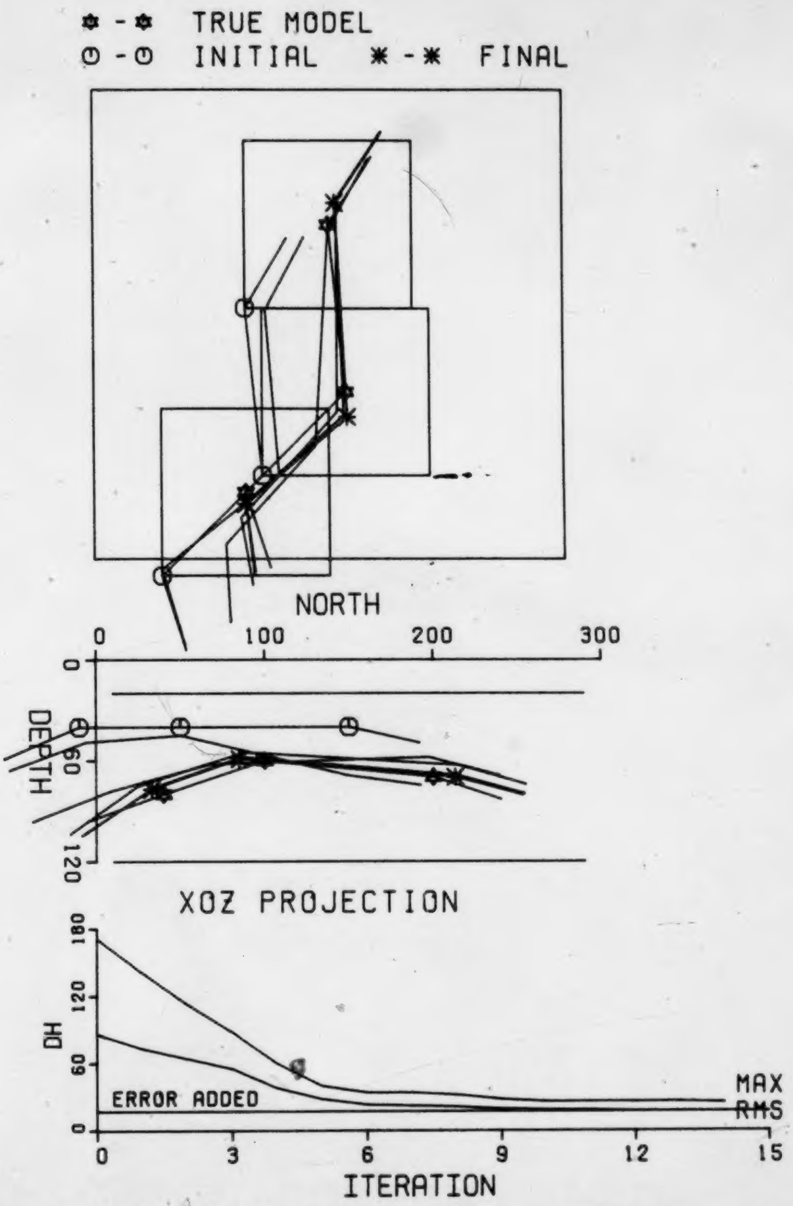

Figure 5.3 Iteration process for the *LDPNL* inversion of test model 1 (Fig.5.4). Top to bottom:
Horizontal projection of line current, only nodes under the array are shown, and constraints on the horizontal positions of nodes are superimposed.
XOZ projection of the current, X north and Z down, two horizontal lines showing constraints on depth of nodes.
Misfit of total field H. Both maximum and root-mean-square values are plotted. The "error added" is the r.m.s error in total field resulting from Gaussian error of 10 nT standard deviations added to each of the three components of field at all the 25 data points. See also Fig.5.4.

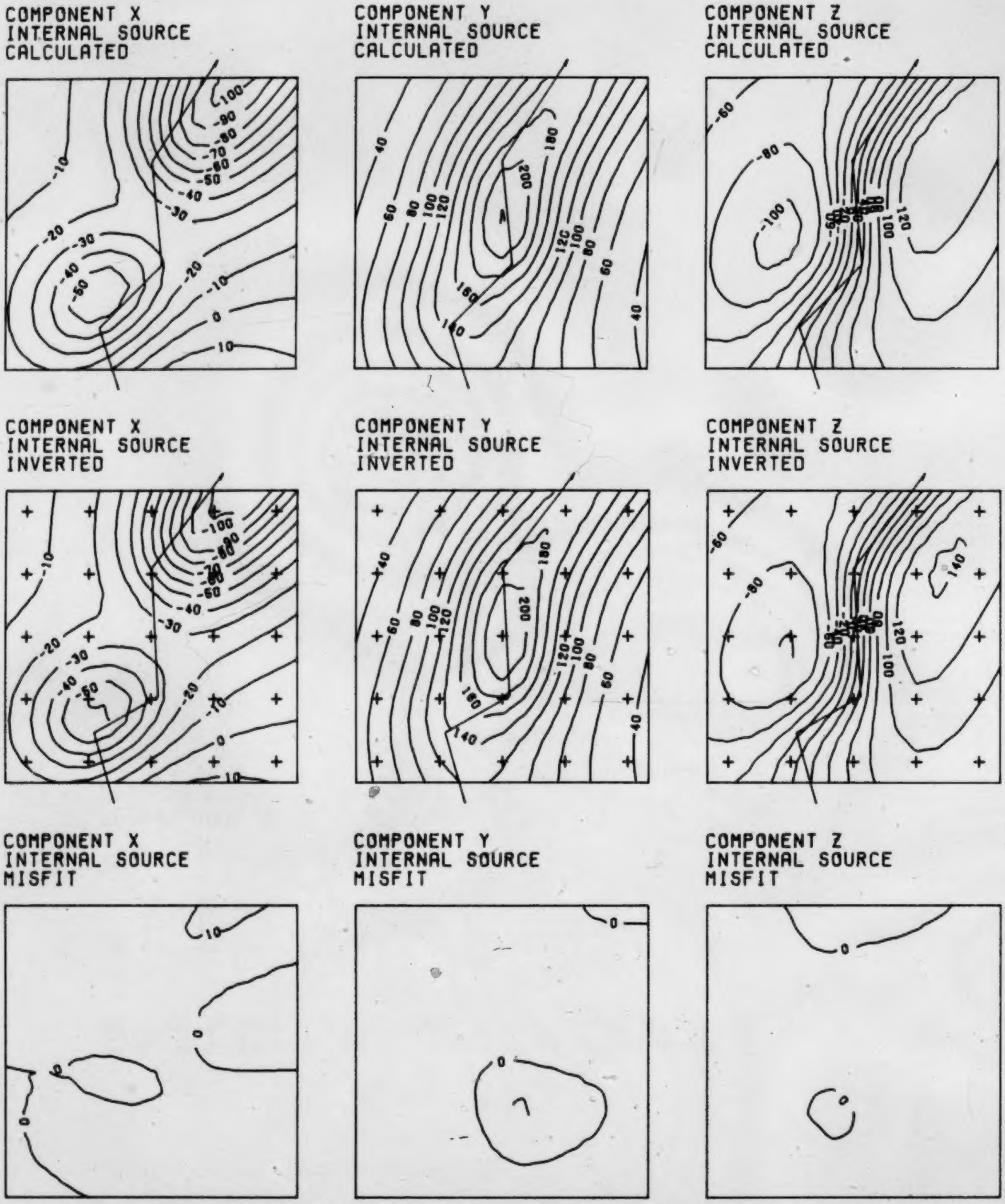
COMPONENT X
INTERNAL SOURCE
CALCULATED

COMPONENT Y
INTERNAL SOURCE
CALCULATED

COMPONENT Z
INTERNAL SOURCE
CALCULATED

COMPONENT X
INTERNAL SOURCE
INVERTED

COMPONENT Y
INTERNAL SOURCE
INVERTED

COMPONENT Z
INTERNAL SOURCE
INVERTED

COMPONENT X
INTERNAL SOURCE
MISFIT

COMPONENT Y
INTERNAL SOURCE
MISFIT

COMPONENT Z
INTERNAL SOURCE
MISFIT

Figure 5.4 Test model 1 is a single line current. The *LSINL* method used for inversion, with an initial model which is the best model achieved by the *LDPNL* inversion (Fig.5.3). The misfit of the inverted model is with respect to calculated accurate data.

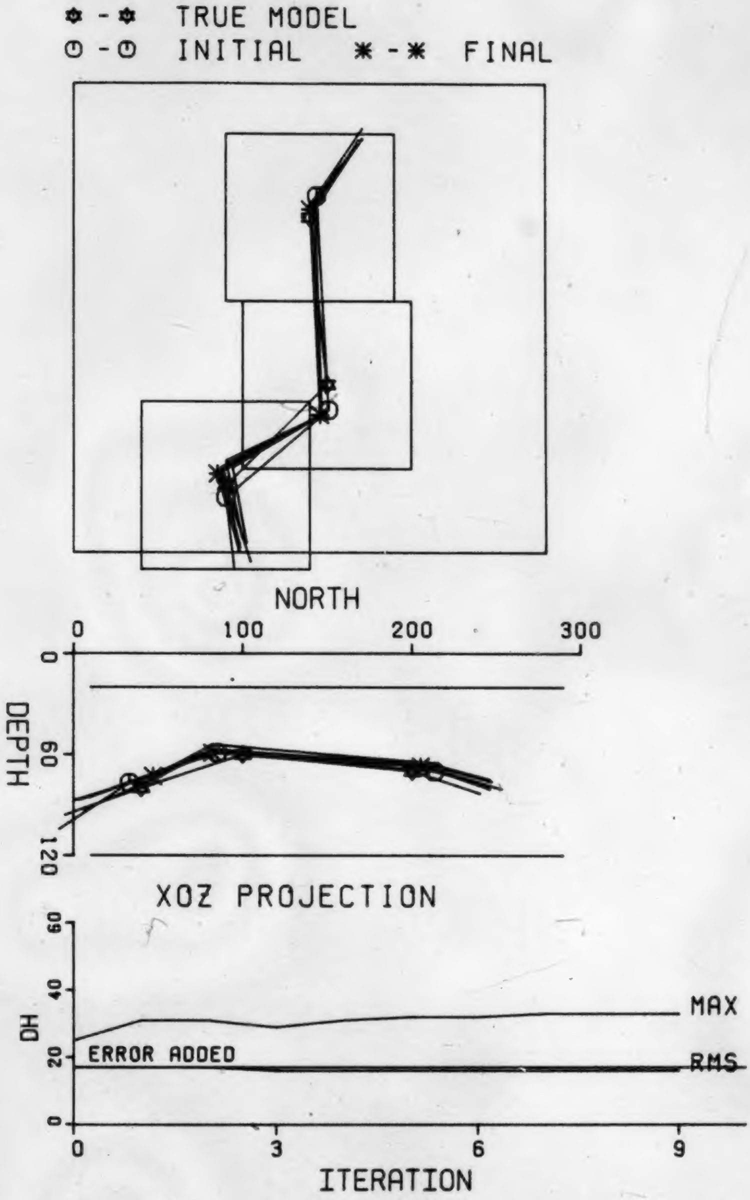

Figure 5.5 Iteration process for the *LSINL* inversion in Fig.5.4. See also Fig.5.3.

quite far from the true model, with nodes at corners of the constraint boxes. The ability to converge to the true model is therefore illustrated. The misfit of the inverted model, Fig.5.3 and Table 5.1, is within the limits of the errors introduced. The misfits plotted in Fig.5.3 (and similar figures to follow) are calculated w.r.t the contaminated data chosen for the inversion. The errors listed in Table 5.1 (and similar tables to follow) are calculated w.r.t. the accurate data over the entire data grid (15 by 15). They give different measures of the model fitting. Using the best model achieved by the *LDPNL* inversion and the same data, *LSINL* inversion (Figs.5.4 and 5.5 and Table 5.2) stabilized after 9 iterations. The inversion ~~is~~ considered stabilized when the improvement of r.m.s misfit falls to 0.3 percent. The *LSINL* inversion somewhat improved the misfit (compare Tables 5.1 and 5.2, Figs.5.3 and 5.5),but the improvement of the model is not significant.

The resolved line currents closely follow the trend of the true model in horizontal positions and depth (Figs.5.3 and 5.5). The maximum offsets of the three nodes under the "survey area" are 1~18 km horizontally and 1~7 km in depth. The positions of the two end nodes are not marked in Figs.5.3-5.5 and are are poorly resolved, but the orientations of the two end current segments, determined by pairs of nodes at each end, are well determined. This is shown in Figs.5.3-5.5 by outward line segments from the outmost nodes shown. The end segments resolved by the *LSINL* inversion are essentially parallel to those in the true model.

W_r, resolved during the step-by-step stabilization shows the uniform field in the *LSINL* inversion to be (13.2, 21.0, 20.5), which is quite close to the field, (16.5, 22.7, 16.5), which was actually subtracted. The difference between the two vectors is well below the size of the error added. This leads one to expect that if one has some insight into the source field then it may be possible to resolve its uniform part, provided that the data are of reasonable quality. It follows that a nearly uniform field can also be isolated if one has some knowledge of its source.

5.11.2 TEST 2: SHEET CURRENT MODEL

The second model is a uniform current sheet of constant width. The geometry of such a sheet current is described in section 5.4. The nodal positions and data are chosen the same as those for the test of the line current model. The random errors added to the calculated field are uniformly distributed (± 20 nT) for all three components of field. This configuration serves to illustrate the effect of a current sheet of appreciable width on the inverted model. The current sheet will smooth the spatial gradients of the fields at the surface, so that a single line current fitted to those fields is expected to overestimate the depth.

The model is first inverted to a line current using the *LDPNL* method and an initial model which differs considerably from the true model (Fig.5.6 and Table 5.3). The convergence of the model is slower than the line current model. In the 22 iterations, the compression factor is 0.7 for the first 4 iterations, 0.837 for the next 2, 0.915 for the next 3 and 0.956 for the last 13. For the last iteration the r.m.s. misfit improved only 0.4 percent and the model was considered to have stabilized. The best line current model achieved by the *LDPNL* method is then refined by the *LSINL* method (Fig.5.7 and 5.8, and Table 5.4). Taking the best line current model determined by the *LSINL* inversion as the initial model and with an initial width of 40 km, the *LSINL* method is used to invert the field to a uniform sheet model (Figs.5.9 and 5.10 and Table 5.5). The width is constrained to be between 10 and 200 km.

Table 5.3

	total field	X	Y	Z
$R(\delta B)$	0.210	0.180	0.199	0.161
$R(\Delta B)$	0.174	0.321	0.104	0.144
$R(\delta/\Delta B)$	1.315	0.750	1.386	1.059
correlation		0.980	0.981	0.986
field subtracted		15.9	23.2	16.1
recovered in W_r		21.3	2.4	14.2

Table 5.4

	total field	X	Y	Z
$R(\delta B)$	0.070	0.087	0.061	0.086
$R(\Delta B)$	0.174	0.321	0.104	0.144
$R(\delta/\Delta B)$	0.508	0.522	0.768	0.772
correlation		0.993	0.995	0.997
field subtracted		15.9	23.2	16.1
recovered in W_r		17.3	20.0	12.1

Table 5.5

	total field	X	Y	Z
$R(\delta B)$	0.051	0.086	0.031	0.059
$R(\Delta B)$	0.174	0.321	0.104	0.144
$R(\delta/\Delta B)$	0.331	0.518	0.551	0.638
correlation		0.992	0.999	0.999
field subtracted		15.9	23.2	16.1
recovered in W_r		18.3	20.2	11.4

The uniform field subtracted from the data before error contamination and those recovered by the W_r vector for the three inversions are listed in Tables 5.3-5.5. The uniform normal field recovered by the *LDPNL* inversion is quite far from that actually subtracted, mainly because the resolved nodal positions are still distant from those of the true model, especially in depth. Such fields recovered by the two *LSINL* inversions are both very close to that subtracted, even though one (Table 5.5) assumes a correct model (sheet), while the other (Table 5.4) a false one (line). The overall fits of the two *LSINL* inversions are equally good over the actual data set (5 by 5 grid) used for the inversions. The

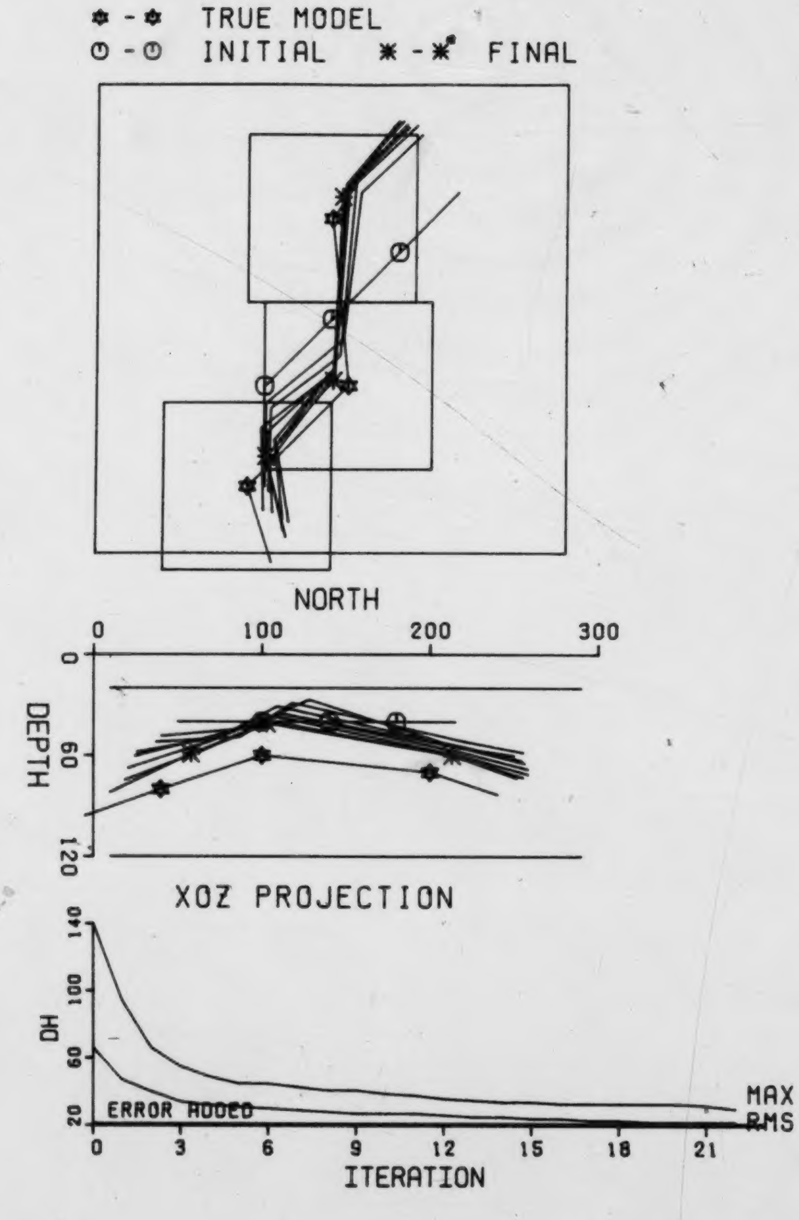

Figure 5.6 Iteration process for the inversion of test model 2, a sheet current 70 km wide. Using the *LDPNL* method the fields are inverted to a line current.

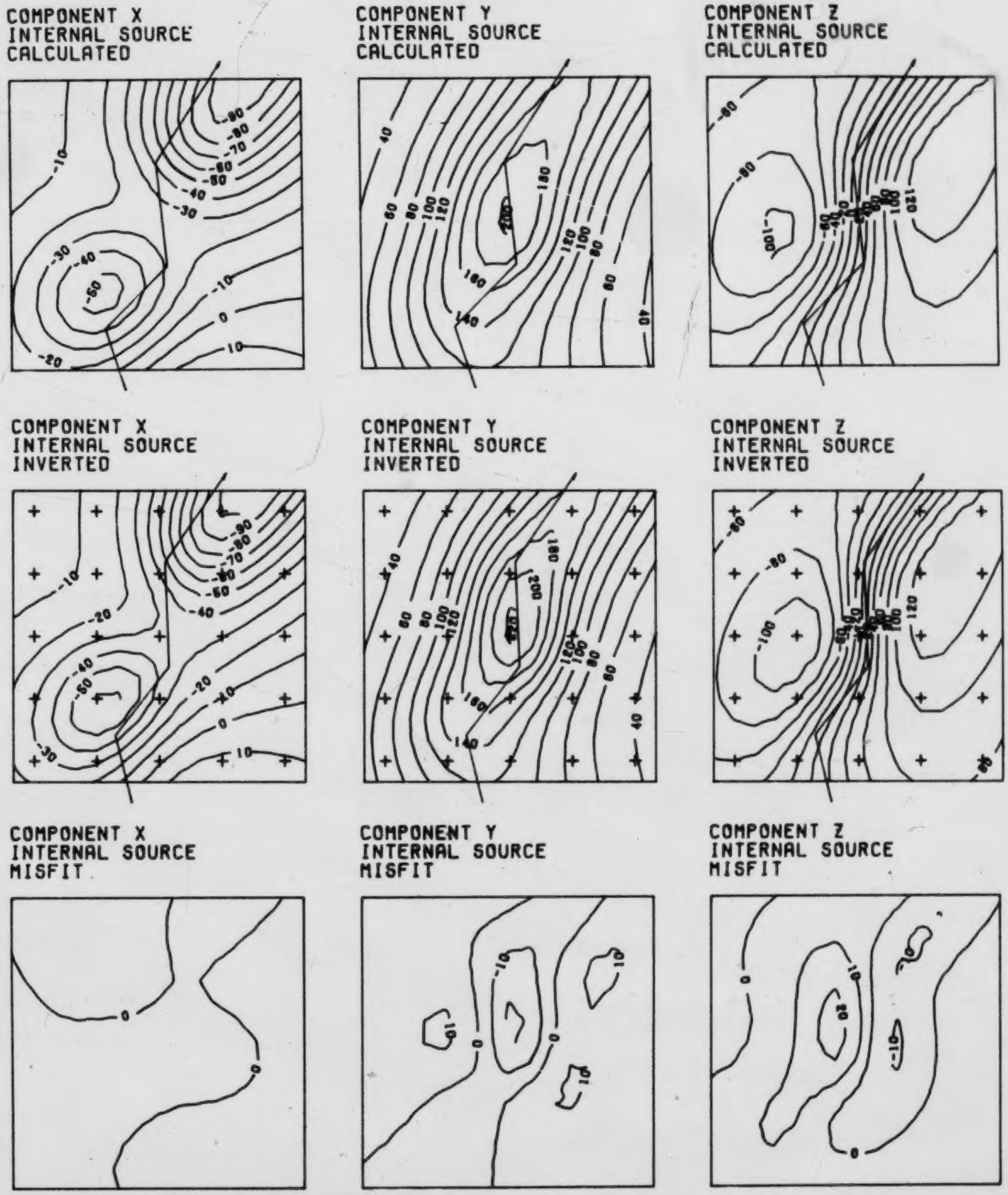

Figure 5.7 Test model 2 (70 km wide sheet) is inverted to a line current using the *LSINL* method. The initial model is the final model inverted by the *LDPNL* method (Fig.5.6).

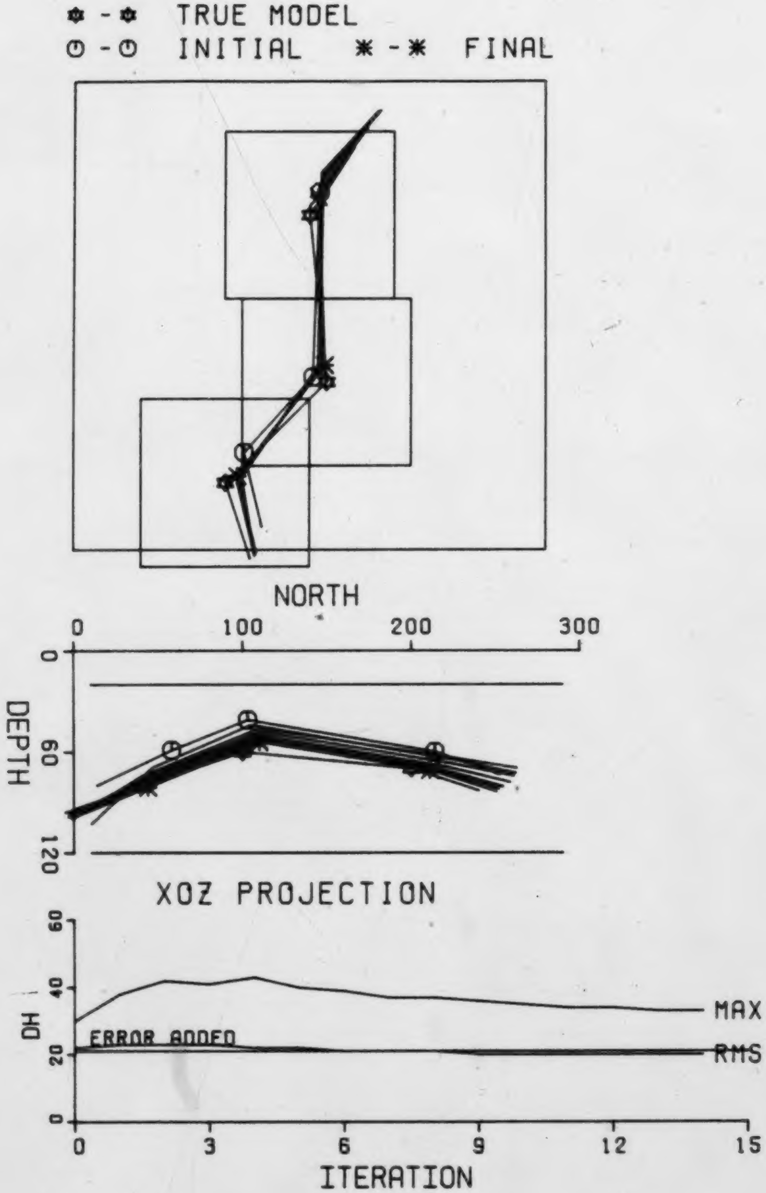

Figure 5.8 Iteration process for the *LSINL* inversion in Fig.5.7.

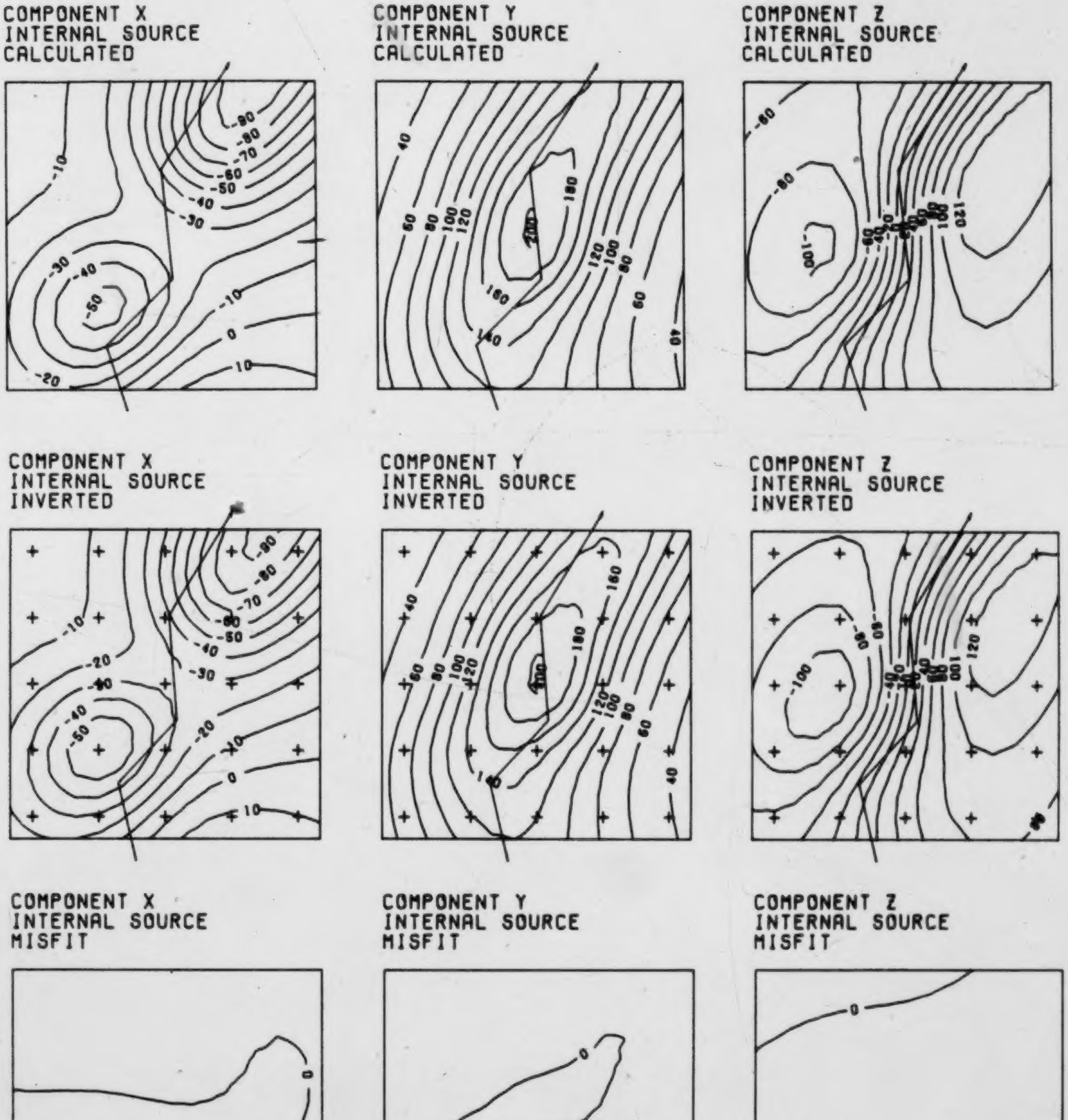

Figure 5.9 Similar to Fig.5.7 but inverted to a sheet current with the *LSINL* method. The width of the sheet is: true model, 70 km; initial model 40 km; final model 77 km.

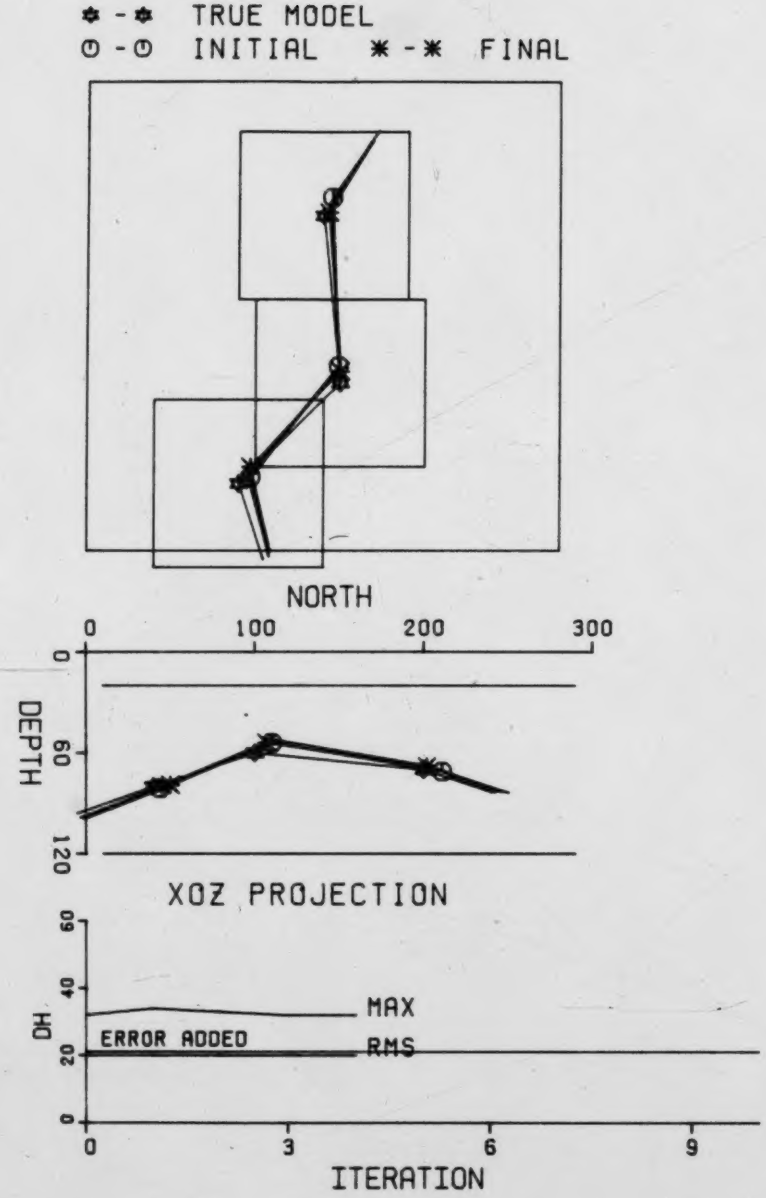

Figure 5.10 Iteration process for the *LSINL* iversion in Fig.5.9.

sheet model inversion fits the data over the entire data grid (15 by 15) better than the line current model (compare Tables 5.4 and 5.5). The inverted width of the sheet is 77 km, 10 percent wider than that of the true model. These results show that such a sheet current, with a width about the same as its depth, will be seen from the surface as not very different from a line current.

The same current is then widened to 100 km width with the data and error contamination unchanged. Such a wider current sheet is expected to show its sheet current character more distinctely in the surface data. Using the *LSINL* method, and an initial model with the horizontal position of the nodes shifted 20 km in both the X and the Y directions (from the true model) and the depths of the three intermediate nodes at 40 km, the fields were inverted to a line current (Fig.5.11 and Table 5.6).

Table 5.6

	total field	X	Y	Z
$R(\delta B)$	0.121	0.148	0.110	0.152
$R(\Delta B)$	0.175	0.328	0.105	0.150
$R(\delta/\Delta B)$	0.879	0.671	1.023	1.009
correlation		0.984	0.983	0.992
field subtracted		15.5	23.7	15.6
recovered in W_r		16.4	18.4	11.1

Taking the result of the line current model and an initial width of 60 km, the field was inverted to a current sheet model by using the *LSINL* method (Figs.5.12 and 5.13 and Table 5.7). As noticed for the case of a narrower sheet (70

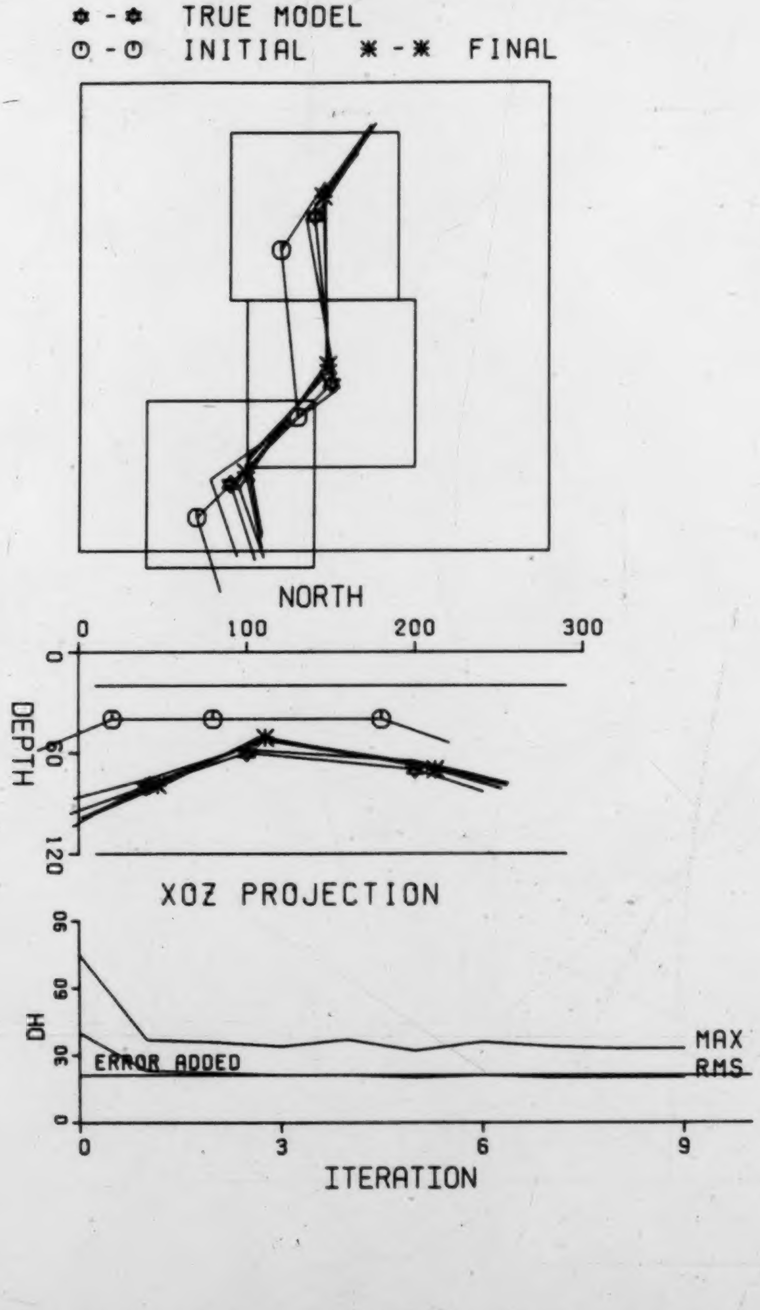

Figure 5.11 Iteration process for test model 2, a wider (100 km) sheet current. Using the *LSINL* method the fields are inverted to a line current. The initial nodes are 20 km off the horizontal positions of the true nodal positions and at 40 km depth for the intermediate nodes.

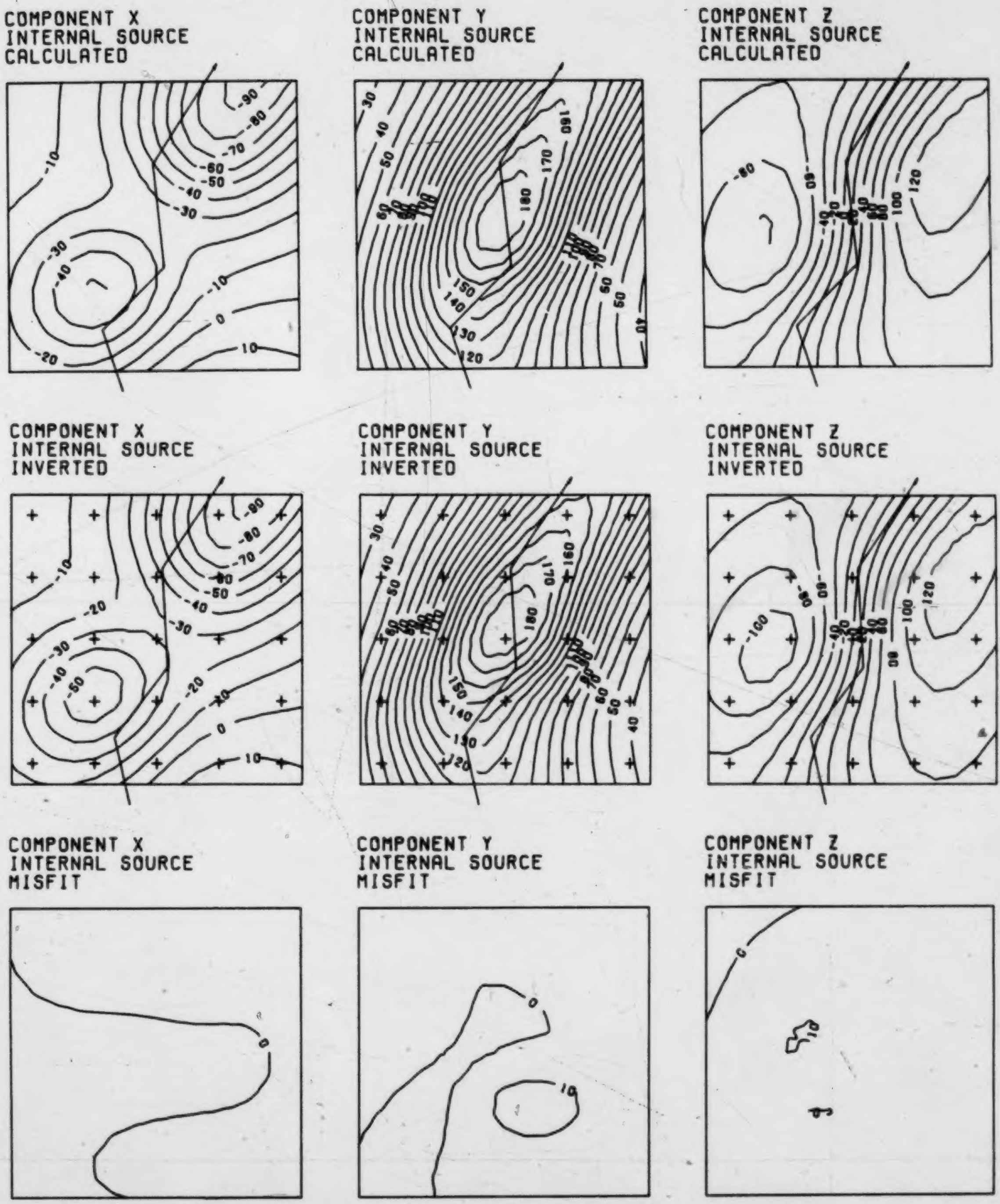

Figure 5.12 Test model 2 (100 km wide sheet) is inverted to a sheet current using the *LSINL* method. The initial model is the best model achieved by line current inversion, Fig.5.11. The initial width is 60 km, finally inverted is 103.7km.

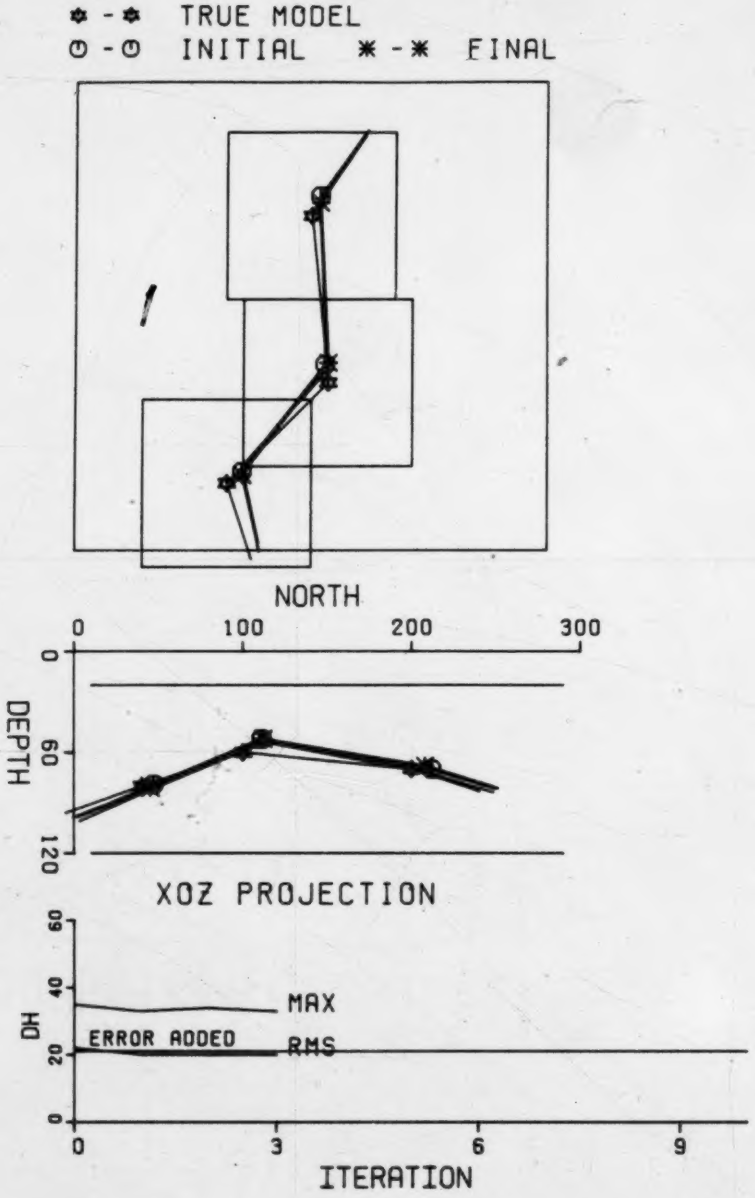

Figure 5.13 Iteration process for the *LSINL* inversion in Fig.5.12.

km), the differences between the two inversions are not significant. For such a sheet of width 100 km, almost twice the data spacing (60 km), the field can still be inverted to give a line current which gives an adequate approximation to the fields. It is therefore not surprising that the line current analogy is often used to present the real current configuration for current channelling studies (Jones, 1982 and references there quoted). Nonetheless, the sheet inversions improve the model fits over the entire data grid (15 by 15) for both cases, especially for the wider sheet (compare Tables 5.3-5.7).

Table 5.7

	total field	X	Y	Z
$R(\delta B)$	0.058	0.074	0.042	0.065
$R(\Delta B)$	0.175	0.328	0.105	0.150
$R(\delta/\Delta B)$	0.363	0.474	0.633	0.658
correlation		0.994	0.998	0.999
field subtracted		15.5	23.7	15.6
recovered in W_r		16.7	19.7	10.5

5.11.3 TEST 3: PRISM CURRENT MODEL

The last model, Figs.5.14-5.17 and Tables 5.8 and 5.9, is a prism with a 60 by 40 km cross section, between vertical planes and planes oriented as the current sheet in the last model. The fields generated by such a current are approximated by 4 by 4 parallel line currents equally spaced over the 60 by 40 cross section. The connection of two segments at a node has features like those noted for the sheet current model. The central line or axis of the prism has 4 nodes. The initial model, a line current with 4 nodes, has 13 unknowns.

Table 5.8

	total field	X	Y	Z
$R(\delta B)$	0.259	0.247	0.230	0.285
$R(\Delta B)$	0.169	0.121	0.117	0.117
$R(\delta/\Delta B)$	2.164	1.430	1.402	10564
correlation		0.953	0.967	0.968
field subtracted		-63.4	91.4	35.9
recovered in W_r		-49.4	67.7	6.7

Table 5.9

	total field	X	Y	Z
$R(\delta B)$	0.053	0.051	0.033	0.066
$R(\Delta B)$	0.169	0.121	0.117	0.117
$R(\delta/\Delta B)$	0.442	0.651	0.528	0.755
correlation		0.998	0.998	0.998
field subtracted		-63.4	91.4	35.9
recovered in W_r		-64.1	89.6	31.0

When compared to the sheet model, the prism model is closer to the real current distribution. Again, the inverted line current is expected to be deeper than the axis of the prism because of the current spreading in space as discussed for the sheet model. However, since the field outside a uniform current in a straight cylinder is the same as that of a line of the same total current at the axis of the cylinder, the line current inverted for the fields of a prism current is expected to be closer to the axis of the

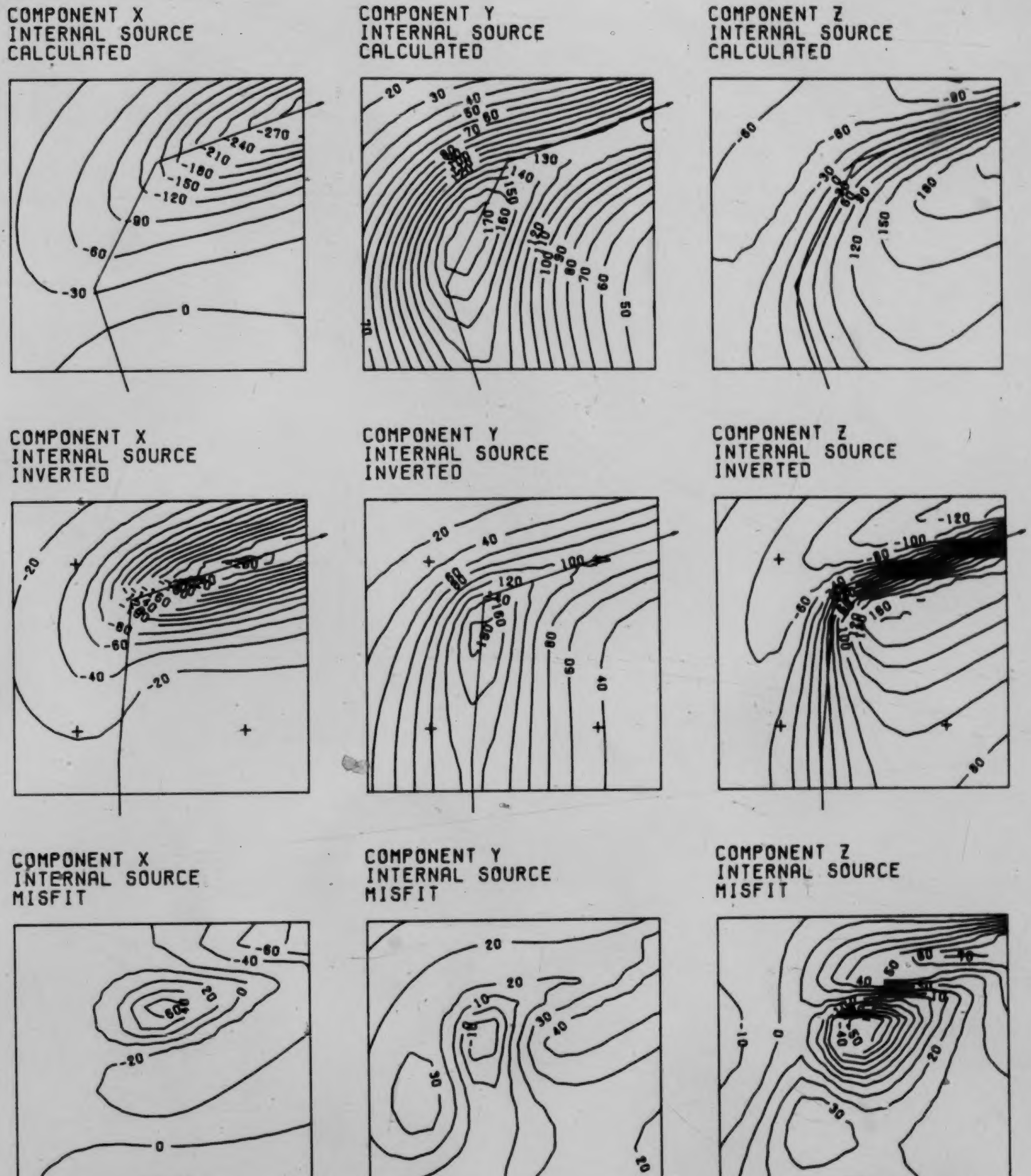
COMPONENT X
INTERNAL SOURCE
CALCULATED

COMPONENT Y
INTERNAL SOURCE
CALCULATED

COMPONENT Z
INTERNAL SOURCE
CALCULATED

COMPONENT X
INTERNAL SOURCE
INVERTED

COMPONENT Y
INTERNAL SOURCE
INVERTED

COMPONENT Z
INTERNAL SOURCE
INVERTED

COMPONENT X
INTERNAL SOURCE
MISFIT

COMPONENT Y
INTERNAL SOURCE
MISFIT

COMPONENT Z
INTERNAL SOURCE
MISFIT

Figure 5.14 Test model 3 is a prism current, inverted to a line current using the *LDPNL* method. 4 data points, 12 data were used for the inversion.

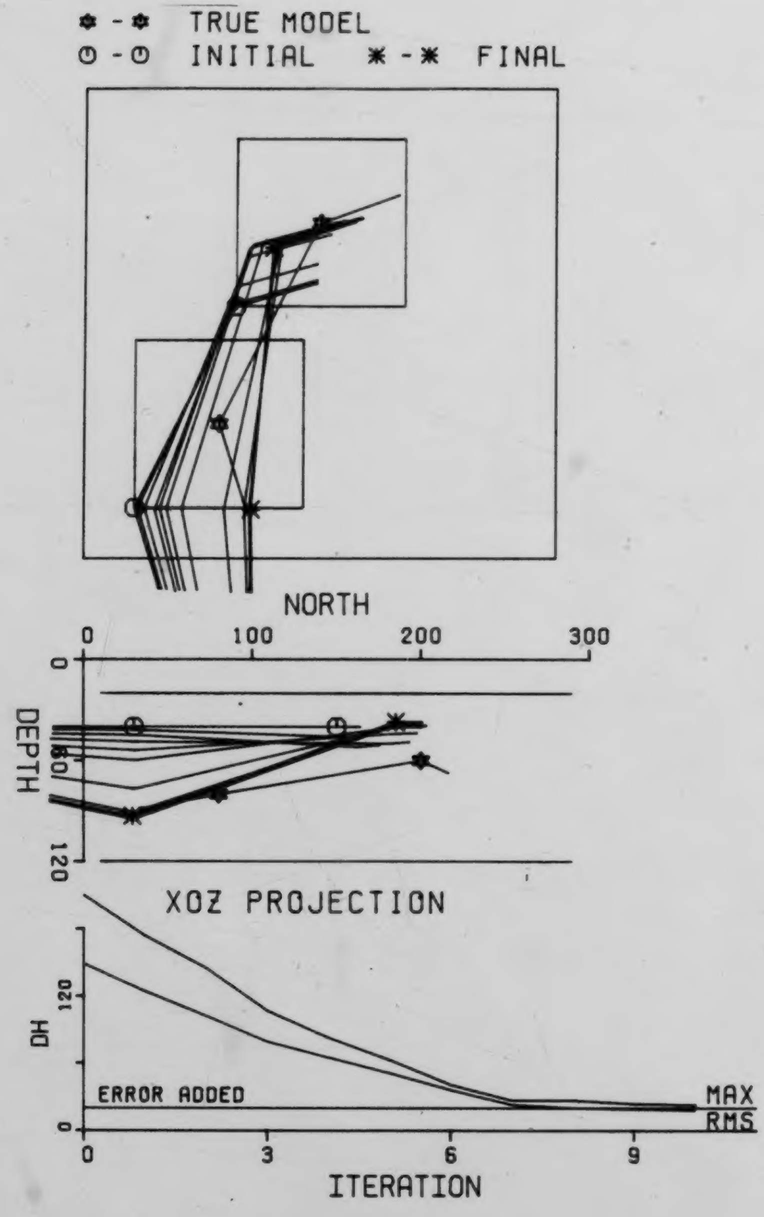

Figure 5.15 Iteration process for the *LDPNL* inversion in Fig.5.14.

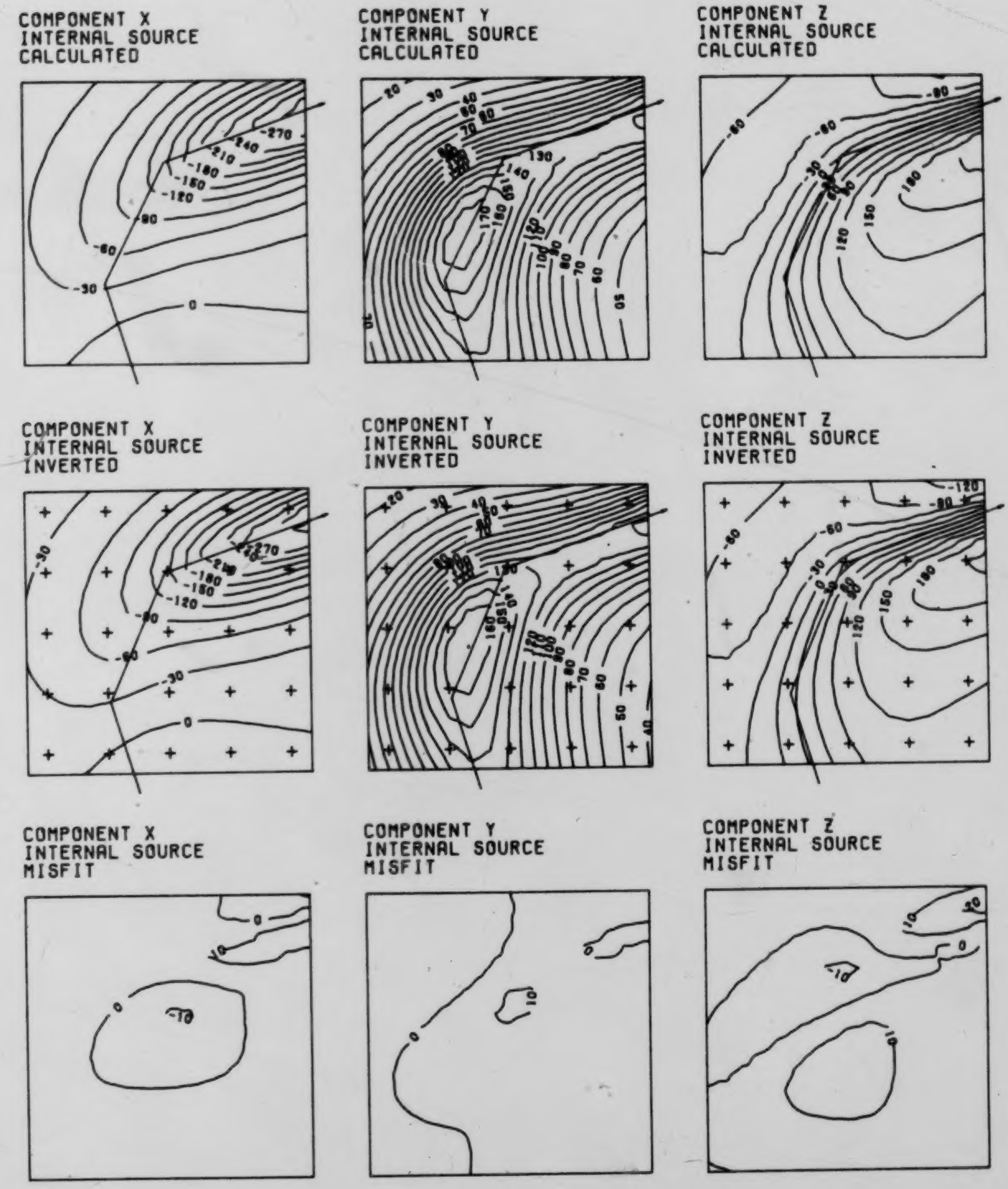

Figure 5.16 Similar to Fig.5.14 but with the *LSINL* method. 5 by 5 data points, 75 data were used for the inversion.

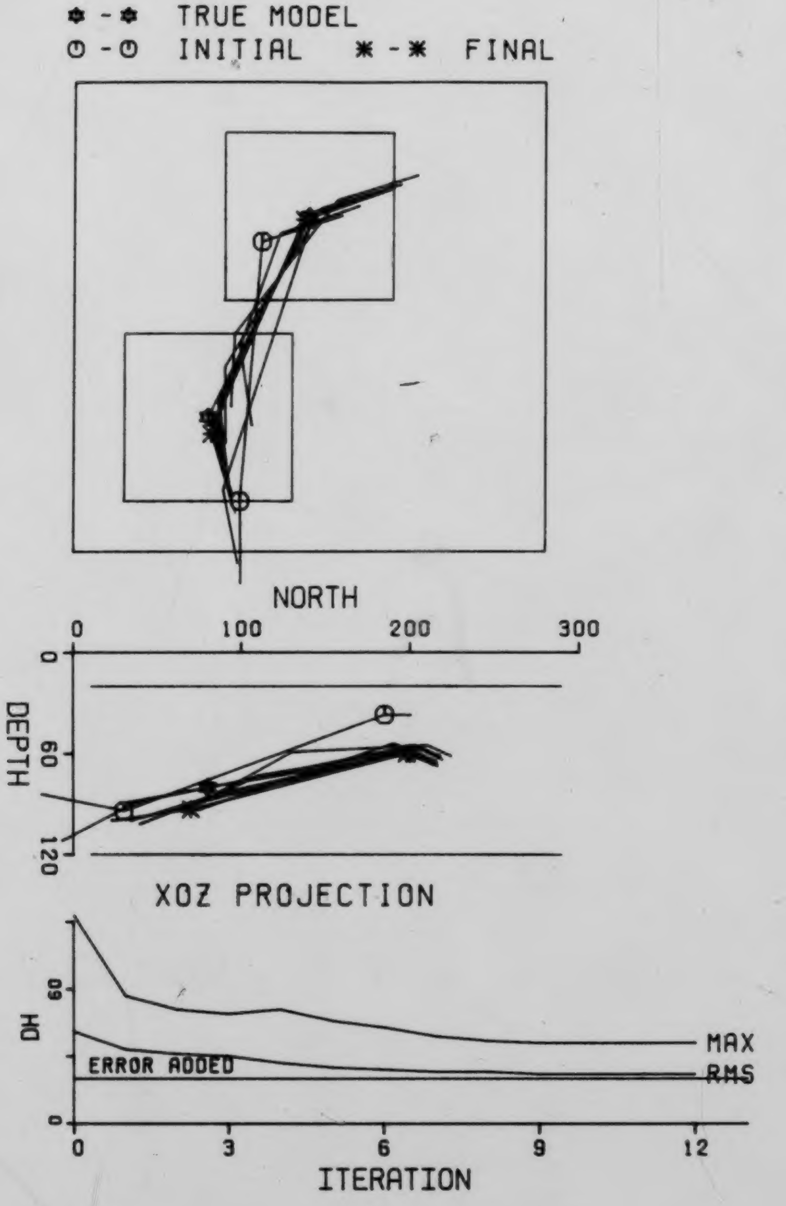

Figure 5.17 Iteration process for the *LSINL* inversion in Fig.5.16.

prism.

The data are first taken at a 2 by 2 grid (12 data), using the *LDPNL* method to give a rough estimate of the model (Fig.5.14 and 5.15 and Table 5.8). Continuing with the model from the *LDPNL* method, a 5 by 5 grid (75 data) are inverted to refine the model using the *LSINL* method (Fig. 5.16 and 5.17 and Table 5.9). In each case a uniform field (Tables 5.8 and 5.9) is subtracted before error contamination (±20 nT uniform) to give zero mean value of each component over the 15 by 15 grid.

Because the number of data points is small for the *LDPNL* inversion, the inverted model is still quite distant from the true model (even though thefit to the data is close to the error limit ,Fig.5.15). The uniform field recovered by the W_r vector (Table 5.8) is far from that actually subtracted, especially in the Z component. The initial model is at 40 km depth, and the inversion stabilized before reaching the true depth (Figs.5.14 and 5.15). The *LSINL* inversion greatly improved the model. The horizontal positions of the resolved nodes almost coincide with those of the true model (Figs.5.16 and 5.17). Overall the inversion is less accurate than the results from the line and sheet models because of the greater model complexity. The resolved depths for the two intermediate nodes are 92 and 60 km as compared with the true values, 80 and 60 km. The uniform field resolved by the W_r vector (Table 5.9) is quite close to that actually subtracted. This shows that the prism current can generally by approximated by a line current along its axis.

5.12 A TEST FOR CURRENT CHANNELLING BY MEANS OF THE KARHUNEN-LOEVE TRANSFORM

Most of the magnetovariation events observed by the 1983 array show line current signatures like that noted in Chapter 3. This feature is much clearer in the separated internal fields (Chapter 3, Figs.3.8-3.10). An first attempt has be made to examine the importance of this feature by means of the Karhunen-Loeve (K-L) transformation (Kramer and Mathews, 1968).

The K-L transform is employed to decompose a set of n signals, here the 2-D X (or Y, Z) component of magnetic fields at frequencies ω_i, i=1,2, $\cdots$ n, into n *basic* components ψ_j:

$$(5.35) \qquad X(\omega_i,x,y) = \sum_{j=1}^{n} R_{ij}\psi_j(x,y)$$

The basic components are linear combinations of the original signals with the same transformation matrix but transposed:

$$(5.36) \qquad \psi_j(x,y) = \sum_{i=1}^{n} R_{ij}X(\omega_i,x,y)$$

To get matrix R we first calculate the inner product matrix Γ:

(5.37) $\Gamma_{ij}=\int\int X(\omega_i,x,y)X(\omega_j,x,y)dxdy$,

then express it in the form

(5.38) $\Gamma=R\Lambda R'$

where, Λ is the diagonal matrix with eigenvalues, $\lambda_k\geq 0$, on the diagonal in descending order, and the columns of R are the corresponding normalized eigenvectors. If in (5.35), instead of the full summation, one retains only the first m, m<n, basic components, the original signals cannot be exactly recovered and one gets their approximations, $X_a(\omega_i,x,y)$. For $X(\omega_i,x,y)$, the error introduced by this truncation is:

$$\begin{aligned}\phi_i&=\int\int[X_a(\omega_i,x,y)-X(\omega_i,x,y)]^2dxdy\\&=\sum_{k=m+1}^{n}R^2_{ik}\lambda_k\end{aligned}$$

The total truncation error for all n signals is:

$$\phi=\Sigma\phi_i=\sum_{k=m+1}^{n}\lambda_k$$

If the set of signals is highly coherent, i.e., the fields have a consistent spacial pattern, the first eigenvalue will be much larger than the others. In this case we call the first basic component the first principal component.

For the array data, the inner product matrix is calculated according to (5.37) by summing the products over the data grid.

Before interpolation of station data onto a grid, the phases of the spectra at a certain period are shifted equally at all stations, to enhance signal in the real (or imaginary) component. This can only be achieved for the fields of a channelled current. Since the surface fields show a line current signature from north-east curling down to the south (or reversed), the fields of a channelled current with such orientation should produce maximum X (most positive), minimum Y (most negative) over the array, especially right above the current channel. Let $B_i(j)$ be the spectrum of component i, i=x,y,z, at station j for period T:

$$B_i(j)=|B_{ij}|\exp[i\theta_{ij}]$$

The average phase in B_x is:

$$E(\Theta_x)=\sum_j \theta_{xj}/M$$

where M is the number of stations. All the phase spectra are then shifted:

$$\theta_{ij} \rightarrow \theta_{ij}-E(\Theta_x)$$

This should give, for a field of channelled current:

$$\begin{aligned} &B_x(j) = \text{real(most positive)} + \text{imag(small)} \\ (5.39)\qquad &B_y(j) = \text{real(most negative)} + \text{imag(small)} \end{aligned}$$

$$B_z(j) = \left\{ \begin{array}{l} \text{real(most positive) + imag(small)} \\ \quad \text{to the north-west} \\ \\ \text{real(most negative) + imag(small)} \\ \quad \text{to the south-east} \end{array} \right.$$

The inevitable imaginary parts, representing the AC components, when compared with the real parts, show the relative importance of induction effects. The phase-shifted data are then interpolated onto a 9 by 9 grid by a combination of Lagrange and cubic spline schemes. The separation into internal and external parts is performed with the same grid data.

For X, Y and Z components of the fields the K-L transforms are performed to examine the coherent signal. The data chosen for this analysis are 5 frequency components with periods 16, 23, 63, 136, and 225 minutes from different magnetovariation events. These frequency components have the semi-major axes of the averaged polarization ellipses (see chapter 2) oriented at different azimuths: 153.8, 87.8, 81.9 100.5, and 75.0 degree (positive anti-clockwise from the east). The five events are chosen to represent fields of different penetration depths and source geometries. The results of the K-L transform are summarized in Table 5.10 and the

Table 5.10

Field component		λ_1/λ_2 Total	λ_1/λ_2 Internal	$\lambda_1/\Sigma\lambda_k$ Total	$\lambda_1/\Sigma\lambda_k$ Internal
X	real	6.71	16.76	0.78	0.91
	imag	6.43	3.43	0.77	0.62
Y	real	5.87	32.01	0.79	0.95
	imag	1.33	2.58	0.42	0.54
Z	real	33.50	44.29	0.97	0.96
	imag	1.24	2.17	0.47	0.57

first and second principal components of the internal real fields are plotted in Fig.5.18. The internal real Z fields from the five events, together with the corresponding first principal component, are given in Fig.5.19. In Table 5.10, λ_1/λ_2 shows the ratio of the energy in the first principal component as compared to the second, and $\lambda_1/\Sigma\lambda_k$ shows the ratio of energy in the first principal component as compared to the total energy. The larger these ratios, the better the fields can be represented by the first principal components, and the more coherent is the pattern the fields exhibit. These ratios for the real fields are always larger than those for the imaginary fields, especially those for the internal fields. This means that the internal fields have an intrinsic pattern which is insensitive to both the geometry (different polarizations) and the penetration depth (different periods) of the primary external fields. One

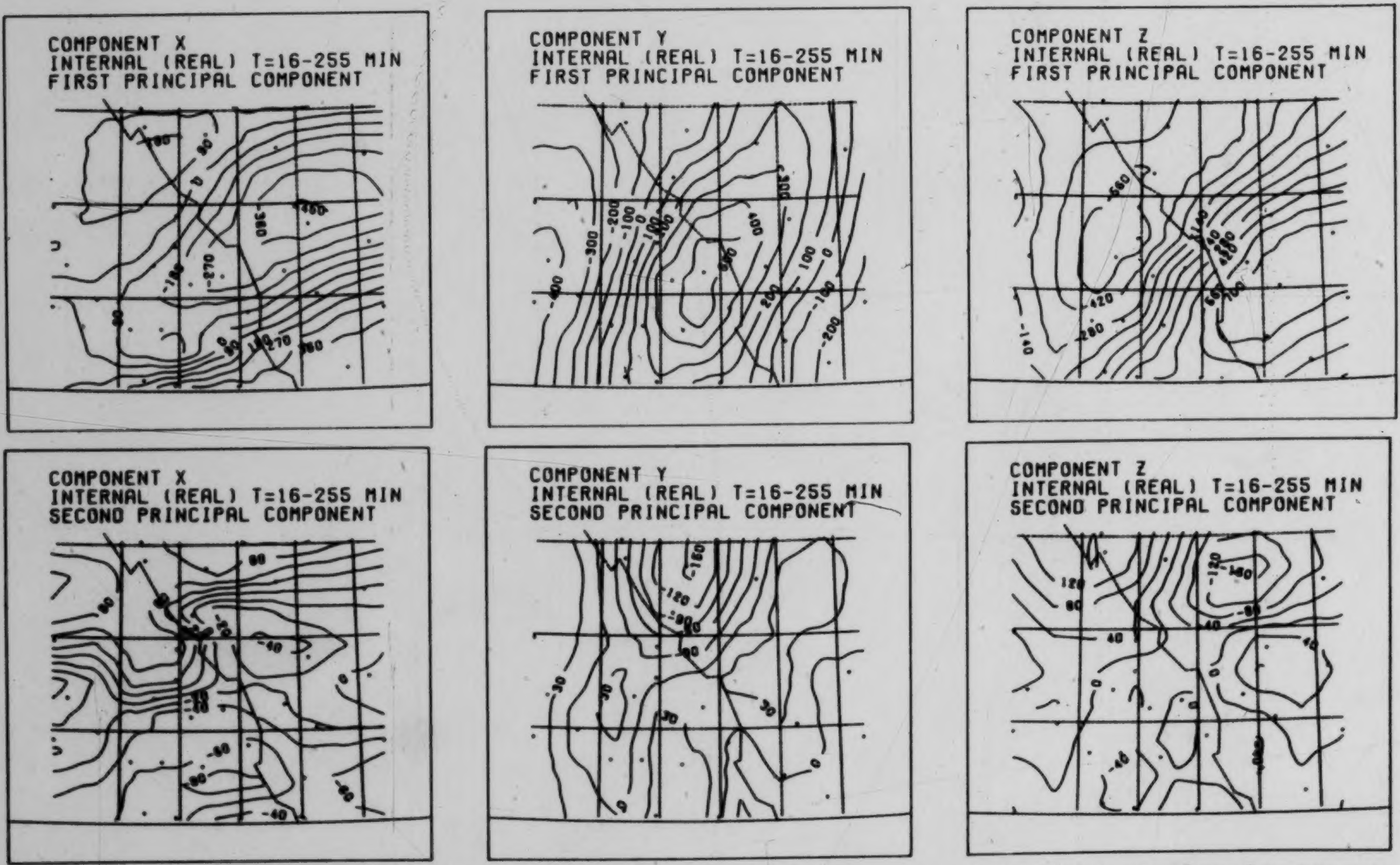
COMPONENT X
INTERNAL (REAL) T=16-255 MIN
FIRST PRINCIPAL COMPONENT
-380
400
-270
-180
270
COMPONENT Y
INTERNAL (REAL) T=16-255 MIN
FIRST PRINCIPAL COMPONENT
-400
-300
-200
-100
0
100
400
300
200
-200
COMPONENT Z
INTERNAL (REAL) T=16-255 MIN
FIRST PRINCIPAL COMPONENT
-560
-420
-280
-140
COMPONENT X
INTERNAL (REAL) T=16-255 MIN
SECOND PRINCIPAL COMPONENT
80
-40
-60
COMPONENT Y
INTERNAL (REAL) T=16-255 MIN
SECOND PRINCIPAL COMPONENT
-150
-120
-90
30
0
COMPONENT Z
INTERNAL (REAL) T=16-255 MIN
SECOND PRINCIPAL COMPONENT
-120
-160
120
80
40
0

Figure 5.18 First two principal components of the internal real Z field of five frequency components analyzed. Notice that the second principal component is much smoother and weaker.

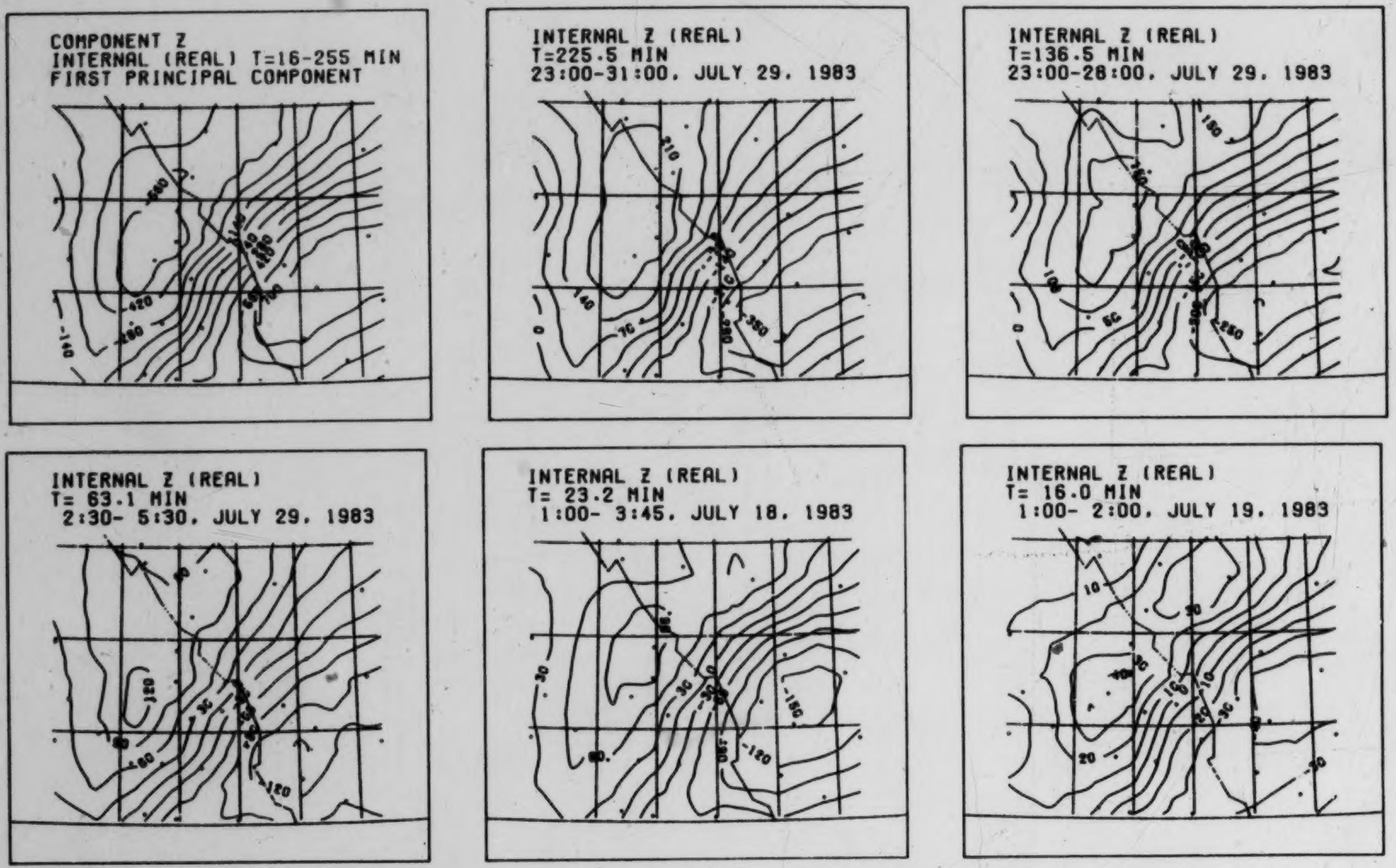
COMPONENT Z
INTERNAL (REAL) T=16-255 MIN
FIRST PRINCIPAL COMPONENT
INTERNAL Z (REAL)
T=225.5 MIN
23:00-31:00, JULY 29, 1983
INTERNAL Z (REAL)
T=136.5 MIN
23:00-28:00, JULY 29, 1983
INTERNAL Z (REAL)
T= 63.1 MIN
2:30- 5:30, JULY 29, 1983
INTERNAL Z (REAL)
T= 23.2 MIN
1:00- 3:45, JULY 18, 1983
INTERNAL Z (REAL)
T= 16.0 MIN
1:00- 2:00, JULY 19, 1983

Figure 5.19 The real Z fields from the 5 periods, which have been taken for the K-L transformation (Fig.5.18), and the first principal component of these.

possible explanation of this is the existance of current channelling phenomenon. As the Earth has finite conductivity everywhere, any magnetovariation fields recorded by an array of detectors must contain contributions from currents induced in conductors beneath the array and from currents induced far from the array. If the latter predominate, the magnetovariation field can be ascribed to currents induced elsewhere and channelled under the array in an elongated conductor.

Such channelled currents appear to be dominant in the Southern Alberta - B.C. (SABC) conductor under the 1983 array. Over a wide period range, 16 to 225 minutes, the separated internal fields show a persistent line current feature. This period range covers a ratio of 3.8 to 1 in the skin depth in a uniform conductor ($=\sqrt{[225/16]}$). If local induction were dominant, the observed fields, especially the separated internal fields, should have shown an obvious dependence of response on period. The K-L transform analysis shows that this is not the case.

As mentioned above, fields produced by locally induced currents always exist. This can be shown from the K-L transform as well. For the total horizontal fields, the ratio (Table 5.10) for real and imaginary components is rather constant, especially for the X fields. This means that the total horizontal components are much less DC-like than the internal horizontal components. However, for the total vertical field, the much larger ratio for the real component is quite similar to that for the internal vertical field. The coherency in the Z fields is nearly the same in both total and internal fields. This is not surprising, since the total horizontal fields are more "normal" (with induction in a layered Earth) and the Z fields are more "anomalous" and so mainly internal. Such characteristics of surface fields commonly observed are consistent with the coherency analysis by K-L transforms.

5.13 INVERSION OF SEPARATED INTERNAL FIELDS OF THE SABC ANOMALY

From the Karhunen-Loeve transform analysis, the non-inductive character of the SABC anomaly is further confirmed. The inversion to a horizontal current sheet in the last chapter indicated that the currents are concentrated in a narrow band across the Canadian Rocky Mountains. These features lead to the conclution that the current producing the SABC anomaly is probably a channelled current in a very narrow conductor. Such anomalous fields have been inverted to 3-D linear currents or constant-width current sheets in free space, using both *LDPNL* and *LSINL* methods. The former is more often used to find a rough model and then *LSINL* is used to refine the model if necessary. Inversions have been carried out with different constraints, data sets and models in an attempt to explore the model space and to evaluate the non-uniqueness of the solutions.

5.13.1 DATA DESCRIPTION

Magnetovariation fields at 10 periods greater than 65 minutes were separated and the internal fields averaged to give the data for inversions. The phase shifting before interpolation was the same as that for the K-L transformation data preparation (section 5.12). This guaranteed that the fields of different periods to be averaged had the same polarities over the survey area as suggested in (5.39). The data interpolation before separation were similar to that for the K-L transformation,, except that the data were interpolated on a finer grid (15 by 15). This makes the choice of data points for inversion more flexible. In separation of these interpolated data, the round-off of shorter wavelength components (chapter 4) was neglected for simplicity. Keeping such terms would change the separation of fields at the surface by less than 3 percent.

Before averaging, the separated fields were biased and normalized. The following procedure was used: (1) add constants to the components to make X positive, Y negative and to give Z zero mean value over the array; (2) normalize the 10 fields to have the same total magnetic field energy. The biasing process (1) has the effect of removing most of any constant field of external origin which cannot be separated from the internal fields. This serves to isolate the internal field which has X positive, Y negative and Z averaged at zero for a NE-SW line current. This biasing procedure is referred to as *PNZ*, Positive-Negative-Zero, biasing. Similarly, the data were also *ZZZ* biased to give different averaged fields. Because of the W_r stabilizing scheme, these averaged fields with different base values should not strongly affect the inversion. However the *PNZ* biasing scheme, despite its advantages noted, does amplify the errors to some degree. Most of the inversion is based on the *PNZ* biased average data, but a comparison with the *ZZZ* biased data is also given for a few cases.

Periods greater than 65 minutes correspond to skin depths greater than 100 km in a uniform half space of conductivity 0.1 S/m. The conductivity in the region is likely to be lower than 0.1 S/m and the skin depth greater than 100 km. The real parts of the *PNZ* averaged fields and their standard deviations are shown in Fig.5.20. The standard deviations for the imaginary fields (not shown) are very large whereas those for the real fields are much smaller. This is consistent with the assumption of a non-inductive current, which should have no significant out-of-phase components.

The reason for choosing this band of very long-period fields is that they will give negligible mutual induction between the channelled current in the line conductor and the surrounding medium. From both chapter 4 and the argument of Jones (1986) the relative importance of induction and channelling depends on the quantity $\mu_0\omega\sigma$ and the characteristic squared wavenumber of the field ν^2. The

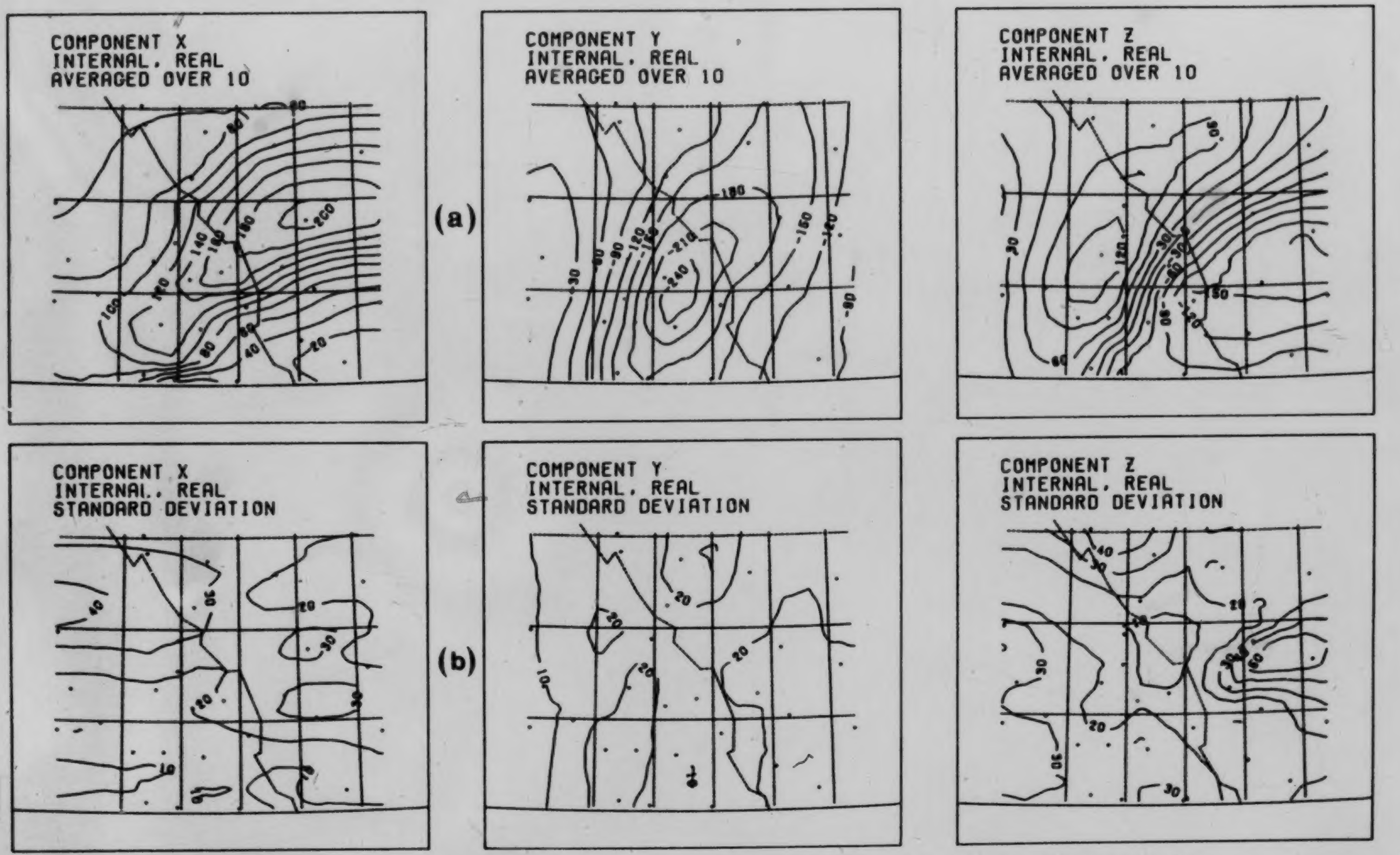
COMPONENT X
INTERNAL, REAL
AVERAGED OVER 10
COMPONENT Y
INTERNAL, REAL
AVERAGED OVER 10
COMPONENT Z
INTERNAL, REAL
AVERAGED OVER 10
(a)
COMPONENT X
INTERNAL, REAL
STANDARD DEVIATION
COMPONENT Y
INTERNAL, REAL
STANDARD DEVIATION
COMPONENT Z
INTERNAL, REAL
STANDARD DEVIATION
(b)

Figure 5.20 (a)*PNZ* averaged internal field from 10 periods (66.7≤T≤225.5 min.);
(b)standard deviation of the averaged data.

induction effect is negligible when

$$(5.40) \qquad \mu_0 \omega \sigma << \nu^2$$

or

$$(5.40a) \qquad \sigma << 300T/\lambda^2$$

in which, σ (in S/m) is the conductivity of the host medium, T is the period in minutes and λ (in km) is the characteristic wavelength. For the field considered here, T=65 minutes, λ=300 km, and (5.40a) requires

$$\sigma << 0.217 \text{ S/m}$$

which is readily satisfied in southern Alberta, southern British Columbia and in most geologic settings.

5.13.2 INVERSION WITH LOOSE CONSTRAINTS ON DEPTH

The fields were inverted to a line current model with 6 nodes under the area covered by the array and 2 nodes outside the array on each side. The constraints on the horizontal positions of nodes are plotted in Fig.5.21. For the 6 nodes inside the survey area these are about 30 km by 100 km strips perpendicular to and centered on the zero contour of the Z field. The constraints on the depths of nodes are loose: intermediate nodes are confined in the

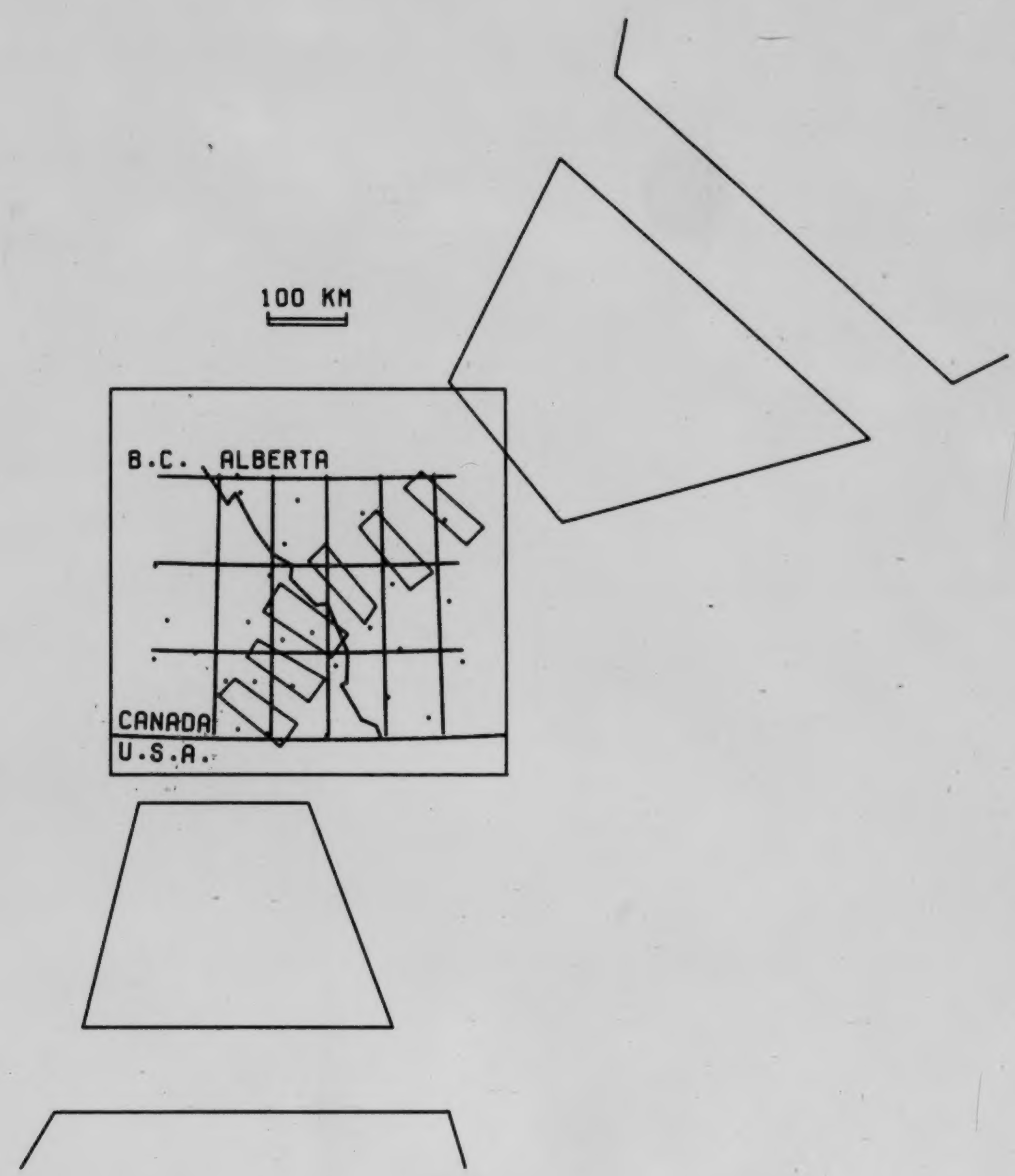
100 KM
B.C.
ALBERTA
CANADA
U.S.A.

Figure 5.21 Constraints on horizontal positions of nodes. For the 6 nodes inside the survey area, the horizontal positions are restricted to fall within the 6 strips, approximately 30 by 100 km.

depth range 20 to 120 km, the two end nodes in the depth range 20 to 900 km, and the two next to the ends 20 to 500 km. The constraints for the 4 nodes outside the survey area are looser in both horizontal (Fig.5.21) and vertical dimensions because of higher uncertainty of these parameters. The model sought is expected to be smooth, therefore the 6 inside nodes, in addition, are constrained to change X and Y coordinates monotonically.

Figs.5.22 and 5.23 show the fields inverted to a line current of 10 nodes, with 31 parameters. The data are from the *PNZ* biased average fields, at 3 by 3 data points, 27 data. This is an underdetermined case and the *LDPNL* method was used. The starting model followed the north-western edge of the constraint strips at 90 km depth. After 8 iterations the solution stabilized (changes to coordinates of each node were less than 3 km). The estimated depths of the middle nodes are in the range 75 - 113 km. The overall fit and the tilting plane normal fields finally resolved are listed in Table 5.11.

Table 5.11

	total field	X	Y	Z
R(δB)	0.382	0.352	0.232	0.297
R(ΔB)	0.340	0.304	0.171	0.285
R(δ/ΔB)	1.156	1.075	1.163	1.021
correlation		0.837	0.887	0.955
normal field		-18.2-0.08X	-21.1+0.17Y	8.9

The overall misfit (Table 5.11) is larger than the error in

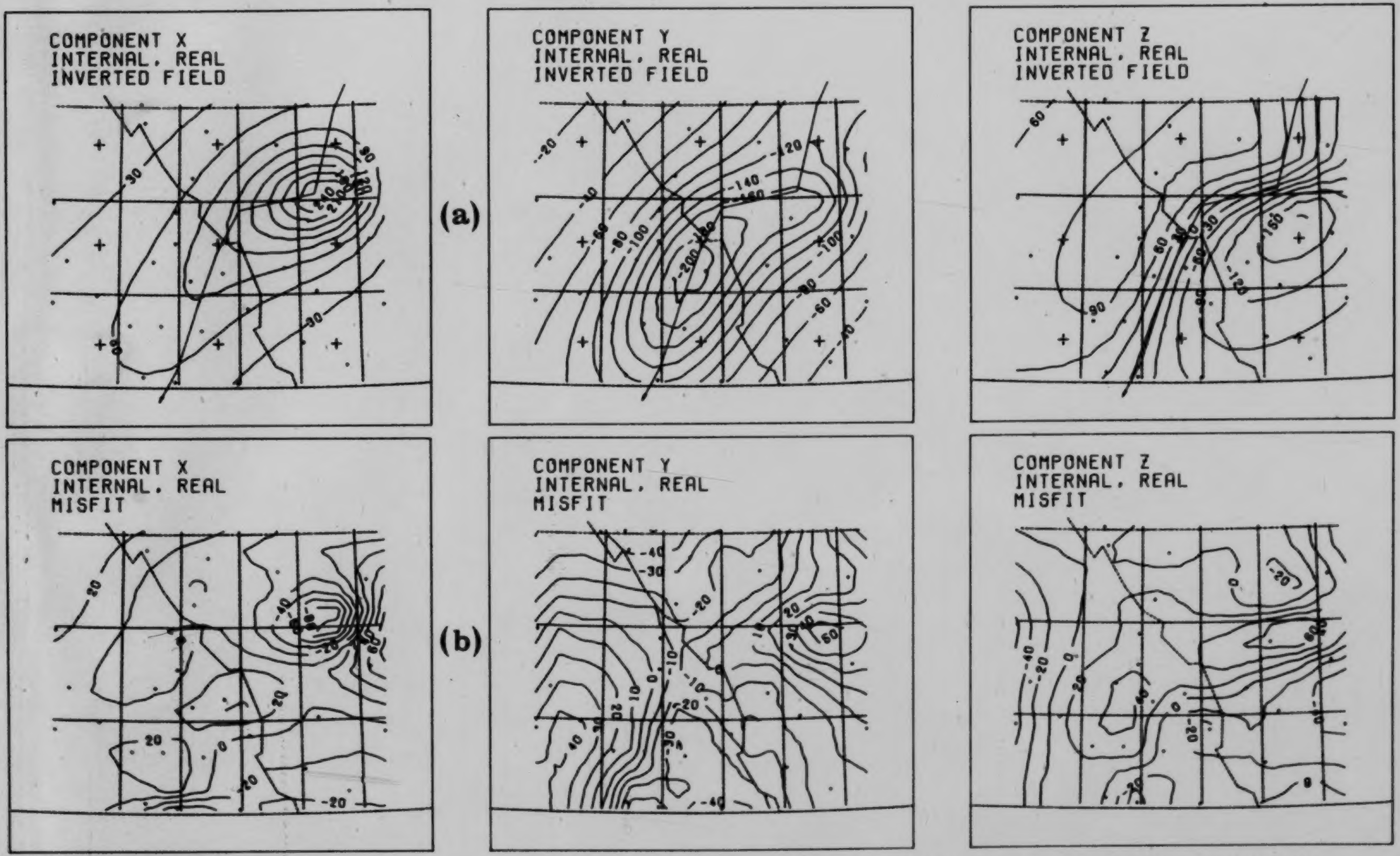
COMPONENT X
INTERNAL, REAL
INVERTED FIELD
COMPONENT Y
INTERNAL, REAL
INVERTED FIELD
COMPONENT Z
INTERNAL, REAL
INVERTED FIELD
(a)
COMPONENT X
INTERNAL, REAL
MISFIT
COMPONENT Y
INTERNAL, REAL
MISFIT
COMPONENT Z
INTERNAL, REAL
MISFIT
(b)

Figure 5.22 The fields of Fig.5.20 have been inverted to a 10 node model by the *LDPNL* method. The 9 grid points are marked, and the resolved current is projected on the map. A tilting plane normal field is added to the data to stabilize the inversion. (a)inverted fields; (b)misfit.

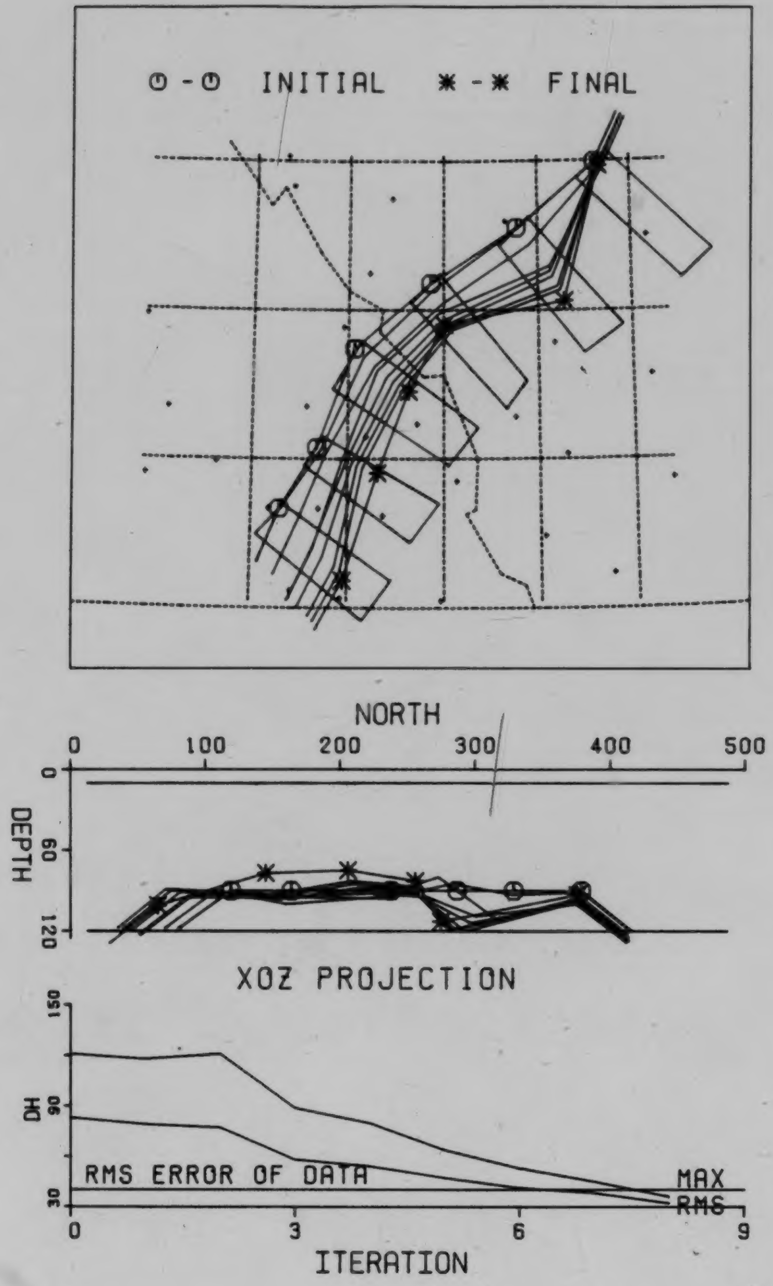

Figure 5.23 Iteration process for the *LDPNL* inversion in Fig.5.22.

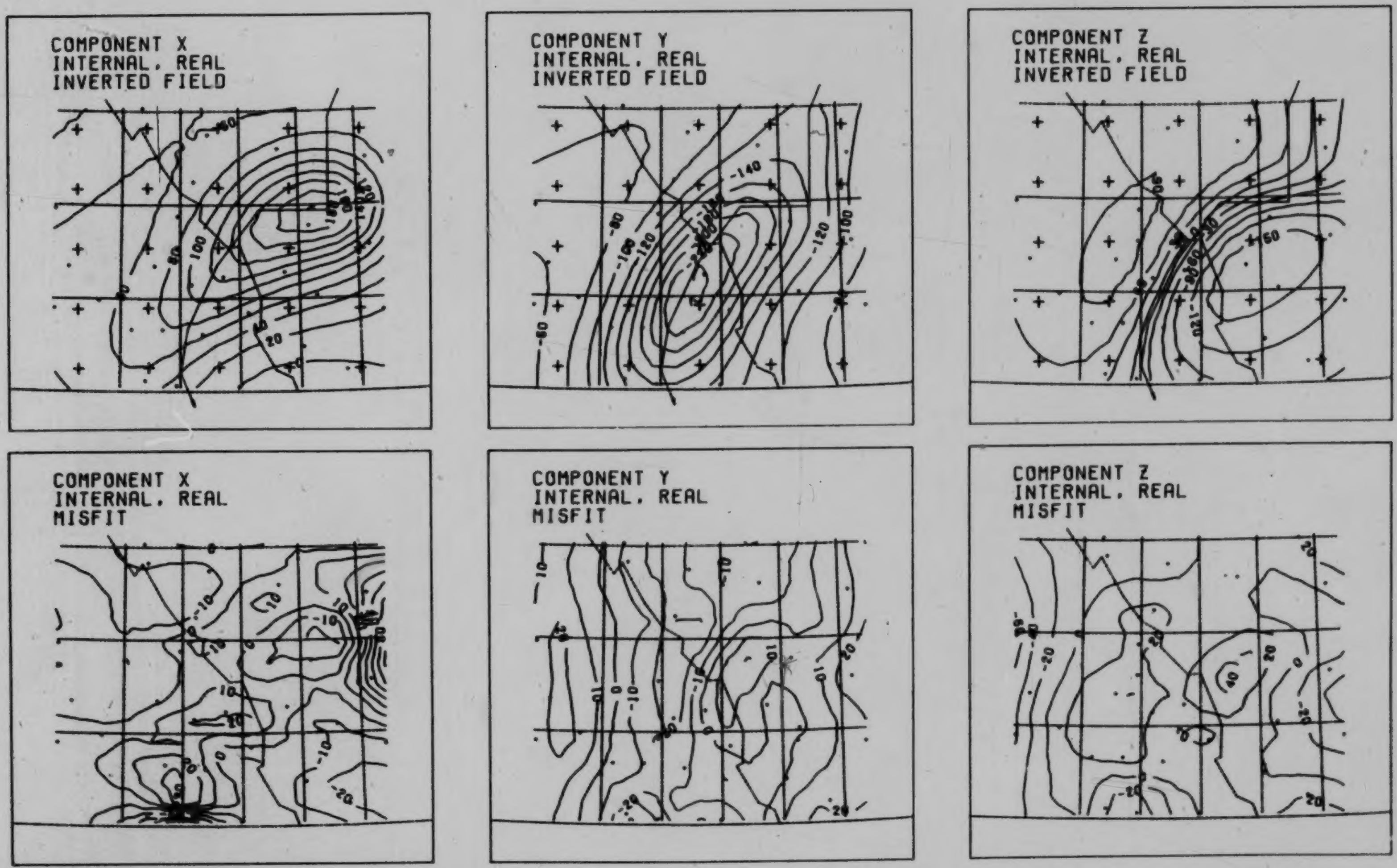
COMPONENT X
INTERNAL, REAL
INVERTED FIELD
COMPONENT Y
INTERNAL, REAL
INVERTED FIELD
COMPONENT Z
INTERNAL, REAL
INVERTED FIELD
COMPONENT X
INTERNAL, REAL
MISFIT
COMPONENT Y
INTERNAL, REAL
MISFIT
COMPONENT Z
INTERNAL, REAL
MISFIT

Figure 5.24 Same as Fig.5.22, but with the *LSINL* method, the initial model is the best model achieved by the *LDPNL* method, Figs.5.22 and 5.23.

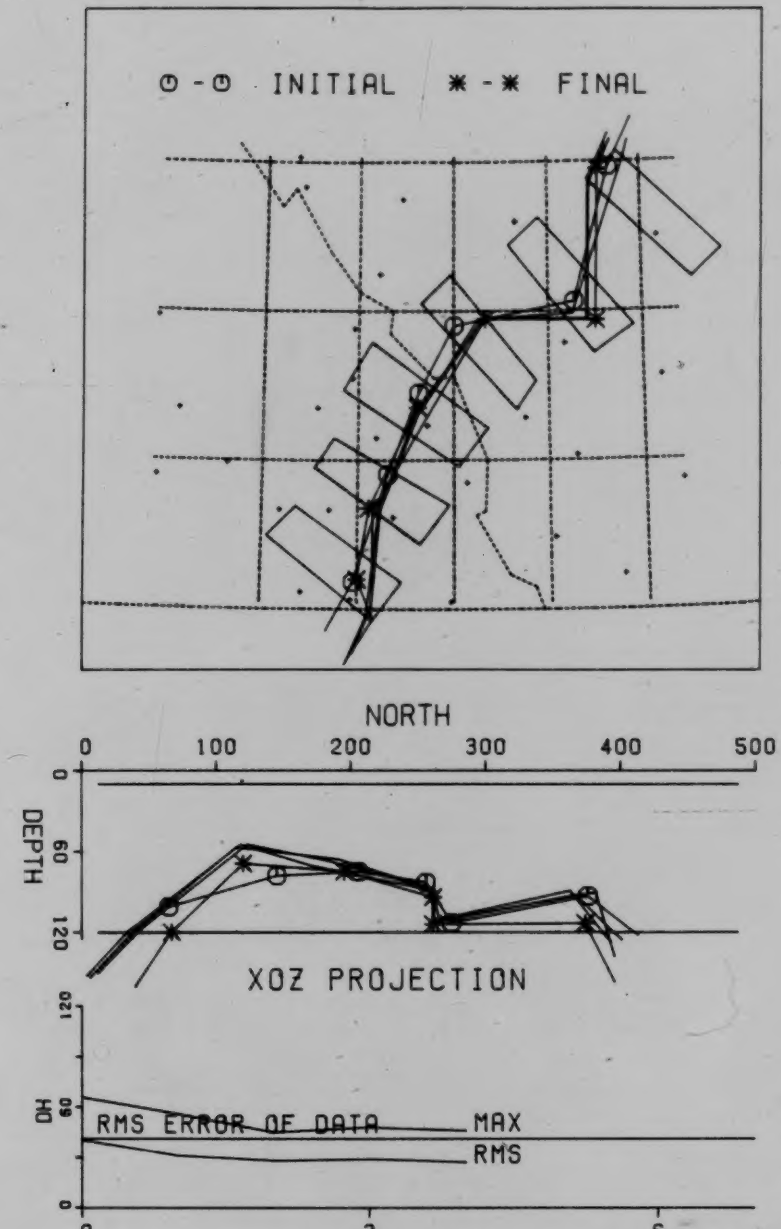

Figure 5.25 Iteration process for the *LSINL* inversion in Fig.5.24. See also Fig.5.22.

the data.

With 5 by 5 data points, 75 data, the fields are inverted to a 10 node model with the *LSINL* method (Figs.5.24 and 5.25, and Table 5.12). The starting model is taken as the best model achieved by ~~the above *LDPNL*~~ method. After 4 iterations the best model was achieved. The estimated depths of the middle nodes are between 69 and 120 km. This model overfits the data, with the R(δ/ΔB) factor 0.777.

The two models have some common features. The nodes south-west of the Canadian Rockies are shallower. Crossing the Rockies, the current plunges and makes a sharp bend towards the east.

Table 5.12

	total field	X	Y	Z
R(δB)	0.246	0.181	0.116	0.245
R(ΔB)	0.292	0.275	0.147	0.287
R(δ/ΔB)	0.777	0.812	0.889	0.924
correlation		0.952	0.967	0.970
normal field		-36.2+0.04X	-45.9+0.19Y	-0.4

5.13.3 INVERSION WITH CONSTRAINTS IN FAVOUR OF SHALLOWER MODELS

In an attempt to bring the model closer to the surface, the constraints were changed to give shallower depth ranges. Only the results of the iteration process are shown in Fig.5.26. The middle nodes are confined in the depth range 10 to 40 km. With 3 by 3 data points, 27 data from the *PNZ* biased fields, an initial model along the north-western edge of the constraint strips, and an initial depth of 30 km, *LDPNL* inversion stabilized after 7 iterations. Fig.5.26 shows that the model gives a poor fit to the data and the root-mean-square misfit in the total field is about three times as large that of the error in the data. To refine the model further with *LSINL* was hopeless and has not been attempted.

Constraining the current in the linear conductor to be weaker than the current resolved in the best-fitting model can also bring the inverted current to a shallower depth. With the *PNZ* biased data, and the current constrained to be 66 percent of the best-fitting *LSINL* inverted model, 5 by 5 data points were inverted by the *LSINL* method (Figs.5.27 and 5.28, and Table 5.13). The estimated depths of the middle nodes are 47 to 120 km. With 5 by 5 points of the *ZZZ* biased data, and current of 55 per cent, *LSINL* gives somewhat different model (Figs.5.29 and 5.30, and Table 5.14). The estimated depths of the middle nodes are 48 to 118 km. These inversions give shallower models and the misfit is not too

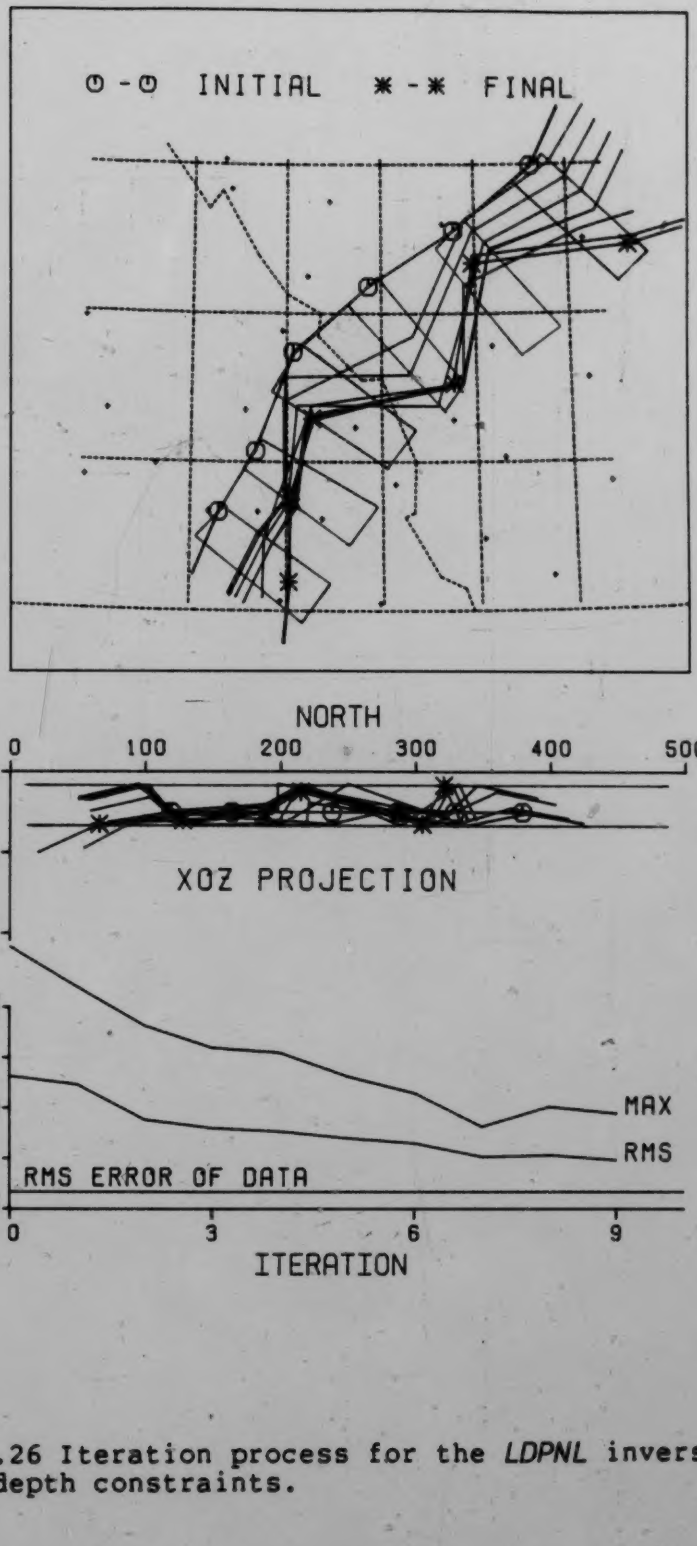

Figure 5.26 Iteration process for the *LDPNL* inversion with shallow depth constraints.

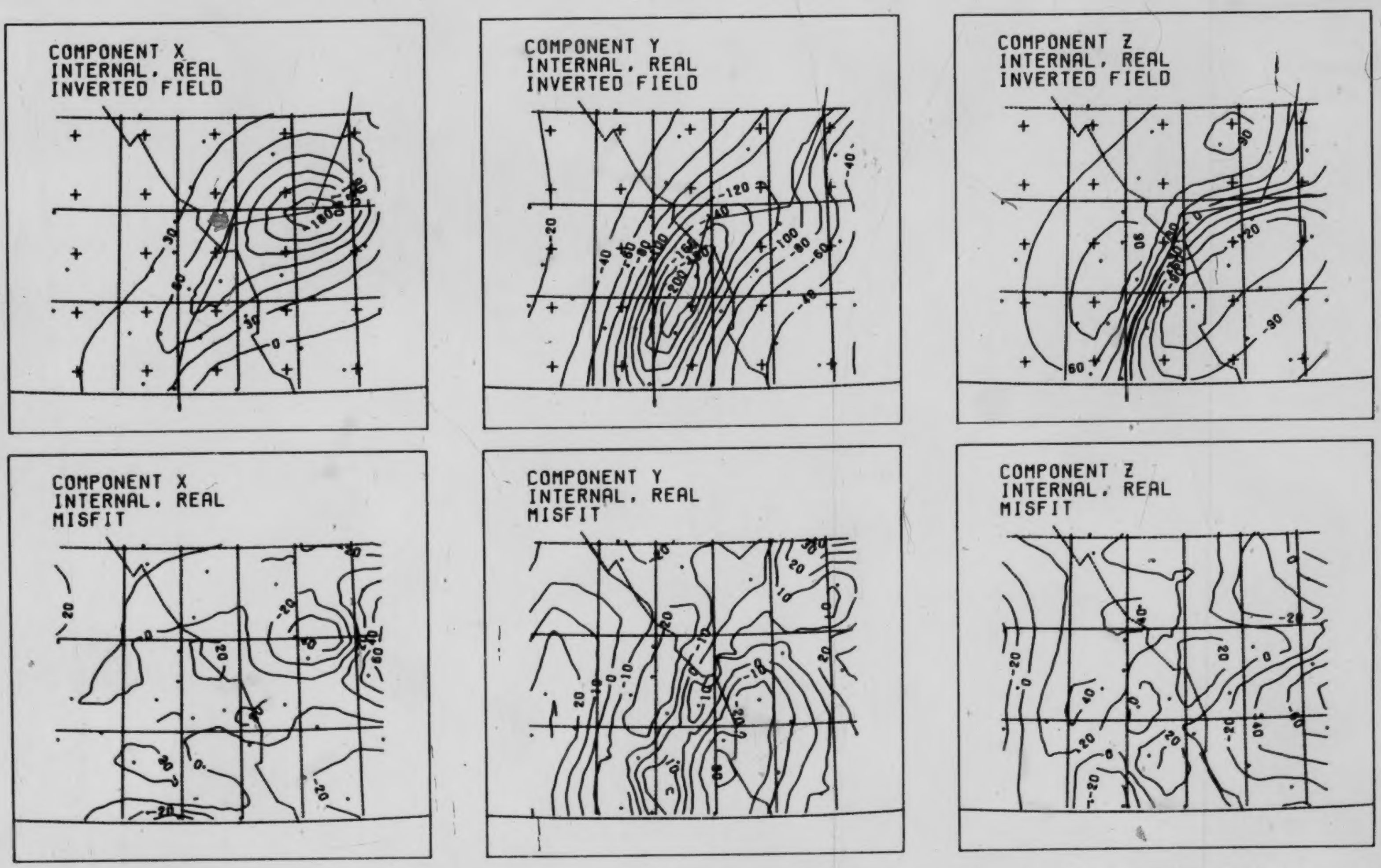
COMPONENT X
INTERNAL, REAL
INVERTED FIELD
COMPONENT Y
INTERNAL, REAL
INVERTED FIELD
COMPONENT Z
INTERNAL, REAL
INVERTED FIELD
COMPONENT X
INTERNAL, REAL
MISFIT
COMPONENT Y
INTERNAL, REAL
MISFIT
COMPONENT Z
INTERNAL, REAL
MISFIT

Figure 5.27 Inversion with weak (66 percent) current constraint using the *LSINL* method.

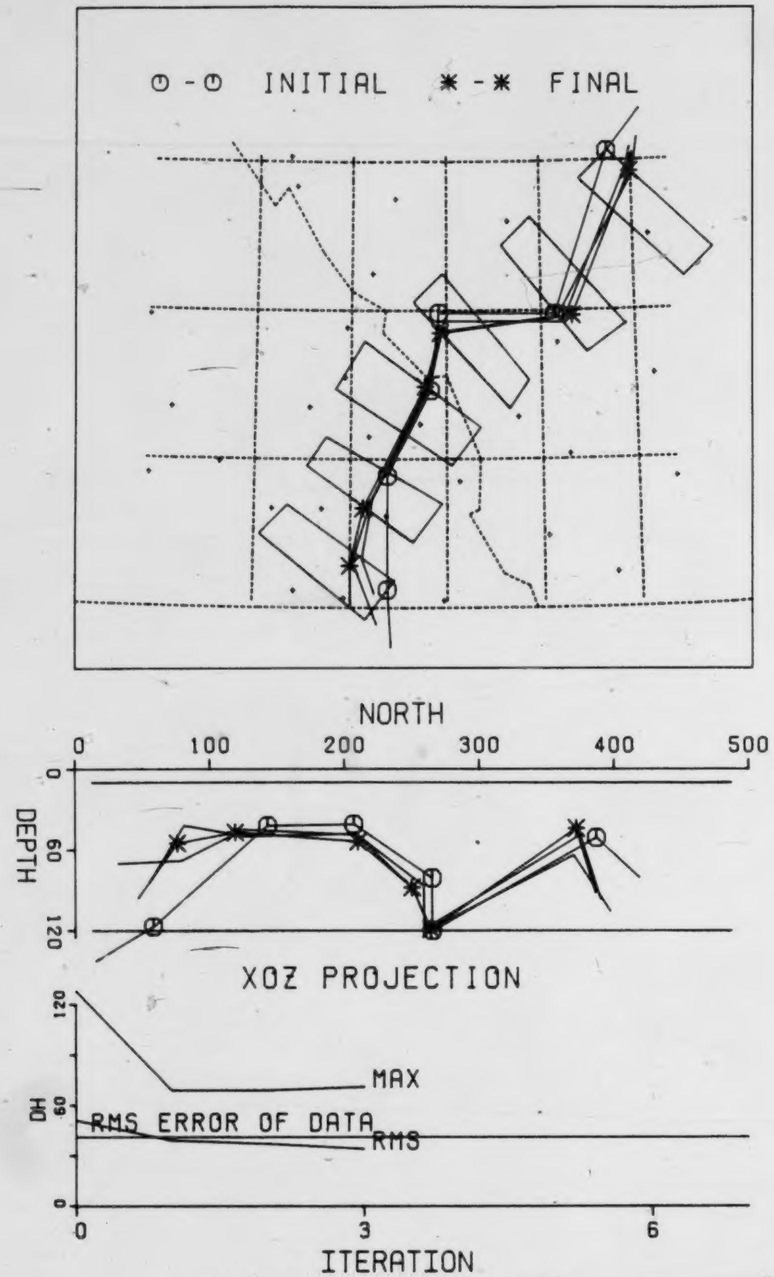

Figure 5.28 Iteration process for the *LSINL* inversion in Fig.5.27.

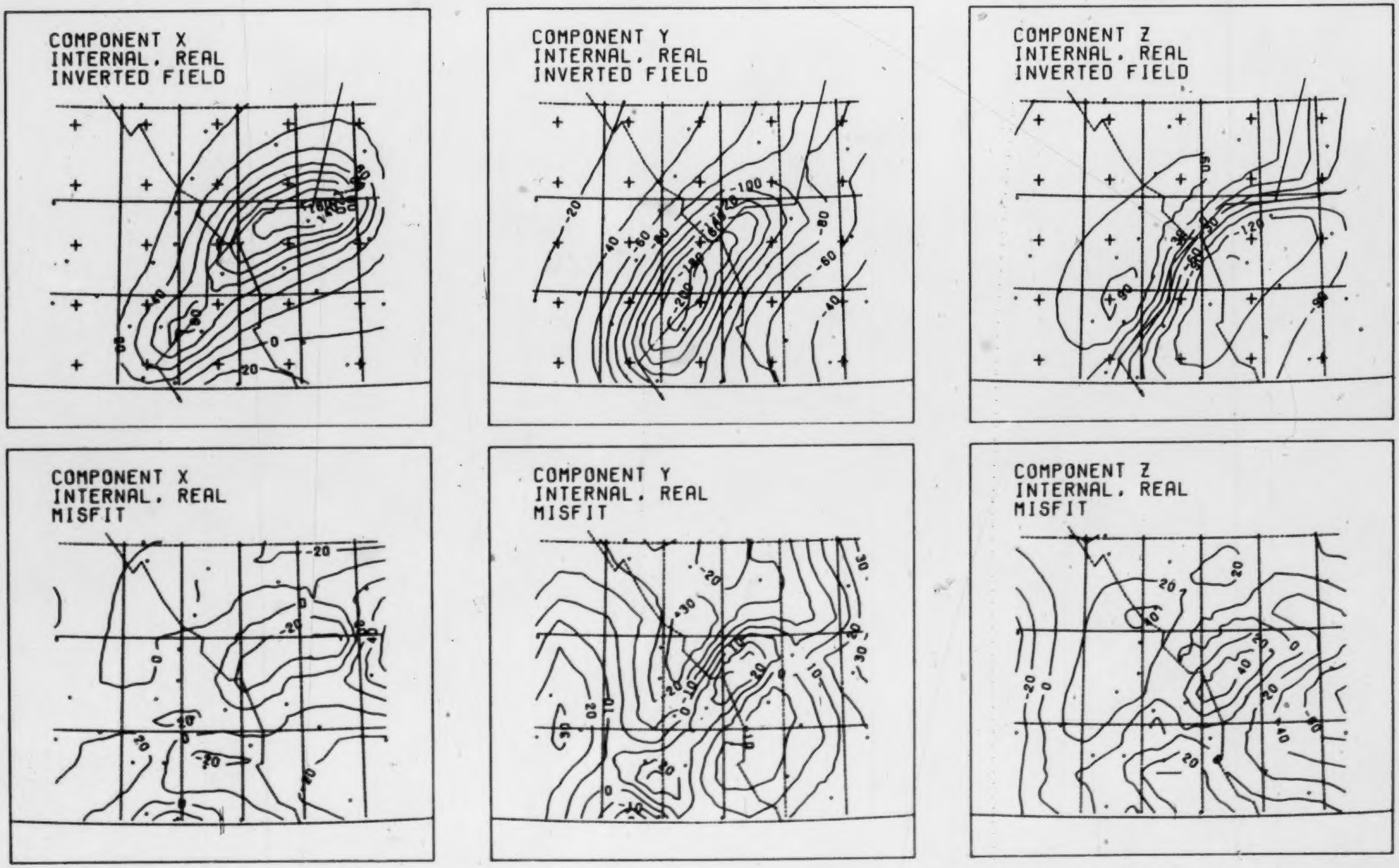
COMPONENT X
INTERNAL, REAL
INVERTED FIELD
COMPONENT Y
INTERNAL, REAL
INVERTED FIELD
COMPONENT Z
INTERNAL, REAL
INVERTED FIELD
COMPONENT X
INTERNAL, REAL
MISFIT
COMPONENT Y
INTERNAL, REAL
MISFIT
COMPONENT Z
INTERNAL, REAL
MISFIT

Figure 5.29 Inversion with weak (55 per cent) current constraint, the *LSINL* method was used with data from the *ZZZ* biased set.

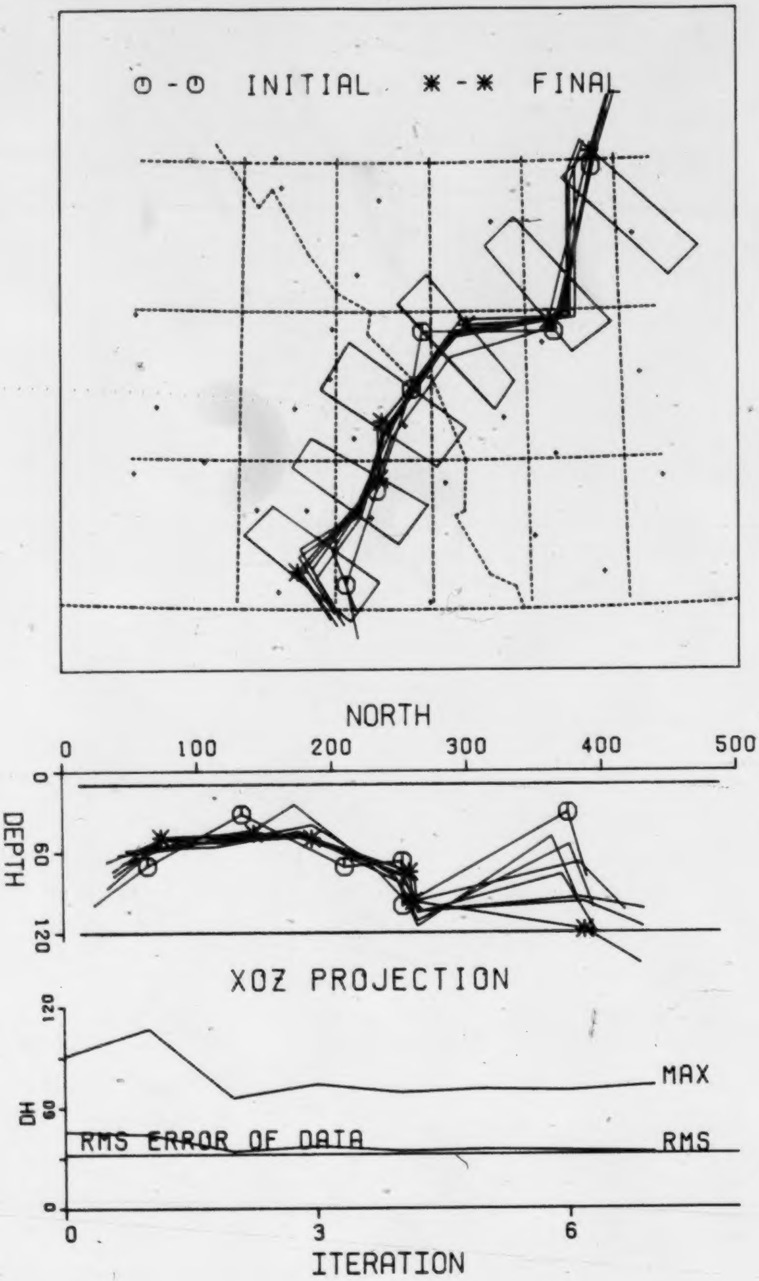

Figure 5.30 Iteration process for the *LSINL* inversion in Fig.5.29.

large when compared to the absolute error in the data. The $R(\delta/\Delta B)$ factor is 0.95 for the inversion with the *PNZ* data and 1.17 for the inversion with the *ZZZ* data. Such measures of fit cannot be evaluated alone. Notice that the relative errors in the data now become large, 0.476 and 0.582 respectively, because the fields to be fitted are weaker. The fields to be fitted are weakened by a normal field resolved by the W_r vector which weakens the original data to make a weak current model fitting the data better. The current inverted at each iteration is at the maximum current allowed by the current constraint, suggesting that the these constraints modify the solution to accommodate a model with less current at shallower depth. The models determined from such relatively noisy data must be evaluated with great caution.

Table 5.13

	total field	X	Y	Z
R(δB)	0.423	0.312	0.203	0.298
R(ΔB)	0.476	0.379	0.215	0.286
R(δ/ΔB)	0.950	0.908	0.972	1.021
correlation		0.909	0.946	0.961
normal field		-47.4-0.04X	1.5+0.19Y	5.5

Table 5.14

	total field	X	Y	Z
R(δB)	0.624	0.370	0.216	0.308
R(ΔB)	0.582	0.308	0.158	0.284
R(δ/ΔB)	1.170	1.095	1.171	1.042
correlation		0.891	0.932	0.955
normal field		45.7-0.07X	-107.0+0.16Y	-8.2

5.13.4 INVERSION TO CURRENT SHEET OF CONSTANT WIDTH

A sheet current of constant width is probably a more realistic model. The weak current constraint, 55 per cent of best-model line current, is again imposed. The width of the sheet is constrained between 20 and 80 km. A current sheet wider than 80 km would not be compatible with the horizontal current sheet inversion in chapter 4, and too narrow a sheet would be hardly any different from a linear current. The inversions to a sheet current occasionally give (during iterations) widths below 80 km. The final sheet current models almost always converge on an 80 km width. From the test model 2 (section 5.11.2), the width of the sheet can be reasonably inverted but sheets of different widths do not change the surface fields very much. Therefore, the constraints on the width are not changed and the estimated width, 80 km, is believed to be a fair estimate of the actual width of the current sheet.

The data are 5 by 5 points from the *PNZ* biased set, and the initial model is the best-fitting sheet model (not shown)

Table 5.15

	total field	X	Y	Z
$R(\delta B)$	0.449	0.341	0.304	0.309
$R(\Delta B)$	0.485	0.377	0.283	0.287
$R(\delta/\Delta B)$	1.021	0.951	1.037	1.038
correlation		0.907	0.927	0.954
normal field		$-51.0-0.03X$	$27.7+0.20Y$	-1.5

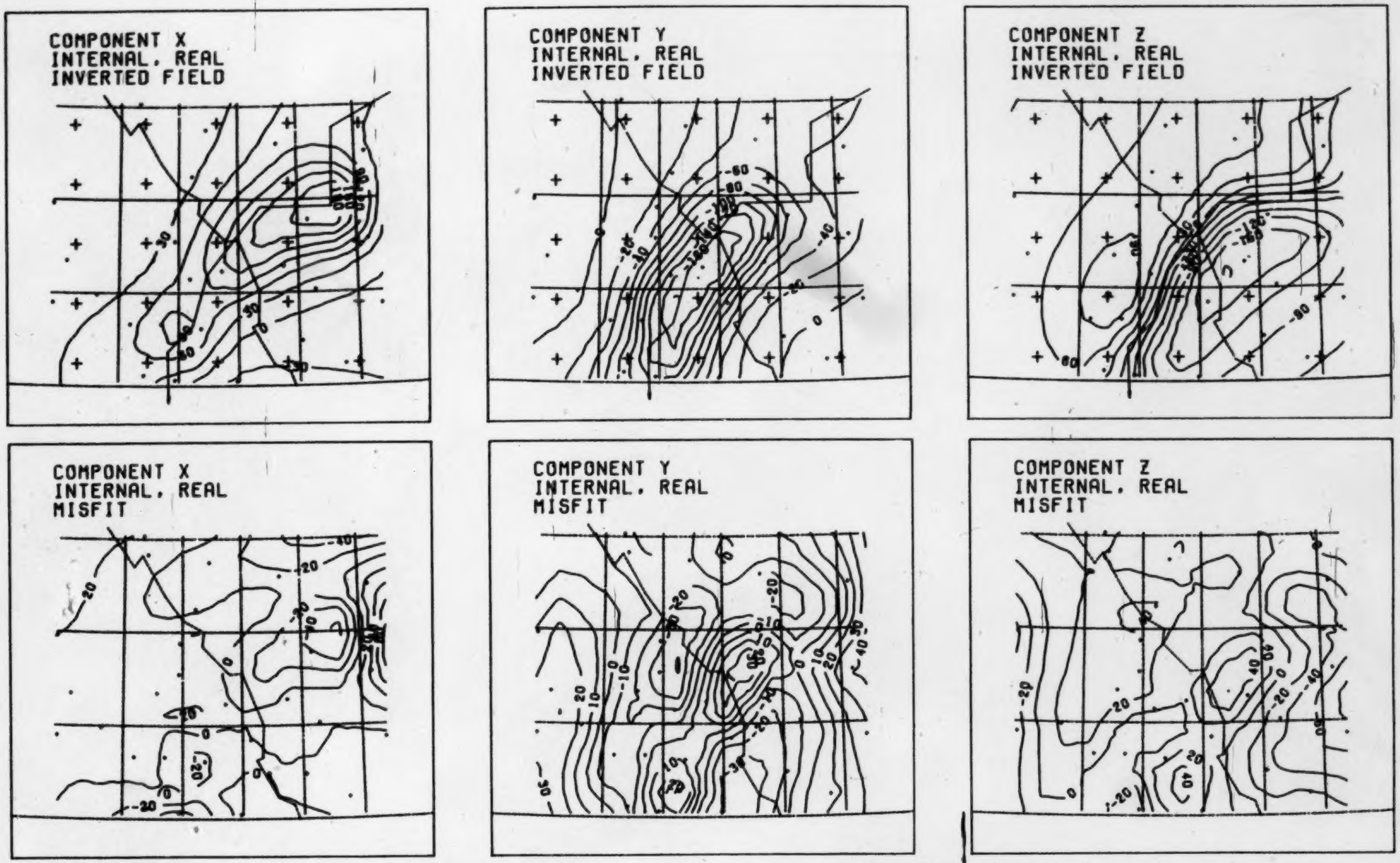
COMPONENT X
INTERNAL, REAL
INVERTED FIELD
COMPONENT Y
INTERNAL, REAL
INVERTED FIELD
COMPONENT Z
INTERNAL, REAL
INVERTED FIELD
COMPONENT X
INTERNAL, REAL
MISFIT
COMPONENT Y
INTERNAL, REAL
MISFIT
COMPONENT Z
INTERNAL, REAL
MISFIT

Figure 5.31 With weak (55 percent) current constraint the *PNZ* biased data have been inverted to a 10 node sheet current of width 80 km (constrained between 20 and 80) using the *LSINL* method.

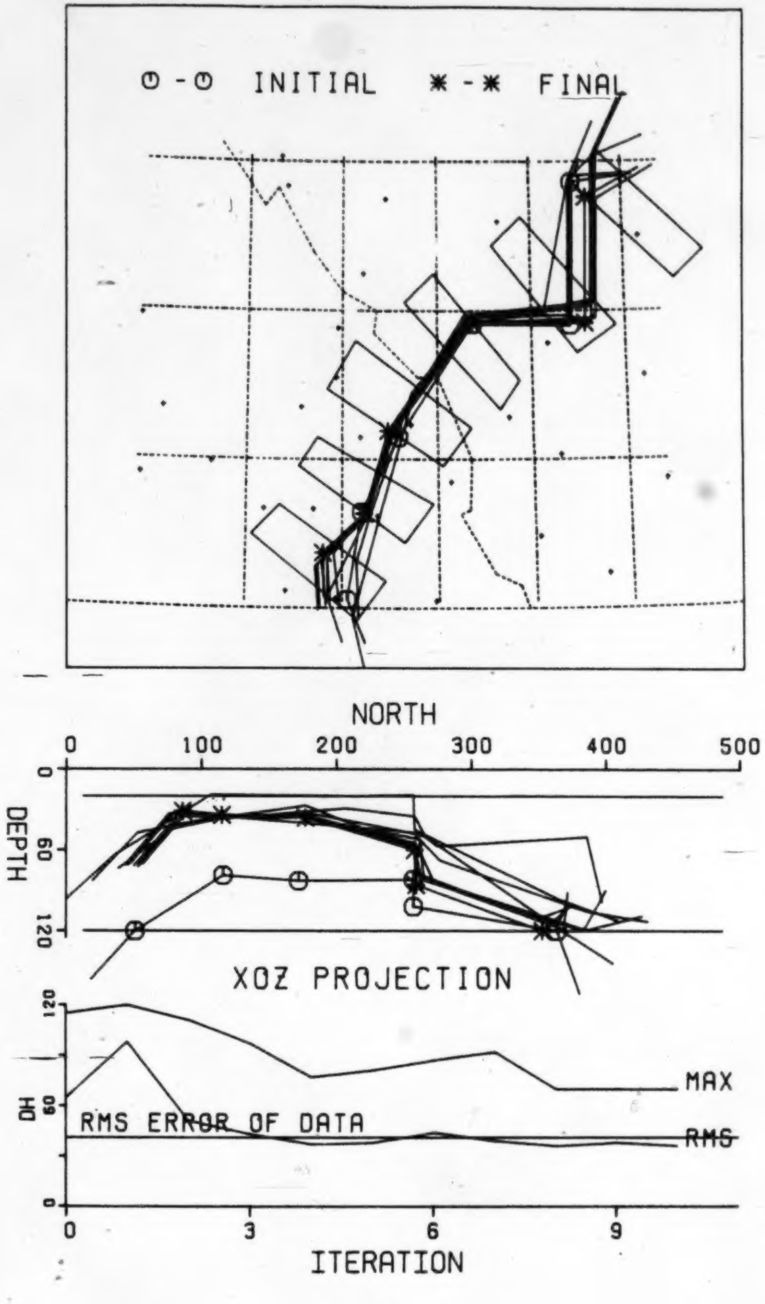

Figure 5.32 Iteration process for the sheet current inversion in Fig.5.31.

obtained with the *LSINL* method. Since the current is constrained to be weaker, the inverted model is expected to be shallower (Figs.5.31 and 5.32 and Table 5.15). The resolved depths of the 6 inside nodes (from south to north) are 32, 35, 37, 60, 87 and 120 km, and are considerably shallower than any of the results of the above inversions. The features of the nodal positions noted in section 5.13.2 remain: the southern nodes are at shallower depths, and the current makes a bend towards the east in the north-east quadrant of the survey area.

5.13.5 INVERSION WITH OTHER MODELS AND DATA SETS

Inversion with different data sets and different models have been attempted. With the above *PNZ* biased average fields, in the period range 65-225 minutes, a 5 nodes model is fitted to the data with weak (55 percent of optimum line current) current constraints. The inverted constant-width sheet-current model is presented in Figs.5.33 and 5.34 and Table 5.16. The overall features of this simple model resemble those noted for the 10 nodes model inverted with the same constraints on current intensity and sheet width (see Figs.5.31 and 5.32). Of the three intermediate nodes, the two to the west are at shallower depths, 32 and 55 km, and the one to the east becomes deeper, 77 km. The bend, after crossing the Rockies, to the east is still an obvious feature.

Table 5.16

	total field	X	Y	Z
$R(\delta B)$	0.484	0.331	0.258	0.325
$R(\Delta B)$	0.560	0.423	0.254	0.286
$R(\delta/\Delta B)$	0.999	0.885	1.009	1.065
correlation		0.913	0.936	0.949
normal field		-32.5-0.15X	21.0+0.18Y	5.2

Some 33 separated internal fields, with periods in the range 16.5 to 37.0 minutes, are averaged (ZZZ biased) to form another data set for the inversion. A 5 nodes sheet current model (not shown) with weak current constraints (55 percent), inverted with the *LSINL* method, closely resembles

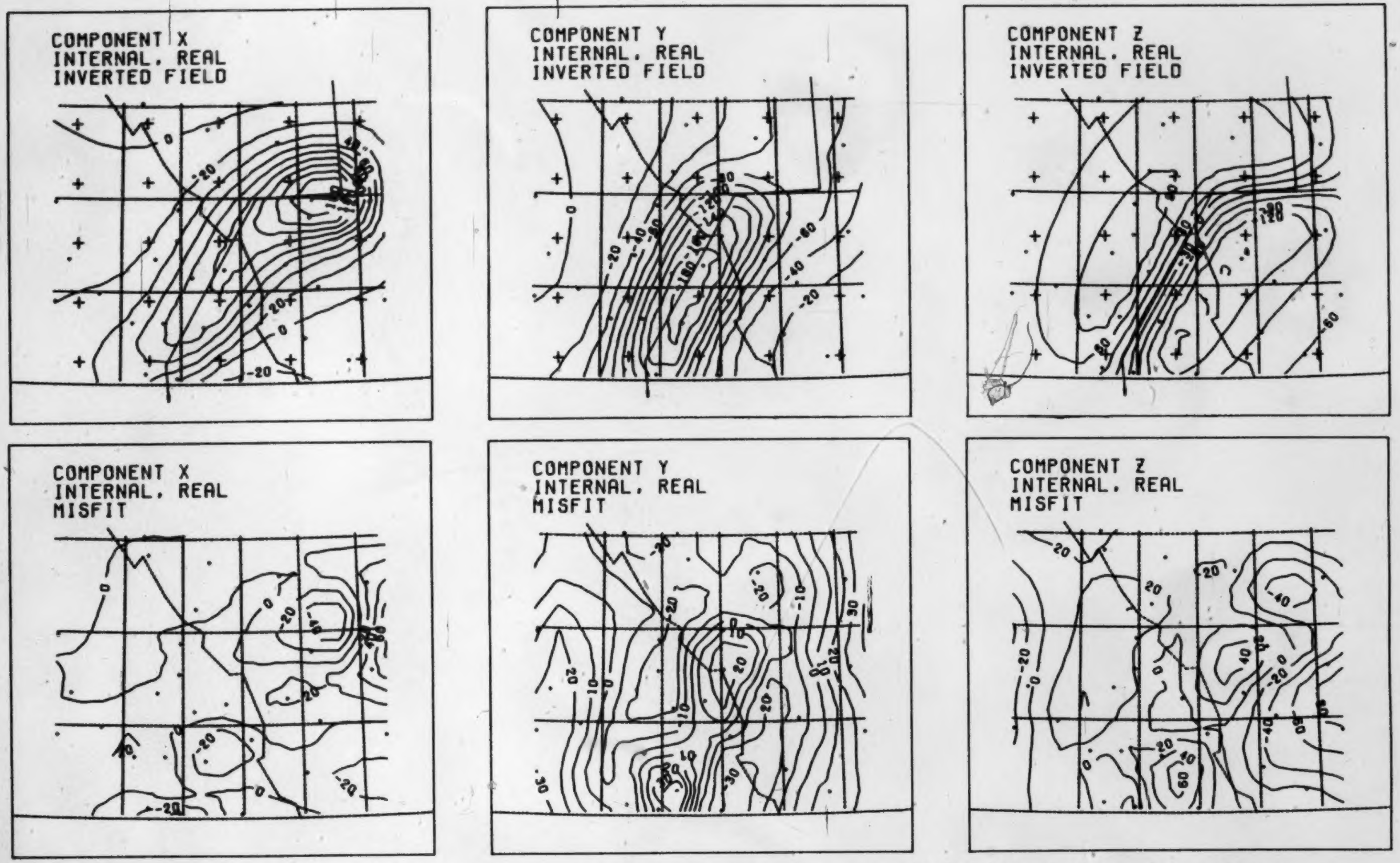
COMPONENT X
INTERNAL, REAL
INVERTED FIELD
COMPONENT Y
INTERNAL, REAL
INVERTED FIELD
COMPONENT Z
INTERNAL, REAL
INVERTED FIELD
COMPONENT X
INTERNAL, REAL
MISFIT
COMPONENT Y
INTERNAL, REAL
MISFIT
COMPONENT Z
INTERNAL, REAL
MISFIT

Figure 5.33 With weak (55 percent) current constraint the *PNZ* biased data have been inverted to a 5 node sheet current of 80 km width (constrained between 20 and 80) using the *LSINL* method.

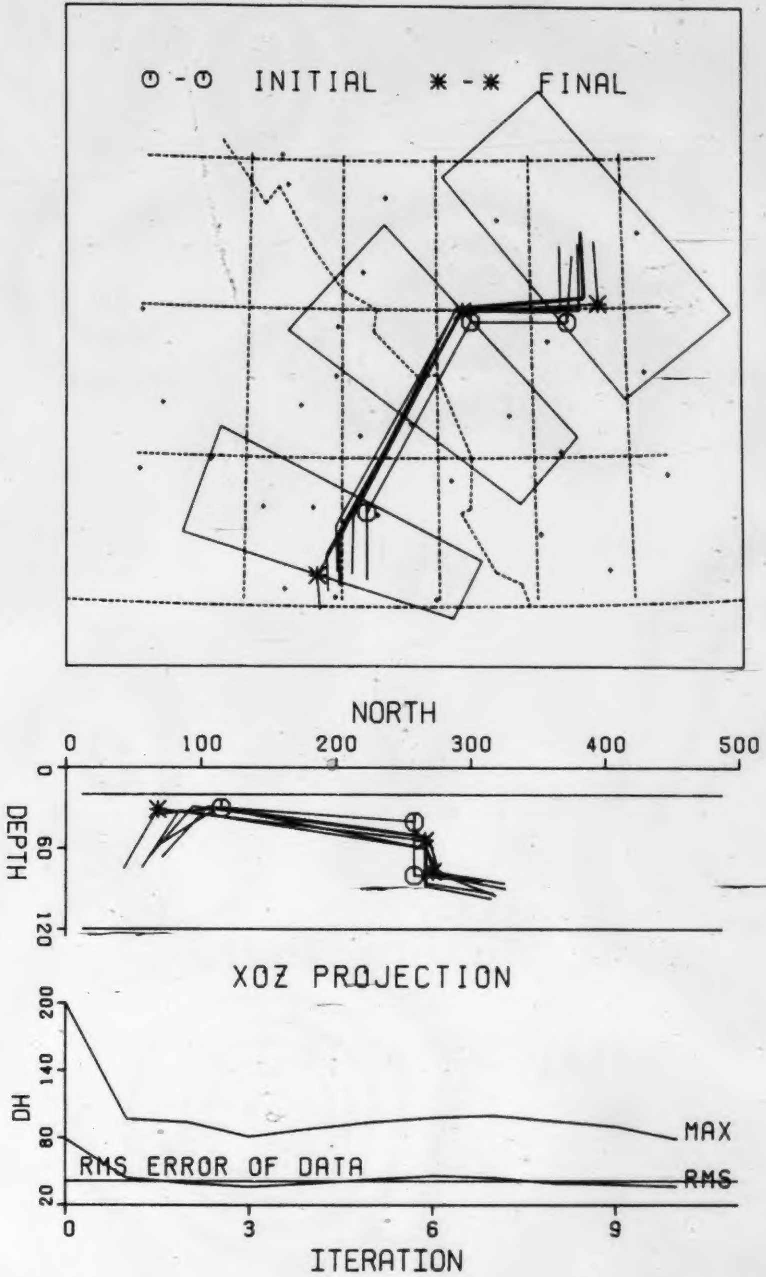

Figure 5.34 Iteration process for the sheet current inversion in Fig.5.33.

the model inverted with the data averaged over longer period fields (Figs.5.33 and 5.34). All previously noted major features of the current remain unchanged. The three intermediate nodes are at slightly greater depths, 39, 66 and 94 km, compared to 32, 55 and 77 km of the model inverted from fields of longer periods. These greater depths show the relative deepening effects (section 5.13.1) on the model inverted from shorter-period fields. The opposite effects, that some shallower depths would be inverted from shorter-period data, are expected for fields dominated by local induction, because currents *induced* by fields of shorter periods are closer to the surface. Therefore this deeper model inverted from shorter-period fields again confirms that the observed anomaly is dominated by channelled currents.

5.14 SUMMARY OF THE GEOMETRY OF THE CURRENT CHANNEL

The resolved depth of the line current is greater than the axis of the current concentration for two reasons. The spreading of actual current tends to bias the inverted current to a greater depth. Further, the mutual induction of the current channel and the surrounding rock shields the field of the channelled current. The effect of the shielding is to smooth out the spatial gradient of the field of the current, and this effect is compensated in the inversion by placing the equivalent line current at a greater depth. The two biasing effects above work in the same sense and add together to overestimate the depth of the actual current. From the test models 2 and 3, in which only the effect of spreading of currents was examined, this deepening effect is not too obvious. The effect of a conducting Earth on the inverted depths of the channelled currents is difficult to test by means of synthesized data. It is expected, however, that such an effect will be less important for fields of longer periods (section 5.13.1). The slightly deepening effect for the model inverted from shorter-period fields (section 5.13.5) implies that the rocks surrounding the current channel have very low conductivity.

The inverted depths for the middle nodes of the current channel (both line and sheet model), are in the range 32 to 120 km. The best-fitting models of various reasonable inversions are depicted in Fig.5.35. The actual depth, because of the biasing effects, may be slightly shallower. The current segments are roughly divided into two groups by the Rocky Mountain Ranges. South-west of the mountains the current is shallower, in the depth range 32 to 90 km, and north-east of the mountain deeper and in the range 70 to 120 km. The maximum depths of nodes in some cases are controlled by the constraints. Relaxing the depth constraints might make the depths of north-eastern nodes (already deep) even deeper. The minimum depths constrained are well below the actual inverted values. Attempts to invert the current at shallower depths (section 5.13.3) were not very successful, and it is likely that the inverted depths set a secure

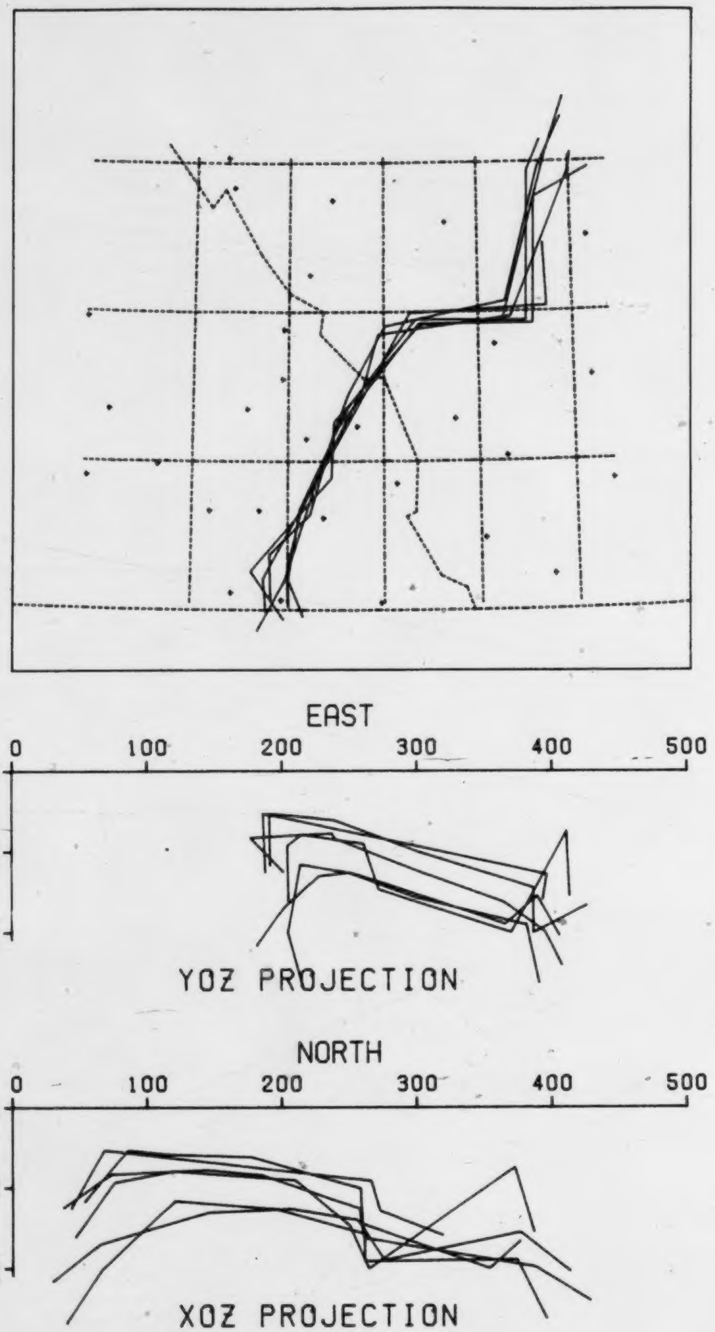

Figure 5.35 Best fitting models from various inversions. Models are from the inversions in Figs.5.23, 5.25, 5.28, 5.30, 5.32, and 5.34. Both XOZ and YOZ projections of the models are given.

minimum for the true depths.

The current sheet inversions in chapter 4 give us a maximum depth of the conductive structure. Before reaching the upper surface of the structure the inverted current sheet shows dominant short wavelength components. Placing the current sheet lower makes the solution divergent. The maximum depth estimated in Chapter 4 is around 55 km. This is not in contradiction with the inversion results in this chapter. The value, 55 km, is the maximum depth of the *shallowest* point of the conductor. The maximum depth thus inferred is very often overestimated (section 9.9 in Grant and West, 1965) because of inevitable loss of short wavelengths from the spectra as a result of sparse station spacing. Therefore, the shallowest point of the conductor is at less than 55 km. The depths of the shallowest nodes inverted in this chapter with loose depth constraints (in favour of deeper models) are around 70-80 km (section 5.13.2), which are supposed to be overestimates. While those inverted with constraints in favour of shallower models are about 30-50 (section 5.13.3). Therefore, the 55 km depth from chapter 4 is between these limits.

Thus the two approaches of current inversion give us a depth range within which the anomalous conductor channels currents. In addition the width of this structure has been estimated to be 60-80 km (Chapters 4 and section 5.13.4). The current inversions have thus to some extent defined the geometry of the structure.

The current inversions offered no direct evidence of the conductivity of this anomalous body beyond order of magnitude estimates. To be effective as a current channel the conductivity of the body has to be at least one order of magnitude larger than the surrounding medium. Taking 10^{-3} S/m, the value for dry rock, as the conductivity of the host medium, then the body has at least a conductivity 10^{-2} S/m. The absolute values of the magnetic fields observed at the surface, the cross section of the body and possible electric field intensity estimates might in principle further limit the conductivity value. MT soundings should in future much improve the estimates of both depth and conductivity of the structure.

5.15 STRUCTURAL IMPLICATIONS OF THE CURRENT INVERSION

Wet sediments at the Earth's surface can sometimes explain most of an observed anomaly, but this is not the case for the 1983 array. The strongest reason to discard such a surface conductor is in the local geology. In this area most near-surface structures have strikes parallel to the Rocky Mountain ridge, notably the Rocky Mountain thrust faulting system down to the depth of a few kilometers (Monger and Price, 1979; Wright, 1984). The magnetovariation fields map a current flowing approximately perpendicular to the regional strike of upper crustal structures. This fact immediately excludes a near-surface origin of the internal fields.

The southern end of the current channel mapped by the array coincides with the Precambrian rift valley proposed by Kanasewich (1968), Fig.5.36 (from Kanasewich, 1968). The depth resolved for that rift is between 30 and 40 km, within the depth range for the nodes of the current models in that area. The Alberta part of the rift was discovered in seismic reflection studies and was then extrapolated by gravity lows and magnetic highs co-existing in its Alberta part down to southern British Columbia. Therefore the southern end of the rift, where it coincides with the current channel, is less certain than its Alberta section. Since the current channel runs SSW-NNE making an angle with the proposed rift, which runs WSW-ENE, and only coincides with the rift at one end, where the rift itself is least securely located, the conductor found is unlikely to be the same rift structure.

In southern Alberta and British Columbia magnetotelluric and geomagnetic depth sounding studies (Gough, 1986, and references there quoted) have revealed complicated conductive structures. The CCR, Canadian Cordilleran Regional conductor (Gough, 1986; Dragert and Clarke 1977; Bingham et al, 1985) is at the south-west corner of the array. Gough (1986) suggested that the north-eastern limit of the CCR conductor lies along the Kootenay Arc (Fig.5.37). From Fig.5.37 (Fig.2 in Gough, 1986) and also from the current inversion of this thesis, the SABC conductor is not in direct contact with the CCR conductor. Camfield et al (1970) in an array, which was in

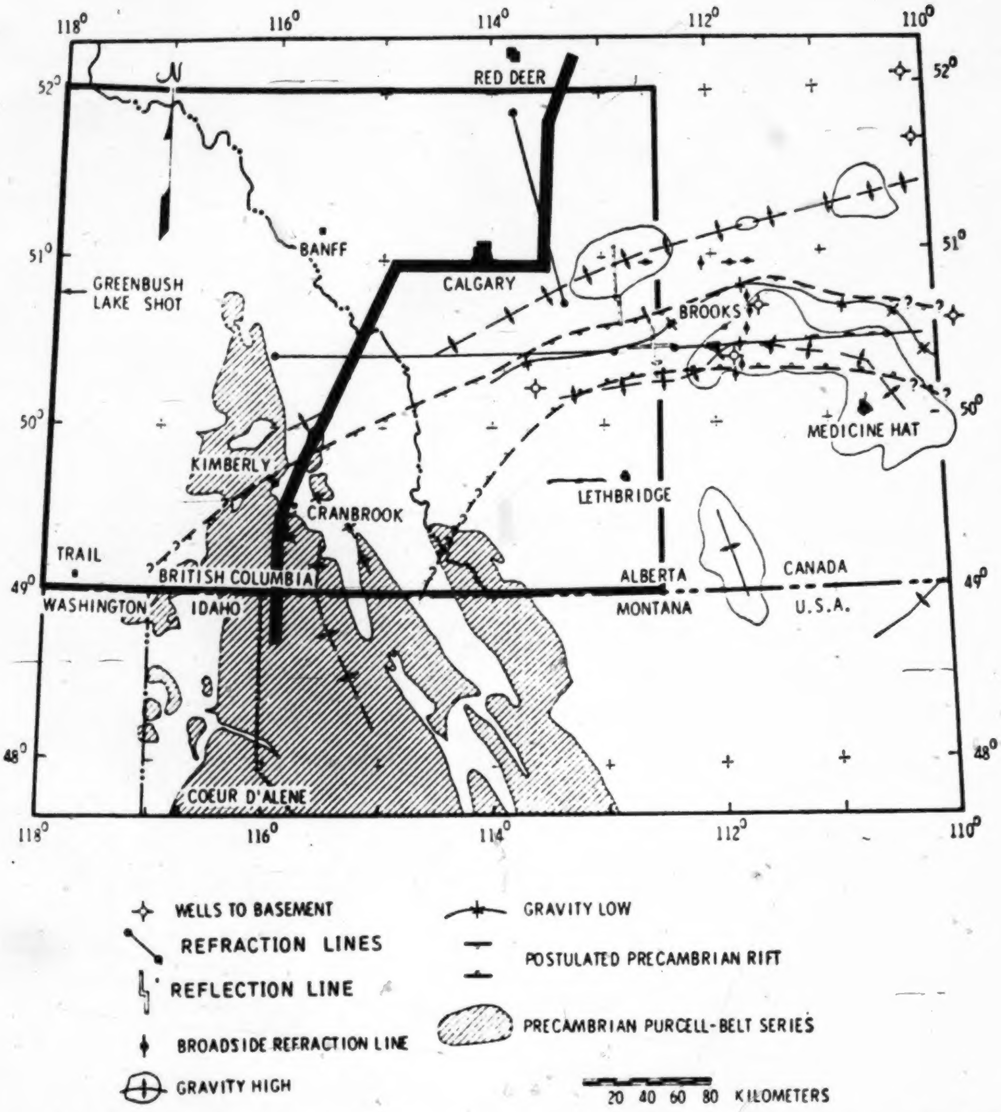
118°
116°
114°
112°
110°
52°
51°
50°
49°
48°
N
RED DEER
BANFF
CALGARY
GREENBUSH LAKE SHOT
BROOKS
KIMBERLY
CRANBROOK
MEDICINE HAT
LETHBRIDGE
TRAIL
BRITISH COLUMBIA
ALBERTA
CANADA
WASHINGTON
IDAHO
MONTANA
U.S.A.
COEUR D'ALENE
WELLS TO BASEMENT
REFRACTION LINES
REFLECTION LINE
BROADSIDE REFRACTION LINE
GRAVITY HIGH
GRAVITY LOW
POSTULATED PRECAMBRIAN RIFT
PRECAMBRIAN PURCELL-BELT SERIES
20 40 60 80 KILOMETERS

Fig. 2. The postulated trace of the Precambrian rift as determined by geophysical evidence. Reflection and refraction profiles and prominent Bouguer gravity anomalies are located, together with Precambrian outcrops in the area.

Figure 5.36 Fig.2 of Kanasewich (1968). The area of the magnetometer array and the current channel inverted are superimposed.

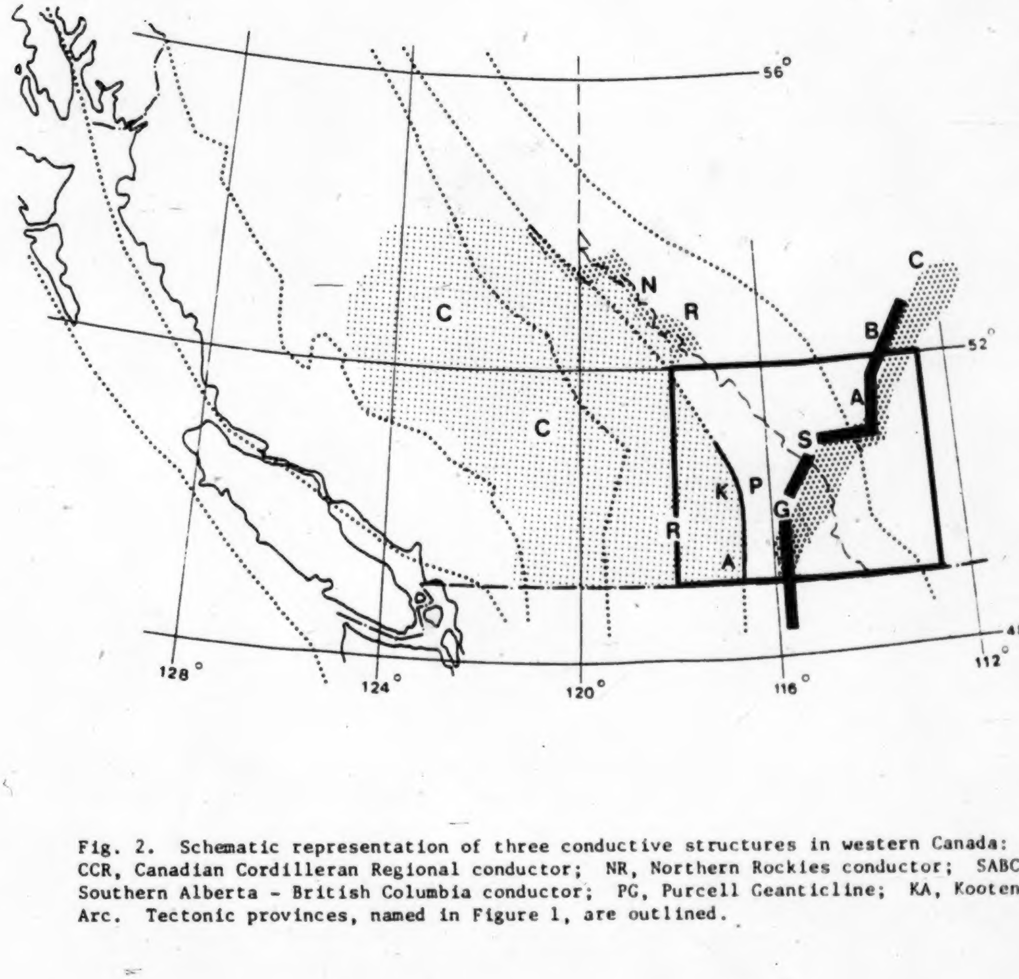

Fig. 2. Schematic representation of three conductive structures in western Canada: CCR, Canadian Cordilleran Regional conductor; NR, Northern Rockies conductor; SABC, Southern Alberta - British Columbia conductor; PG, Purcell Geanticline; KA, Kootenay Arc. Tectonic provinces, named in Figure 1, are outlined.

Figure 5.37 Fig.2 of Gough (1986). The area of the magnetometer array and the current channel inverted are superimposed.

the northwestern United States and southwestern Canada, partly overlapping our array, noticed current flowing to SSW into Washington State. This is the SSW extension of the SABC conductor. Porath et al (1971) modelled it in the depth range 40-60 km, which is very close to the depths resolved by the current inversions in this thesis with loose constraints on depths (section 5.13.2). Such extension is likely to connect the SABC conductor to the massive CCR conductor. Therefore the CCR conductor is possibly serving as one end of the reservoir of induced current, which is channelled though SABC conductor.

Cochrane and Hyndman (1970) calculated transfer functions along an east-west profile across our array at about 49.5°N latitude. They inverted the Grand Forks-Lethbridge (118.5°W-112.5°W) reduced data over a period range of 10-240 minutes to give a 1-D geoelectrical model. A moderately conductive (0.01 S/m) layer is at about 50 km depth for the eastern portion, and a better conductor (0.1 S/m) at about 25 km depth for the western portion. Caner et al (1969) and Caner (1971), combining GDS and MT data, give similar 1-D model for the same area. This dipping of the conductor from west to east is consistent with the plunging of the narrow SABC conductor here reported, and the depths are slightly shallower than those inferred from these current inversions.

Magnetotelluric measurements in southern Alberta by Vozoff and Ellis (1966) partly coincided with the 1983 array. One of their stations (Beiseker) is on the track of the current channel at 51.6°N. The depth of conductivity increase, from 10^{-4} to 10^{-2} S/m, is at 80 km depth, which is consistent with the depths of currents (nodes in that area) resolved with weak current constraints (section 5.13.3). The depth of the Moho north-east of the Rockies has a local maximum, shown in Fig.5.38 (Fig.10 in Kanasewich et al, 1987) The plunging of the SABC conductor follows the deepening of the Moho west of 114°W and continues to plunge while the depth of the Moho along the conductor decreases gently (Fig.5.38). The north-easterly plunging of the SABC conductor is therefore supported by other geophysical results. The conductor may well be very close to the Moho, either above or below it.

Seismic refraction studies in the southern Rocky mountain trench from 50°N to 53°N revealed a low velocity zone 8 km beneath the Moho, at 50 km, and approximately 7 km thick (Bennett et al, 1975). Wickens (1971) used phase velocities of Rayleigh and Love surface waves to study the lithosphere structure in Canada. He also noticed a profound LVZ in western Canada, V_s as low as 4.20 km/sec. between 50-90 km depths. This LVZ might coincide with a good conductor. The LVZ is likely to have larger horizontal extent than the narrow SABC conductor. If the LVZ is lifted along the proposed location of the SABC conductor, it can serve the purpose as well. Actually, the model suggested by Porath et al (1971) to explain the linear conductor (the

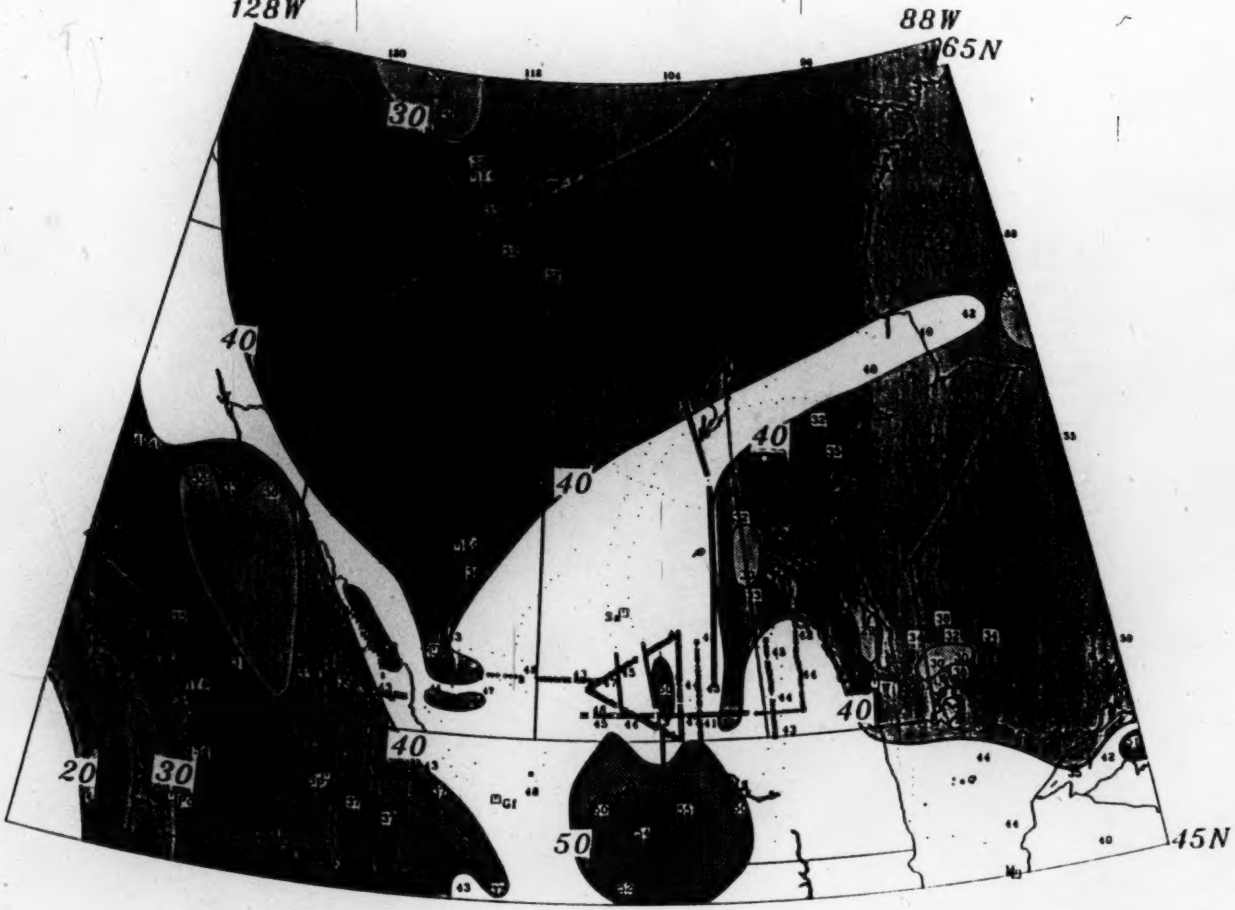
128W
88W
65N
45N
30
40
40
40
40
40
40
20
30
50

Figure 5.38 Depth of the Moho in km, Fig.10 of Kanasewich et al (1987).

extension of SABC conductor), is a local uplifting of a highly conductive layer at the proposed position of the linear conductor.

This part of the Canadian Cordillera has been found to have high geothermal flux (Davis and Lewis, 1984). Hot material in the upper mantle necessarily explains the LVZ and high conductivity (Stacey, 1977, chap.8; Gough, 1986).

Even with constraints in favour of a shallower model the depths of nodes east of the Rockies are always considerably deeper than the depth of Moho there. Consequently, at least the north-eastern portion of the SABC conductor is unlikely to be within the crust. The south-western nodes can be as shallow as in the crust with some specific constraints imposed during inversion. A conductor connecting the crust and mantle is difficult to explain, unless an active subduction is involved, say, along the plunging portion of the conductor. Therefore, the deeper mantle models are preferred. Considering that the current inversion tends to give results of biased (to greater) depths, a shallower model of crustal origin cannot be excluded.

The plunging portion of the SABC conductor (Fig. 5.35) runs mainly east-west. This segment of current produces mainly the X (north) component of the fields. The model misfit has an obvious gradient near the point where the current makes a sharp turn to the north (e.g. Fig.5.33). This shows the inadequacy of both the line and the constant-width sheet current models. The reality of the plunging of the SABC conductor is therefore open to question. If the plunging of the conductor is less emphasized, the depths resolved for the south-western portion of the conductor are considered to be more reliable. The structure, then, may very well reside in the lower crust. The lower crust conductor could be related to conductive mineralization or to saline water (Gough and Ingham, 1983; Gough, 1986a).

6. CONCLUSIONS

The major contributions of this thesis can be divided into two categories, data representation (chapters 2 and 3) and inversion (chapters 4 and 5).

The normal-field estimation by the plane-wave representation (chapter 2) is essentially a smoothing scheme. This smoothing is suitable for the analysis of substorm events observed at middle and low latitudes over an anomalous conductive structure in the lower crust or upper mantle. For such an external-internal current source configuration, the normal field is expected to be smooth. Two major advantages of this representation are the ability to recognize the weights of contributions from internal and external sources and the ability to use this representation as a guide in the choice of frequency components for further analysis. Using the methods developed in chapter 3, It may be possible to separate the long-wavelength components into external and internal parts. However, rigorous tests are needed in order to confirm the accuracy of such separations since they may not be very reliable for fields with spatial wavelengths much larger than the array dimensions.

The separation of fields into internal and external parts in the wave-number domain is computationally efficient. Applications to both synthesized and field data have proved to be satisfactory and easy to use. In addition, the results of the separation are in a form which allows further analysis in both space and wave-number domains. This form of the separated data allows easy comparison of the separated data with wave number domain solutions of the Maxwell equations and is a prerequisite for the current sheet inversions in chapter 4.

The inversion of fields to a horizontal current sheet in a conducting medium is suitable for some configurations of both locally induced and channelled currents. For the former case, the choice of a normal geoelectric section may be important especially for a short period fields. For the channelled currents of long period fields, however, any model with low conductivity is adequate.

The inversion to 3-D line or constant-width sheet current is geometrically the most complicated set of models chosen for current inversion in this thesis. It best suits the inversion of channelled currents and offers no direct estimates of the conductivity of the anomalous structure. The next step in sophistication for such models is to place the model current in a conducting medium to allow the estimation of the shielding effects of that medium. The solution of the combined fields of local induction and current channelling in general, as a solution of the Maxwell equations, would require better data coverage both in time and space.

The schemes developed in this thesis, for regulating the inversion iteration process, are applicable to parametric inversions in general.

The W-stabilization scheme is a simple and practical approach to the control of systematic errors in the data. An understanding of the nature of any systematic errors is the key to the proper formation of such **W** vectors. A uniform systematic error is the simplest case and is suggested for most inversions to compensate for any baseline shifts due to either instrumentation or digitization errors.

The programming technique *LSINL* is suitable for overdetermined problems, and resembles the ordinary least squares solution when the linear inequality constraints are dropped (or set very loose). It is possible to implement the concept of *damped least squares* (e.g. Menke, 1984) into the *LSINL* programming to make it more general and flexible.

The *LDPNL* programming is applicable to both over- and under-determined problems. A model can be inverted to fit the data with the desired accuracy by compressing the error bars to preset lower limits only. The error compression method provides a flexible way to control the iteration process, and can be further improved to speed up the convergence to a stable solution.

At present the *LSINL* and the *LDPNL* methods cannot directly estimate the errors in the resolved model parameters. The ranges in of the model parameters can be obtained by changing the constraints on the model as illustrated in chapter 5. It is possible to study the errors mapped into the model parameters from those in the data by examining the variation of the estimates of the parameters of the model when the error bars for the *LDPNL* inversion are changed.

The strategy developed in this thesis has proved to be successful in the estimation of the 3-D geometry of the SABC conductor especially when the models are compared with other geophysical and geological data for the same area. With some modifications, this strategy is expected to be applicable to investigating the geometry of the external ionosphere and magnetosphere sources of the magnetovariation fields.

BIBLIOGRAPHY

Alabi, A.O., Camfield, P.A. and D.I. Gough, The North American central planes conductivity anomaly, Geophys. J. R. astr. Soc., **43**, 815-833, 1975.

Bailey, R.C., Inversion of the geomagnetic induction problem, Proc. Roy. Soc London **A315**, 185-194, 1970.

Bailey, R.C., Edwards, R.N., Garland, G.D., Kurtz, R. and D. Pitcher, Electrical conductivity studies over a tectonically active area in eastern Canada, J. Geomagn. Geoelec., **26**, 125-146, 1974.

Banks, R.J., Geomagnetic variations and the electrical conductivity of the upper mantle, Geophys. J. R. astr. Soc., 17, 457-487, 1969.

Banks, R.J., The use of equivalent current systems in the interpretation of geomagnetic deep sounding data, Geophys. J. R. astr. Soc., **56**, 139-157, 1979.

Bennett, G.T., Clowes, R.M. and R.M. Ellis, A seismic referaction survey along the Southern Rocky Mountain trench, Canada, Bull. Seismo. Soc. America, **65**, 37-54, 1975.

Berdichevsky, M.N. and M.S. Zhdanov, Advanced theory of deep geomagnetic sounding, Elsevier, 408 pp., 1984.

Bingham, D.K., Gough, D.I. and M.R. Ingham, Conductive structure under the Canadian Rocky Mountains, Can. J. Earth Sci., **22**, 384-398, 1985.

Brewitt-Taylor, C.R. and J.T. Weaver, On the finite difference solution of two-dimensional induction problems, Geophys. J. R. astr. Soc., **41**, 193-218, 1975.

Camfield, P.A., Gough, D.I. and H. Porath, Magnetometer array studies in the north-western United States and south-western Canada, Geophys. J. R. astr. Soc., **22**, 201-221, 1970.

Caner, B., Camfield, P.A., Anderson, F. and E.R. Neblett, A large-scale magnetotelluric survey in western Canada, Can. J. Earth Sci., **6**, 1245-1261, 1969.

Caner, B., Quantitative interpretation of geomagnetic depth-sounding in western Canada, J. Geophys. Res., **76**, 7202-7216, 1971.

Chandra, N.N. and G.L. Cumming, Seismic refraction studies in western Canada, Can. J. Earth Sci., 9, 1099-1109, 1972.

Chapman, S. and J. Bartels, Geomagnetism, Oxford University Press, 1049 pp., 1940.

Chen, P.F. and P.C.W. Fung, Significance of the sign changing of the imaginary arrows in geomagnetic induction investigation, Geophys. J. R. astr. Soc., 80, 257-263, 1985.

Cochrane, N.A. and R.D. Hyndman, A new analysis of geomagnetic depth-sounding data from western Canada, Can. J. Earth Sci., 7, 1208-1218, 1970.

Cushing, J.T., Applied analytical mathematics for physical scientists, John Wiley and Sons, 651 pp., 1975.

Davis, E.E. and T.L. Lewis, Heat flow in a back-arc environment: Intermontane and Omineca crystalline belts, southern Canadian Cordillera, Can. J. Earth Sci., 21, 715-726, 1984

Dawson, T.W. and J.T. Weaver, Three-dimensional electromagnetic induction in a non-uniform thin sheet at the surface of a uniform conducting Earth, Geophys. J. R. astr. Soc., 59, 445-462, 1979.

Dragert, H. and G.K.C. Clarke, A detailed investigation of the Canadian Cordillera geomagnetic transition anomaly, J. Geophys., 42, 373-390, 1977.

Fowler, R.A., Kotick, B.J. and R.D. Elliott, Polarization analysis of natural and artificially induced geomagnetic micropulsation, J. Geophys. Res., 72, No.11, 2871-2883, 1967.

Fu, C.-Y., Zeng, R.-S., Chen, Y.-T. and G.-Z. Qi, Basics of geophysics, in Chinese, Graduate School Press, Graduate School, Scientifia Sinica, P.R.China, 899 pp., 1978.

Gough, D.I. and J.S. Reitzel, A portable three-component magnetic variometer, J. Geomagn. Geoelec., 19, 203-215, 1967.

Gough, D.I. and M.R. Ingham, Interpretation methods for magnetometer arrays, Rev. Geophys. Space Phys., 21, 4, 805-827, 1983.

Gough, D.I., Mantle upflow tectonics in the Canadian Cordillera, J. Geophys. Res., 91, No.B2, 1909-1919, 1986.

Gough, D.I., Seismic reflectors, conductivity, water and stress in the continental crust, Nature, **323**, No.6084, 143-144, 1986a.

Grant, F.S. and G.F. West, Interpretation theory in applied geophysics, MaGraw-Hill, 584 pp., 1965.

Gregori, G.P. and L.J. Lanzerotti, Geomagnetic depth sounding by induction arrow presentation: a review, Rev. Geophy. Space Phys., **18**, No.1, 203-209, 1980.

Ingham, M.R., Bingham, D.K. and D.I. Gough, A magnotovariational study of a geothermal anomaly, Geophys. J. R. astr. Soc., **72**, 597-618, 1983.

Jackson, J.D., Classical electrodynamics, John Wiley and Sons, 848 pp., 1975.

Jones, A.G., On the difference between polarization and coherence, J. Geophys., **45**, 223-229, 1979.

Jones, A.G., Geomagnetic induction studies in Scandinavia I. Determination of inductive response function from the magnetometer array data, J. Geophys., **48**, 181-194, 1980.

Jones, A.G., Comment on "Geomagnetic depth sounding by induction arrow presentation: a review" by G.P. Gregori and L.J. Lanzerotti, Rev. Geophy. Space Phys., **19**, No.4, 687-688, 1981.

Jones, A.G., The problem of current channelling: A critical review, paper presented at Sixth Workshop on Electromagnetic Induction in the Earth and Moon, Working Group I-3, IAGA., Vectoria, B.C., Canada, 1982.

Jones, A.G., On the use of line current analogues in geomagnetic depth sounding, J. Geophys., **60**, 56-62, 1986.

Jones, F.W. and L.J. Pascoe, A general computer program to determine the perturbation of alternating electric currents in a two-dimensional model of a region of uniform conductivity with an embedded inhomogeneity, Geophys. J. R. astr. Soc., **24**, 3-30, 1971.

Kamide, Y., The relationship between field-aligned currents and the auroral electrojets: A review, Space Sci. Rev., **31**, 127-243, 1982.

Kanasewich, E.R., Precambrian rift: genesis of strata-bound ore deposits, Science, **161**, 1002-1005, 1968.

Kanasewich, E.R., Time sequence analysis in geophysics, University of Alberta Press, 480 pp., 1981.

Kanasewich, E.R., Hajnal, Z., Green, A.G., Cumming, G.L., Mereu, R.F., Clowes, R.M., Morel-a-l'Huissier, Chiu, S., Congram, A.M., Macrides, C.G. and M. Shahriar, Seismic studies of the crust under the Williston Basin, Can. J. Earth Sci., submitted 1987.

Kaufman, A.A. and G.V. Keller, The magnetotelluric sounding method, Elsevier, 595 pp., 1981.

Kramer, H.P. and M.V. Mathews, A linear coding for transmitting a set of correlated signals, 38th Annual ISEG meeting, Denver, Co., 1968.

Kuckes, A.F., Relations between electrical conductivity of a mantle and fluctuating magnetic fields, Geophys. J. R. astr. Soc., **32**, 119-131, 1973.

Laczos, C., Linear differential operators, Van Nostrand-Reinhold, Princeton, New Jersey, 1961.

Lavin, P.M. and S.J. Devane, Direct design of two-dimensional digital wavenumber filters, Geophysics, 35, No.6, 1970.

Lawson, C.L. and D.J. Hanson, Solving least squares problems, Prentice-Hall, Englewood Cliffs, New Jersey, 340 pp., 1974.

Lilley, F.E.M. and B.R. Bennett, An array experiment with magnetic variometers near the coasts of south-east Australia, Geophys. J. R. astr. Soc., **29**, 49-64, 1972.

Lilley, F.E.M. and B.R. Arora, The sign convention for quadrature Parkinson arrows in geomagnetic induction studies, Rev. Geophy. Space Phys., **20**, No.3, 513-518, 1982.

Marquardt, D.W., An algorithm for least-squares estimation of non-linear parameters, J. SIAM 11, 431-441, 1963.

McKirdy, D.McA., Weaver, J.T. and T.W. Dawson, Induction in a thin sheet of variable conductance at the surface of a stratified Earth-II. three dimensional theory, Geophys. J. R. astr. Soc., **80**, 177-194, 1985.

McKirdy, D.McA., Two-dimensional modelling using the "thick sheet approximation", 8 th Induction Workshop, Neuchatel, Switzerland, 1986.

McMechan, G.A. and I. Barrodale, Processing electromagnetic data in time domain, J. Geomagn. Geoelec., **81**, 277-293, 1985.

Means, J.D., Use of the three-dimensional covariance matrix in analyzing the polarization properties of plane waves, J. Geophys. Res., 77, No.28, 5551-5559, 1972.

Menke, W., Geophysical data analysis: discrete inverse theory, Academic Press, Inc., 260 pp., 1984.

Monger, J.W.H. and R.A. Price, Geodynamic evolution of the Canadian Cordillera—progress and problems, Can. J. Earth Sci, **16**, 770-791, 1979.

Neumann, G.A., Smooth two dimensional inversion of magnetic variation data, 8 th Induction Workshop, Newchatel, Switzerland, 1986.

Oldenburg, D.W., Separation of magnetic substorm fields for mantle conductivity studies in the western United States, unpublished M. Sc. thesis, Univ. of Alberta, Edmonton, 1969.

Oldenburg, D.W., An introduction to linear inverse theory, IEEE Transactions on Geoscience and Remote sensing, **GE-22**, No.6, November, 1984.

Parkinson, W.D. and F.W. Jones, The geomagnetic coast effect, Rev. Geophy. Space Phys., **17**, No.8, 1999-2015, 1979.

Parkinson, W.D., Introduction to geomagnetism, Elsevier, 433 pp., 1983.

Porath, H., Oldenburg, D.W. and D.I. Gough, Separation of magnetic variation fields and conductive structures in the western United States, Geophys. J. R. astr. Soc., **19**, 237-260, 1970.

Porath, H., Gough, D.I. and P.A. Camfield, Conductive structures in north-western United States and south-west Canada, Geophys. J. R. astr. Soc., **23**, 387-398, 1971.

Price, A.T., Electromagnetic induction in a semi-infinite conductor with a plane boundary, Quart. J. Mech. Applied Math. **3**, Pt.4, 385-410, 1950.

Price, A.T. and G.A. Wilkins, New methods for the analysis of geomagnetic fields and their application to the Sq field of 1932-3, Philos. Trans. R. Soc. London, Ser. A, **256**, 31-98, 1963.

Rikitake, T., Electromagnetic shielding within the Earth and geomagnetic secular variation, Bull. Earthq. Res. Inst. Tokyo Univ., **29**, 263-269, 1951.

Rokityansky, I.I., Geoelectromagnetic investigation of the

Earth's crust and mantle, Springer-Verlag, 381 pp., 1982.

Rostoker, G., Polar magnetic substorms, Rev. Geophys. Space Phys., 10, No.1, 157-211, 1972.

Samson, J.C. and J.V. Olson, Some comments on the descriptions of the polarization states of waves, Geophys. J. R. astr. Soc., 61, 115-129, 1980.

Samson, J.C., The spectral matrix, eigenvalues and principal components in the analysis of multichannel geophysical data, Annales Geophys., 1, 2, 115-119, 1983.

Schmuker, U., Anomalies of geomagnetic variation in the south-western United States, J. Geomagn. Geoelec., 15, 193-221, 1964.

Schmuker, U., Anomalies of geomagnetic variations in the Southwestern United States, Bull. Scripps Inst. Oceanogr, Univ. of California, 13, 1970.

Spence, G.D., Clows, R.M. and R.M. Ellis, Depth limits on the M discontinuity in the southern Rocky Mountain Trench, Canada, Bull. Seismol. Soc. Am., 67, 543-546, 1977.

Stacey, F.D., Physics of the Earth, 2nd edition, John Wiley, 414 pp., 1977.

Stinson, K. and D.W. Oldenburg, 2-D inversion of geomagnetic depth sounding data, paper presented at Sixth Workshop on Electromagnetic Induction in the Earth and Moon, Working Group I-3, IAGA., Vectoria, B.C., Canada, 1982.

Tikhonov, A.N., Mathematical basis of the theory of electromagnetic soundings, Zh. vychisl. Mat. mat. Fiz., 5, 3, 545-548, 1965.

Tripp, A.C. and G.W. Hohmann, Block diagonalization of the electromagnetic impedance matrix of a symmetric buried body using group theory, IEEE Trans. Geosci. Remote Sensing, GE-22, 62-69, 1984.

Vestine, E.H., On the analysis of surface magnetic fields by integrals, part I, Terr. Magn. Atmos. Electr., 46, 27-41, 1941.

Vozoff, K. and R. Ellis, Magnetotelluric measurements in southern Alberta, Geophysics, 31, 1153-1157, 1966.

Wannamaker, P.E., Hohmann, G.W. and W.A. SanFilipo, Electromagnetic modeling of three-dimensional bodies in layered Earth using integral equations, Geophysics, 49, 60-74, 1984.

Weaver, J.T., On the separation of local geomagnetic fields into external and internal parts, Zeits. Für Geophys., 30, 29-36, 1964.

Wickens, A.J., Variation in lithosphere thickness in Canada, Can. J. Earth Sci., 8, 1154-1162, 1971.

Wiese, H., Geomagnetische Tiefentellurik, Deutsche Akad. Wiss. Berlin, Geomagn. Inst. Potsdam, Abh. 36, 1-146, 1965.

Wiggins, R.A., The general linear inverse problem: implication of surface waves and free oscillations for Earth structure, Rev. Geophys. space Phys., 10, 251-285, 1972.

Woods, D.V. and F.E.M. Lilley, Geomagnetic induction in central Australia, J. Geomagn. Geoelec., 31, 449-458, 1979.

Woods, D.V. and F.E.M. Lilley, Anomalous geomagnetic variations and the concentration of telluric currents in south-west Queensland, Australia, Geophys. J. R. astr. Soc., 62, 675-689, 1980.

Wright, G.N., editor, The western Canada sedimentary basin (map), Canadian Petroleum Geologists, 1984.

APPENDIX 1: NATURE OF THE INDUCTION MATRIX D

For components of fields with the same space (m,n) and time (ω) dependence, layers of a given conductivity are characterized by the same parameter θ as defined in (4.20). In this section the **D** matrix of a layer of thickness h will be denoted $\mathbf{D}(\theta,h)$, and the nature of these matrices will be examined.

1. **D** is a quasi-equal-power matrix:

$$(A.1) \qquad \mathbf{D}(\theta,h_1+h_2) = \mathbf{D}(\theta,h_1)\cdot\mathbf{D}(\theta,h_2)$$

From (4.35), the r.h.s of (A.1) becomes

$$\mathbf{D}(\theta,h_1)\cdot\mathbf{D}(\theta,h_2) =$$

$$= \begin{bmatrix} ch(\theta h_1) & sh(\theta h_1)\cdot\theta \\ sh(\theta h_1)/\theta & ch(\theta h_1) \end{bmatrix} \begin{bmatrix} ch(\theta h_2) & sh(\theta h_2)\cdot\theta \\ sh(\theta h_2)/\theta & ch(\theta h_2) \end{bmatrix}$$

As

$$sh(a)ch(b)+ch(a)sh(b)=sh(a+b)$$
$$ch(a)ch(b)+sh(a)sh(b)=ch(a+b)$$

the above product becomes

$$= \begin{bmatrix} ch[\theta(h_1+h_2)] & sh[\theta(h_1+h_2)]\cdot\theta \\ sh[\theta(h_1+h_2)]/\theta & ch[\theta(h_1+h_2)] \end{bmatrix} = \mathbf{D}(\theta,h_1+h_2)$$

2. The **D** matrix is quasi-Abelian (Cushing, 1975, p.539):

(A.2) $$\mathbf{D}(\theta,h_1)\cdot\mathbf{D}(\theta,h_2) = \mathbf{D}(\theta,h_2)\cdot\mathbf{D}(\theta,h_1)$$

From (A.1):

$$\mathbf{D}(\theta,h_1)\cdot\mathbf{D}(\theta,h_2) = \mathbf{D}(\theta,h_1+h_2) \equiv \mathbf{D}(\theta,h_2+h_1) = \mathbf{D}(\theta,h_2)\cdot\mathbf{D}(\theta,h_1)$$

3. A layer of zero thickness and finite conductivity does not modify the field propagation. This implies that

(A.3) $$\lim \mathbf{D}(\theta,h\to 0) \to \mathbf{I}.$$

When

$$\theta h = h\cdot\sqrt{(i\omega\mu\sigma+\nu^2)} \to 0, \quad \theta^2 h \to 0 \text{ and}$$
$$ch(\theta h) \cong 1+\theta^2h^2 \to 1$$
$$sh(\theta h)/\theta \cong h \to 0$$
$$sh(\theta h)\cdot\theta \cong \theta^2 h \to 0$$

Thus in this case (4.35) reduces to:

(A.4) $$\mathbf{D}(\theta,h\to 0) \cong \begin{bmatrix} 1 & \theta^2 h \\ h & 1 \end{bmatrix} \to \mathbf{I}$$

Equation (A.4) can be extended to show that the induction matrix of an infinitesimally thin layer is the sum of an identical matrix I and an infinitesimal matrix $\delta D(\theta,h)$ proportional to h:

(A.5) $$\delta D = Q(z)\cdot h$$

where Q(z) is a function of z determined by the z dependence of the conductivity $\sigma(z)$:

(A.6) $$Q(z) = \begin{bmatrix} 0 & \theta^2 \\ 1 & 0 \end{bmatrix} = \begin{bmatrix} 0 & i\omega\mu_0\sigma(z)+\nu^2 \\ 1 & 0 \end{bmatrix}$$

Thus the induction matrix of such a layer is:

(A.7) $$D(z) = I+Q(z)\cdot h$$

APPENDIX 2: ANALYTIC SOLUTION FOR ARBITRARY DEPTH-DEPENDENCE OF THE CONDUCTIVITY

In the recursive method of solving for the electromagnetic field immediately below $z=z_j$ the observed field v_0 is transformed by the following matrices of (4.27c):

$$(D_{j+1}^{-})^{-1} \{ D_j \cdots D_1 \} D_0^{+} \tag{4.28d}$$

For $\sigma(z)$ an arbitrary function of z, the Earth can be considered as an infinite number of infinitesimally thin layers. The induction matrix corresponding to each infinitesimal layer is:

$$D(z) = I+Q(z)\cdot dz \tag{A.8}$$

The set of Q(z)'s depends on a continuum z and is a continuous function of it.

The product of an infinite number of induction matrices of all the layer elements in a layer with upper surface at $z=z^-$ and lower surface at $z=z^+$ can be reduced to a sum of integrations:

$$\prod_{z-}^{z+} D(z) \cong I + \sum_{z-}^{z+} Q(x)\delta x + \sum_{z-}^{z+} Q(x)\delta x\cdot\sum_{y=z-}^{x} Q(y)\delta y + \\ + \sum_{z-}^{z+} Q(x)\delta x\cdot\sum_{y=z-}^{x} Q(y)\delta y\cdot\sum_{z=z-}^{y} Q(z)\delta z + \cdots \tag{A.9}$$

$$(\delta x \cdot\cdot \to 0) \to \; I + \int_{z^-}^{z^+} Q(x)dx + \int_{z^-}^{z^+} Q(x)dx \cdot \int_{z^-}^{x} Q(y)dy \; +$$

$$+ \int_{z^-}^{z^+} Q(x)dx \cdot \int_{z^-}^{x} Q(y)dy \cdot \int_{y}^{y} Q(z)dz + \cdots$$

Rewrite the above as an infinite series:

$$\text{(A.10)} \qquad D(\theta, z^+ - z^-) = \sum_{i=0}^{\infty} W_i(z^+)$$

in which,

$$\text{(A.11)} \qquad W_0(z^+) \equiv I$$

$$\text{(A.12)} \qquad W_1(z^+) = \int_{z^-}^{z^+} Q(x)dx$$

$$\text{(A.13)} \qquad W_j(z^+) = \int_{z^-}^{z^+} Q(x) \cdot W_{j-1}(x)dx \qquad j = 2, 3, \cdots$$

At first glance it seems forbidding to predict the form of W terms of higher orders. Because of the special form of matrix Q, it is easy to prove that

$$\text{(A.14)} \qquad W_j(z^+) = \int_{z^-}^{z^+} dx_1 \int_{z^-}^{x_1} dx_2 \; \cdots \; \int_{z^-}^{x_{j-1}} dx_j \; w_j(x_1, x_2, \; \cdots \; x_j)$$

Here for j even,

$$\text{(A.15)} \qquad w_j = \begin{bmatrix} \Theta(x_1)\Theta(x_3)\cdots\Theta(x_{j-1}) & 0 \\ 0 & \Theta(x_2)\Theta(x_4)\cdots\Theta(x_j) \end{bmatrix}$$

$$j = 2, 4, 6, \cdots$$

while for j odd,

$$(A.16) \qquad w_j = \begin{bmatrix} 0 & \Theta(x_1)\Theta(x_3)\cdots\Theta(x_j) \\ \Theta(x_2)\Theta(x_4)\cdots\Theta(x_{j-1}) & 0 \end{bmatrix}$$

$$j = 3,\ 5,\ 7,\cdots$$

The complex parameter $\Theta(x)$ is:

$$(A.17) \qquad \Theta(x) = i\omega\mu_0\sigma(x)+\nu^2$$

It is easy to prove that a series of the type of (A.9) or (A.10) converges for an N*N matrix Q if there is a definite upper limit for all the matrix element Q_{ij} between the integration limits.

Suppose we have, for all i and j,

$$|\ Q_{ij}(z)\ | \le M, \qquad z^+ \ge z \ge z^-$$

Then,

$$\begin{aligned} |\ D_{ij}(\theta,z^+-z^-)\ | &\le \delta_{ij} + \sum_{k=1}^{\infty} \{\ N^{k-1}M^k \int_{z-}^{z+}dx_1 \int_{z-}^{x1}dx_2 \cdots \int_{z-}^{xk-1}dx_k\ \} \\ &\le \sum_{k=0}^{\infty} \{\ N^k M^k (z^+-z^-)^k/k!\ \} \\ &= \exp[NM(z^+-z^-)] \end{aligned}$$

Numerical integration of (A.9) is tedious and only for very long wavelengths and very long periods does it converge reasonably fast. Semi-analytical integration is preferred. Representing the conductivity profile as a polynomial function of depth, analytical integration of (A.9) can be performed by a computer to determine coefficients of the integrated polynomial. The convenience of this type of solution is that it depends on only a standard school of functions, here the function in (4.7), and one only has to determine the coefficients of this standard function through matrix integration like (A.9). Of course the derived coefficients are only valid for the immediate neighborhood of the depth to which the integration is carried from the surface.

APPENDIX 3: W_l VECTOR

The solution of the least square problem (5.24b) is denoted as $\mathbf{W}_l$ referring to stabilization from the left hand side of the misfit equation. For simplicity I take uniform normal field as

$$\text{(A.18)} \qquad \mathbf{B}_n = \{B_{ox}, B_{oy}, B_{oz}\}$$

Now the **W** vector has the form:

$$\text{(A.19)} \qquad \mathbf{W} = \{\cdots,\ B_{ox},\ B_{oy},\ B_{oz},\ \cdots\}$$

or,

$$\text{(A.20)} \qquad W_k = \begin{array}{ll} B_{ox} & k=1,4,7 \cdots 3M-2 \\ B_{oy} & k=2,5,8 \cdots 3M-1 \\ B_{oz} & k=3,6,9 \cdots 3M \end{array}$$

The objective function for the least square problem (5.24b) is

$$\text{(A.21)} \qquad \phi_l = \sum_i \sum_k [A_i{}^{\dagger}{}_k \delta(D_k^o + W_k)]^2$$

Substitute (A.20) into (A.21) and set $\partial\phi_r/\partial a$ to zero, $a = B_{ox}$, B_{oy}, B_{oz}, we get $\mathbf{B}_o$ as the solution of the following set of linear equations:

$$\text{(A.22)}\qquad \sum_{k=1}^{3} F_{ik}B_{0k}=M_i \qquad i=1,2,3$$

where,

$$M_i=\sum_{k=1}^{3n+1} D_{ki}C_k$$

$$\text{(A.23)}\qquad F_{ik}=-\sum_{s=1}^{3n+1} D_{si}D_{sk}$$

$$D_{ki}=\sum_{s=0}^{m-1} A^{\dagger}_{k,3s+1}$$

$$C_k=\sum_{s=1}^{3m} A^{\dagger}_{ks}\delta D^{\circ}_s$$

From a simple test (not presented here), with the $\mathbf{W}_1$ vector included in the model misfit vector the norm of $\delta\mathbf{D}^{+}$, the modified misfit vector, is found to be smaller than that of $\delta\mathbf{D}^{\circ}$, the unmodified one. Even though the $\mathbf{W}_1$ vector is designated to minimize the model correction *not* the misfit vector. Similarly, the $\mathbf{W}_r$ modified misfit vector produces smaller model correction, though it is designated to minimize the model misfit vector. This is physically plausible, since smaller model misfit usually requires smaller correction to the model and *vice versa*. Mathematically matrix manipulation does not always give such results.